



National Library  
of Canada

Acquisitions and  
Bibliographic Services Branch

395 Wellington Street  
Ottawa, Ontario  
K1A 0N4

Bibliothèque nationale  
du Canada

Direction des acquisitions et  
des services bibliographiques

395, rue Wellington  
Ottawa (Ontario)  
K1A 0N4

*Your file - Votre référence*

*Our file - Notre référence*

## NOTICE

The quality of this microform is heavily dependent upon the quality of the original thesis submitted for microfilming. Every effort has been made to ensure the highest quality of reproduction possible.

If pages are missing, contact the university which granted the degree.

Some pages may have indistinct print especially if the original pages were typed with a poor typewriter ribbon or if the university sent us an inferior photocopy.

Reproduction in full or in part of this microform is governed by the Canadian Copyright Act, R.S.C. 1970, c. C-30, and subsequent amendments.

## AVIS

La qualité de cette microforme dépend grandement de la qualité de la thèse soumise au microfilmage. Nous avons tout fait pour assurer une qualité supérieure de reproduction.

S'il manque des pages, veuillez communiquer avec l'université qui a conféré le grade.

La qualité d'impression de certaines pages peut laisser à désirer, surtout si les pages originales ont été dactylographiées à l'aide d'un ruban usé ou si l'université nous a fait parvenir une photocopie de qualité inférieure.

La reproduction, même partielle, de cette microforme est soumise à la Loi canadienne sur le droit d'auteur, SRC 1970, c. C-30, et ses amendements subséquents.

**Transverse Energy and Charged Particle Multiplicity in  
14.6 GeV/c Proton-Nucleus Collisions**

**Gang Wang  
Physics Department  
McGill University, Montréal  
September, 1994**

**A Thesis submitted to the Faculty of Graduate Studies and Research  
in partial fulfillment of the requirements for the degree of  
Doctor of Philosophy**

**© Gang Wang, 1994**



National Library  
of Canada

Bibliothèque nationale  
du Canada

Acquisitions and  
Bibliographic Services Branch

Direction des acquisitions et  
des services bibliographiques

395 Wellington Street  
Ottawa, Ontario  
K1A 0N4

395, rue Wellington  
Ottawa (Ontario)  
K1A 0N4

Your file    *Notre référence*

*Our file    Notre référence*

THE AUTHOR HAS GRANTED AN IRREVOCABLE NON-EXCLUSIVE LICENCE ALLOWING THE NATIONAL LIBRARY OF CANADA TO REPRODUCE, LOAN, DISTRIBUTE OR SELL COPIES OF HIS/HER THESIS BY ANY MEANS AND IN ANY FORM OR FORMAT, MAKING THIS THESIS AVAILABLE TO INTERESTED PERSONS.

L'AUTEUR A ACCORDE UNE LICENCE IRREVOCABLE ET NON EXCLUSIVE PERMETTANT A LA BIBLIOTHEQUE NATIONALE DU CANADA DE REPRODUIRE, PRETER, DISTRIBUER OU VENDRE DES COPIES DE SA THESE DE QUELQUE MANIERE ET SOUS QUELQUE FORME QUE CE SOIT POUR METTRE DES EXEMPLAIRES DE CETTE THESE A LA DISPOSITION DES PERSONNE INTERESSEES.

THE AUTHOR RETAINS OWNERSHIP OF THE COPYRIGHT IN HIS/HER THESIS. NEITHER THE THESIS NOR SUBSTANTIAL EXTRACTS FROM IT MAY BE PRINTED OR OTHERWISE REPRODUCED WITHOUT HIS/HER PERMISSION.

L'AUTEUR CONSERVE LA PROPRIETE DU DROIT D'AUTEUR QUI PROTEGE SA THESE. NI LA THESE NI DES EXTRAITS SUBSTANTIELS DE CELLE-CI NE DOIVENT ETRE IMPRIMES OU AUTREMENT REPRODUITS SANS SON AUTORISATION.

ISBN 0-612-05811-5

Canada

## Abstract

Transverse energy and charged particle multiplicity produced in 14.6 GeV/c p+Al and p+Pb collisions have been studied using the E814 set-up at the BNL-AGS. Measurements of  $d\sigma/dE_T$ ,  $dE_T/d\eta$ ,  $d\sigma/dN_c$ , and  $dN_c/d\eta$  are presented. From the present data the mean transverse energy per particle is obtained and it is compared to values observed in Si induced collisions at the same energy. In contrast to what is observed in nucleus-nucleus collisions, a very weak correlation is found between the transverse energy and the charged particle multiplicity. These results are compared to the predictions of various theoretical models used to describe heavy-ion collisions. The event generators RQMD and HIJET reproduce well the pseudorapidity distribution of both the transverse energy and charged particle multiplicity, whereas FRITIOF fails to reproduce the measured distributions. Contrary to what had been suggested previously in a Si+A study, the present study shows that the pseudorapidity dependence of charged particle multiplicity distributions do not follow KNO scaling.

## Résumé

L'énergie transverse et la multiplicité de particules chargées produites dans les collisions  $p+Al$  et  $p+Pb$  ont été étudiées à l'aide du dispositif de l'expérience E814 à l'AGS du BNL. De nouvelles mesures de  $d\sigma/d\eta$ ,  $d\eta/d\eta$ ,  $d\sigma/d\eta$  et  $d\eta/d\eta$  sont présentées. L'énergie transverse moyenne par particule est déduite des présentes données et cette énergie est comparée aux valeurs observées dans les collisions induites par un faisceau de Si à la même énergie. Contrairement à ce qui est observé dans les collisions noyau-noyau, une très faible corrélation est observée entre l'énergie transverse et la multiplicité. Les présents résultats sont comparés aux prédictions de divers modèles théoriques. Les générateurs d'événement RQMD et HIJET reproduisent très bien la distribution en pseudorapidité de l'énergie transverse et de la multiplicité de particules chargées. Par contre FRITIOF ne reproduit pas les distributions mesurées. Contrairement à ce qui a été suggéré dans une étude précédente des collisions  $Si+A$ , les présents résultats montrent que les distributions de multiplicité ne présentent pas de propriétés d'échelles du type KNO.

## Preface

In this thesis, I will present the results of research on the global observables produced in proton-nucleus collisions at AGS energy. This experiment was performed at Brookhaven National Laboratory (BNL) in April 1991 as a part of the ES14 research program. The main goal of the ES14 experiment is the investigation of heavy-ion collisions at AGS energy. One of the research topics of the ES14 experiment is the study of global observables resulting from such collisions. One motivation of the present experiment is to test our understanding of the reaction mechanism of nucleus-nucleus collisions. In particular, this experiment allows us to test how nucleus-nucleus collisions evolve from simple superposition of nucleon-nucleon collisions and to test the validity of the models used to describe reactions.

In the first chapter of this thesis, I will briefly review the new and quickly developing field of relativistic heavy-ion physics. I will also discuss why transverse energy and charged particle multiplicity measurements are interesting in the study of relativistic heavy-ion collisions, and then discuss the motivation of the proton-nucleus experiment. Three existing models for the current studies of proton-nucleus and nucleus-nucleus collisions at ultra-relativistic energy will be briefly discussed. In Chapter 2, I will describe the experimental setup used for this experiment, paying particular attention to the charged particle multiplicity detector and the two calorimeters in the target region since these detectors provide most of the data for this study. Chapter 3 will discuss the experimental conditions and data taking procedure. Chapter 4 will focus on data analysis, and in particular, discuss the various corrections used to obtain the transverse energy and charged particle multiplicity distributions. The final data will be presented and discussed in Chapter 5, where it will also be compared with the data

for Si-nucleus collisions and the predictions of three theoretical models. In Chapter 6, a summary together with the relevant conclusions will be given for the present work.

## Original Material and Contributions of the Candidate

The present work provides original results on energy flow for 1.4.6 GeV/c proton-nucleus collisions over a large acceptance. From these data and charged multiplicity data which were measured at forward angles, the correlation between the transverse energy and the charged particle multiplicity has been studied. The transverse energy per charged particle has also been investigated and scaling properties of the charged particle multiplicity distribution have been determined. These new data are compared to similar data obtained by the ES14 collaboration for Si on nucleus collisions at the same energy per nucleon. This is a contribution to original knowledge.

## Acknowledgements

I would like to express my deepest gratitude to my thesis supervisor, Professor Jean Barrette, for his instruction and guidance throughout this work.

My special thanks go to Dr. Claude Pruneau and Dr. Marzia Rosati for many helpful discussions and for sharing their knowledge and expertise. The data analysis part of this work would have been much more difficult without their efforts.

I wish to acknowledge Prof. Tommy S.K. Mark for his constant support for this work.

Special acknowledgement is due to Zhing Z. Zhang for valuable discussions on the response matrix method for the participant calorimeter.

I would also like to thank my fellow graduate students in our group, Mr. Roger Lacasse and Mr. Gilbert Sylvain, and all the people of Foster Radiation Lab for their help and friendship over all these years.

The work involved in the experimental setup and data taking phase was a collaborative effort of the E814 collaboration. I must thank all the members of this collaboration, and particularly those who took actively part in this experiment running period.

Finally, I want to express my heartfelt thanks to my wife, Jie, for her love and support throughout my studies.

## Table of Contents

Abstract . . . . .	ii
Résumé . . . . .	iii
Preface . . . . .	iv
Original Material and Contributions of the Candidate . . . . .	vi
Acknowledgements . . . . .	vii
List of Figures . . . . .	xi
List of Tables . . . . .	xx
<b>1. INTRODUCTION . . . . .</b>	<b>1</b>
1.1. The Physics of Relativistic Heavy-ion Collisions . . . . .	1
1.2. Transverse Energy and Particle Multiplicity . . . . .	4
1.3. Theoretical Models . . . . .	6
1.4. Objectives . . . . .	10
<b>2. EXPERIMENTAL SETUP . . . . .</b>	<b>11</b>
2.1. Overall layout . . . . .	11
2.2. Beam Definition Detectors . . . . .	13
2.2.1. Beam Telescope . . . . .	13
2.2.2. Beam Vertex Detector . . . . .	15
2.2.3. Čerenkov Counter . . . . .	15
2.3. Detectors in Target Region . . . . .	17
2.3.1. Target Calorimeter . . . . .	17
2.3.2. Participant Calorimeter . . . . .	21
2.3.3. Multiplicity Detector . . . . .	23

2.3.4. Racketon . . . . .	25
2.4. Forward Spectrometer . . . . .	25
<b>3. EXPERIMENTAL PROCEDURE . . . . .</b>	<b>27</b>
3.1. Beam . . . . .	27
3.2. Experiment . . . . .	27
3.3. Trigger Conditions . . . . .	28
3.4. Targets . . . . .	30
3.5. Detector Calibration . . . . .	33
<b>4. DATA ANALYSIS AND RESULTS . . . . .</b>	<b>35</b>
4.1. Good Beam Selection . . . . .	35
4.2. Normalization . . . . .	38
4.3. Correction of Data from Target Calorimeter . . . . .	41
4.3.1. Coherent Noise Correction . . . . .	41
4.3.2. Background Subtraction . . . . .	47
4.3.3. Data Sample . . . . .	49
4.3.4. Corrections for Target Calorimeter Response . . . . .	58
4.4. Correction of Data from Participant Calorimeter . . . . .	74
4.4.1. Raw Data . . . . .	74
4.4.2. Monte Carlo Corrections of Participant Calorimeter Response . . . . .	87
4.5. Data Analysis of Charged Particle Multiplicity . . . . .	101
4.5.1. Raw Data . . . . .	101
4.5.2. Charged Particle $dN_c/d\eta$ Distributions . . . . .	109
4.5.3. Charged Particle $d\sigma/dN_c$ Distributions . . . . .	110
<b>5. DISCUSSIONS . . . . .</b>	<b>116</b>
5.1. Transverse Energy Distributions . . . . .	116
5.2. Charged Particle Multiplicity Distributions . . . . .	122
5.3. Correlation Between $E_T$ and $N_c$ . . . . .	128

5.4. Transverse Energy per Particle . . . . .	131
5.5. Scaling of Charged Particle Multiplicity . . . . .	139
<b>6. SUMMARY AND CONCLUSIONS . . . . .</b>	<b>147</b>
<b>Appendix A. Members of the E814 Collaboration . . . . .</b>	<b>150</b>
<b>References . . . . .</b>	<b>151</b>

## List of Figures

1.1. Schematic of the predicted QCD phase diagram. . . . .	3
1.2. Schematic representation of the interaction of two hadrons forming two strings through longitudinal excitation [WE90]. . . . .	8
2.1. A schematic diagram of the ES14 experimental apparatus. . . . .	12
2.2. The ES14 apparatus in the beam defining region. . . . .	14
2.3. Horizontal beam hit patterns in the beam vertex detector. (a) BVER1 hit pattern. (b) BVER2 hit pattern. . . . .	16
2.4. A schematic diagram of the ES14 experimental apparatus near the target. . . . .	18
2.5. Schematic views of the Target Calorimeter. a) A (y-z) side view of the calorimeter showing NaI crystals mounted projectively. b) A x-y view of the calorimeter showing the housing of crystals in the five walls. . . . .	20
2.6. A schematic front view of the Participant Calorimeter. . . . .	22
2.7. A schematic view of the silicon multiplicity detector set. . . . .	24
3.1. Comparison of the transverse energy distribution for 2% Pb target (full line) and 1% Pb target (dotted line). . . . .	32
4.1. Pulse height distribution of signal measured in the four beam counters: (a) S1, (b) S2, (c) S3 and (d) S4. . . . .	37
4.2. A correlation cut in the plane of $T_{cal} - E_T - noback$ versus $T_{cal} - E_{tot}$ . Those events on the right of the line are rejected in the data analysis. . . . .	39
4.3. Pedestal energy distribution of sum over all the crystals of the target calorimeter. . . . .	43

4.4. Measured cluster distribution in the target calorimeter for 14.6 GeV/c protons on Pb target (solid curve) and on Al target (dashed curve) with multiplicity level 1 trigger. . . . .	45
4.5. Pseudorapidity distributions of clusters measured in the target calorimeter. These are not corrected for detector efficiency. . . . .	46
4.6. Empty target correction of the differential cross-section for (a) the Pb target for pretrigger, (b) the Al target for pretrigger, (c) the Pb target for multiplicity level 1 trigger and (d) the Al target for multiplicity level 1 trigger. Solid histograms denote data with target, and dotted histograms denote data without target. . . . .	48
4.7. $d\sigma/dE_T$ spectra for three different triggers for proton on the lead target.	50
4.8. Transverse energy spectra measured in the target calorimeter for (a) p+Pb and (b) p+Al. . . . .	51
4.9. Energy cluster distributions for various $E_T$ regions measured in the target calorimeter for (a) p+Pb and (b) p+Al. . . . .	53
4.10. Differential cross-sections of the transverse energy per cluster for various $E_T$ regions measured in the target calorimeter for (a) p+Pb and (b) p+Al. . . . .	54
4.11. $\eta$ distribution of the transverse energy measured in the back wall of the target calorimeter calculated: (a) by locating the center face of the crystal with the maximum signal in each cluster and (b) by using energy weighted cluster center. . . . .	56
4.12. Pseudorapidity distribution of transverse energy measured in the target calorimeter for the reaction of 14.6 GeV/c proton beam on lead target (solid curve) and on aluminum target (dotted curve). These distributions are not corrected for leakage and efficiency. . . . .	57
4.13. Pseudorapidity distribution of transverse energy for the Pb target for various $E_T$ slices. . . . .	59

4.14. Comparison of kinetic energy spectra for all charged particles in the multiplicity detector acceptance for 14.6 GeV/c RQMD p+Pb events: (a) spectrum without energy filter and (b) spectrum with a total energy filter at 999 MeV. . . . .	61
4.15. Trigger efficiency for multiplicity level 1 trigger relative to pretrigger. The solid histogram represents the ratio of charged multiplicity data $d\sigma/dN_c$ from multiplicity level 1 trigger to that from pretrigger, and the dashed line represents the assumed trigger efficiency for multiplicity level 1 trigger. . . . .	63
4.16. Calculated effect of the triggers on the $d\sigma/dE_T$ in the target calorimeter acceptance for (a) p+Pb and (b) p+Al. The solid lines are for unbiased spectra; the dotted lines are for pretrigger; the dashed lines are for multiplicity level 1 trigger. . . . .	64
4.17. Correlation between the transverse energy in the target calorimeter after tracking with the transverse energy before tracking. . . . .	66
4.18. Tracking effect on $dE_T/d\eta$ distribution in the acceptance of the target calorimeter. The solid line is the distribution before tracking and the dotted lines are the distribution after tracking. . . . .	67
4.19. Target calorimeter $E_T$ response calculated using ten thousand RQMD p+Pb events. . . . .	68
4.20. Target calorimeter $E_T$ response calculated from five runs of the same two thousand RQMD p+Pb events. . . . .	70
4.21. Comparison of efficiency of the target calorimeter calculated from three models: RQMD (solid curves), HIJET (dashed curves) and FRITIOF (dotted curves). . . . .	71
4.22. Comparison of the target calorimeter efficiency calculated from RQMD p+Pb events (solid curves) and RQMD p+Al events (dotted curves). . . . .	72

4.23. Experimental $dE_t/d\eta$ distributions as measured by the target calorimeter before corrections for leakage (dotted histogram) and after corrections are applied (solid histogram) for p+Pb (upper part) and for p+Al (lower part) . . . . .	73
4.24. Correlation between $E_T$ and the FERA sum in the participant calorimeter. The dashed lines correspond to $E_T$ level 1 trigger, solid lines to $E_T$ level 2 trigger and dotted lines to $E_T$ level 3 trigger. . . . .	75
4.25. FERA sum spectra for three level $E_T$ triggers in the participant calorimeter. The dashed lines correspond to $E_T$ level 1 trigger, solid lines to $E_T$ level 2 trigger and dotted lines to $E_T$ level 3 trigger. . . . .	76
4.26. Effect of multiplicity cut on the contribution of background interaction to the $E_T$ spectra measured in the participant calorimeter. The solid histograms are for data with the target in the frame, the dashed histograms are for data with the empty target frame. The spectra shown in (a) for the Al target and (b) for the Pb target are obtained without applying the offline multiplicity cut. The spectra shown in (c) for the Al target and (d) for the Pb target are obtained after applying the offline multiplicity cut. The offline multiplicity cut reduces background contribution significantly. . . . .	78
4.27. Transverse energy spectra for (a) Al target and (b) Pb target as measured by the participant calorimeter. The solid lines correspond to $E_T$ level 1 trigger, dotted lines to $E_T$ level 2 trigger and dashed lines to $E_T$ level 3 trigger. . . . .	79
4.28. Comparison of trigger effect on the $d\sigma/dE_T$ for p+Al (a) and p+Pb (b) measured in the target calorimeter. The solid lines correspond to $E_T$ level 1 trigger and the dotted lines correspond to the multiplicity pretrigger. . . . .	81

4.29. Energy deposition in 512 cells of the participant calorimeter for p+Pb from data (a) and simulation (b). The calorimeter cells are numbered by looping on $\phi = 1$ to 16, $r = 1$ to 8 and $z = 1$ to 4 corresponding to channels 1 through 512. . . . .	82
4.30. The uncorrected pseudorapidity distribution of $E_T$ for p+Al using $E_T$ level 1 trigger. The solid curve corresponds to the data measured by the participant calorimeter and the dashed curve corresponds the data measured by the target calorimeter. The distributions measured by the two calorimeters do not match due to different detector response. . . . .	84
4.31. Projective segmentation of the participant calorimeter into eight rings used in the leakage correction correction. . . . .	85
4.32. Uncorrected $dE_T/d\eta$ distribution for p+Al in the acceptance of the target calorimeter (solid curves) and the participant calorimeter with projective binning (dashed curves). . . . .	86
4.33. Trigger simulations with three generated events: the dotted lines are for RQMD; dashed lines are for HIJET; solid lines are for FRITIOF. Each model produces four curves corresponding to minimum bias, $E_T$ level 1 trigger, $E_T$ level 2 trigger and $E_T$ level 3 trigger respectively. . . . .	93
4.34. Correlation between unfolded transverse energy and the original incident transverse energy in the acceptance of the participant calorimeter. . . . .	95
4.35. $\eta$ bin distribution of $E_T$ (in arbitrary unit) calculated using generated events:(a) RQMD; (b) HIJET; (c) FRITIOF. The solid lines are for distributions before tracking, dashed lines for distributions after tracking and dotted lines for unfolded distributions. . . . .	96

4.36. Experimental $dE_t/d\eta$ distributions as measured by the participant calorimeter for the p+Pb (upper part) and p+Al (lower part) reactions. The dotted histograms correspond to distributions before corrections for leakage and the solid histograms correspond to distributions after corrections. . . . .	98
4.37. Corrected $dE_t/d\eta$ distribution for p+Pb (upper part) and p+Al reaction (lower part). The open dots are obtained with the target calorimeter while the close dots are obtained with the participant calorimeter.	100
4.38. Beam track x projection in the target plane for all events. The shaded areas correspond to the events rejected using beam position cut. .	102
4.39. Beam track x projection versus the average x position of the multiplicity detector hits. The data are fitted with a line. . . . .	104
4.40. Hit distribution in 512 channels for each of the multiplicity detector disk: (a) Disk 1 and (b) Disk 2. . . . .	105
4.41. Hit distribution in each pad for ring 15 of the multiplicity detector. The dashed line represents the calculated value for the average number of hits. . . . .	107
4.42. Multiplicity hit spectrum for random triggers. . . . .	108
4.43. Contribution of background interactions to $dN_c/d\eta$ . (a) $dN_c/d\eta$ for p+Pb before empty target frame correction, (b) $dN_c/d\eta$ for p+Al before empty target frame correction, (c) $dN_c/d\eta$ for p+Pb after empty target frame correction, (d) $dN_c/d\eta$ for p+Al after empty target frame correction. The dashed histograms are for distributions as measured using empty target frame. . . . .	111

4.44. Contribution of background interactions to $d\sigma/dN_c$ . (a) $d\sigma/dN_c$ for p+Pb before empty target frame correction; (b) $d\sigma/dN_c$ for p+Al before empty target frame correction; (c) $d\sigma/dN_c$ for p+Pb after empty target frame correction; (d) $d\sigma/dN_c$ for p+Al after empty target frame correction. The dashed histograms are for distributions as measured using empty target frame. . . . .	112
4.45. Effect of the multiplicity detector efficiency correction on $d\sigma/dN_c$ distributions for (a) p+Pb and (b) p+Al. The dotted histograms correspond to distributions before corrections for efficiency and the solid histograms correspond to distributions after corrections. . . .	114
5.1. Comparison between measured and calculated transverse energy spectra for 14.6 GeV/c proton induced collisions in the target calorimeter acceptance: (top) for Pb target and (bottom) for Al target. Dots denote experimental data, and the histograms denote model predictions. . . . .	117
5.2. Comparison between measured and calculated transverse energy spectra for 14.6 GeV/c proton induced collisions in the participant calorimeter acceptance: (top) for Pb target and (bottom) for Al target. . .	119
5.3. Comparison between measured and calculated pseudorapidity distributions of transverse energy for 14.6 GeV/c proton induced collisions: (top) for Pb target and (bottom) for Al target. . . . .	121
5.4. Comparison between measured and calculated charged particle multiplicity spectra for 14.6 GeV/c proton induced collisions for Pb target (closed dots) and for Al target (open dots) with models: RQMD (dotted lines), HIJET (dashed lines) and FRITIOF (solid lines) . .	123
5.5. Effect of $\pi^0$ conversion on the charged particle multiplicity distribution. The dotted line shows the distribution before $\pi^0$ conversion and the solid line shows the distribution after $\pi^0$ conversion. . . . .	124

5.6. Comparison between measured and calculated pseudorapidity distributions of charged particle multiplicity for 14.6 GeV/c p+Pb (solid dots) and p+Al (open dots) reactions. . . . .	126
5.7. Upper part: pseudorapidity distributions of charged particle multiplicity $dN_c/d\eta$ for p+Pb reaction for various cuts in the total multiplicity. Lower part: same distributions for p+Al reaction. . . . .	127
5.8. Comparison of pseudorapidity distributions of charged particle multiplicity $dN_c/d\eta$ for p+Pb reaction (solid dots) and for p+Al reaction (open dots) for the same multiplicity window ( $N_c = 5 - 7$ ). . . . .	129
5.9. Correlations between transverse energy measured in the participant calorimeter and charged particle multiplicity measured in the multiplicity detector for (a) Si+Pb reactions 14.6 GeV/c per nucleon [SI91] and (b) p+Pb reactions at 14.6 GeV/c. . . . .	130
5.10. Correlation between $E_T$ before tracking and the $E_T$ after tracking in the participant calorimeter. The error bars indicate the $E_T$ magnitude of the event-to-event fluctuations. . . . .	132
5.11. Charged particle multiplicity production for various cuts in the transverse energy measured in the participant calorimeter for 14.6 GeV/c p+Pb reactions. . . . .	133
5.12. Comparison of the mean value and variance of the charged particle multiplicity distributions as a function of the transverse energy in the participant calorimeter for the Pb target (solid dots) with the results from RQMD (open dots). . . . .	134
5.13. Transverse energy per charged particle for the p+Pb (upper part) and p+Al (lower part) reactions. . . . .	136
5.14. Detection efficiency for (a) protons, (b) neutrons, (c) $\pi^+$ and $\pi^-$ , (d) $\pi^0$ and $\gamma$ in the acceptance of the side wall of the target calorimeter. . . . .	137

5.15. Transverse energy per cluster for p+Pb (upper part) and p+Al (lower part) over the pseudorapidity acceptance of the target calorimeter. The histograms are predictions of various event generators. . . . .	138
5.16. Transverse energy per particle for the p+Pb (upper part) and Si+Pb (lower part) reactions. The data for Si+Pb are obtained from refs. [BA92B] and [ZH93]. . . . .	140
5.17. Observed multiplicity distributions, plotted in KNO variables for Si induced reactions at various pseudorapidity intervals[BA92B]. . . . .	142
5.18. Relative multiplicity distributions, plotted in KNO variable for reactions from Si on the three targets at the same pseudorapidity interval [BA92B]. . . . .	143
5.19. Experimental multiplicity distribution plotted in KNO variable for the p+Pb reaction at various pseudorapidity intervals. . . . .	144

## List of Tables

3.1. Trigger conditions used in the forward transverse energy measurement (first experiment) . . . . .	29
3.2. Trigger conditions used in the forward multiplicity and backward trans- verse energy measurements (second experiment) . . . . .	30
3.3. Statistics of events for each target in the first experiment with transverse energy triggers . . . . .	31
3.4. Statistics of events for each target in the second experiment with charged multiplicity triggers . . . . .	31
4.1. Total cross-sections of $E_T$ and mean $E_T$ measured in the target calorimeter	52
4.2. $E_T$ (GeV) per cluster measured in the target calorimeter with multiplic- ity level 1 trigger . . . . .	55
4.3. Pseudorapidity binning for the participant calorimeter . . . . .	87
4.4. Model comparison for mean $E_T$ measured in the participant calorimeter	99
4.5. Model comparison for mean $E_T$ measured in the target calorimeter . . .	101
4.6. Multiplicity detector ring-by-ring detection efficiency . . . . .	110
4.7. Multiplicity detector ring-by-ring average occupancy . . . . .	115
5.1. Relative width $\sigma / \langle N_c \rangle$ of the multiplicity distribution for p+Pb. The third column gives average number of particles in the $\eta$ range considered. The last column gives the expected statistical variance for $N_c$ . . . . .	141
5.2. Same as Table 5.1 for Si+Pb . . . . .	146
5.3. Same as Table 5.1 for Si+Cu . . . . .	146
5.4. Same as Table 5.1 for Si+Al . . . . .	146

## Chapter 1

### INTRODUCTION

This thesis is concerned with the study of global features in proton-nucleus collisions at AGS energy. The work was done as a part of the ES14 research program. The ES14 collaboration consists of about fifty people from nine universities and laboratories, as listed in Appendix A. The team has performed a series fixed target experiments at BNL-AGS. The main goal of the collaboration is the study of reaction mechanism of ultra-relativistic heavy-ion collisions. The following part of this chapter is an overview of the new field of ultra-relativistic heavy-ion physics, a description of the relevance of this proton-nucleus experiment to the current research on heavy-ion collisions and a description of the main observables which will be discussed throughout this thesis.

#### 1.1 The Physics of Relativistic Heavy-ion Collisions

With the study of ultra-relativistic heavy-ion collisions at the Super Proton Synchrotron (SPS) of Centre European pour la Recherche Nucleaire (CERN) and at the Alternating Gradient Synchrotron (AGS) of Brookhaven National Laboratory (BNL) in 1986, a new field of ultra-relativistic heavy-ion physics emerged from the traditional domains of particle physics and nuclear physics. In combining methods and concepts from both areas, the study of heavy ion collisions at very high energies ( $E/m \gg 1$ ) provides a unique approach in investigating the properties of matter at high baryon density and high temperature within the laboratory.

The primary goal of this field is to search for a new state of matter called Quark Gluon Plasma (QGP) which should have been present in the first microsecond after the formation of the universe. The theory of Quantum Chromodynamics (QCD) predicts that at low temperature and densities quarks, gluons and colour fields are confined by strong force to the interiors of hadrons. At sufficiently high temperature and densities the hadrons overlap and the strong force becomes so small that a phase transition may occur towards the QGP. As a result quarks, gluons and colour fields are no longer confined within hadrons but can move freely wherever such extreme conditions exist.

Figure 1.1 shows the predicted phase diagram of nuclear matter in the temperature-baryon density plane, where the hadron and QGP phases are separated. In the low temperature and baryon density region, the nuclear matter is in the form of hadronic gas consisting of nucleons, mesons and resonances. While in either the high temperature or the high baryon density region, (i.e., for temperatures in excess of 200 MeV at low baryon density or of densities well in excess of five times of the normal nuclear density ( $0.16 \text{ GeV}/\text{fm}^3$ ) at low temperature), it exists in the form of quark-gluon plasma. Between these regions there may be a transition phase. The two trajectories in the figure show respectively the evolution of the early universe, and how nuclear phase transition may be explored by relativistic heavy-ion (RHI) collisions which create a large number of particles in a finite volume, forming a fairly large energy density.

There is now a major experimental effort under way at CERN and BNL to search for QGP through the study of relativistic heavy-ion collisions. The main results are summarized in the series of Quark Matter conference proceedings (for recent results see [QM93]) and in HIPAGS conference proceedings for AGS experimental results in general (for recent results see [HI93]). As part of the heavy-ion program at the BNL-AGS, a lot of research work has been reported on the study of nucleus-nucleus collisions with  $^{16}\text{O}$  and  $^{28}\text{Si}$  beams [AB92, AB91, AB89, AD92, AH94, AK94, AK92, BA93A, BA94, BA92A, BA92B, BA92C, BA90A, BA90B, BA90C, BA90D, LO94, NA92, ST92, ZA92]. In 1992 the  $^{197}\text{Au}$  beam became available at the AGS and the first results of the experiment with this beam have been reported [AH94, BA93B, GO94]. The present

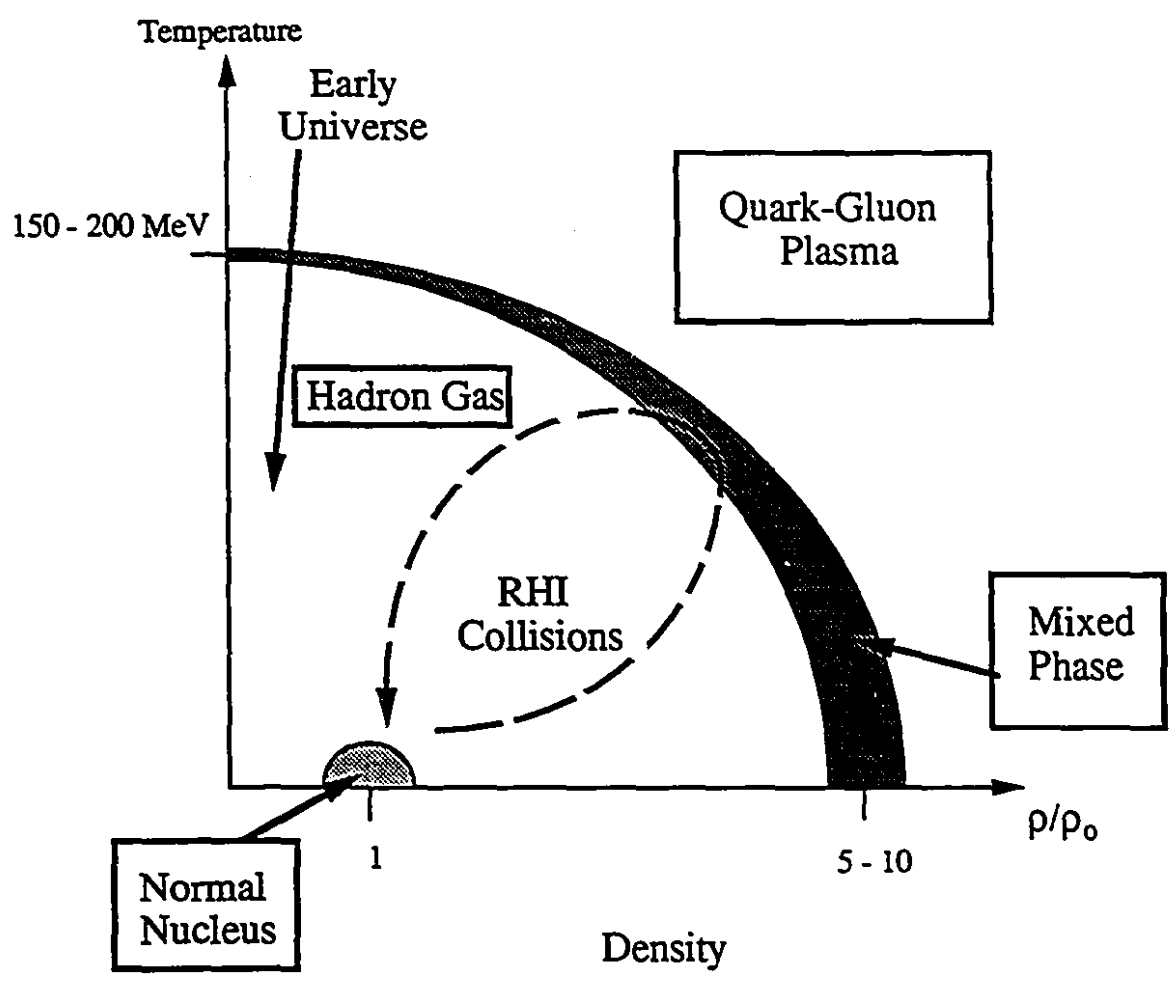


Figure 1.1: Schematic of the predicted QCD phase diagram.

experiment concentrates on the study of global properties, mainly transverse energy and particle multiplicity, of proton-nucleus reactions.

## 1.2 Transverse Energy and Particle Multiplicity

Theoretical models [BJS3] have indicated that the thermodynamic variables, such as entropy and temperature, which characterize the QGP or nuclear matter after collision may be inferred from the properties of the multiparticle final state which can be measured in the laboratory. Among the key observables in such studies are transverse energy and particle multiplicity which characterize the number of particles emitted after a collision and the energy they carry.

The transverse energy in a collision is defined as the sum of transverse energies of all emerging particles

$$E_T = \sum_{i=1}^n E_i \sin \theta_i \quad (1.1)$$

where  $E_i$  is the kinetic energy for baryons and the total energy for mesons, leptons and photons;  $\theta$  is the angle of emission or scattering in the laboratory system. The measurement of the number of particles is usually restricted to the number of charged particles ( $N_c$ ) for experimental reasons.

The global variables of particle multiplicity and energy flow resulting from reactions can both be measured as a function of polar angle in the laboratory. It is convenient to characterize relativistic heavy-ion reactions using kinematic variables which have well defined properties under Lorentz transformations. Therefore, longitudinal velocity or momentum of a particle is often expressed in terms of rapidity or pseudorapidity. The rapidity (pseudorapidity) distributions do not change when the rapidity (pseudorapidity) scale is shifted, for example, when we pass from the nucleon-nucleon center-of-mass system to the lab system and vice versa.

The rapidity ( $y$ ) and pseudorapidity ( $\eta$ ) are defined as

$$y = \frac{1}{2} \ln \left( \frac{E + P_Z}{E - P_Z} \right) \quad (1.2)$$

and

$$\eta = \frac{1}{2} \ln \left( \frac{1 + \cos \theta}{1 - \cos \theta} \right) = -\ln \left( \tan \frac{\theta}{2} \right) \quad (1.3)$$

The energy, momentum, transverse and longitudinal momenta, mass and angle of the outgoing particles are denoted by  $E$ ,  $P$ ,  $P_T$ ,  $P_Z$ ,  $m$  and  $\theta$ , respectively.  $\eta = y$  only for massless particles or for particles with  $P_Z = 0$ . Generally,  $\eta$  is approximately equal to  $y$  at very high energy when  $|P| \gg m$ .

The pseudorapidity  $\eta$  is a very convenient variable in experiment, since it depends only on the polar angle ( $\theta$ ) of emission or scattering relative to the beam direction. One can measure  $\eta$  without knowing the momentum of the particle. Therefore, the corresponding spatial observables of energy flow and particle multiplicity are the pseudorapidity distributions of transverse energy  $dE_T/d\eta$  and charged particle  $dN_c/d\eta$ .

As global variables in ultra-relativistic heavy-ion collisions, transverse energy and charged particle multiplicity are good indicators of reaction dynamics. In particular, they provide information on energy deposition and degree of stopping of the incident projectile, energy density achieved in the collision, and the impact parameter of the reaction. For example, the magnitude of  $dE_T/d\eta$  may be used to estimate the thermal energy density in a model-dependent manner [BJS3]. The initial energy density after a collision is estimated to be about four times that of the normal density of nuclear matter [ST92] for S+Pb and is about eight times the energy density of the normal density of nuclear matter of Au+Au at AGS energy [BA93B].

In the last few years, studies of Si and Au beam induced heavy-ion collisions at  $\approx 10 - 15$  GeV per nucleon on heavy targets have shown that there is full stopping of the projectile at AGS energy [BA90A, BA93B]. The large transverse energy observed at backward angles in Si on Pb reactions and the evolution of the mean particle rapidity

with centrality of the reactions imply non-negligible rescattering effects at AGS energy [BA92A,BA92C].

To test our understanding of the reaction mechanism of the nucleus-nucleus collisions, it is important to study more fundamental processes such as proton induced reactions. When the incident proton strikes the target nucleus at certain impact parameters, it interacts with a nucleon. The nucleon recoils and mesons may be produced. As hadrons propagate through the nucleus, they make subsequent collisions with other nucleons. The study of the way hadrons propagate in the nuclear medium may provide more insight on the importance of rescattering, the stopping power of normal nuclear matter, and the effect of the nuclear matter density on the hadronic cross sections.

The present data for proton-nucleus collisions have been obtained as part of the ES14 research program. Therefore, these data are readily comparable to the ES14 data obtained for  $^{28}\text{Si}$  induced reaction at the same energy per nucleon [BA92A,BA92B,ST91]. Another AGS-based relativistic heavy-ion experiment, the ES02 experiment, has also measured transverse energy for proton-nucleus and Si-nucleus reactions in the pseudorapidity range  $1.25 < \eta < 2.50$ . These data can be compared to our results in the overlapping pseudorapidity region. Since the ES14 setup covers almost the full solid angle for the transverse energy measurement and a wide acceptance in the forward region for charged particle multiplicity, the present data provide a more complete picture of global observables and thus form a good basis for evaluating theoretical predictions.

### 1.3 Theoretical Models

Theoretical models allow us to make predictions about ultra-relativistic heavy-ion collisions. By comparing the calculations from these theoretical models to the experimental data, one can obtain a better understanding of the reaction mechanism. The deviations between experimental data and predictions from models may indicate unexpected properties of the reaction.

Many relativistic macroscopic models have been developed to describe ultra-relativistic heavy-ion collisions [AN87, LU85, SH89, SO89, SO90, PA92, WE90, WE93]. Proton-nucleus collisions can be considered as very asymmetric nucleus-nucleus collisions. To illuminate the underlying physics of the nucleon-nucleus collision process at AGS energy, this thesis will focus on RQMD [SO89, SO90], FRITIOF [AN87] and HIJET [LU85, SH89] models. All these models which have been used in the study of heavy-ion collisions in the AGS experiments are based on string models and assume the superposition of nucleon-nucleon collisions to form the nucleon-nucleus or nucleus-nucleus collisions, although the formation or the final hadronization schemes for the strings can be different.

In the RQMD scheme, the nucleons of the projectile and target nuclei move through each other on straight-line trajectories. Interaction between two nucleons occur when they come closer than some geometrically defined minimal distance. The interaction may lead to the creation of strings which are longitudinally stretched quark-diquark pairs. Figure 1.2 shows that two nucleons exchange their momenta while interacting, forming two excited strings, and each string contains exactly the quarks of one of the incident hadrons. The interaction of nucleons can result in excitation of baryon resonances or strings. If several strings are overlapping, they combine to form highly charged ropes which decay due to quark-pair creation from the vacuum, thus screening the original charge. After decay of these unstable objects - resonance, strings and ropes - the secondaries are produced. After formation, secondary hadrons are allowed to interact with all other particles.

FRITIOF is also based on the string picture of hadron-hadron interactions. In this picture, each nucleon-nucleon interaction leads to the excitation of the nucleon by the stretching of a string between the valence of a quark and diquark, which is similar to the longitudinal excitation process in RQMD. A phenomenological excitation function determines the mass and momentum of the string after each interaction. In nucleon-nucleus and nucleus-nucleus collisions each incident nucleon is permitted to interact more than once. As a result, strings become more and more excited while

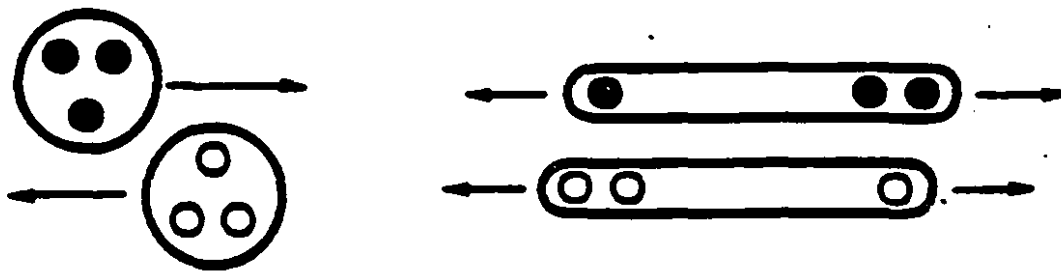


Figure 1.2: Schematic representation of the interaction of two hadrons forming two strings through longitudinal excitation [WE90].

passing through the target nucleus. After the last interaction the string decays to produce particles. One of the major differences of FRITIOF from RQMD is its lack of reinteractions of produced particles. FRITIOF was originally developed for the experiments at CERN. To adapt to the AGS lower energy a set of parameters which govern the fragmentation of strings in the standard FRITIOF (FRITIOF version 1.7) has been modified. As a result the calculated proton and pion cross-sections are in good agreement with the measured cross-sections for proton-proton and proton-nucleus events at the forward angles [COSS]. This modified FRITIOF is used in the present study of the proton-nucleus reactions.

The HIJET event generator considers proton-nucleus or nucleus-nucleus collisions to be a sum of independent nucleon-nucleon collisions, with the nucleon-nucleon cross-section and scattering dynamics independent of whether the nucleon has previously participated in an interaction. In the HIJET scheme, nucleons are distributed randomly in the nuclear volume according to a Woods-Saxon function. Each nucleon is assigned a Fermi momentum which has Gaussian distribution with a width of 200 MeV/c, while the total momentum of the nucleons in the nucleus frame is zero. An interaction between a projectile nucleon and a target nucleon takes place if the distance of closest approach is shorter than

$$b = \sqrt{\frac{\sigma_{inelastic}^{n-n}}{\pi}}. \quad (1.4)$$

With nucleon-nucleon inelastic cross-section  $\sigma_{inelastic}^{n-n} = 33mb$ ,  $b \cong 1fm$ . String formation through nucleon-nucleon interactions are calculated in the nucleon-nucleon center-of-mass frame by the MINBIAS routine of the program ISAJET [PA90]. HIJET uses the Field-Feynman formalism for string fragmentation. This formalism considers two partons fragmenting independently into two jets of particles. Interactions of secondary particles with cold spectator matter are included in this model.

These models by now seem to have successfully reproduced many of the presently available nucleus-nucleus data. For example, all three models have described very well the distribution of  $E_T$  differential cross-section in the forward region [ZH93], but this

agreement between data and models may be accidental. In this regard, the proton-nucleus collisions at AGS energy can be particularly interesting in understanding how nucleus-nucleus collisions differ from simple superposition of nucleon-nucleon collisions and they may be used to test the validity of theoretical models in describing the transition from a single collision problem to a thermodynamic problem mainly defined by a few observables.

#### 1.4 Objectives

The objectives of this thesis are to study the global observables, transverse energy and charged particle multiplicity, in proton-nucleus collisions at AGS energy. This study will extract transverse energy distributions and charged particle multiplicity distributions and the correlation between these two variables. Comparison of the data with predictions from the RQMD, HIJET and FRITIOF models will be made. Results of the correlation between the two global variables, and the transverse energy per particle will be compared to the corresponding results for the reactions with the  $^{28}\text{Si}$  beam at the same energy per nucleon. As KNO scaling of charged particle multiplicity has been reported [BA92B] for  $^{28}\text{Si}$ +nucleus reactions at AGS energy, the present study also looks into the possibility such scaling in proton-nucleus collisions.

## Chapter 2

# EXPERIMENTAL SETUP

### 2.1 Overall layout

The data presented in this thesis were taken with E814 setup installed in C5 beam line of the Alternate Gradient Synchrotron (AGS) at Brookhaven National Laboratory (BNL). A schematic top view of the setup is shown in Figure 2.1. The E814 setup consists mainly of three sections: beam definition detectors, target region detectors and a forward spectrometer.

In the following description of the detectors, the right-handed Cartesian coordinate system will be used, with the origin at the target. The positive  $z$  direction is defined along the beam. The polar angle  $\theta$  is defined with respect to the  $z$  axis and the azimuthal angle is measured counterclockwise from the  $x$  axis. In Figure 2.1, the beam goes from left to right and it arrives at the beam definition detectors upstream from the target.

The beam definition detectors consisting of a set of plastic scintillation counters were used to select valid beam particles. The accepted incident beam particles pass through the center opening of the back wall of the target calorimeter and then hit the target. Global variables were measured with the target calorimeter, the participant calorimeter and a multiplicity detector installed in the target region. Leading particles passing through the aperture defined by the participant calorimeter were measured and identified by the forward spectrometer which consists of a dipole magnet (M1), two drift chambers (DC2 and DC3), two groups of scintillators (forward scintillators and

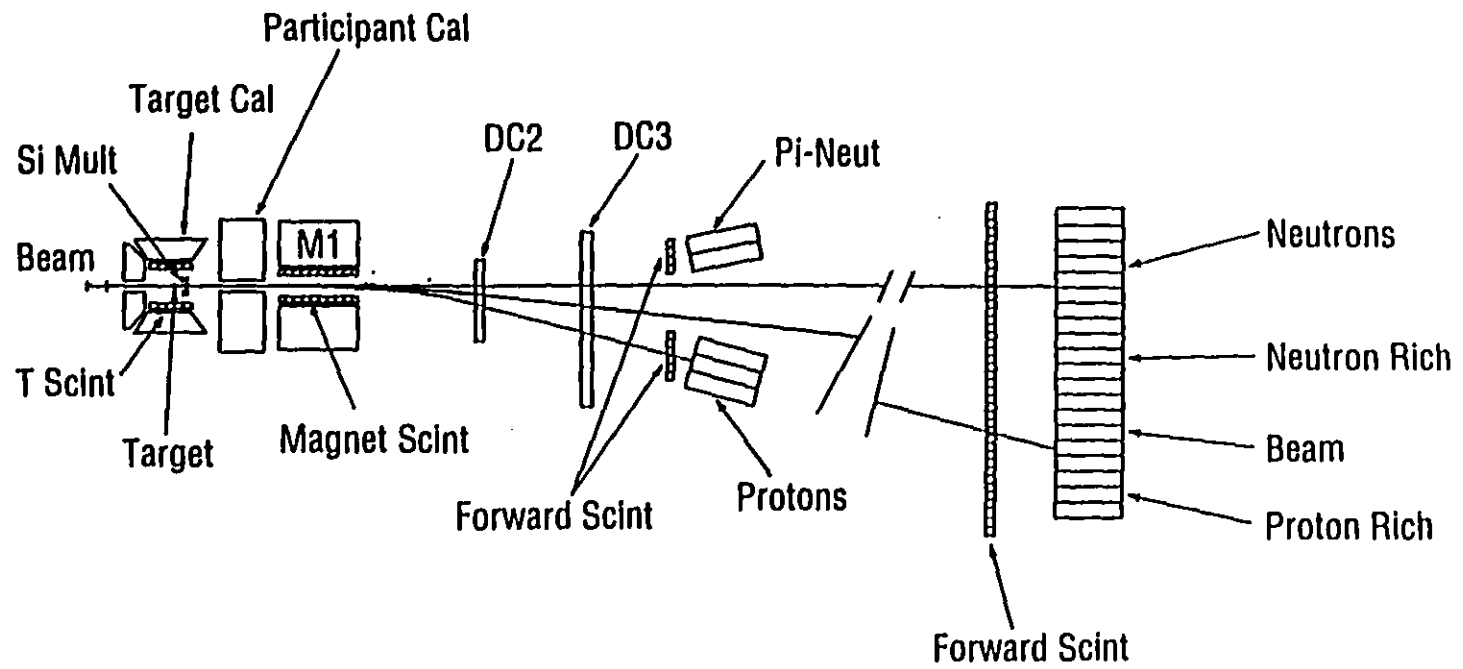


Figure 2.1: A schematic diagram of the E814 experimental apparatus.

magnet scintillators) and several uranium calorimeters. The major components of the E814 setup will be described separately in the following sections of this chapter.

## 2.2 Beam Definition Detectors

The main function of the beam definition detectors is to select valid beam particles. In this experiment we used a proton beam which was a secondary beam from the production target in the C beam line of the AGS. The main purposes of the beam definition detectors were to define the emittance of accepted particles and to reject other particles (electrons, muons, pions) that are present in the incident beam. The beam definition detectors for the April 1991 experiment include a beam scintillator telescope, a beam vertex detector and a Čerenkov detector.

### 2.2.1 Beam Telescope

The beam telescope consists of four scintillator counters (S1, S2, S3 and S4) mounted upstream of the target, as shown in Figure 2.2. They are thin solid plastic counters made of BC422 scintillator. S2 and S4 each has 2.5 mm and 1.3 mm thickness, and 10 mm and 4 mm radius respectively. S1 and S3 are veto counters with center holes of 15 mm and 10 mm diameter respectively. The outer radii of S1 and S3 are both 190.5 mm. The thickness of S1 and S3 are 15.7 mm and 11.4 mm respectively. Good beam particles must pass through the center holes of S1 and S3 counters. Those events which produce signals above a set threshold in either S1 or S3 counter are rejected.

S1 and S3 counters are read out by four photomultiplier tubes; S2 and S4 are each read out by two tubes. All the four scintillation counters were mounted in light-tight boxes and installed in the beam-line vacuum which were maintained at 10 micron (or 1.33 Pascal). The vacuum was terminated 69 cm in front of the target. During the proton run in April 1991, the acceptable beam was defined by requiring the coincidence

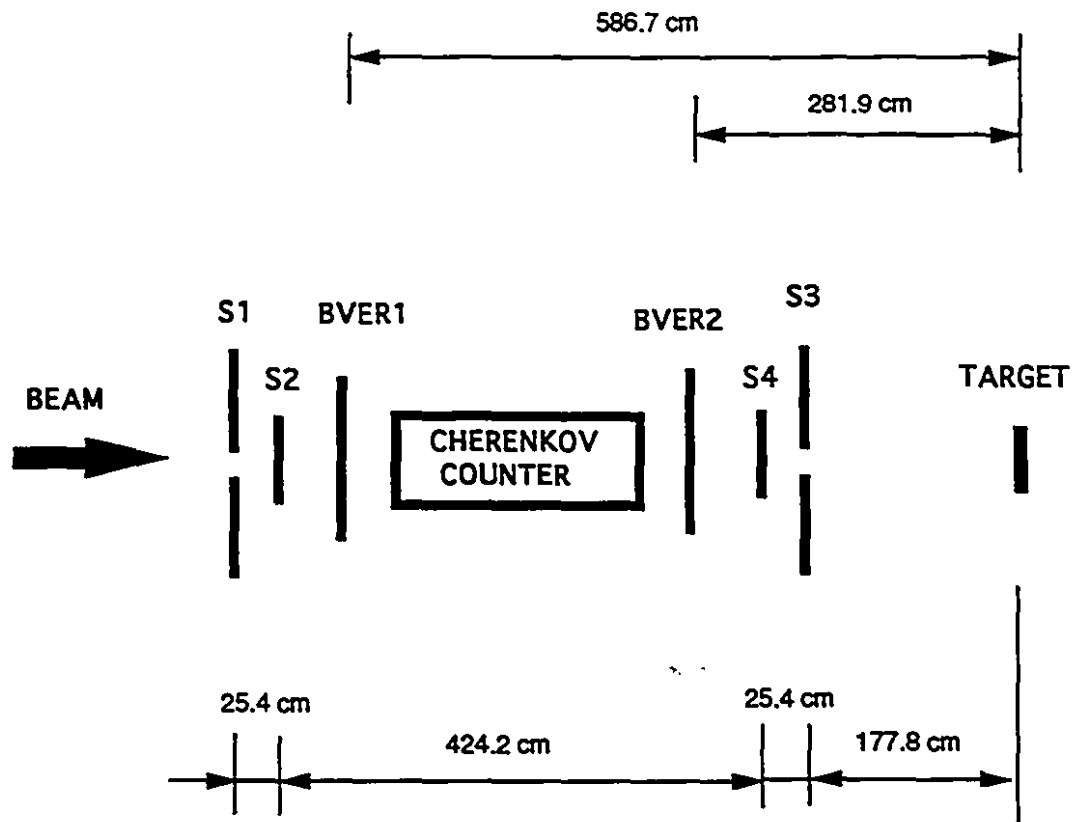


Figure 2.2: The E814 apparatus in the beam defining region.

of  $\bar{S}_1 S_2 \bar{S}_3 S_4$ . More details on the selection of good particles using this telescope is given in chapter 4. The counter  $S_4$  was also used to provide the start time measurement for the downstream time-of-flight spectrometer.

### 2.2.2 Beam Vertex Detector

The beam vertex detector (BVER) consists of two multistrip silicon detectors, mounted 5.63 and 2.58 meters in front of the target, as shown in Figure 2.2. The two detectors are made of 200 micron thick silicon wafers and contain 320 strips spaced by 50 microns. The strips of the two detectors are oriented vertically. They determine the horizontal position and incident angle of the beam particles at the target with a precision of about 0.07 mm and 0.012 mr respectively. The read-out of the beam vertex detector is done by PCOS electronics which consists of a preamplifier and a level discriminator for each channel. The strip detector electronics, originally designed to handle large energy loss from Si beam particles, were adapted for the proton beam by removing the attenuation resistance at the input to the discriminator. Figure 2.3 shows a typical hit pattern in the beam vertex detector for accepted beam particles. Those channels with few hits in the middle of the distributions are dead channels. The patterns indicate the horizontal spread of the incoming beam at two detector positions. The observed width is partly determined by the geometry of the beam telescope, and the fact that the beam is focused near the position of the target.

### 2.2.3 Čerenkov Counter

A threshold Čerenkov detector, also shown in Figure 2.2, served for discriminating against lighter beam particles in the experiment. The 2.5 meter long Čerenkov counter was located between the two multistrip silicon detectors and operated with freon gas at atmospheric pressure as radiator. In the 14.6 GeV/c proton beam running condition,

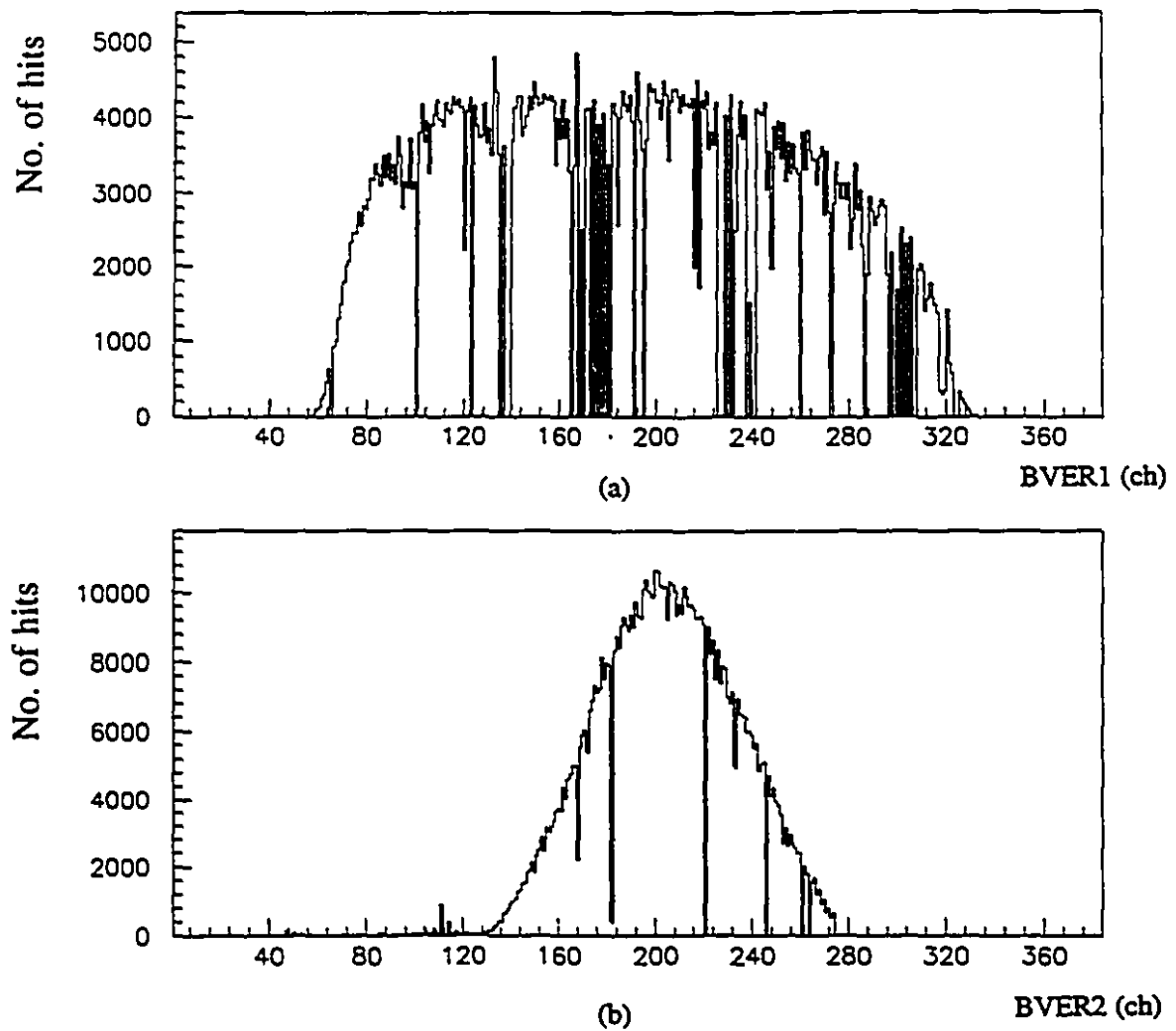


Figure 2.3: Horizontal beam bit patterns in the beam vertex detector. (a) BVER1 hit pattern. (b) BVER2 hit pattern.

contamination from lighter particles such as pions, muons and electrons in the beam was vetoed by this Čerenkov counter. To reduce dead time the veto was done by hardware at the level of the beam electronic logic.

## 2.3 Detectors in Target Region

The main focus of this thesis is on the global observables which were measured with the detectors near the target. Figure 2.4 shows the E814 experimental apparatus in the target region. The detectors includes the Target Calorimeter, the Target Paddle Scintillation Detectors, the Participant Calorimeter, the Charged Multiplicity Detector, and the Racketon. The beam enters the region from the left along the z-axis in the figure. The Participant Calorimeter, the Charged Multiplicity Detector and the Racketon cover the forward angles while the Target Calorimeter and the Target Paddle Detector cover the backward angles.

### 2.3.1 Target Calorimeter

One unique feature of the E814 setup is its near  $4\pi$  calorimetric coverage obtained from the Target Calorimeter and the Participant Calorimeter that surround the target. The primary function of the Target Calorimeter is to detect the products of target fragmentation. The calorimeter is azimuthally symmetric and separated into five walls - four side walls (left, right, top and bottom) and a back wall (upstream). It measures energy flow into the polar angle range  $40^\circ < \theta < 123^\circ$  with the side walls and  $135^\circ < \theta < 165^\circ$  with the back wall, corresponding to pseudorapidity range  $-0.5 < \eta < 1.0$  and  $-2.3 < \eta < -0.5$  respectively.

The Target Calorimeter is mainly an electromagnetic calorimeter made out of 992 NaI(Tl) crystals with approximately five radiation length thickness and a  $4 \times 4 \text{ cm}^2$  face cross section. The 992 NaI crystals were stacked in five aluminum cases, forming four



side walls and one back wall. The housing and mapping of crystals in the five walls are illustrated in Figure 2.5 [WA90]. Figure 2.5(a) shows a side (x-y plane) view of the Target Calorimeter. The crystals are arranged in a nearly projective geometry from the target so that energy deposition from a particle is limited to a small number of crystals. Figure 2.5(b) shows view of the calorimeter in the x-y plane (facing the beam). The back wall was stacked 13 crystals in height and 13 crystals in width, with 9 crystals (3x3) removed at the center to allow passage of the beam. The sides of the aluminum cases facing the target are 1 mm thin to minimize the energy loss of the particles before reaching the crystals. These housing cases were also made airtight with dry nitrogen gas circulating through to avoid moisture contamination of the NaI crystals. Signals from the crystals were read out by vacuum photodiodes. After preamplification the signals were transmitted through 100 meter long twisted pair cables to the shaping amplifiers in the ES14 counting house and then digitized with charge integrating ADCs (LeCroy 2280). For the convenience of data analysis, each crystal in side walls of the Target Calorimeter has been assigned a pair of numbers for its azimuthal ( $\phi$ ) and polar ( $\theta$ ) angles from the target. Crystals in the back wall are labelled in a different way from those in side walls. This and the analysis of procedure for the calorimeter will be discussed in detail in next two chapters. More details on the construction and performance of this detector can be found in [WA90].

The Target Paddle Scintillators consists of 52 plastic scintillator slabs. Each counter is made of  $0.64 \times 3.5 \times 49 \text{ cm}^3$  BC400 plastic, which attach to and completely cover the inner sides of the four Target Calorimeter side walls, positioning parallel to the z-axis, as shown in Figure 2.5. These scintillation detectors provide a crude measurement of charged particle multiplicity for the trigger system in the study of heavy-ion induced collisions and also serve as a shield to prevent delta electrons from entering the Target Calorimeter. They were not used in the trigger of the present experiment.

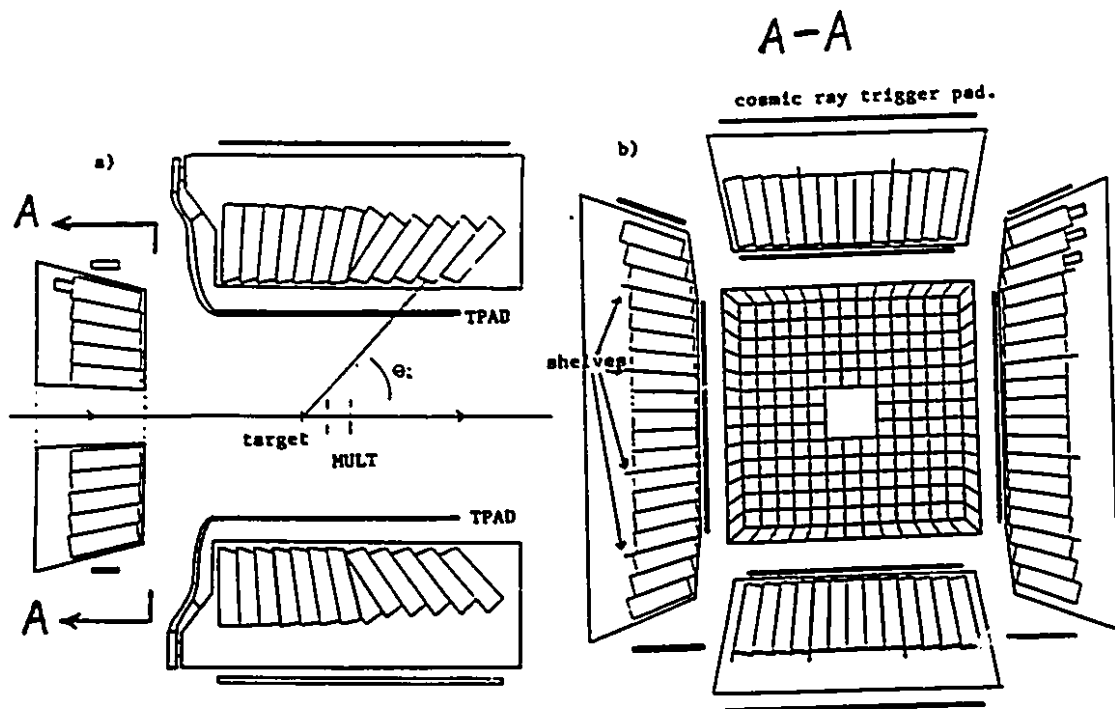


Figure 2.5: Schematic views of the Target Calorimeter. a) A (y-z) side view of the calorimeter showing NaI crystals mounted projectively. b) A x-y view of the calorimeter showing the housing of crystals in the five walls.

### 2.3.2 Participant Calorimeter

The Participant Calorimeter is a lead/iron/scintillator sampling calorimeter. It measures energy flow in the forward region, covering polar angles between  $1.0^\circ < \theta < 47^\circ$ , which corresponds to pseudo-rapidity range  $0.83 < \eta < 4.7$ . Figure 2.6 [RO91] shows a schematic front view of the Participant Calorimeter. Being axially symmetric, the calorimeter has the shape of a revolved trapezoid and is built with four identical quadrants with its front face positioned 74 cm from the target. Each quadrant is 96 cm deep with a radius of 86 cm, and is segmented into four azimuthal slices of  $22.5^\circ$ . Each slice is divided radially into eight towers. The Participant Calorimeter has a rectangular opening through its center to allow particles to enter the forward spectrometer. Since the calorimeter was constructed in a way that the four quadrants can move relative to each other, the size of the central opening is adjustable. For the proton-nucleus experiment performed at AGS in April of 1991, the opening of the participant calorimeter was fixed at  $\delta x = \pm 3.1\text{cm}$ ,  $\delta y = \pm 2.5\text{cm}$ .

The Participant Calorimeter is built mainly of lead absorber layers and plastic scintillator layers coupled with optical fibers for readout. The calorimeter consists of 59 pairs of passive and active layers divided into 4 longitudinal sections, 2 electromagnetic sections and 2 hadronic sections. Beginning with a 1.6cm thick iron face plate, a layer of 0.3cm scintillator (plastics BC408 and KSTI-430 for electromagnetic section and hadronic section respectively) is interleaved with a 1.0cm layer of lead absorber. In every sixth pair, a 1.6cm iron plate substitutes for the lead to maintain structural stability. Each electromagnetic section containing 6 absorber/scintillator pairs forms 0.4 interaction lengths (or 10 radiation lengths) while each hadronic section constitutes about 1.6 interaction lengths. The longitudinal and radial segmentation of the Participant Calorimeter, and eight pseudorapidity bins corresponding to the first electromagnetic section with respect to the target are shown in Figure 4.31. The readout of the calorimeter is divided into  $22.5^\circ(\phi)$  segments azimuthally, about  $5^\circ$  segments radially ( $r$ ) and 4 segments in longitudinal ( $z$ ) direction. Each cell of the calorimeter is

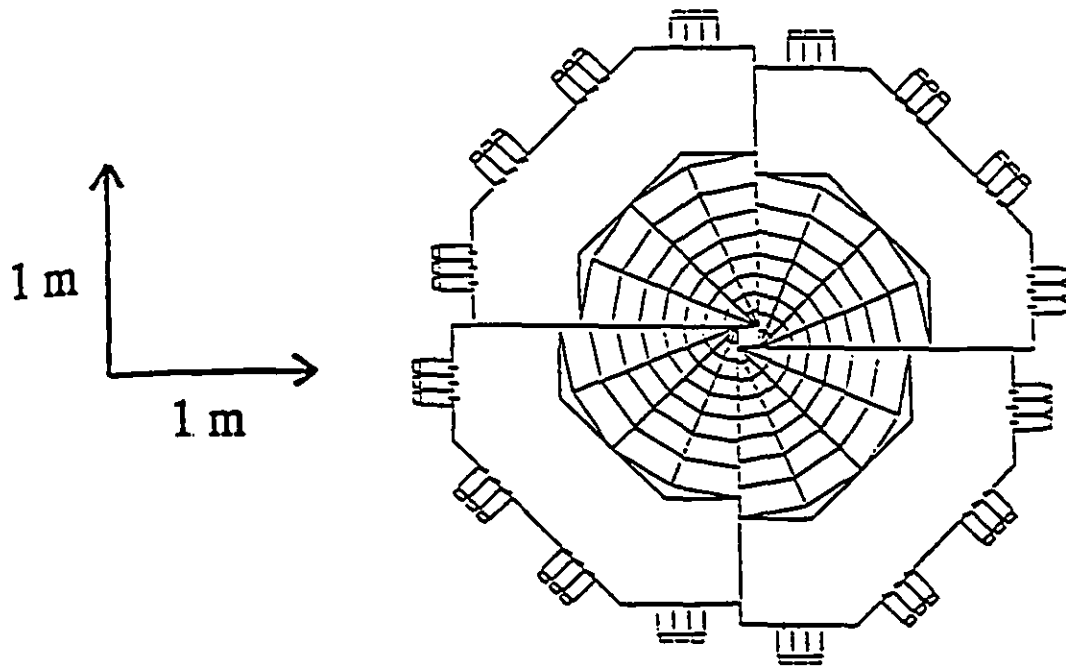


Figure 2.6: A schematic front view of the Participant Calorimeter.

defined in terms of  $(r, \phi, z)$ . The total readout channels of the Participant Calorimeter are 512 ( $8 \times 16 \times 4$ ). The data taking procedure will be discussed in next chapter. More details on the construction of the participant calorimeter can be found in [SI91].

### 2.3.3 Multiplicity Detector

Charged particle multiplicity was measured by a multiplicity detector which is mounted inside the Target Calorimeter shown in Figure 2.4. The multiplicity detector consists of two  $300\mu\text{m}$  thick silicon disks as shown in Figure 2.7 [BA92B]. Each silicon disk is divided into 512 pads and has an active region up to 3.4 cm radius. The first disk has 8 rings and 64 pads on each ring, is positioned 3.37cm from the target and covering pseudo-rapidity range  $0.9 < \eta < 2.0$ . The second disk has 12 rings: the two inner rings have 16 pads each, the next three rings have 32 pads each, then four rings have 48 pads each, and the outer three rings have 64 pads each. Mounted 8.17cm from the target, the second disk was designed to cover the pseudo-rapidity range  $1.8 < \eta < 3.8$ . During the April 1991 proton-nucleus run, the inner ring of the second silicon disk of the charged multiplicity detector was not working, therefore the effective pseudo-rapidity coverage of this multiplicity detector was  $0.9 < \eta < 3.4$ , which corresponds to a polar angle range  $3.7^\circ < \theta < 45^\circ$ . The multiplicity detector registers a charged particle whenever an individual silicon pad records a signal above threshold. The signal is read out by a preamplifier and the discriminator threshold is set to a value approximately one half of the most probable energy loss of a minimum ionizing particle.

Signals from the multiplicity detector are read out by 64 PCOS discriminator cards. Each card consists of 16 channels of high gain differential preamplifiers and time-over-threshold discriminators. The output signals from the discriminators, which are located close to the detector, are transmitted through a 10 meter long cable to the latch units

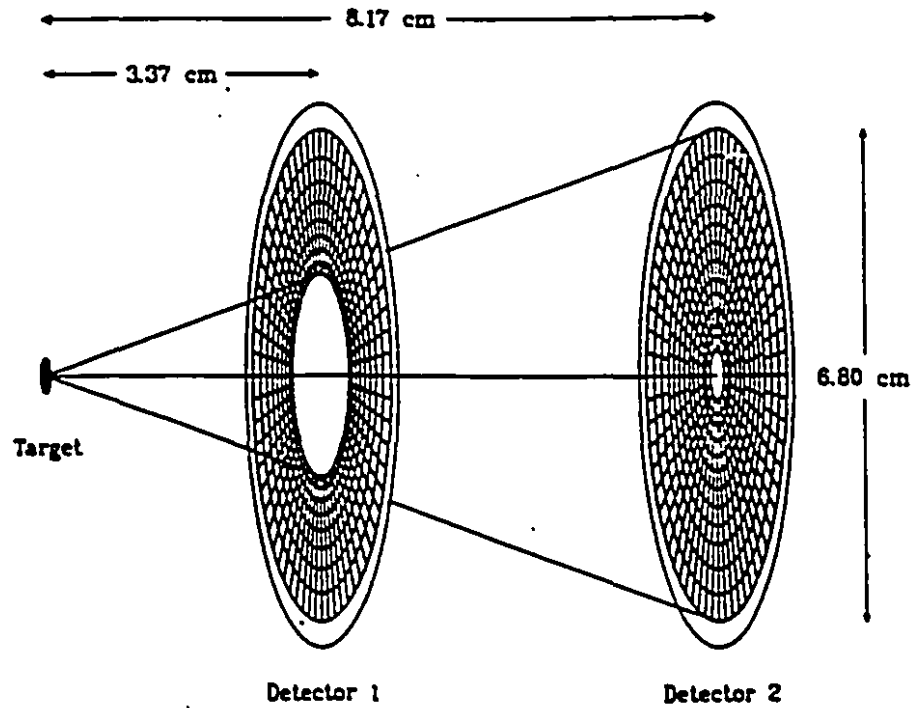


Figure 2.7: A schematic view of the silicon multiplicity detector set.

outside the target area, and then sent to the ES14 counting house for computer processing. For details on the construction and testing of the Si multiplicity detector one can refer to [JA91].

#### 2.3.4 Racketon

For this proton-nucleus experiment an additional trigger scintillator counter called Racketon was used when the Participant Calorimeter was removed out of the beam line to increase the acceptance of the forward spectrometer. The Racketon is made from a 1 cm thick plastic scintillator with a shape similar to a racket. The detector has a outer diameter of 41 cm and a circular hole of 3.8 cm diameter at the center to allow the passage of the beam. It is mounted 65 cm downstream of the target and the angular coverage of that detector is  $3^\circ < \theta < 17^\circ$ .

### 2.4 Forward Spectrometer

The forward spectrometer is located downstream of the participant calorimeter. With an overall length of 36 meters the forward spectrometer allows the determination of charge, momentum and energy of the particles produced in the reaction. As shown in Figure 2.1, the forward spectrometer for the run of 1991 consists of one dipole magnet (M1), a set of tracking chambers (DC2 and DC3), two scintillator hodoscopes and a set of uranium/copper/scintillator sampling calorimeters (UCAL).

The dipole magnet M1 has a length of 0.91 m. Its center is located at  $z = 3.1$  m downstream of the target. The magnet can generate a maximum magnetic field of 2.2 Tesla.

The tracking chambers of the spectrometer consists of two drift chambers DC1 and DC2. The centers of these chambers are located at 6.9 m and 11.6 m downstream of the target respectively. Each chamber has six drift planes, which determine the

horizontal track of the incident particle, and one pad plane, which measures coarse vertical positions. The wire spacing is 6.4 mm in DC2 and 12.7 mm in DC3. The active area of DC2 is 80 cm x 30 cm and centered horizontally at  $x = -20.5$  cm to maximize the acceptance for positively charged particles; while DC3 is 200cm x 50cm and centered horizontally at  $x = -51.0$ cm.

Two forward scintillator hodoscopes are used in the spectrometer to measure the charge, time of flight and position of particles. The upstream scintillator hodoscope is located right after the drift chamber DC3, 12.11 m from the target. Their dimensions are  $10 \times 60 \times 1$  cm<sup>3</sup> and are grouped into two walls: one on each side of the neutral line. They cover the particles with the smallest magnetic rigidity (largest deflection). The downstream hodoscope consisting of 39  $10 \times 120 \times 1$  cm<sup>3</sup> plastic scintillator (BC404) slabs is installed 31.3 m from the target. All the scintillators are positioned vertically and read out on both ends with EMI-9954B photomultipliers.

25 uranium/copper/scintillator sampling-calorimeter modules are used to measure the energy of the particles in the forward spectrometers. Twenty of these modules are located 36.3 m downstream of the target and the other five are positioned 12.67 m from the target, right behind the upstream scintillators: three are located after the upstream scintillator section in the proton region and two are placed after the section in the  $\pi$ -neutron region, as shown in Figure 2.1. Each calorimeter module has an active area of 20 cm wide by 120 cm high and consists of 40 longitudinal sections including one 5 mm copper plate and 13 stacks of two 3 mm uranium plates interleaved with one 2.5mm scintillator layer. The overall thickness of a calorimeter module is 4.2 interaction lengths. The data obtained with this spectrometer are the subject of another work where more details on the spectrometer detectors can be found [GI94].

## Chapter 3

# EXPERIMENTAL PROCEDURE

### 3.1 Beam

For the proton-nucleus experiment performed in April of 1991, we used a secondary proton beam provided by the BNL-AGS accelerator complex. The beam was produced at the C target of the AGS C beam line 81 meters in front of the E814 target. The beam was deflected by two pairs of dipole magnets. The beam intensity varied from  $5 \times 10^5$  to  $15 \times 10^5$  protons per spill. (The AGS spill was about a second long and one spill every 4 seconds). By changing the size of a collimator in the C5 beam line the intensity of the beam was adjusted. Due to the poor emittance of the secondary beam only about 10% of the beam particles were accepted by the beam scintillator telescope upstream to the target and were therefore considered valid beam particles. The average momentum of the beam measured in the forward spectrometer was 14.6 GeV/c with a resolution of 14% [GI94].

### 3.2 Experiment

Data on the transverse energy and charged particle multiplicity for the April 1991 run were accumulated during two separate periods. In the first experiment the participant calorimeter was inserted to be able to allow for the measurement of the transverse energy produced in forward angles. During these runs we used an interaction trigger

based on energy deposited in the participant calorimeter.

The main purpose of the second experiment was the measurement of the particle spectra in the forward spectrometer. For this experiment the participant calorimeter was moved out of the beam line and replaced by a lead collimator in order to expand the acceptance of the forward spectrometer. The trigger was produced by the multiplicity detector.

The data for the present experiment were initially recorded on 433 standard 6250 BPI computer tapes and then copied to 8 mm video tapes for convenience of the offline analysis. The data analysis was carried out on the computer station VAX 4000 at the Foster Radiation Laboratory of McGill University.

### 3.3 Trigger Conditions

The primary function of trigger system is to quickly decide whether a event is interesting and worth recording on tape. The ES14 trigger system used for the proton-nucleus experiment performed in April 1991, were composed of the beam trigger, the interaction trigger and an empty trigger.

The beam trigger was used for selecting good beam particles, which were defined by the coincident signals of

$$B = \bar{S}_1 S_2 \bar{S}_3 S_4, \quad (3.1)$$

where the discriminator threshold on the sum of phototube signals for each scintillator was set to 20% of the signal left by a minimum ionizing particle (MIPS). Therefore, only those particles that produce a signal greater than 0.2 MIPS in S2 and S4, while producing a signal of less than 0.2 MIPS in S1 and S3 are passed by the trigger. As the ES14 data acquisition system can handle only about 40 events per spill, the beam trigger was downscaled to record on tape roughly one or two beam trigger events per spill. The downscaling factors for beam trigger are listed in Table 3.1 and Table 3.2.

The data on transverse energy and charged particle multiplicity produced in the proton-nucleus reactions were collected by requiring coincidence of beam triggers and interaction triggers. Two types of interaction triggers were used in the April 1991 runs. For the first experiment, the transverse energy data measured with the participant calorimeter in the forward angles were taken using three parallel triggers, which were set to select event samples corresponding to increasing levels of transverse energy. The output of every phototube of the participant calorimeter was split into two signals: one signal was sent to the electronic summing boxes for forming triggers; the other went to the fastbus ADC. The online total transverse energy from the participant calorimeter was generated by summing signals weighted by the  $\sin\theta$  values of the calorimeter phototubes over all the 512 detector towers. The pretrigger is formed by requiring a small amount of transverse energy to be detected in the participant calorimeter. The three levels of reaction triggers, defined by three discriminator thresholds on the transverse energy, were set to correspond to 0.6GeV, 2.2GeV and 3.2GeV respectively. Table 3.1 lists the triggers and their downscaling factors used in the forward transverse energy measurements. The downscaling factors decrease with trigger level on the transverse

Table 3.1: Trigger conditions used in the forward transverse energy measurement (first experiment)

Trigger type	Trigger condition	Downscaling factor
Empty trigger	at random	22
Beam trigger	$\bar{S}_1 S_2 \bar{S}_3 S_4$	20005
Pre-trigger	small $E_T$	401
$E_T$ level 1	0.6 GeV	81
$E_T$ level 2	2.2 GeV	8
$E_T$ level 3	3.2 GeV	1

energy ( $E_T$ ) to produce approximately equal statistics over the entire  $E_T$  range. The empty trigger shown in the table was taken randomly and independently of other trigger conditions. This trigger is used for monitoring the pedestals of the ADC and various other effects. In the offline analysis, the pretrigger data were found to have very low

statistics which were not consistent with the downscaling factor of 401, for reasons which are still unclear. Therefore, the data with  $E_T$  pretrigger will be not presented.

For the second experiment, the  $E_T$  data from the target calorimeter were taken using mixed triggers. The lowest reaction trigger, the pretrigger, was formed by requiring at least one minimum ionizing particle in Racketon and more than two hits recorded by the multiplicity detector array. Because of the noise in the multiplicity detector, the pretrigger still contains a large fraction of events where no interaction has occurred in the target. To ensure good statistics of the events for real reactions in the target we have also introduced a second level trigger. This second level trigger, called multiplicity level 1 trigger, requires at least five charged particles to register in the multiplicity detector. Table 3.2 shows the triggers and their downscaling factors used in this experiment.

Table 3.2: Trigger conditions used in the forward multiplicity and backward transverse energy measurements (second experiment)

Trigger type	Trigger condition	Downscaling factor
Empty trigger	at random	22
Beam trigger	$\bar{S}^1 S^2 \bar{S}^3 S^4$	16004
Pre-trigger	multiplicity > 2	13
level 2 trigger	multiplicity > 4	3

An event is recorded to tape if the trigger conditions are met and the timing requirement, i.e., before and after protection, is satisfied. The timing of the previous particle or the next particle to the current event must have more than  $1 \mu$  second interval to ensure the discriminators only process one signal at a time.

### 3.4 Targets

The targets used were Pb and Al, both constructed with a cylindrical geometry of 30 mm diameter. In the first experiment we used Al and Pb with thickness of approximately 1.2% nuclear interaction lengths ( $\lambda$ ) for protons to reduce  $\pi^0$  conversion.

In the second experiment we used thicker targets. Pb and Al targets of 2.4% nuclear interaction lengths. The main reason to choose Al and Pb for the proton-nucleus experiment is that these nuclides had been used for Si-nucleus experiment at the same AGS energy per nucleon. Therefore, the proton-nucleus data are more easily comparable to the known Si-nucleus data. Table 3.3 and Table 3.4 list the targets used in the first and the second experiment, respectively. Both tables also show the number of events recorded for each target. The empty target shown in the tables implies no target in the target frame. The runs without target were used to measure the background interactions.

Table 3.3: Statistics of events for each target in the first experiment with transverse energy triggers

Target	Atomic weight A	Thickness in gram/cm <sup>2</sup>	No. of events on tape
Pb	207.19	2.216 (1.2%λ)	5.74 x 10 <sup>4</sup>
Pb	207.19	4.359 (2.4%λ)	9.63 x 10 <sup>3</sup>
Al	26.98	1.300(1.2%λ)	3.88 x 10 <sup>4</sup>
Empty			2.74 x 10 <sup>4</sup>

Table 3.4: Statistics of events for each target in the second experiment with charged multiplicity triggers

Target	Atomic weight A	Thickness in gram/cm <sup>2</sup>	No. of events on tape
Pb	207.19	4.359 (2.4%λ)	1.23 x 10 <sup>6</sup>
Al	26.98	2.596(2.4%λ)	1.16 x 10 <sup>6</sup>
Empty			1.92 x 10 <sup>5</sup>

The thick targets were used in the second experiment in order to increase the event rate in the forward spectrometer. The secondary particles from a first collision may interact with another nucleus in the target, causing enhancement of transverse energy. This effect is more pronounced with a thicker target. The effect of target thickness on transverse energy production is shown in Figure 3.1. The solid curve displays the differential cross-section of transverse energy production of 14.6 GeV/c proton on the

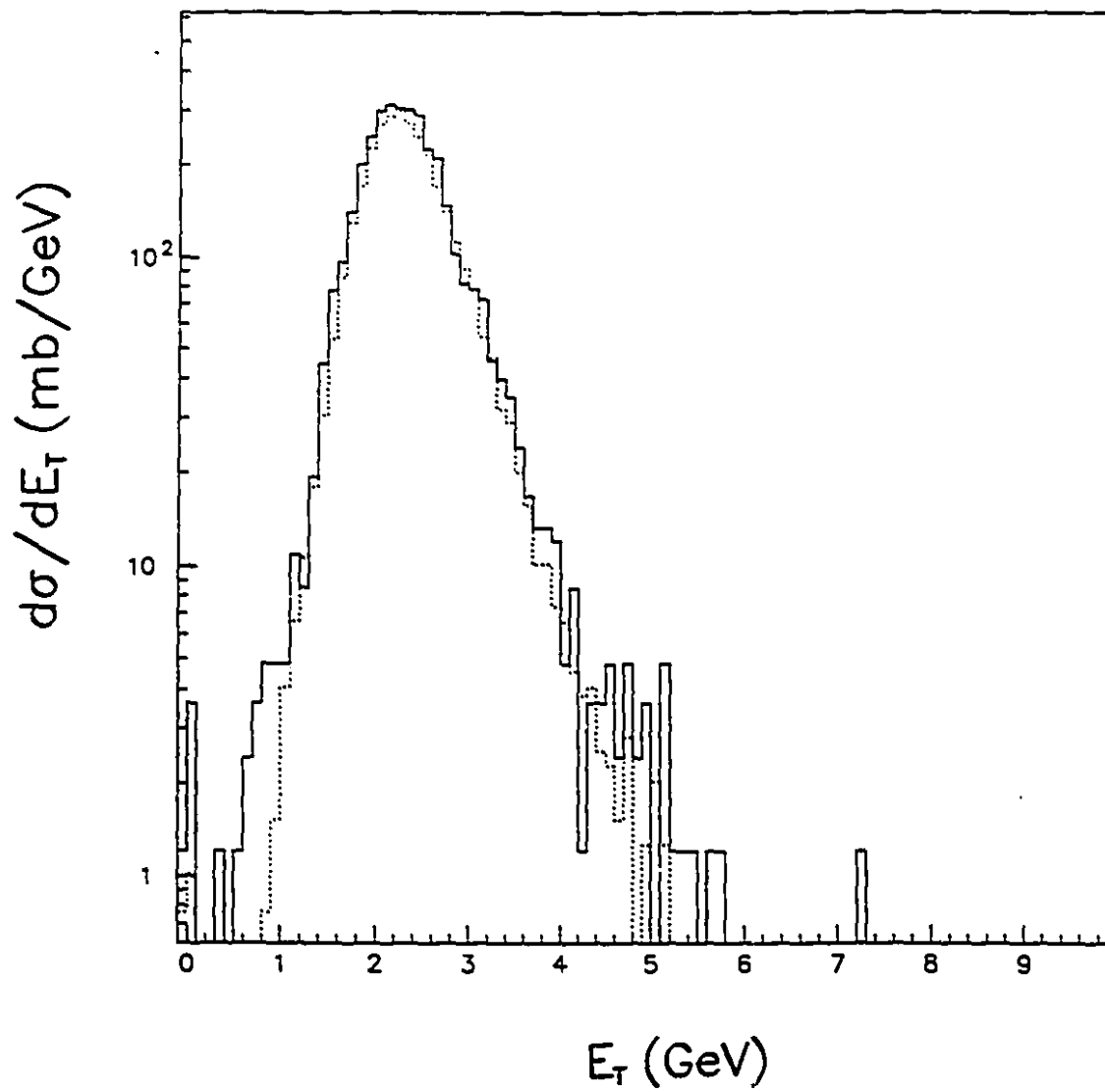


Figure 3.1: Comparison of the transverse energy distribution for 2% Pb target (full line) and 1% Pb target (dotted line).

Pb target with 2.4% interaction length for protons, and the dotted curve displays the data on Pb target with 1.2% interaction length. The figure shows that the difference of transverse energy production due to the change of target thickness is negligible. No target thickness corrections were done for the data presented here.

### 3.5 Detector Calibration

The measurements of transverse energy and charged particle multiplicity require an extensive understanding of related detector response. The energy response of the target calorimeter was calibrated with cosmic ray muons accumulated during two long calibration runs before and after the proton beam experiment. As muons rarely decay or scatter in medium, their energy loss is mainly caused by the process of minimum ionizing, which can be calculated by the Bethe-Bloch formula. In the April 1991 runs, arrays of scintillator paddles were installed above and below the target calorimeter back wall and each of the side wall to provide triggers for the incident minimum ionizing cosmic ray muons, which travel vertically to the ground. The calibration gain factors were adjusted by comparing the cosmic ray data to the simulations with the tracking program GEANT [Br87]. The stability studies of the gains in each crystal have shown that the gains fluctuate at the 1% level during the run period. Such small variations are negligible. The pedestal levels of electronic channels were found to vary noticeably over the run time. They were monitored run by run from empty trigger events and were adjusted accordingly in offline analysis.

The absolute scale for the energy deposited in the participant calorimeter was calibrated with muon beam. The response of the participant calorimeter to protons, pions, muons and electrons of energies ranging from 1.5 GeV to 10 GeV has been studied in detail [FO92, Zh93]. The participant calorimeter has two monitoring systems: an optical source system, which is used to set and monitor the photomultiplier gains, and a 2.4 mCi  $^{60}\text{Co}$  source system, which is used to determine the long term stability and

the relative plate to plate response of the calorimeter. The measured electron energy resolution for each of the 512 towers of the calorimeter fluctuates from  $0.23/\sqrt{E}$  to  $0.32/\sqrt{E}$ , where  $E$  is the incident energy in GeV. The hadronic energy resolution has been found to be approximately  $0.4/\sqrt{E}$ . A number of tests were performed to measure the reproducibility and stability of the gain settings. Mean gain shifts smaller than 3% were measured over the duration of the forward transverse energy experiment. For such small shifts no gain corrections were applied to time dependence. Pedestal shifts of the calorimeter electronics were monitored and adjusted run by run.

The procedure for going from the measured energy to the corrected transverse energy is different for the target calorimeter and the participant calorimeter. It will be discussed in detail in the next chapter.

## Chapter 4

# DATA ANALYSIS AND RESULTS

In this chapter, the discussion will focus on the reduction of raw experimental data: the data measured in the target calorimeter with multiplicity trigger, the data measured in both the participant calorimeter and the target calorimeter with transverse energy trigger, and the data measured by the charged multiplicity detector in both cases. The analysis procedure includes applying various offline cuts on the raw data, making noise correction on the detectors, performing empty target subtraction from the data, and correcting for the detector response and efficiency. The detector efficiency correction involves extensive Monte Carlo simulations which will also be discussed in this chapter.

### 4.1 Good Beam Selection

The raw data recorded on the computer tapes include various background and unwanted interactions such as double beam interactions, upstream interactions and detector noise. Double beam interactions happen when multiple beam particles arrive within a short time (20 ns) so that they are treated as single particle by the data acquisition electronics. Upstream interactions occur when beam particles interact with the materials such as the beam pipe, beam exit window, beam vertex detectors, beam telescope scintillators and air prior to the target.

Good events are selected by applying various offline cuts to ensure that only a single beam particle is incident on the target. For that purpose a combination of offline cuts

on the signal pulse heights from beam telescope scintillators and the energy detected in the back wall of the target calorimeter is used.

A good beam event is defined by the coincidence signal of the beam telescope which consists of four sets of scintillator counters: S1, S2, S3 and S4 (shown in figure 2.2). As stated in the previous chapter, a good beam particle signal occurs when a beam particle passes through the beam scintillators S2 and S4 and the holes of veto counters S1 and S3. Signals on the scintillator counters of S1, S2, S3 and S4 are shown in Figure 4.1(a), Figure 4.1(b), Figure 4.1(c) and Figure 4.1(d) respectively. The scintillators S2 and S4 each has two photo tubes; while S1 and S3 each has four. The signals shown in the figure are the sums of the signals from all the tubes for each scintillator. The peaks near zero channel in S1 and S3 are pedestals, while the peaks in S2 and S4 are signals produced by minimum ionizing particles. The cuts applied to these signal amplitudes are shown with short vertical lines in the figure. The beam particle is considered to be good if the signal pulse heights from the sum of signals from the phototubes for each beam detector satisfy following cuts:

$$S1 \leq 30, \quad (4.1)$$

$$50 \leq S2 \leq 325, \quad (4.2)$$

$$S3 \leq 64, \quad (4.3)$$

$$9 \leq S4 \leq 75. \quad (4.4)$$

Most of the unwanted multiple beam particles which pass through the beam definition counters within one ADC gate are thus removed by the upper threshold in S2 and S4. Approximately 10% of the events recorded on tapes are rejected using this offline cut. Most rejected events are those which do not satisfy the signal amplitude requirement for S2 or S4.

Interactions occurring upstream of the target are vetoed by applying the cut on energy measured in the back wall of the target calorimeter. Figure 4.2 shows the transverse energy measured in the side walls of the target calorimeter ( $T_{cal} - E_T - noback$  in the figure) versus total energy deposited in all the walls of the target calorimeter

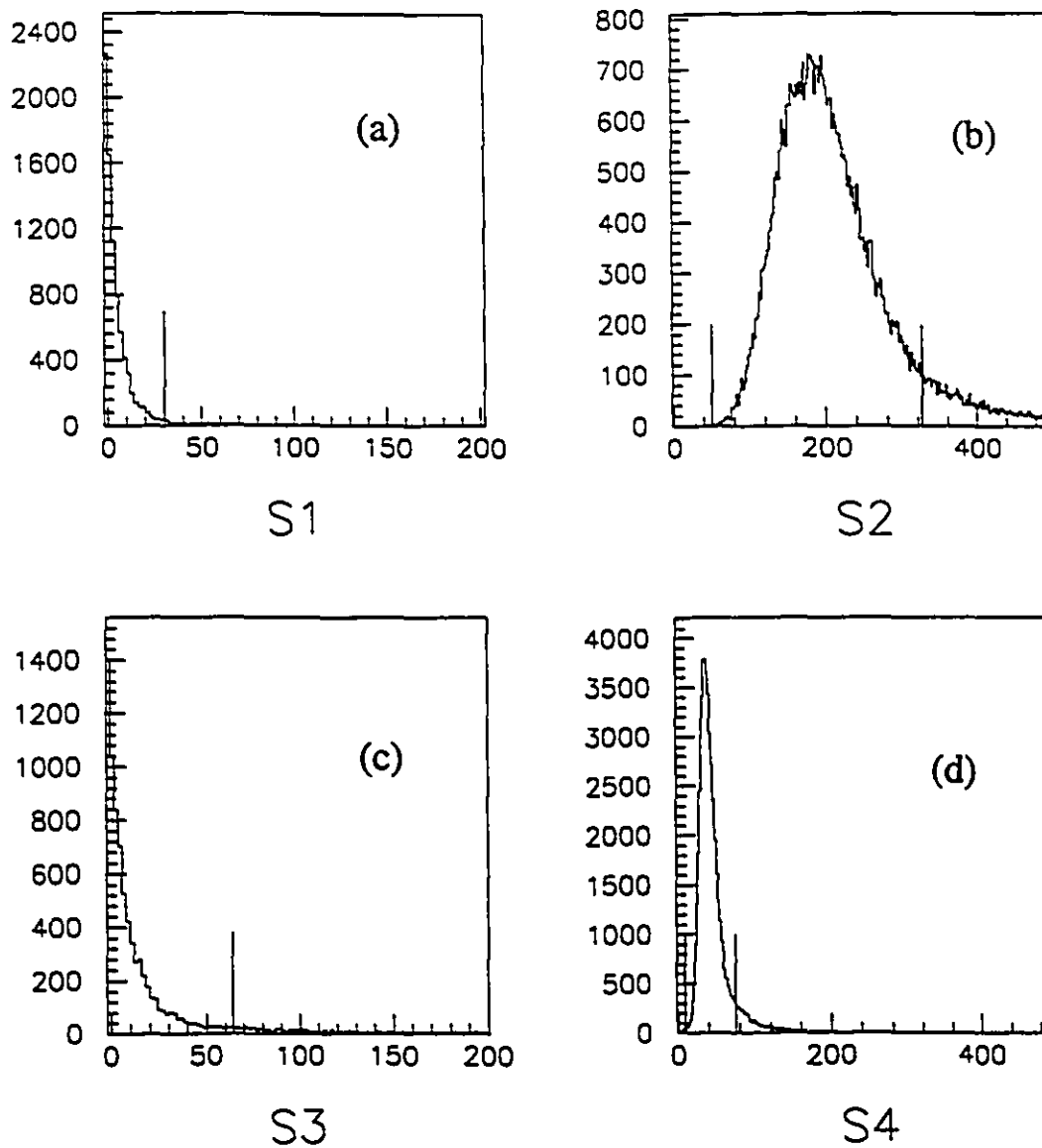


Figure 4.1: Pulse height distribution of signal measured in the four beam counters: (a) S1, (b) S2, (c) S3 and (d) S4.

( $T_{cal} - E_{tot}$  in the figure). Two bands of events can be seen in this figure. The upper band indicates the interactions at the target, which we want to keep. Their behavior shows a strong correlation between  $T_{cal} - E_T - n_{oback}$  and  $T_{cal} - E_{tot}$ . The lower band of the events in the figure indicates upstream interactions which tend to deposit large amount of energy in the back wall of the target calorimeter but relatively small amount in the side walls of the calorimeter. The events below the line drawn in Figure 4.2 are removed. The veto for upstream interactions (the lower band the figure) is expressed as:

$$E(TCAL) > K * E_T(TCAL)_{n_{oback}} + C \quad (4.5)$$

where  $E(TCAL)$  is the total energy detected in the target calorimeter including its back wall, and  $E_T(TCAL)_{n_{oback}}$  is the transverse energy detected with the target calorimeter's side-walls only. The slope parameter  $K$  of the line is chosen to be 0.80 and the constant  $C$  chosen to be - 0.56 GeV. For the proton-nucleus experiment discussed here with the trigger condition discussed in Chapter 3, the upstream interactions vetoed using the above cut amounted to  $\approx 2.9\%$  of the events only.

## 4.2 Normalization

The differential cross-section is calculated from the number of events in each  $E_T$  bin, the beam rate and the target thickness. The number of nuclei per  $cm^2$  in the target is given by

$$T = \frac{\rho_s N_A}{A} \quad (4.6)$$

where  $\rho_s$  is the target thickness in  $g/cm^2$  as listed in Table 3.2 of Chapter 3,  $N_A = 6.022 \times 10^{23}$  atoms per mole is the Avogadro constant,  $A$  is the atomic weight of the target material in  $g/mole$ .

To achieve the absolute normalization of cross-sections, we need to use the effective beam as the flux value. The effective beam is the total number of beam particles detected while the data acquisition system is active. The number of good beam particles

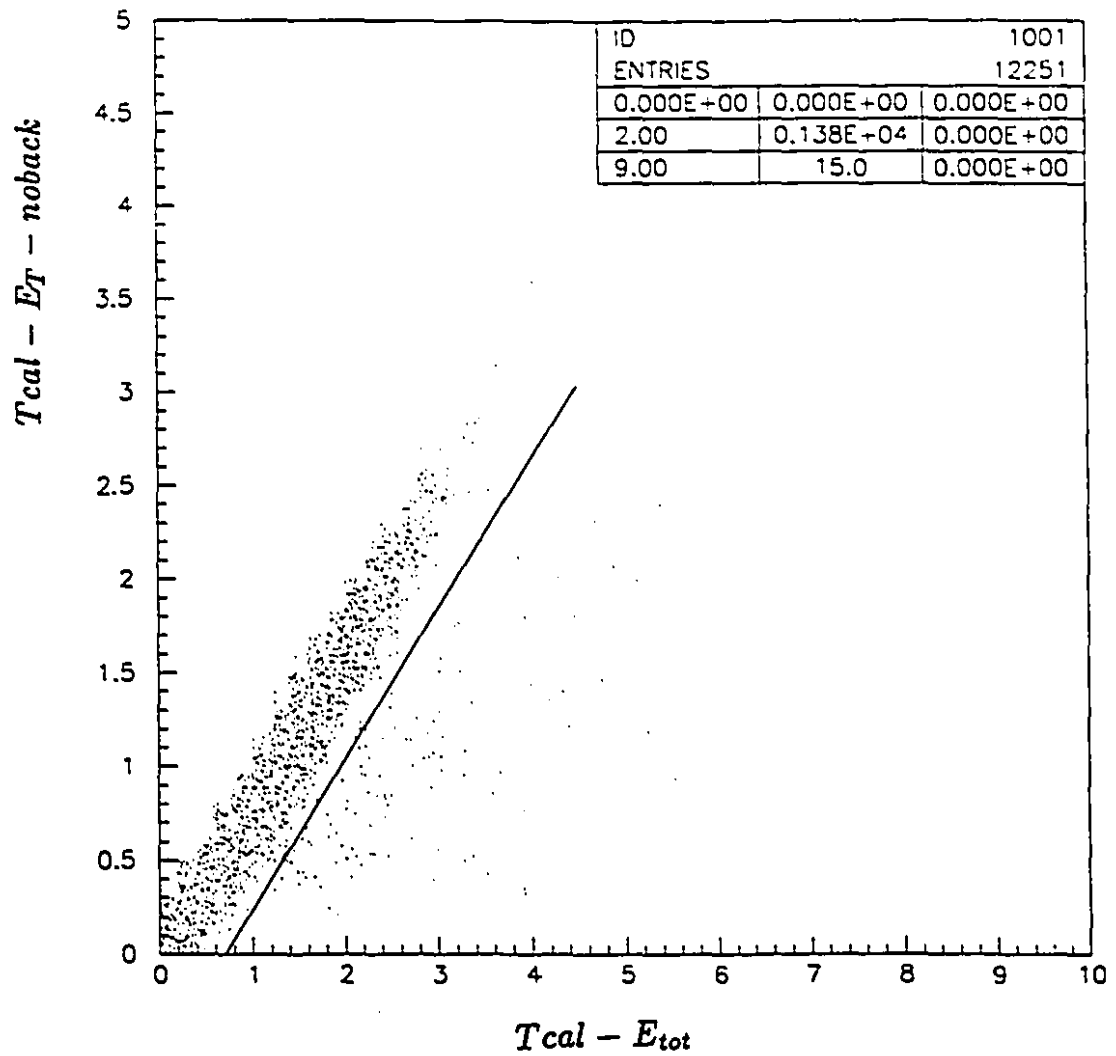


Figure 4.2: A correlation cut in the plane of  $T_{cal} - E_T - noback$  versus  $T_{cal} - E_{tot}$ . Those events on the right of the line are rejected in the data analysis.

is the actual number of particles satisfying the beam trigger logic. The gated beam is given by the total number of beam particles arriving at the target that satisfy the beam logic vetoed for the fraction of the time when the data acquisition is busy. To maintain a high rate of data on tape the live time was kept between 70-80% during the experiment.

Since the data are taken with different downscaling factors for different triggers and offline cuts are applied in the analysis, we need to adjust the cross-section calculations to take these affects into account. Therefore, the absolute differential cross-section for transverse energy measured in the target calorimeter is expressed as:

$$\frac{d\sigma}{dE_T}(mb/GeV) = \frac{10^{27}}{T} \left[ \frac{\frac{dN}{dE_T(target)} F_1 * DS_1}{B_1} - \frac{\frac{dN}{dE_T(empty)} F_2 * DS_2}{B_2} \right] \quad (4.7)$$

where  $d\sigma$  represents an integrated cross-section or differential cross-section per unit energy or multiplicity and  $N$  is the number of events for the bin. The number  $10^{27}$  is conversion factor from  $cm^2$  to  $mb$ ,  $dN/dE_T(target)$  is the number of events in certain  $E_T$  bin with target in frame,  $dN/dE_T(empty)$  is the number of events in certain  $E_T$  bin with target out of frame,  $F_1$  is the ratio of events read to events analyzed which is the number of events after offline cuts,  $DS_1$  is the downscaling factor for a particular trigger condition (see Table 3.4 in Chapter 3),  $B_1$  is the effective number of beam particles,  $F_2$ ,  $DS_2$  and  $B_2$  are corresponding parameters for the empty target.

The total multiplicity event by event was evaluated by summing over all the hits. The differential cross-section (in mb) of charged particle multiplicity production is normalized using the following formula:

$$\frac{d\sigma}{dN_c} = \frac{10^{27}}{T} \left[ \frac{\frac{dn}{dN_c(target)} F_1 * DS_1}{B_1} - \frac{\frac{dn}{dN_c(empty)} F_2 * DS_2}{B_2} \right] \quad (4.8)$$

where  $dn/dN_c(target)$  is the number of events for certain  $N_c$  with target-in,  $dn/dN_c(empty)$  is the number of events for certain  $N_c$  with target-out, and the other symbols have the same definitions as above.

The normalized  $dE_T/d\eta$  distribution is calculated in a similar way:

$$\frac{dE_T}{d\eta}(GeV/\eta) = \left[ \frac{E_{T1} * DS_1}{B_1} - \frac{E_{T2} * DS_2}{B_2} \right] \frac{K}{\frac{N_1 * DS_1}{B_1} - \frac{N_2 * DS_2}{B_2}} \quad (4.9)$$

where subscripts 1 and 2 refer to runs with and without target respectively,  $E_T$  is the transverse energy for all the crystals in a  $\eta$  bin,  $B$  the effective number of beam particles,  $DS$  the downscaling factor for a particular trigger,  $K$  the number of bins per  $\eta$ ,  $N$  the total number of events for a target or for empty.

The normalized  $dN_c/d\eta$  distribution is calculated by using the above equation where all  $E_T$ s are replaced by  $N_c$ .

### 4.3 Correction of Data from Target Calorimeter

#### 4.3.1 Coherent Noise Correction

The energy response of the target calorimeter is calibrated with cosmic-ray muons. The gains for each crystal were found to be fairly stable, within 1% fluctuation between the two calibration runs which were performed before and after the p-nucleus experiment of April 1991. The pedestal levels of the ADC channels for the target calorimeter were found to vary substantially over an extended period of time of several runs. They were monitored from empty trigger events, which were taken using a random trigger during a time when no beam is present. The mean value of the pedestal for each crystal is first calibrated using the calibration file generated by the calibration runs of the target calorimeter, and then adjusted offline run by run according to empty trigger events. In the offline analysis, each run is scanned twice. The first scan is to correct pedestal shift. The analysis program first reads the mean pedestals and the gain values for the 992 crystals of the target calorimeter from the calibration file, it then checks the raw data on each crystal with the empty trigger events recorded during the run. The mean pedestal shift for a crystal is calculated as following:

$$M_1 = \frac{1}{N} \sum_{k=1}^N [RTCAL_k(i, j) - Tped_{cali}(i, j)] \quad (4.10)$$

$$M_2 = \frac{1}{N} \sum_{k=1}^N [RTCAL_k(i, j) - Tped_{cali}(i, j)]^2 \quad (4.11)$$

where  $M_1$  indicates the mean pedestal shift for the channel  $(i, j)$  during the run, and the index  $i$  and  $j$  define the position of the crystal at certain polar and azimuthal angles.  $N$  is the total number of events with empty trigger in that run.  $RTCAL_k(i, j)$  the raw ADC counts from the crystal at  $(i, j)$  position at the  $k^{th}$  empty trigger event in that run; while  $Tped_{cali}(i, j)$  is the mean pedestal value at  $(i, j)$  channel given by the target calorimeter calibration file. The pedestal for each crystal is thereby updated run by run in the following manner:

$$Tped_{corr}(i, j) = Tped_{cali}(i, j) + M_1 \quad (4.12)$$

where  $Tped_{corr}(i, j)$  is the new pedestal mean value corrected for the mean shift during the run. The sum of all the pedestal shifts is typically 5 MeV over one run time which lasts approximately 30 minutes. By this method the pedestal for each crystal is effectively averaged at zero GeV.

Figure 4.3 shows the pedestal energy distribution for empty trigger summed over all the crystals of the target calorimeter. The data is taken from 459 empty trigger events during a typical run corrected for the fine shift on the pedestal mean. Pedestal fluctuations for each crystal are typically below 1 MeV, while the fluctuations over the sum of all crystals are about 180 MeV.

Comparison of the width of the pedestal for a single crystal and the sum of the pedestals indicates the presence of coherent noise which broadens the energy distribution measured in the detector. To minimize the effect of this coherent noise, we use a cluster search algorithm to determine the transverse energy measured in the calorimeter.

Theoretically, transverse energy is defined as the sum of the energies of particles weighted by the sine of their angles to the beam. In the present analysis, we calculate the transverse energy in the target calorimeter in the following way:

$$E_T = \sum_{i=1}^n E_i \sin \theta_i \quad (4.13)$$

where  $E_T$  is the transverse energy measured in the target calorimeter,  $E_i$  the energy deposited in the  $i^{th}$  cluster of crystals,  $\theta_i$  the polar angle between the center front face of the center crystal of the cluster ( $i$ ) and the beam axis.

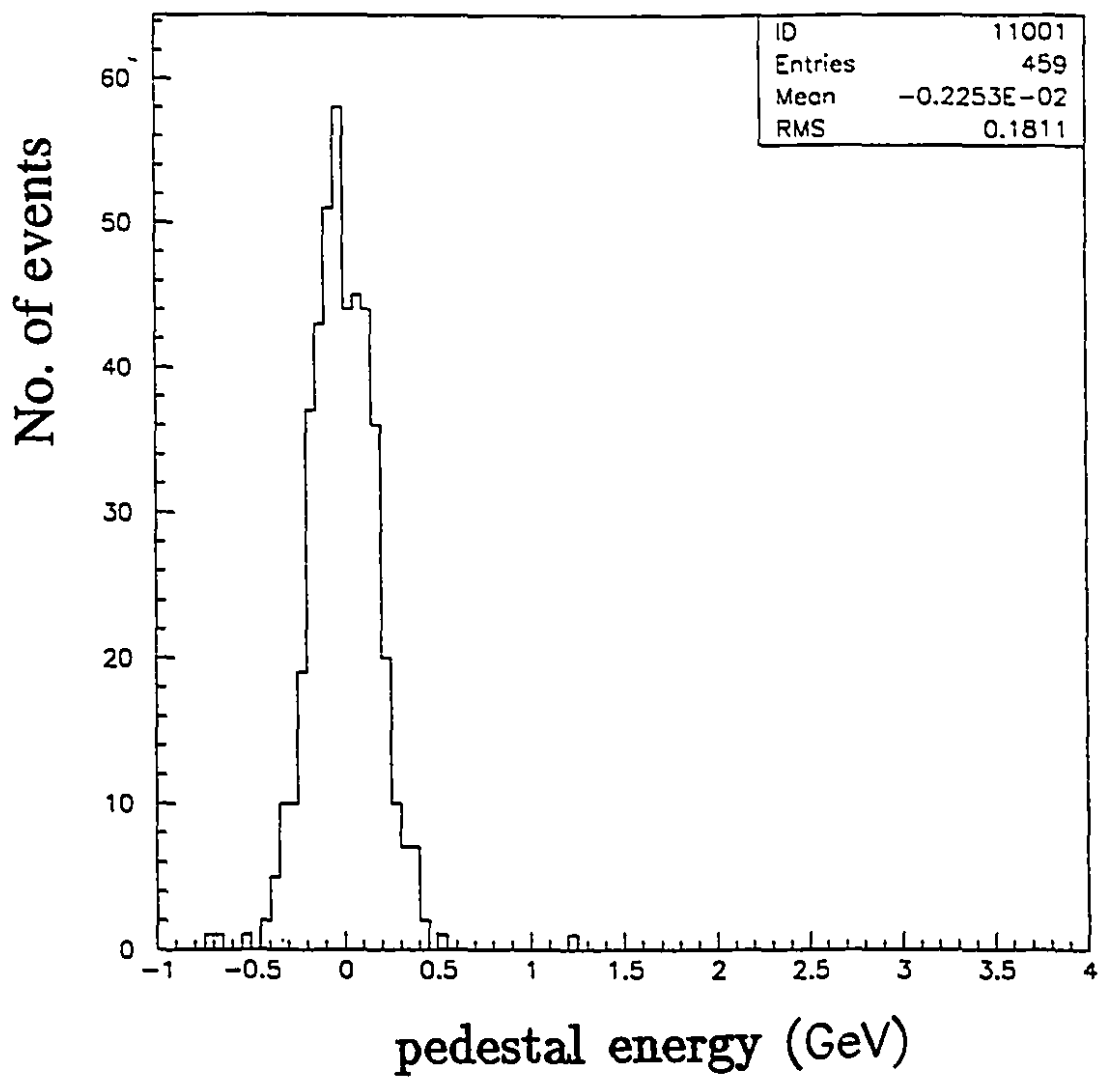


Figure 4.3: Pedestal energy distribution of sum over all the crystals of the target calorimeter.

A cluster of crystals fired in the target calorimeter is defined as being composed of one or more adjacent crystals having at least 5 MeV of deposited energy and more than 30 MeV energy in the crystal with the largest deposited energy. The crystal with the maximum energy defines the center of the cluster. The cluster searching program first searches for energy local maxima, and then the energy (above the threshold of 5 MeV) of the neighboring crystals are summed up to obtain the cluster energy. The energy in those crystals that do not belong to any clusters is set to zero. Some neighboring crystals may be common neighbors of two or more local maxima or clusters, in which case the energy in each common neighbor crystal is shared between the clusters according to the ratio of energy in the center crystals. Generally one particle from the reaction entering the target calorimeter acceptance fires one cluster of crystals. Each cluster is composed of three crystals on average, with a standard deviation of 0.7. Some clusters may consist of as many as 7 crystals. Near the edge of the target calorimeter there is leakage and the centers of the clusters will be artificially moved inward. This effect will be included in the calculation of the detector acceptance done by a GEANT simulation which will be discussed later.

Figure 4.4 shows the measured cluster distribution from the target calorimeter for 14.6 GeV/c protons on the Pb target (solid curve) and on the Al target (dashed curve) with multiplicity level 1 trigger which requires more than four charged particles registered in the multiplicity detector. The number of clusters per event extends from zero up to about 30 for p+Pb reactions with the decrease of the differential cross-section by a factor of  $10^4$ . The average number of clusters produced in each event is 6 for the Pb target or 4 for the Al target, suggesting more particles are produced in reactions on a heavier target. The spatial distributions of the number of clusters per event are shown in figure 4.5. The solid curve is for the Pb target and the dashed curve is for the Al target. Each of the  $\eta$  distribution of clusters is composed of two sections :  $-0.6 < \eta < 1.0$  for the side walls of the target calorimeter and  $-2.3 < \eta < -0.9$  for the back wall of the target calorimeter. The figure shows that most clusters are fired in the four side walls. The structures in the distribution are mainly due to the geometry of the target

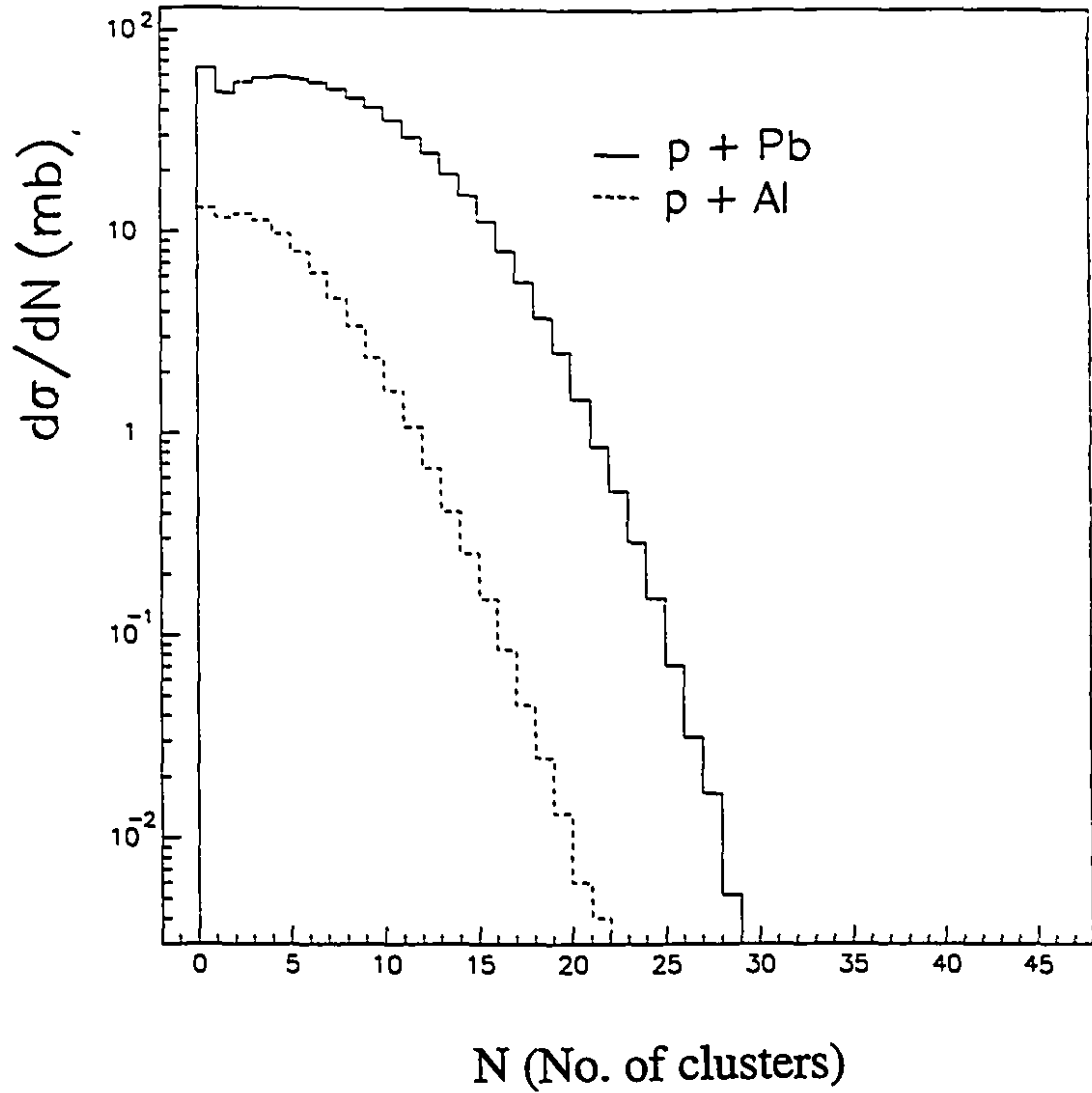


Figure 4.4: Measured cluster distribution in the target calorimeter for 14.6 GeV/c protons on Pb target (solid curve) and on Al target (dashed curve) with multiplicity level 1 trigger.

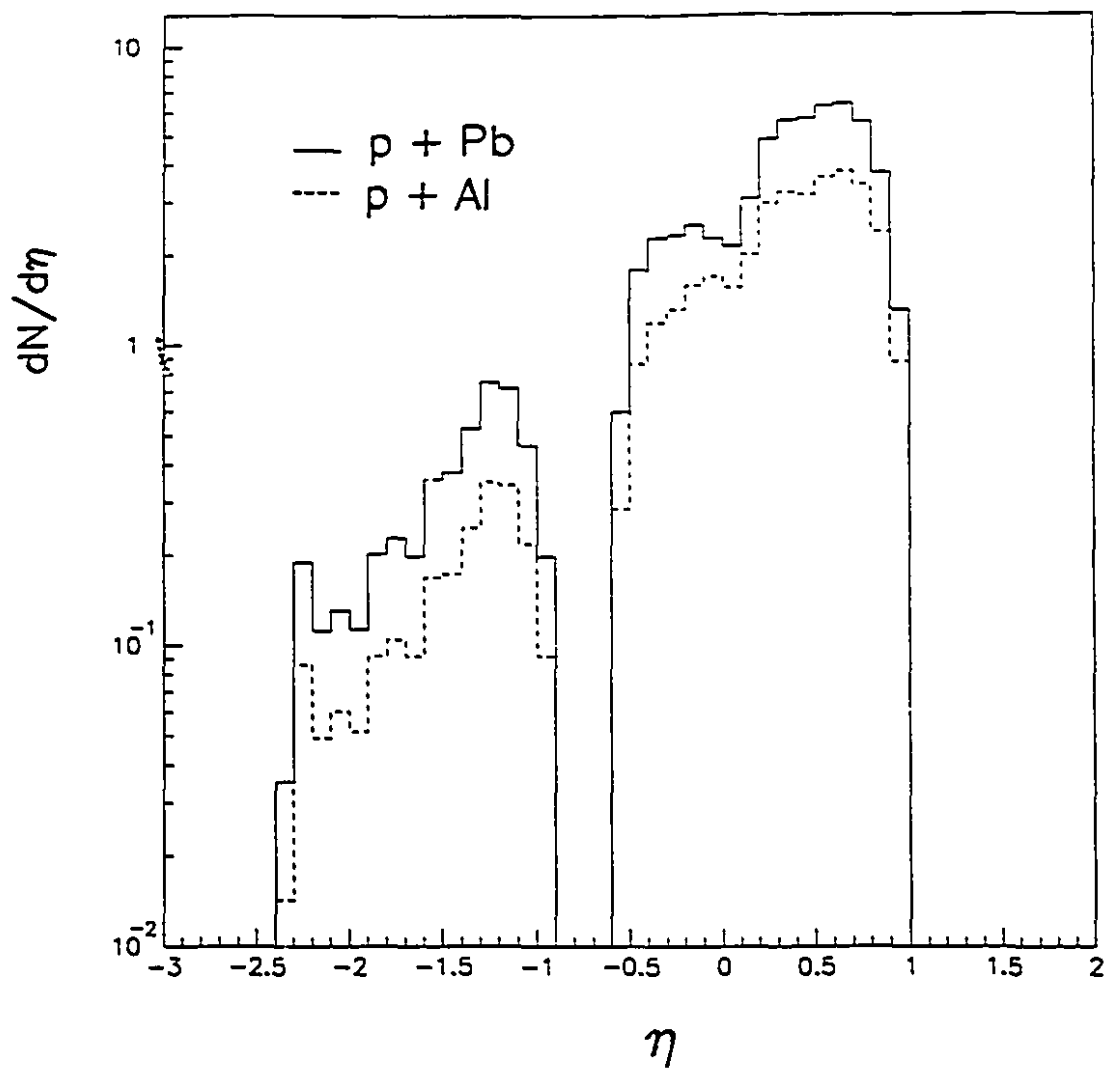


Figure 4.5: Pseudorapidity distributions of clusters measured in the target calorimeter. These are not corrected for detector efficiency.

calorimeter. The  $\eta$  distribution of clusters is related to the energy flow, and therefore the transverse energy of the reaction, which will be discussed later in the section on  $dE_T/d\eta$  data.

### 4.3.2 Background Subtraction

Many unwanted events have been removed by applying various offline cuts. However, some events, such as those corresponding to upstream interactions that produce very low transverse energy or that occur between the back wall of the target calorimeter and the target, are difficult to identify. In order to correct for those remaining background interactions, data are taken in the empty target frame and are subtracted from the data with the target in place at normalized beam rates. Figure 4.6 shows the empty target correction of the differential cross-section for the collisions of protons on the lead (Figure 4.6(a) and Figure 4.6(c)) and aluminum targets (Figure 4.6(b) and Figure 4.6(d)). The solid line histograms in the figure illustrate the differential cross-section of transverse energy production before the empty target correction and the dotted histograms show the contribution from empty target interactions. The spectra shown in the figure are obtained with two kinds of reaction triggers: pretrigger (Figure 4.6(a) and Figure 4.6(b)) and multiplicity level 1 trigger (Figure 4.6(c) and Figure 4.6(d)) which is a higher level reaction trigger. As seen in the figures, with the pretrigger the empty target subtraction is important at low transverse energy or at very high transverse energy. In this case, the empty target subtraction corresponds to about 20% of the integrated cross-section. This large fraction is due to the fact that the pretrigger is close to a minimum bias trigger and is thus more sensitive to any background interactions. For the spectra of transverse energy with multiplicity level 1 trigger, the empty target subtraction corresponds to 2-3% of the integrated cross-section.

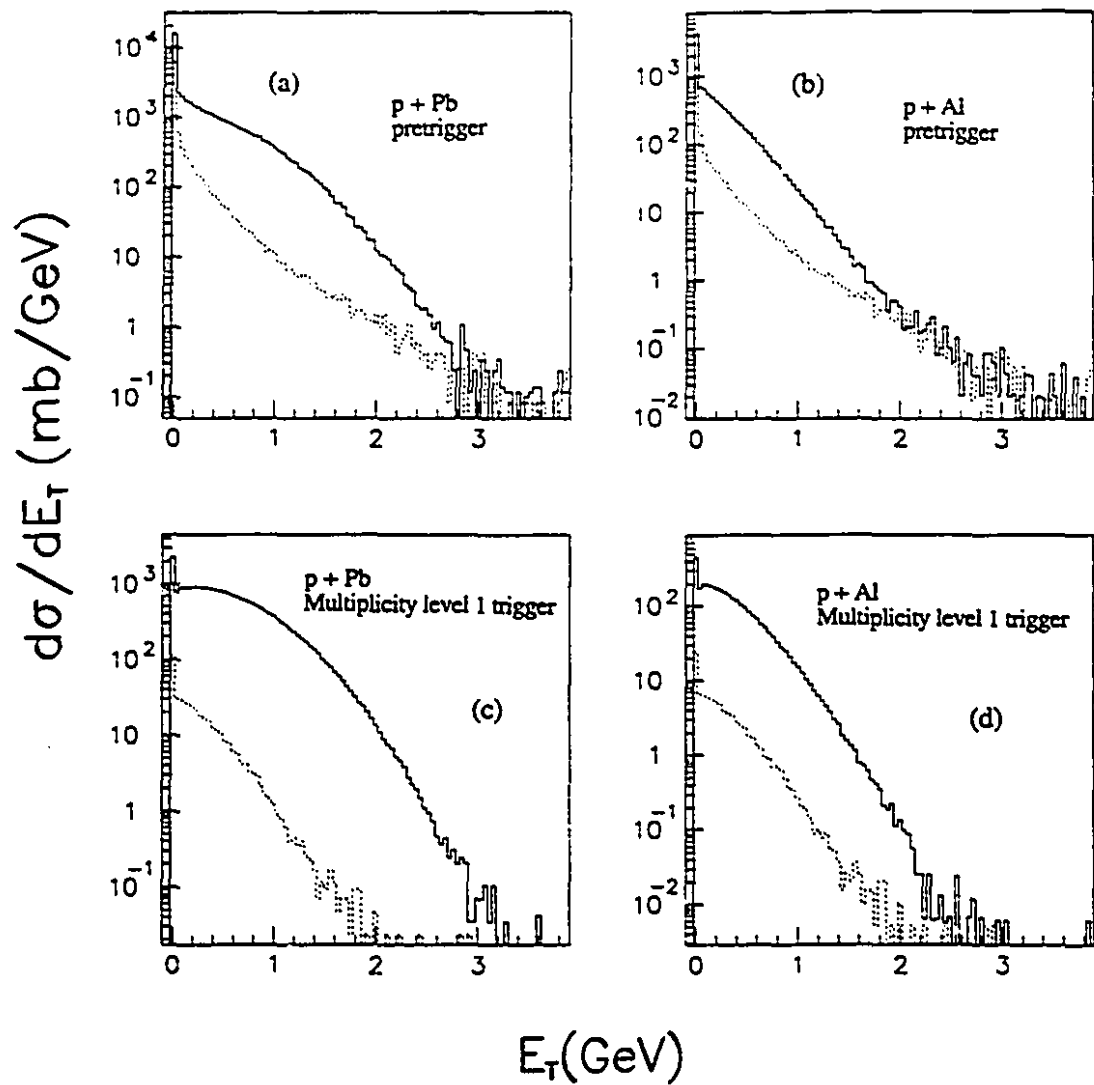


Figure 4.6: Empty target correction of the differential cross-section for (a) the Pb target for pretrigger, (b) the Al target for pretrigger, (c) the Pb target for multiplicity level 1 trigger and (d) the Al target for multiplicity level 1 trigger. Solid histograms denote data with target, and dotted histograms denote data without target.

### 4.3.3 Data Sample

In this section I will present a summary of the data obtained with the target calorimeter. It should be noted that these data are not yet corrected for detector leakage. Leakage correction will be discussed in the following section.

Figure 4.7 shows normalized transverse energy spectra with three different triggers for proton on the lead target. The solid curve is beam trigger data, the dashed curve is pretrigger data, and the dotted is multiplicity level 1 data. The  $E_T$  spectra with beam trigger are measured when the incoming beam particles satisfy the beam trigger logic. The unbiased  $E_T$  spectrum shows a huge peak at  $E_T$  zero representing incoming beam particles that do not interact in the target. The pretrigger as a low level reaction trigger requires more than two charged particles to be registered in the multiplicity detector. As seen in the figure, it is also a relatively minimum bias reaction trigger and the bias is mainly in the part of spectrum with  $E_T$  less than 0.2 GeV. To improve the statistics on the cross-section measurement at high  $E_T$ , a higher level trigger, the multiplicity level 1 trigger which requires more than four charged particles registered in the multiplicity detector, is used. The bias of the multiplicity level 1 trigger on the pretrigger happens mainly in the section of the spectrum with  $E_T$  less than 0.5 GeV. The different statistical errors in the histograms with three triggers are caused by the different event downscaling factors.

Figure 4.8 shows the differential cross-sections of transverse energy production for reactions of 14.6 GeV/c proton beam on the lead target (Figure 4.8(a)) and on the aluminum target (Figure 4.8(b)) measured in the acceptance of the target calorimeter - the pseudorapidity range from -2.3 to 1.0, with the empty target contribution subtracted. The differential cross-sections with pretrigger for both lead and aluminum targets are plotted in solid lines, while the differential cross-sections with multiplicity level 1 trigger are plotted in dotted lines. The measured differential cross-sections decrease monotonically with  $E_T$ , and extends up to 3 GeV for proton on the lead target and to 2 GeV for proton on the aluminum target. The measured total cross-sections

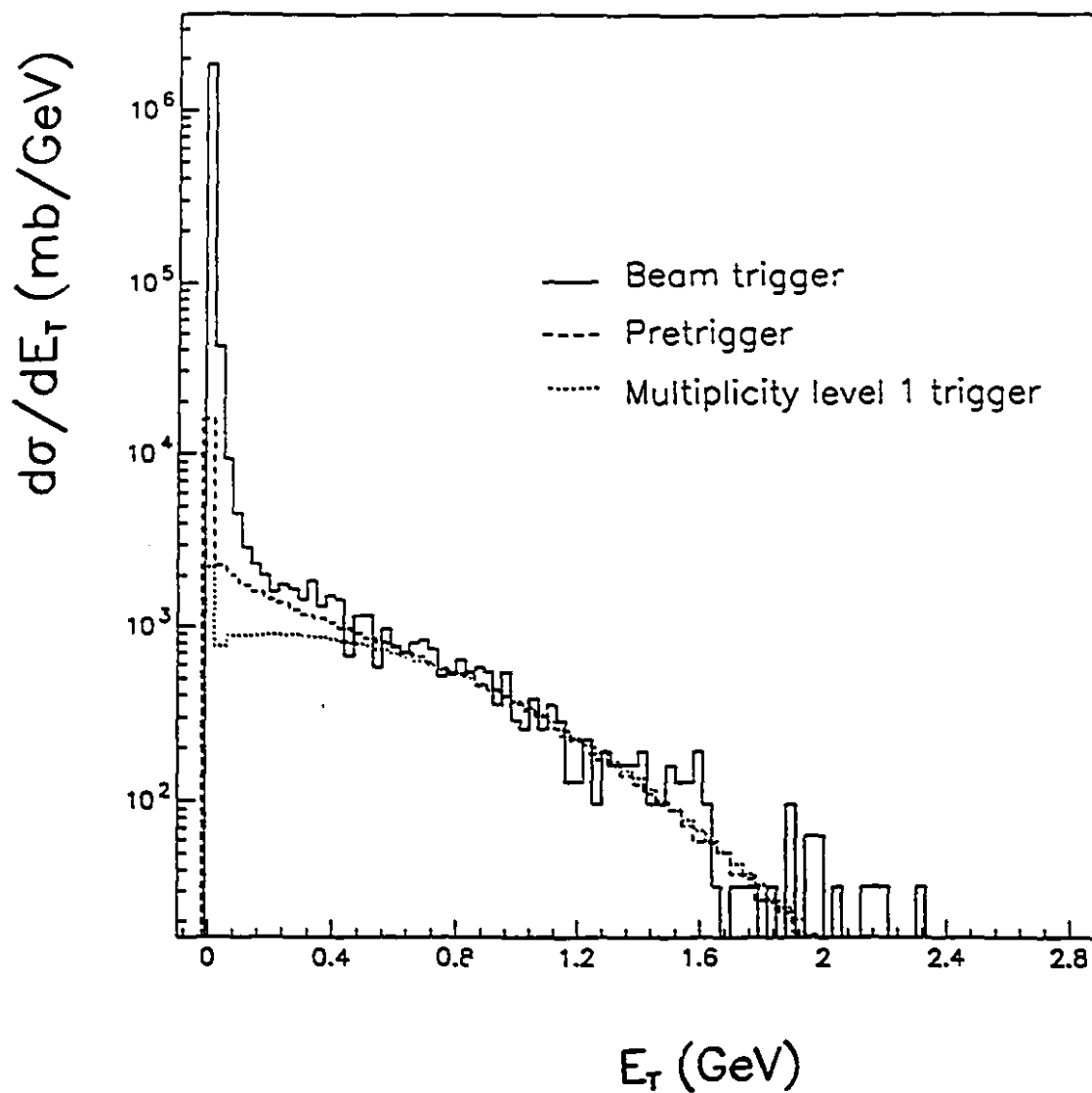


Figure 4.7:  $d\sigma/dE_T$  spectra for three different triggers for proton on the lead target.

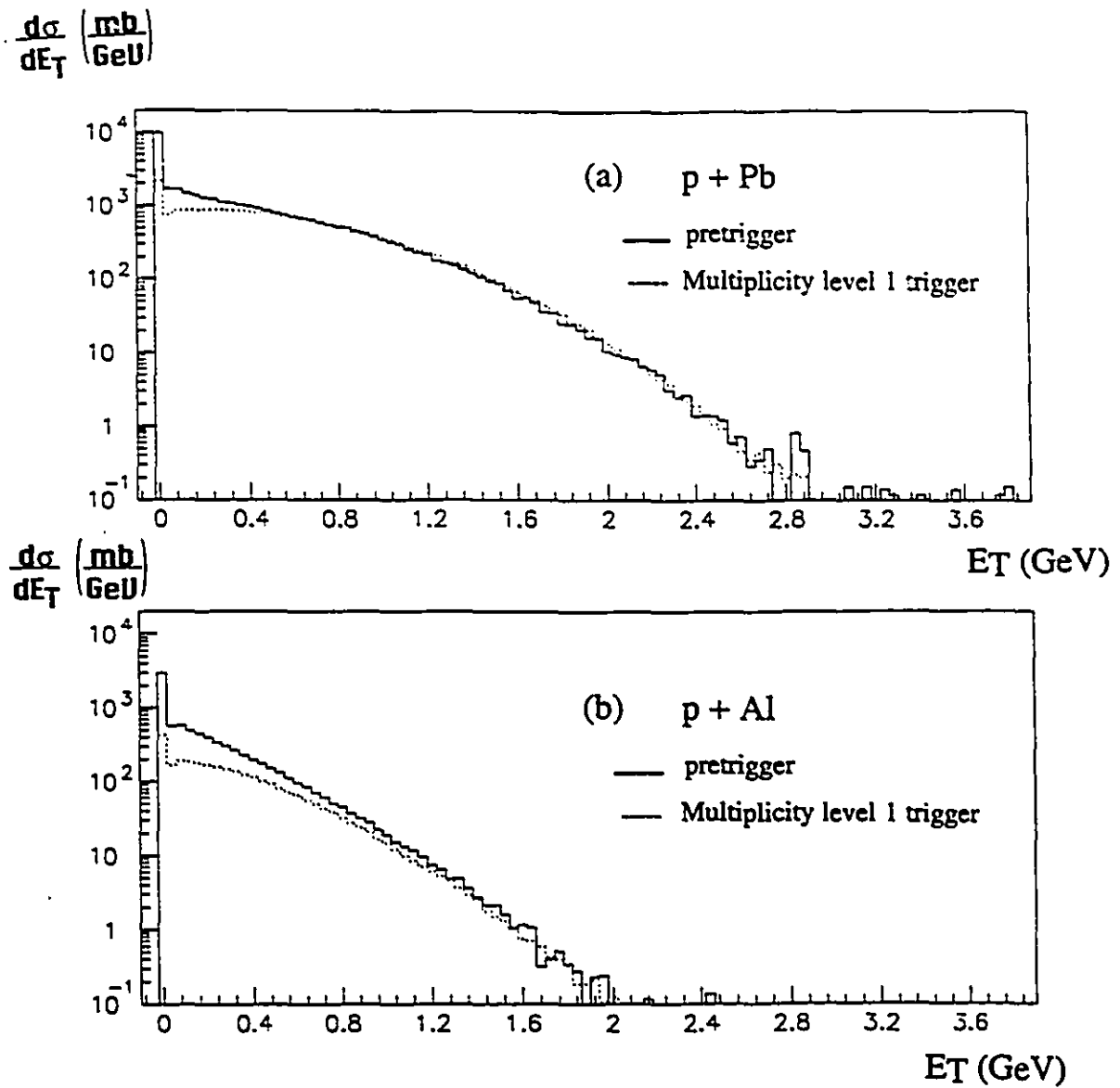


Figure 4.8: Transverse energy spectra measured in the target calorimeter for (a) p+Pb and (b) p+Al.

and mean transverse energies for the aluminum and lead targets in the acceptance of the target calorimeter are listed in Table 4.1. Due to the bias of the multiplicity level 1 trigger as compared to the pretrigger at low  $E_T$ , the data from the multiplicity level 1 trigger have smaller total  $E_T$  cross-section but higher mean  $E_T$  per event.

Table 4.1: Total cross-sections of  $E_T$  and mean  $E_T$  measured in the target calorimeter

Target	Trigger	Cross-section (mb)	Mean $E_T$ (GeV)
Pb	Pretrigger	$1.38 \times 10^3$	0.37
	Multiplicity level 1 trigger	698	0.55
Al	Pretrigger	318	0.21
	Multiplicity level 1 trigger	87	0.33

As stated previously, the energy deposited in the target calorimeter is determined by the cluster search algorithm. With the total transverse energy deposited and the number of clusters per event, the mean transverse energy deposited in each cluster can be evaluated.

Figure 4.9 shows cluster production for the lead target (Figure 4.9(a)) and the aluminum target (Figure 4.9(b)) in different  $E_T$  ranges. The data shown in the figure are taken with multiplicity level 1 trigger. It can be seen that higher  $E_T$  events lead to more clusters or particles. In the same  $E_T$  slice, the reactions on the Pb target generally produce more clusters than the reactions of the Al target.

Figure 4.10 shows differential cross-sections ( $d\sigma/dE_T$ ) of the transverse energy in a cluster for lead target (Figure 4.10(a)) and aluminum target (Figure 4.10(b)) in different total  $E_T$  regions. The mean  $E_T$  per cluster in each  $E_T$  range is determined by dividing the  $E_T$  by the average number of clusters, both terms being weighted by the cross-section. The results are listed in Table 4.2.

The mean  $E_T$  per cluster increases slowly with the  $E_T$ . The effect of target is rather small. A slightly higher  $E_T$  per cluster is obtained for the Al target in each  $E_T$  region. The fact that the mean  $E_T$  in Table 4.1 for the lead target is higher than the

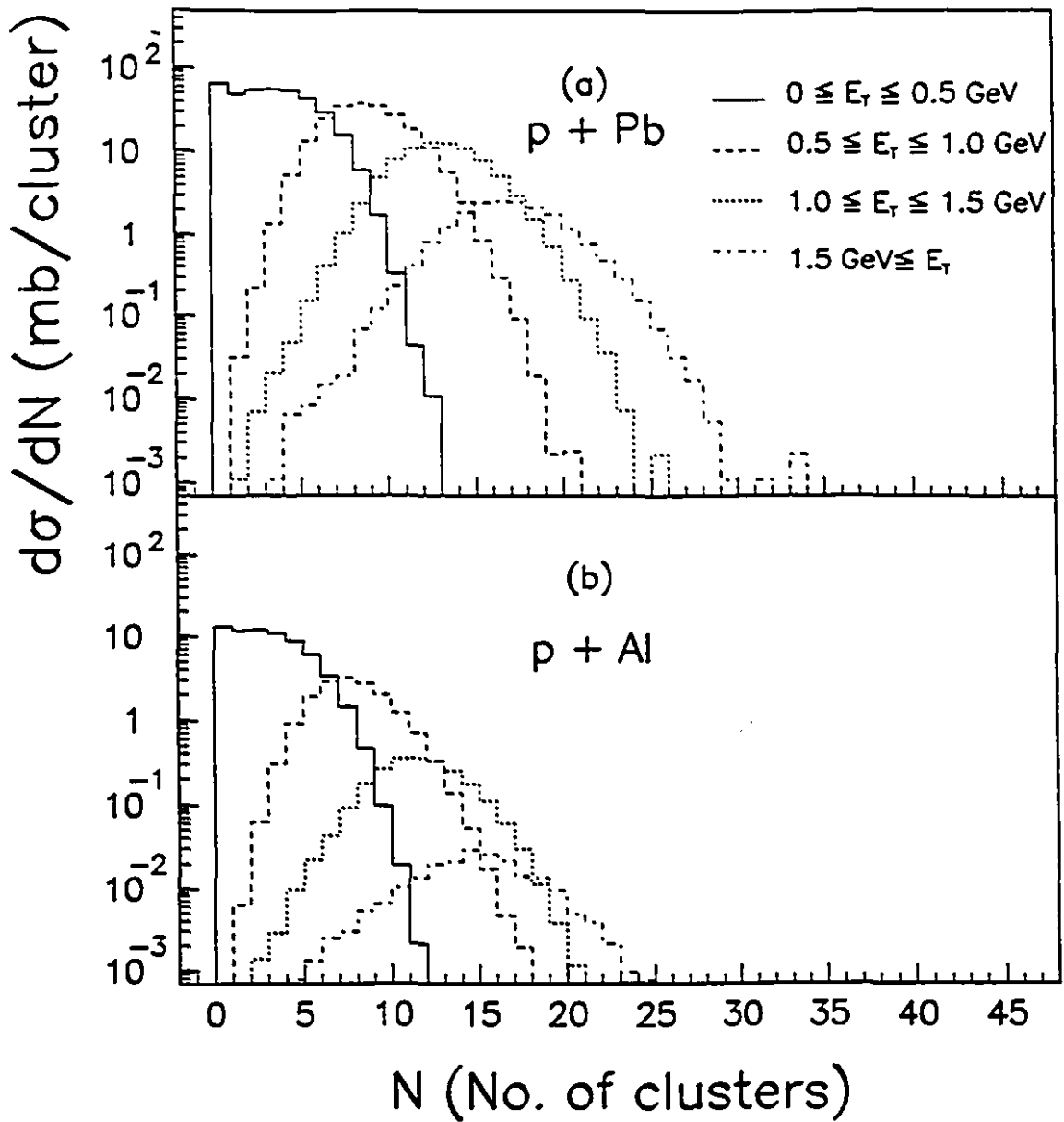


Figure 4.9: Energy cluster distributions for various  $E_T$  regions measured in the target calorimeter for (a)  $p+Pb$  and (b)  $p+Al$ .

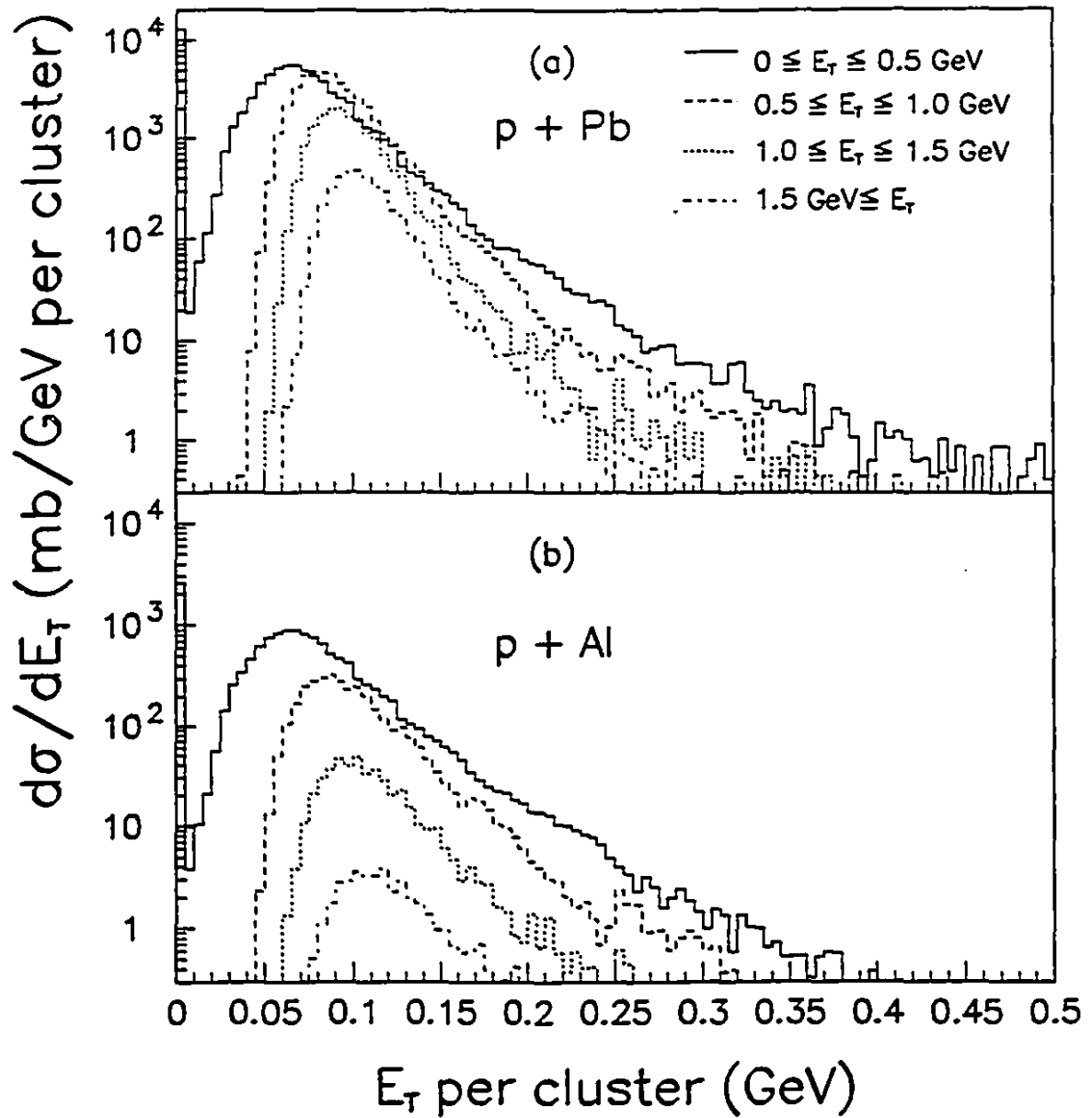


Figure 4.10: Differential cross-sections of the transverse energy per cluster for various  $E_T$  regions measured in the target calorimeter for (a) p+Pb and (b) p+Al.

Table 4.2:  $E_T$  (GeV) per cluster measured in the target calorimeter with multiplicity level 1 trigger

$E_T$ range	Pb target	Al target
$0 \leq E_T(\text{GeV})$	0.086	0.087
$0 \leq E_T(\text{GeV}) < 0.5$	0.073	0.075
$0.5 \leq E_T(\text{GeV}) < 1.0$	0.086	0.092
$1.0 \leq E_T(\text{GeV}) < 1.5$	0.095	0.104
$1.5 \leq E_T(\text{GeV})$	0.105	0.117

distribution for the aluminum target indicates there is more backward energy flow for the heavier target. A better way to illustrate this target dependence is to examine the spatial distribution of  $E_T$ , i.e.  $dE_T/d\eta$ .

In the offline data analysis,  $dE_T/d\eta$  spectra are obtained by plotting the  $E_T$  in each cluster in every event against the pseudorapidity of the clusters. Most particles produced in the reaction within the target calorimeter acceptance fire only one or two crystals though a few may fire up to six crystals, i.e., one center crystal and five neighboring crystals. To calculate the  $\eta$  position of each cluster we assume for each crystal that the center is at the polar angle of the front face and then find the energy weighted center of each cluster. In this way we reduced fluctuations which are produced if the center of a cluster is determined by the position of the crystal where more energy has been deposited [WA90]. Figure 4.11 shows the  $\eta$  distribution of the transverse energy measured in the back wall of the target calorimeter obtained in the two different ways. The  $\eta$  distribution obtained by locating the center face of the crystal with the maximum signal in each cluster is shown in Figure 4.11(a), while the  $\eta$  distribution obtained by using energy weighted cluster center is shown in Figure 4.11(b). It can be seen that fluctuations are reduced by using the energy weighted centers for  $\eta$  positions.

Figure 4.12 shows the pseudorapidity distribution of transverse energy for the reaction of 14.6 GeV/c proton beam on the lead target (solid curve) and on the aluminum target (dotted curve). Similar to Figure 4.6, the  $dE_T/d\eta$  spectra in the figure contain two parts: the spectra for  $\eta$  from -2.3 to -0.9 are measured in the back wall of the target

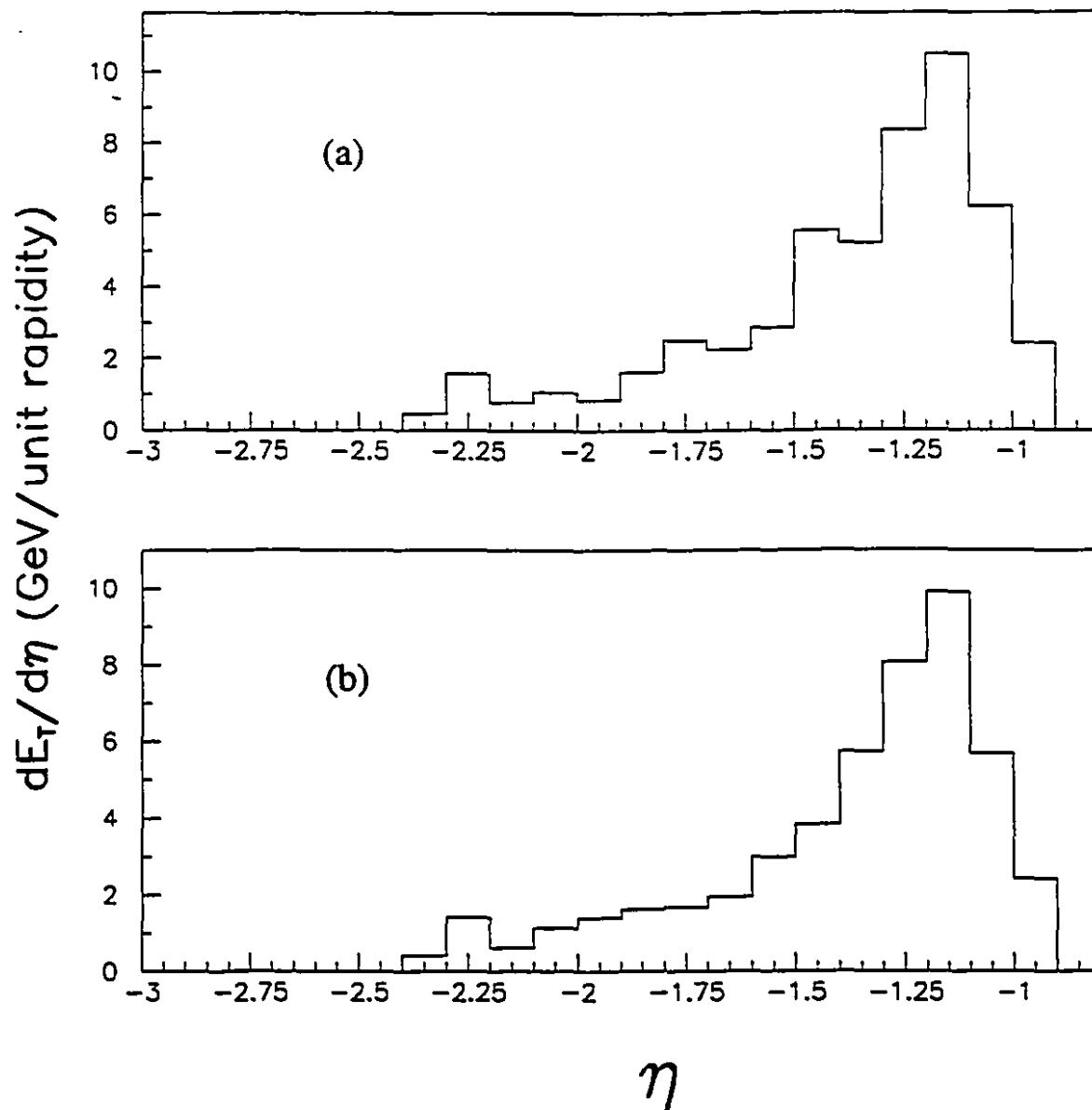


Figure 4.11:  $\eta$  distribution of the transverse energy measured in the back wall of the target calorimeter calculated: (a) by locating the center face of the crystal with the maximum signal in each cluster and (b) by using energy weighted cluster center.

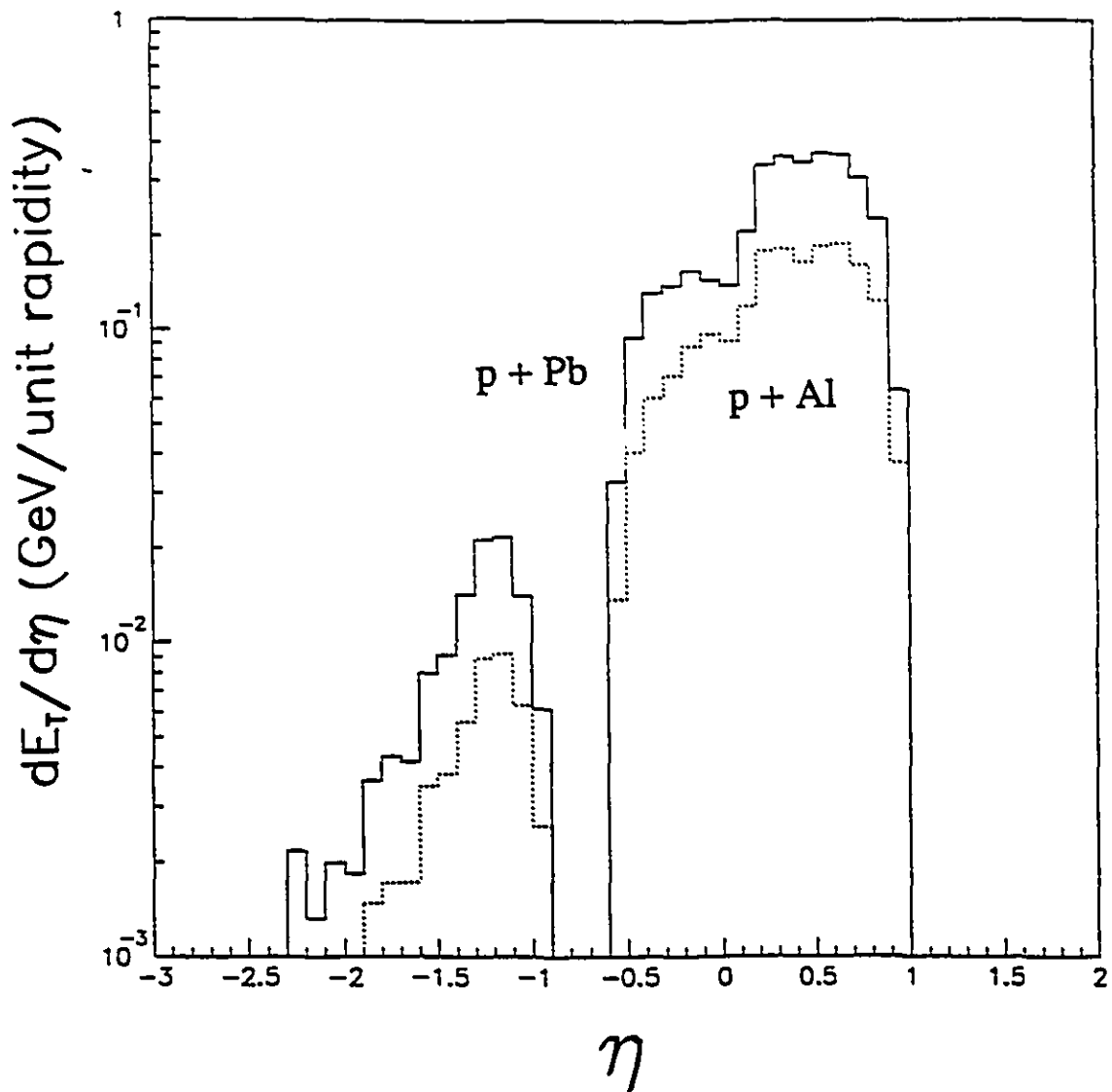


Figure 4.12: Pseudorapidity distribution of transverse energy measured in the target calorimeter for the reaction of 14.6 GeV/c proton beam on lead target (solid curve) and on aluminum target (dotted curve). These distributions are not corrected for leakage and efficiency.

calorimeter, and the spectra for  $\eta$  from -0.6 to 1.0 are measured in the side walls of the target calorimeter. The integral of the area under the histogram leads to the mean transverse energy per event listed in Table 4.1 obtained from the  $d\sigma/dE_T$  distributions. The structure of the distributions is mainly due to detector acceptance and efficiency. Therefore, these data on pseudorapidity distribution of transverse energy are sensitive to correction for detector efficiency and leakage.

Figure 4.13 shows the pseudorapidity distribution of transverse energy per event for the Pb target sliced according to four transverse energy ranges. Consequently, a higher  $E_T$  slice leads to higher  $dE_T/d\eta$  spectra. By comparing the  $dE_T/d\eta$  spectra in the four  $E_T$  ranges, it is observed that events in different  $E_T$  ranges result in very similar  $dE_T/d\eta$  distributions, moving slightly backward for higher  $E_T$  as seen from the  $\eta$  section of the back wall of the calorimeter. As stated previously, due to the limited thickness of the NaI crystal walls, the energy deposited in the target calorimeter is only a fraction of the incident energy. Therefore, the energy leakage from the target calorimeter needs to be evaluated to correct the  $dE_T/d\eta$  distributions. This is discussed in the next section.

#### 4.3.4 Corrections for Target Calorimeter Response

To correct the experimental data for detector response and to compare experimental results with theoretical predictions, Monte Carlo simulations have been performed. The response of the target calorimeter to incoming energy was simulated with the GEANT 3.15 package [BR87]. GEANT is a computer program package which simulates particle propagation through matter. GEANT allows users to define what type of material a detector is made of, and to specify geometrical dimensions and the position of each detector. Detectors can be designated as either sensitive or insensitive. GEANT tracks particles taking into consideration of all possible physics interactions or decays. Information such as particle identification, spatial coordinates, particle momentum and energy loss are recorded when a particle traverses a sensitive detector, but are not

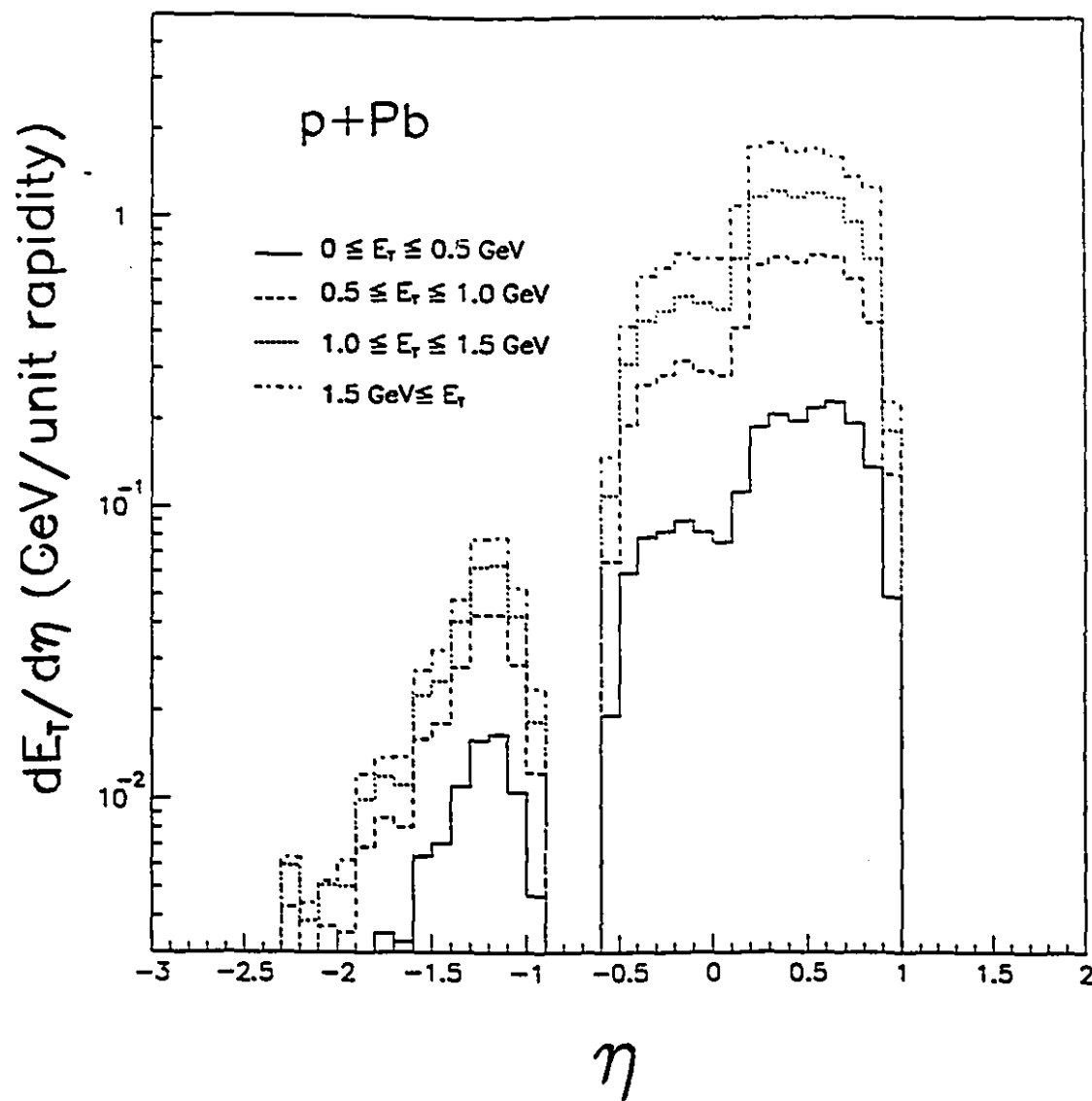


Figure 4.13: Pseudorapidity distribution of transverse energy for the Pb target for various  $E_T$  slices.

recorded in an insensitive detector where multiple scattering and other interactions are still taken into consideration. The program loops over all the particles from a generated event. The tracking proceeds in small steps through each detector until particles exhaust all the energy or escape the experimental setup defined in GEANT.

To calculate the correction we used events generated with RQMD, HIJET and FRITIOF models, all of which are being used in current studies of nucleus-nucleus collisions. One feature of these models is that the nucleons in the target nucleus are given Fermi momentum and are thus not bound. Therefore in the calculation, nucleons which have not interacted will nevertheless be emitted with their Fermi momentum. In order to select valid particles we should reject those very low energy nucleons which come from this unphysical dissociation of the target. Figure 4.14 shows the kinetic energy spectra for all charged particles in the multiplicity detector acceptance for RQMD p+Pb events. The low energy peak shown in Figure 4.14(a) represents those particles associated with target dissociation. In the analysis a cut at 999 MeV total energy is selected for the nucleons. The particle is only tracked when the total energy of a nucleon is higher than this cut (60 MeV kinematic energy). The spectra of the particles passing this cut is shown in Figure 4.14(b). The few particles below the cut correspond to low energy charged particles other than a proton. This cut has a negligible effect on the calculation of the target calorimeter response since most of these low energy particles are stopped in the target or in the target paddle counters in front of the calorimeter. It does however, have an effect on the charged particle multiplicity measurement that will be discussed in section 4.5.

The energy flow within the target calorimeter acceptance is determined from the generated p-nucleus reactions by propagating the emitted particles through the calorimeter. The photons which come from  $\pi^0$  decay in the target may convert into electron-positron pairs before entering the target calorimeter. This process will change the effective particle incident angle and energy. As a result it may change the resulting transverse energy deposited in the target calorimeter. Therefore,  $\pi^0$  conversions in the target have been included in the particle tracking.

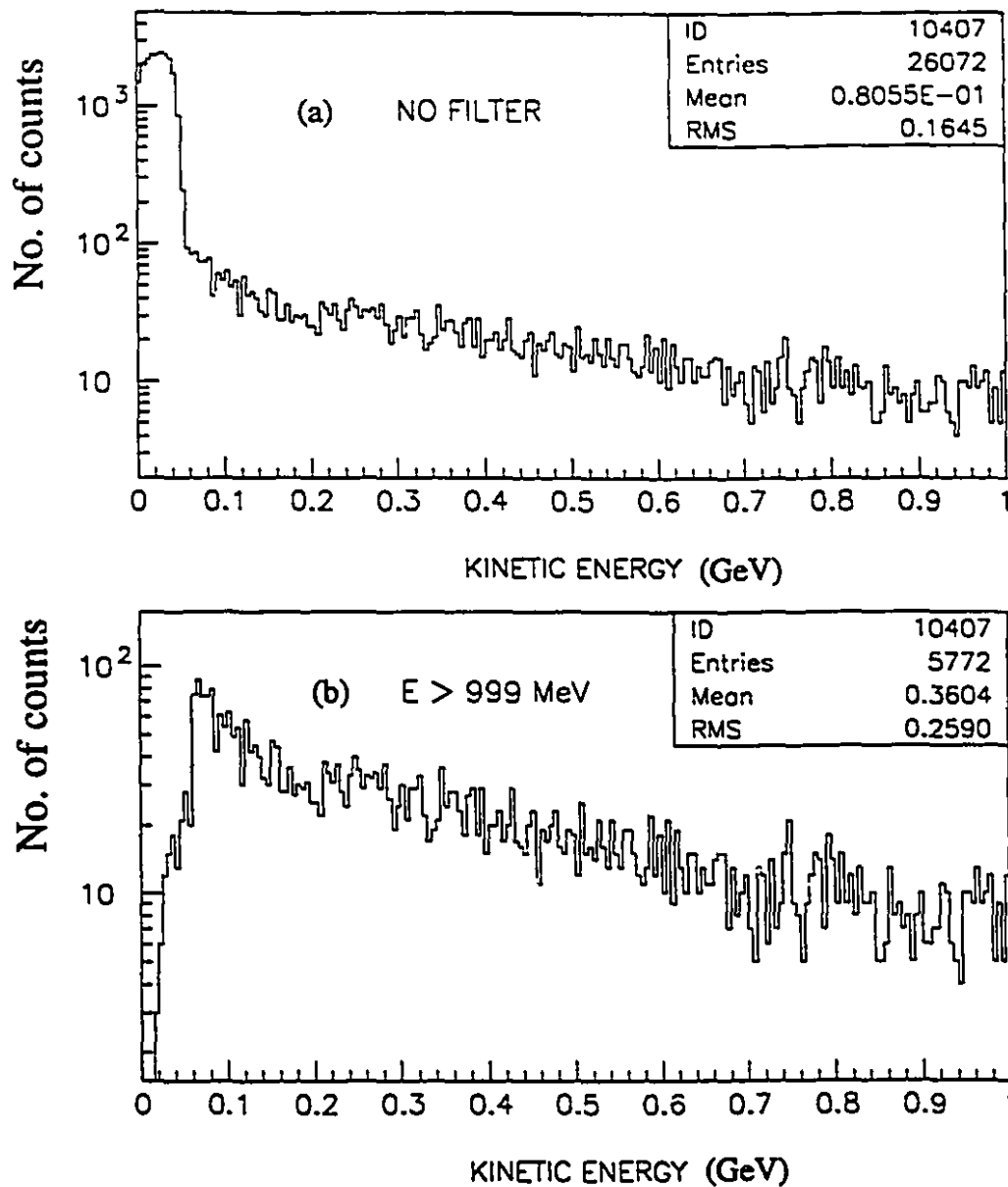


Figure 4.14: Comparison of kinetic energy spectra for all charged particles in the multiplicity detector acceptance for 14.6 GeV/c RQMD p+Pb events: (a) spectrum without energy filter and (b) spectrum with a total energy filter at 999 MeV.

The transverse energy distributions are reconstructed with simulated triggers to approximate the actual multiplicity triggers used in the experiment. As stated in Chapter 2, the pretrigger requires more than two hits registered in the silicon multiplicity detector, and level 1 requires more than 4 hits. Both online triggers are soft cuts in multiplicity due to electronic noise. By taking the ratio of charged multiplicity data  $d\sigma/dN_c$  from multiplicity level 1 trigger to that from the pretrigger, we obtain the trigger efficiency histogram for level 1 trigger relative to pretrigger, as shown in Figure 4.15. The trigger efficiency drawn in the dashed line in the figure can be expressed as

$$Eff_{lev1} = -0.35 + 0.17N_c, \quad (3 < N_c < 8) \quad (4.14)$$

where  $N_c$  represents the charged multiplicity registered in the multiplicity detector. The trigger efficiency for level 1 trigger,  $Eff_{lev1}$ , is zero when the registered multiplicity is less than 3, or becomes 100% when the registered multiplicity larger or equal to 8. To simulate pretrigger we assume that it has the same trigger efficiency slope as level 1 trigger, but that one has 50% efficiency when 2 charged particles hit the multiplicity detector. Then the trigger efficiency of pretrigger is expressed as

$$Eff_{pre} = 0.16 + 0.17N_c, \quad (2 < N_c < 7) \quad (4.15)$$

Therefore tracking histograms are filled for each trigger with a weighting factor determined by the corresponding trigger efficiency. Figure 4.16 shows the calculated effect of the triggers on the  $d\sigma/dE_T$  in the target calorimeter acceptance for RQMD p+Pb events (top figure) and for RQMD p+Al events (bottom figure). Histograms with no bias, pretrigger and multiplicity level 1 trigger are shown by solid curves, dotted curves and dashed curves respectively. As expected the triggers mainly affect low  $E_T$ , but they do not change slope of the distributions and maximum  $E_T$ .

Since  $E_T$  distributions were measured with two calorimeters having different responses, we need to correct the detector efficiency and leakage in order to match the  $dE_T/d\eta$  distributions over the full range of the calorimetry acceptance. To correct  $dE_T/d\eta$  distributions, the calculated energy deposition in the target calorimeter is

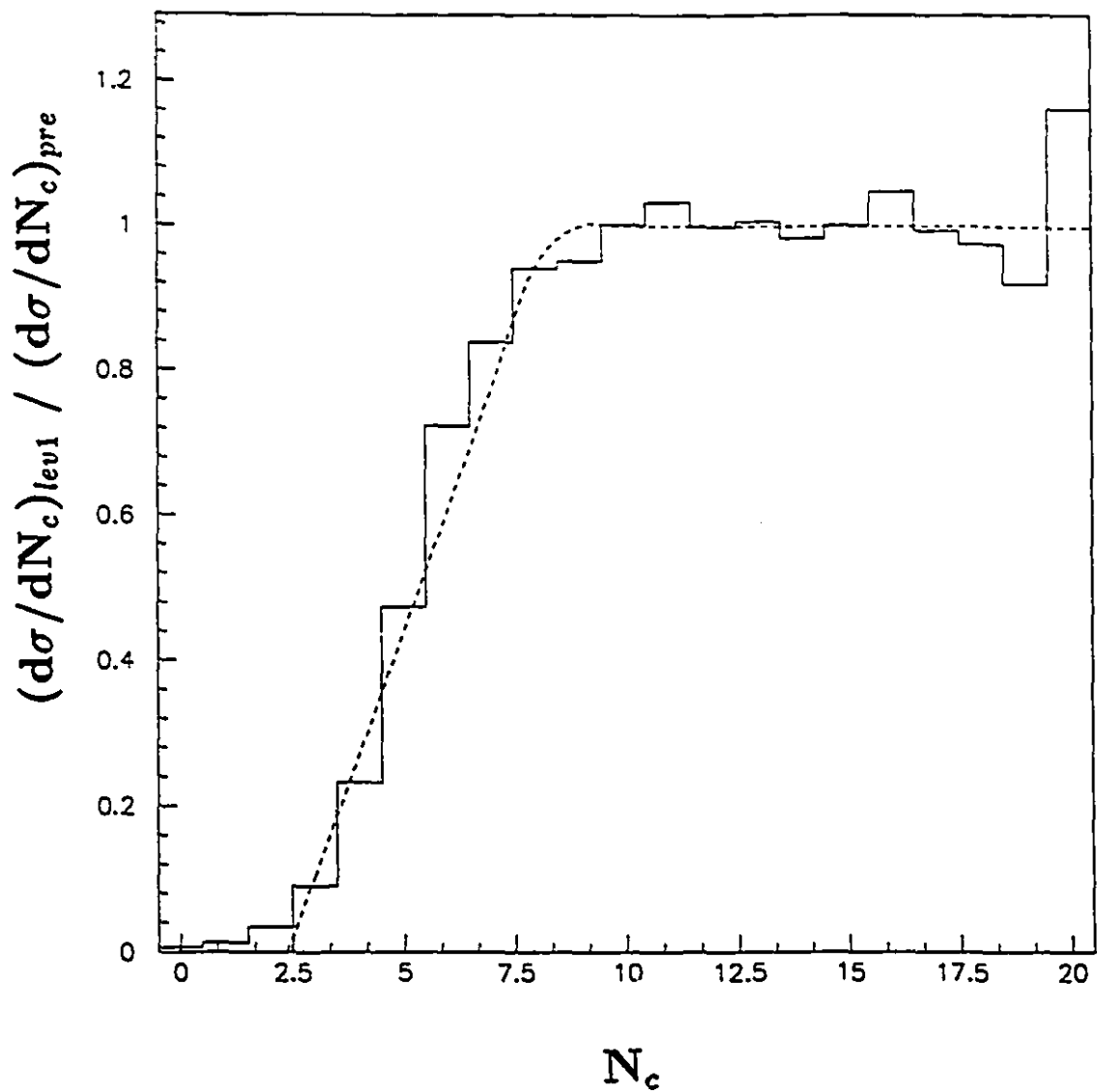


Figure 4.15: Trigger efficiency for multiplicity level 1 trigger relative to pretrigger. The solid histogram represents the ratio of charged multiplicity data  $d\sigma/dN_c$  from multiplicity level 1 trigger to that from pretrigger, and the dashed line represents the assumed trigger efficiency for multiplicity level 1 trigger.

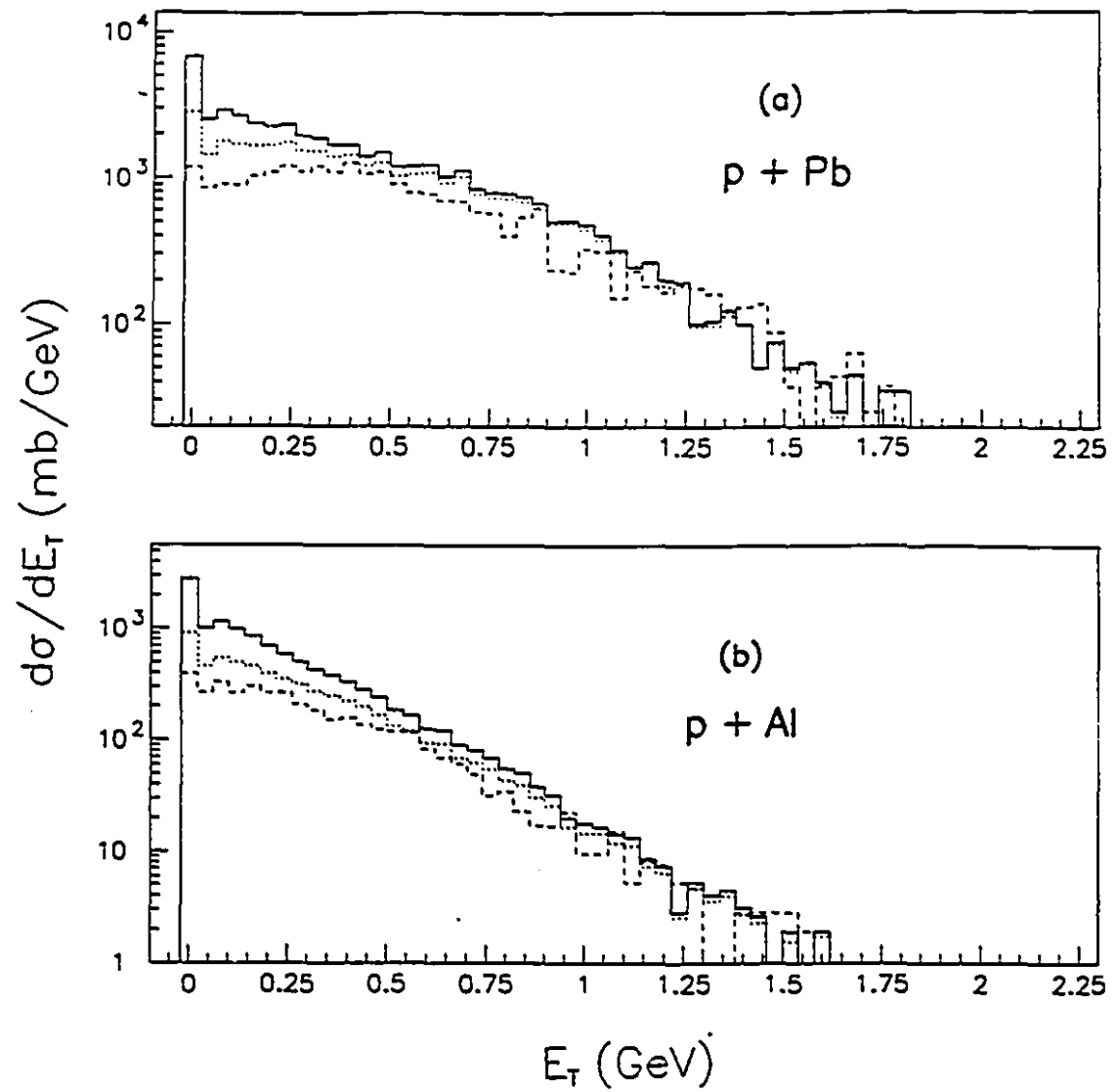


Figure 4.16: Calculated effect of the triggers on the  $d\sigma/dE_T$  in the target calorimeter acceptance for (a) p+Pb and (b) p+Al. The solid lines are for unbiased spectra; the dotted lines are for pretrigger; the dashed lines are for multiplicity level 1 trigger.

compared to the energy incident on the calorimeter. Figure 4.17 shows the correlation between transverse energy before tracking and the transverse energy after tracking using RQMD p+Pb events. The response of the target calorimeter to transverse energy is quite linear, with a average slope of about 0.3. This linearity indicates that the correction factor for the detector efficiency is approximately independent of incident transverse energy.

In order to make corrections on  $dE_T/d\eta$  distributions in the acceptance of the target calorimeter, we evaluate the detector efficiency by calculating the ratio of  $\eta$  distributions of the transverse energy after tracking (dotted curves in Figure 4.18) to the transverse energy incident on the detector before tracking (solid curve in figure 4.18).

Figure 4.19 shows the calculated  $\eta$  dependence of the detector response. The simulated energy deposition amounts to about 1/3 of the energy incident on the target calorimeter. The structures in the distribution of detector efficiency shown in the figure are mainly caused by calorimeter geometry (see figure 2.5).

The fraction of energy deposited by a particle will fluctuate considerably depending on the process of the energy loss. The uncertainties in the detector response will thus depend on the number of events used in the simulation and the multiplicity of particles in a given  $\eta$  bin. The detector efficiency shown in Figure 4.19 is calculated from ten thousand RQMD p+Pb events over five runs, each run containing two thousand events. The error bars in the figure represent estimated uncertainties in the calculated correction factor. These error bars are calculated as the following:

$$\sigma_{Eff} = \frac{1}{\langle Eff \rangle} \left[ \frac{1}{5} \sum_{i=1}^5 (\langle Eff \rangle - Eff_i)^2 \right]^{\frac{1}{2}}, \quad (4.16)$$

where

$$\langle Eff \rangle = \frac{1}{5} \sum_{i=1}^5 Eff_i, \quad (4.17)$$

in which  $Eff_i$  represents the calculated detector efficiency in the  $i$ th run and  $\langle Eff \rangle$  represents the average detector efficiency over five runs. In the forward angle the error is relatively small but it becomes significant at small  $\eta$  covered by the back wall of the

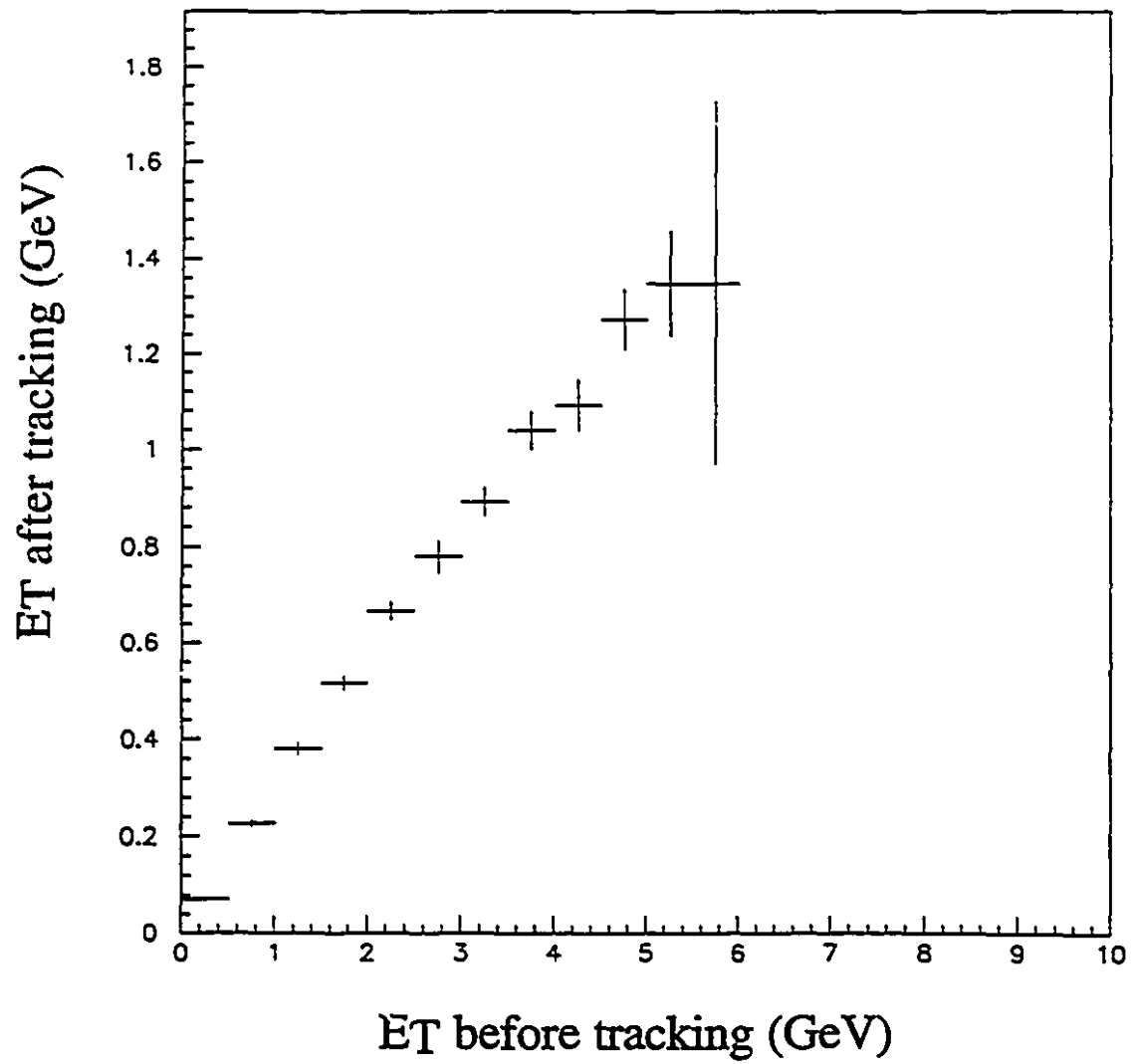


Figure 4.17: Correlation between the transverse energy in the target calorimeter after tracking with the transverse energy before tracking.

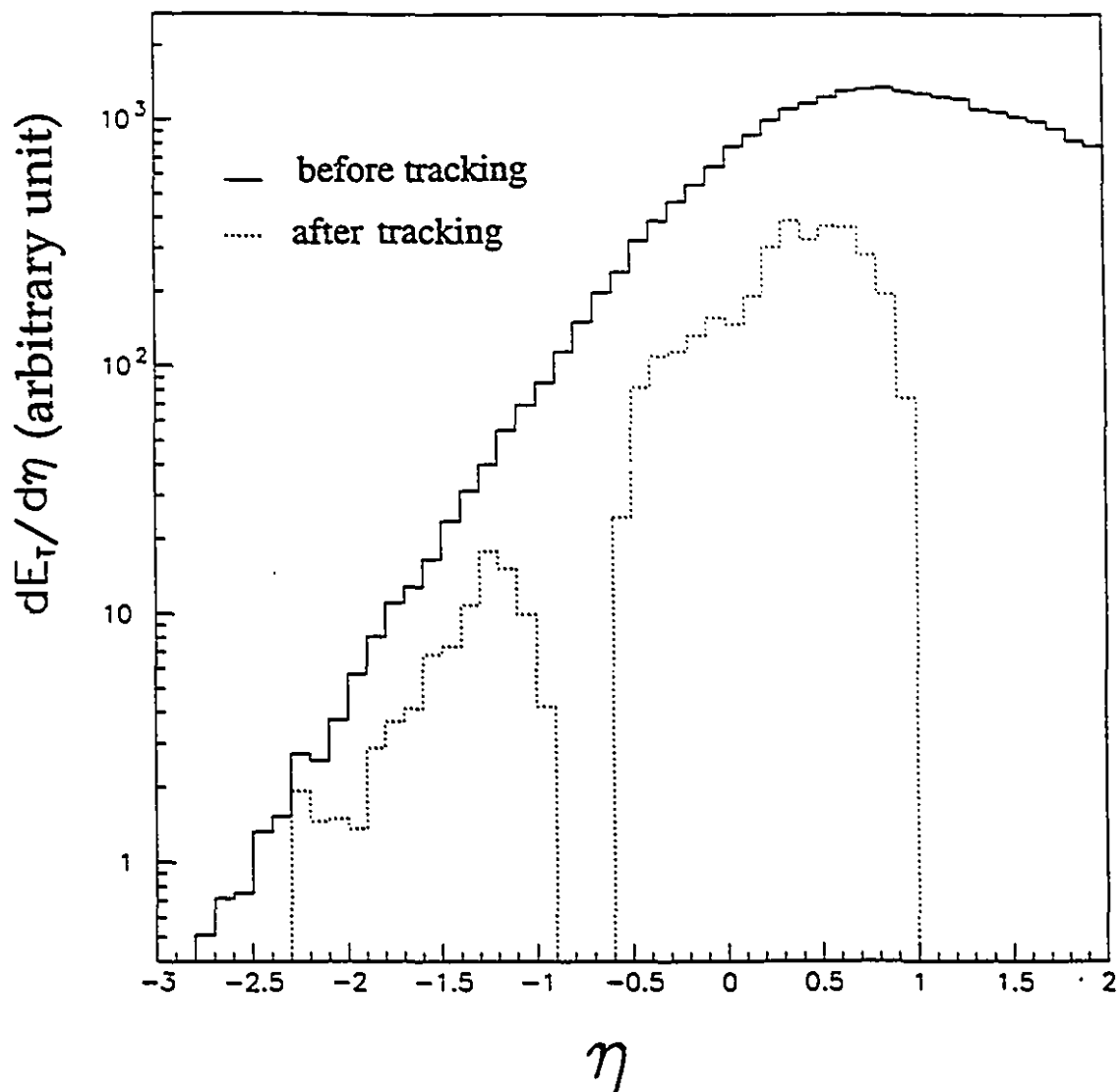


Figure 4.18: Tracking effect on  $dE_T/d\eta$  distribution in the acceptance of the target calorimeter. The solid line is the distribution before tracking and the dotted lines are the distribution after tracking.

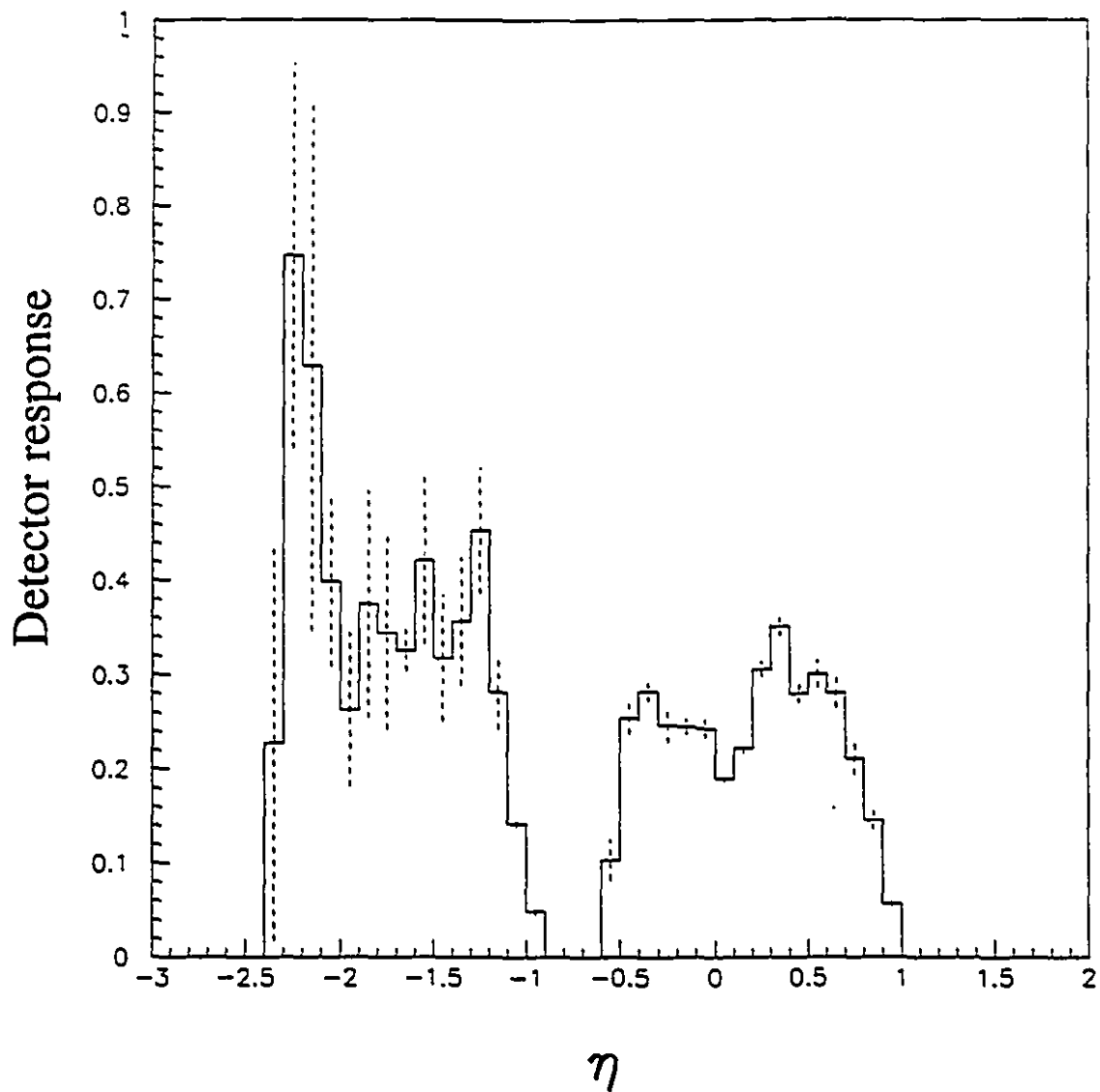


Figure 4.19: Target calorimeter  $E_T$  response calculated using ten thousand RQMD p+Pb events.

calorimeter, due to the small multiplicity of particles in that region (see Figure 4.5). This uncertainty is included in the calculation of  $dE_T/d\eta$ .

The systematic errors from GEANT tracking are studied by tracking the same set of events several times, each time with different random seeds leading to different interaction of the particles in the target calorimeter. Figure 4.20 shows the  $\eta$  distributions of the detector efficiency calculated from five runs of the same two thousand events. The resulting fluctuations in efficiency (dashed lines in Figure 4.20) are comparable or somewhat smaller than the statistical uncertainties discussed in the previous paragraph.

The systematic errors due to the model used are evaluated by tracking events generated from different models. Figure 4.21 shows the  $\eta$  distributions of the detector efficiency calculated from three models, RQMD (solid curves), HIJET (dashed curves) and FRITIOF (dotted curves). Although these three models produce different particle distributions, their tracking results arrive at very similar  $\eta$  dependence of the correction factors. The main difference is in the absolute value of the correction, where differences up to 10% are observed.

The energy leakage as a function of the particle's pseudorapidity is slightly dependent on the target. Figure 4.22 shows the detector efficiency calculated from RQMD p+Al events (solid lines) and from RQMD p+Pb events (dotted lines). The leakage correction factor is slightly higher for lead target mainly in the side walls of the calorimeter. We have not investigated the source of the difference, but it is probably due to the larger absorption in the target peddle scintillation counters for the low energy particles associated with the lead target.

The leakage and geometrical corrections of the  $dE_T/d\eta$  distributions in the acceptance of the target calorimeter are performed by applying the calorimeter response correction factors obtained using the RQMD model. The effect of this correction is shown in Figure 4.23, which presents the experimental  $dE_T/d\eta$  distributions for the p+Pb reaction (top figure) and for the p+Al reaction (bottom figure). The solid histograms show the corrected data whereas the dotted histograms correspond to the measured

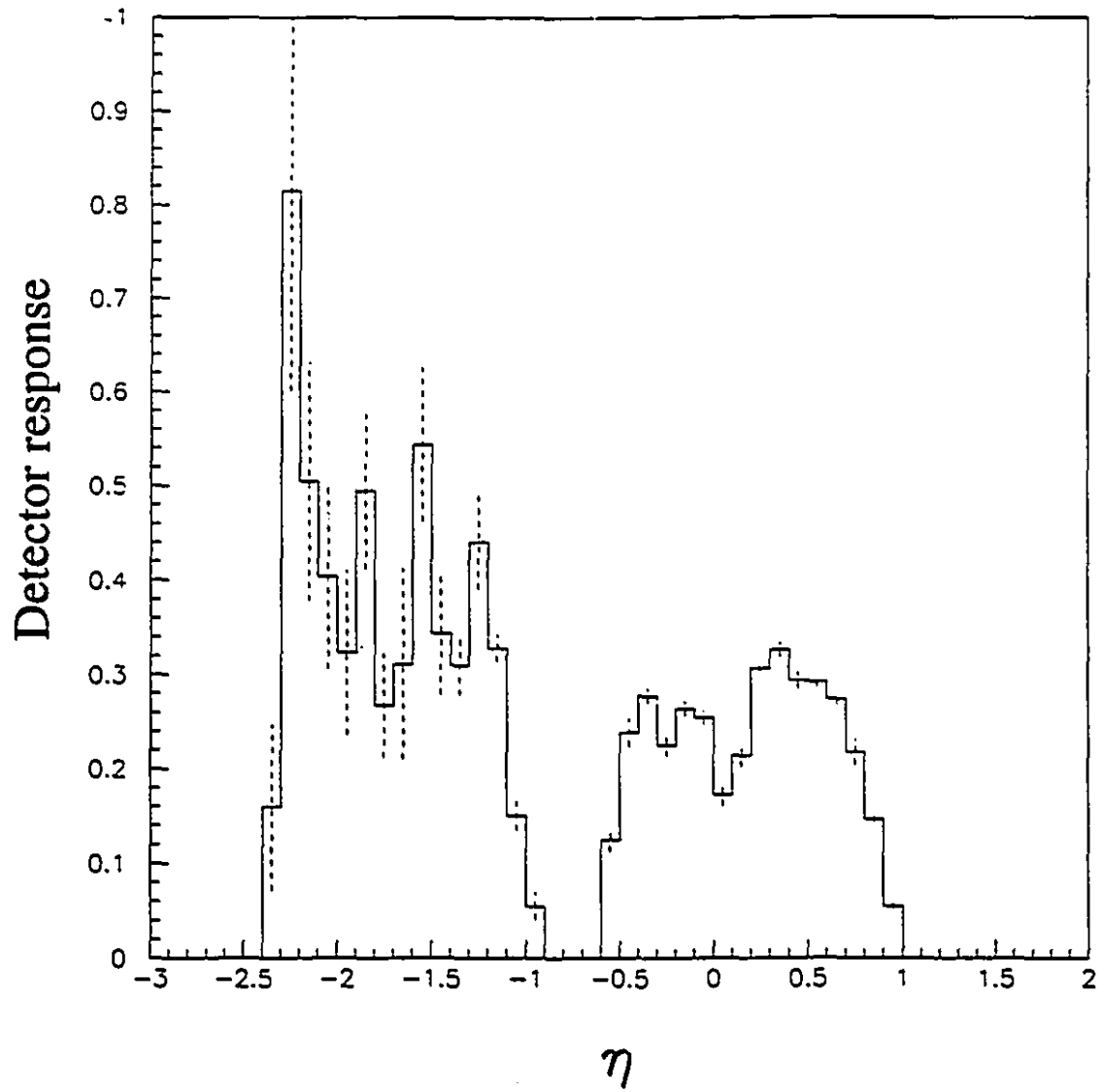


Figure 4.20: Target calorimeter  $E_T$  response calculated from five runs of the same two thousand RQMD p+Pb events.

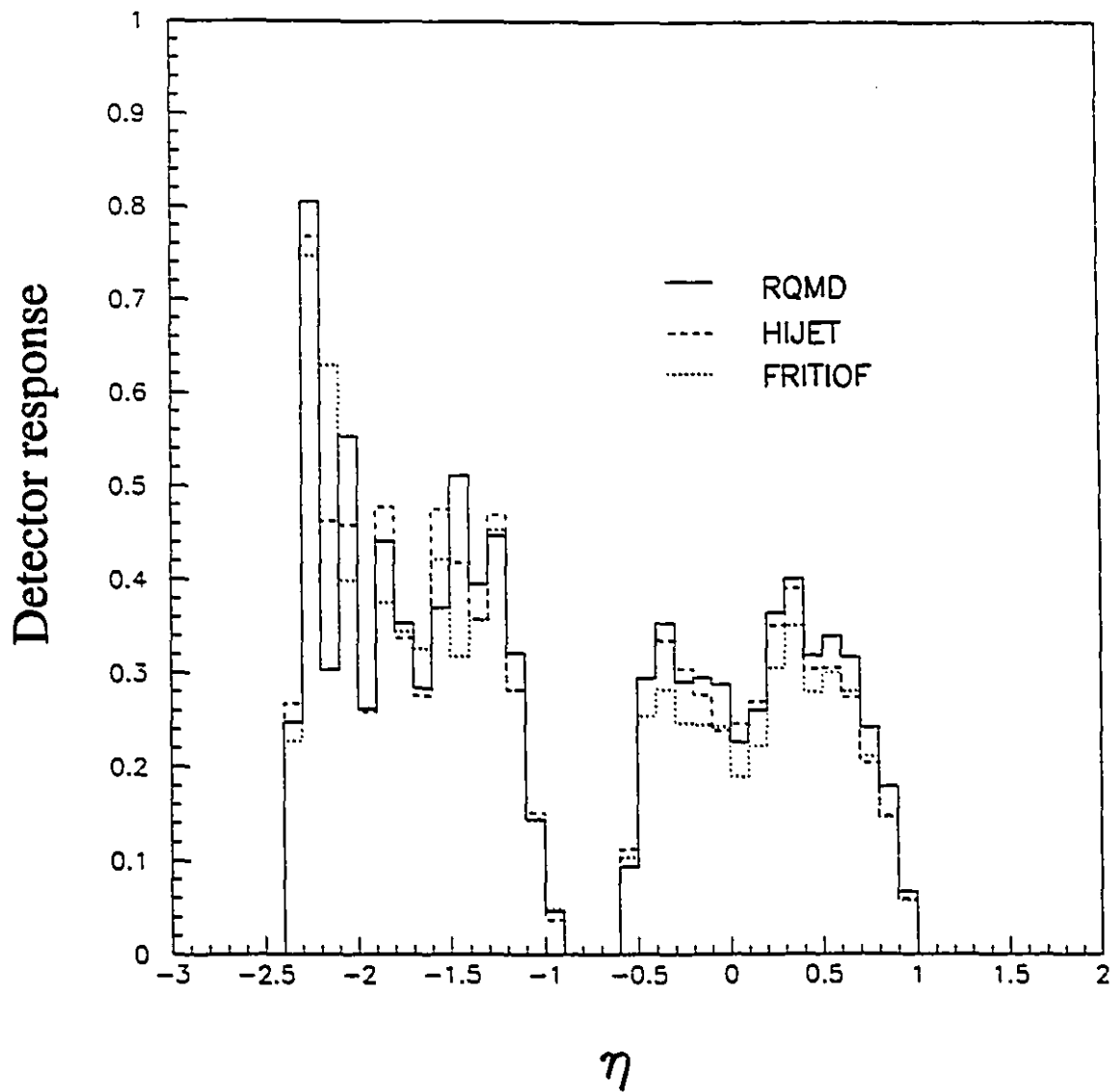


Figure 4.21: Comparison of efficiency of the target calorimeter calculated from three models: RQMD (solid curves), HIJET (dashed curves) and FRITIOF (dotted curves).

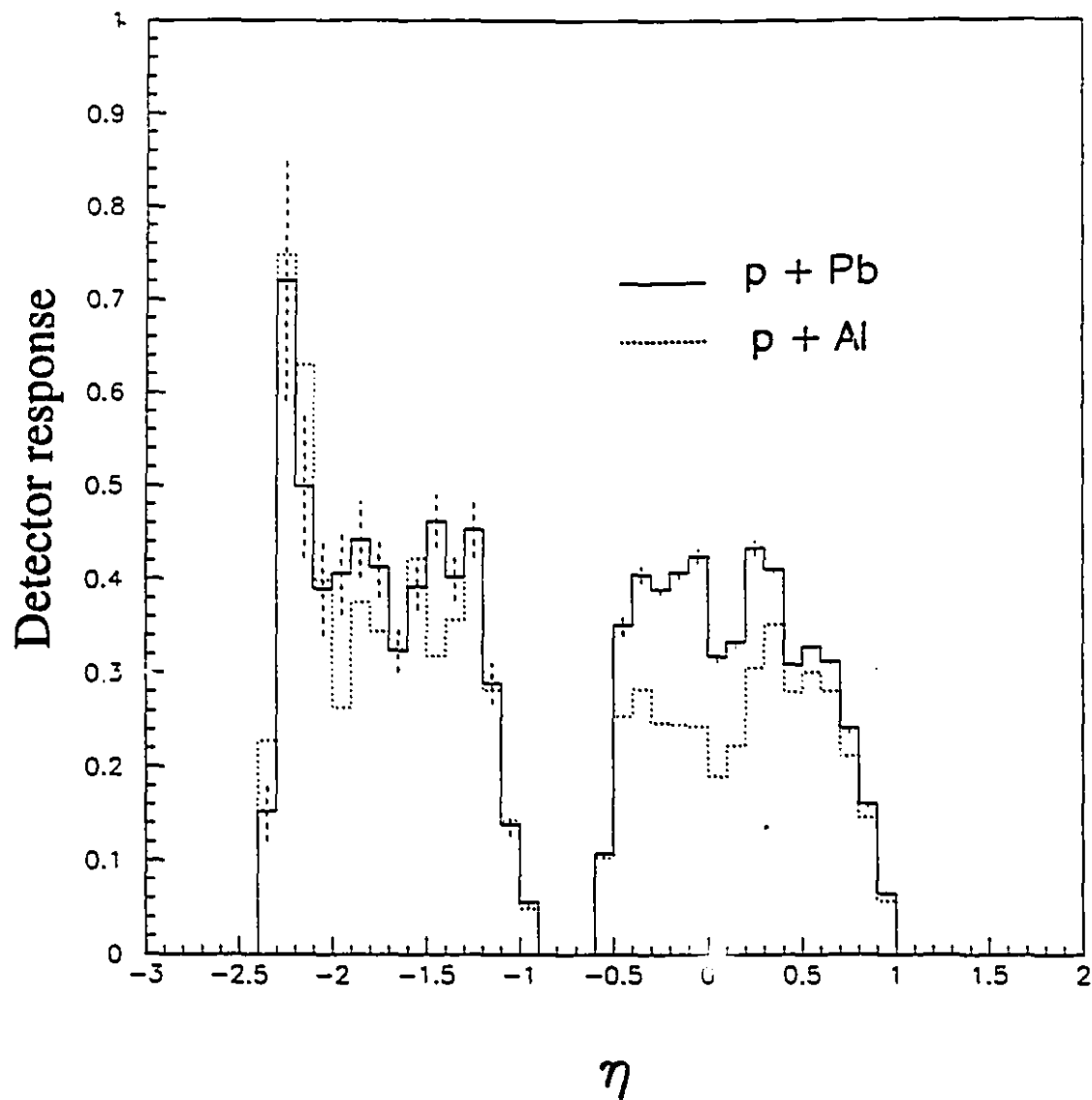


Figure 4.22: Comparison of the target calorimeter efficiency calculated from RQMD p+Pb events (solid curves) and RQMD p+Al events (dotted curves).

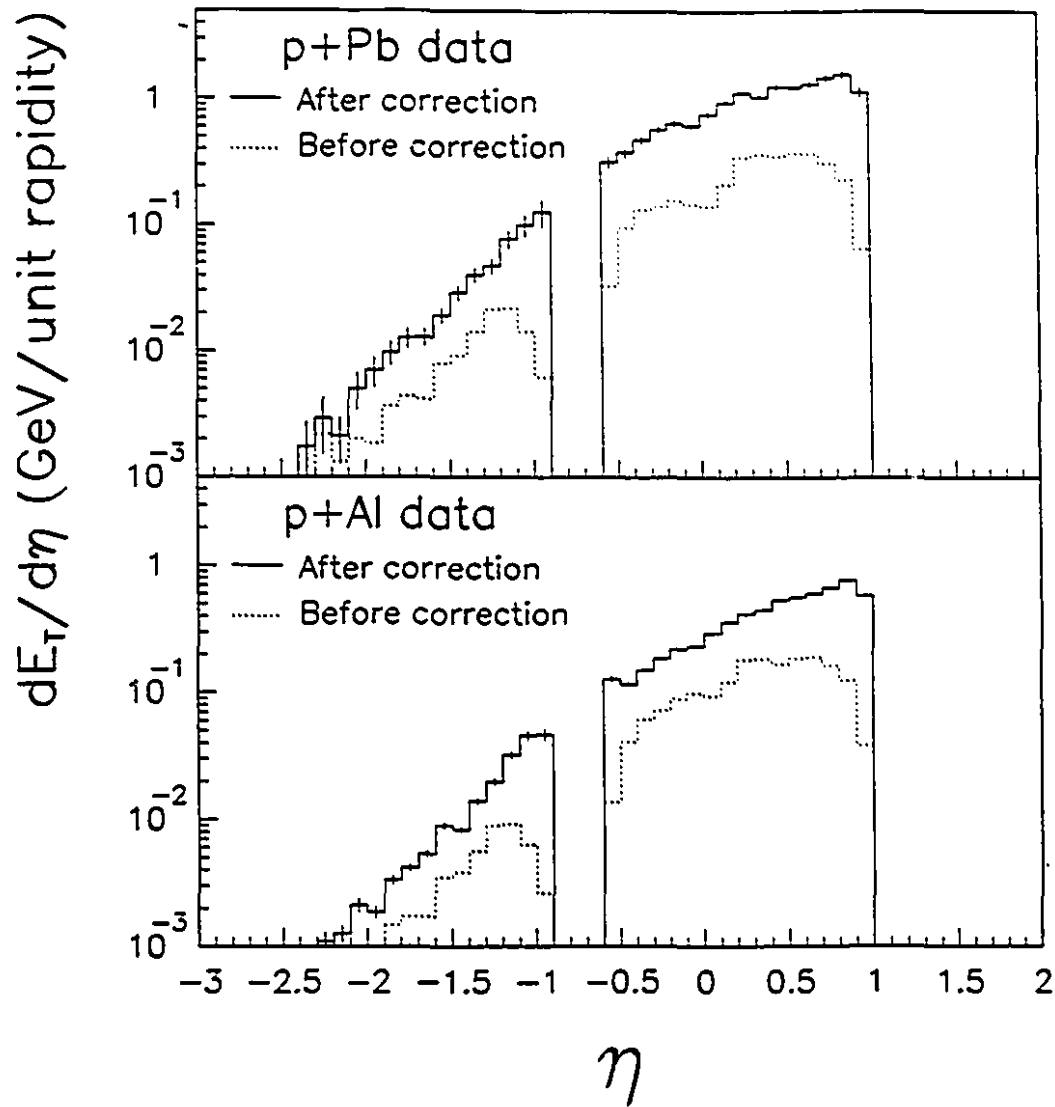


Figure 4.23: Experimental  $dE_t/d\eta$  distributions as measured by the target calorimeter before corrections for leakage (dotted histogram) and after corrections are applied (solid histogram) for p+Pb (upper part) and for p+Al (lower part) .

energy before corrections for the response of the target calorimeter. One observes that many of the structures in the  $\eta$  distribution due to geometrical effect have disappeared, and that the distribution in the side walls and back wall of the calorimeter match nicely. It can also be seen that at  $\eta = 0$  the energy absorption due to the target wheel and the target support has been significantly corrected.

## 4.4 Correction of Data from Participant Calorimeter

### 4.4.1 Raw Data

The energy flow in the forward region is measured with the participant calorimeter (Figure 2.6) in a separate run. As the data were acquired within two days, the gain shift of the participant calorimeter was smaller than 3% over such a short period of time. Therefore, no corrections have been applied to the time dependence of the gain. Pedestals shifts were monitored and adjusted run by run.

The parallel trigger on transverse energy requires the total analog sum of FERA ADC (fast ADC) in the participant calorimeter to be larger than the corresponding threshold value. Good statistics over wide transverse energy range are achieved by using different down scaling factors (listed in Table 3.3). Figure 4.24 shows the correlation between measured  $E_T$  and the total sum of FERA in the participant calorimeter. The dashed lines correspond to level 1 threshold, solid lines to level 2 threshold and dotted lines to level 3 threshold. A nice linear relationship is observed between  $E_T$  and FERA sum, though the correlation is not ideally narrow due to noise and non-uniformity in the calibration. The three thresholds in FERA leads to three  $E_T$  triggers, which are more clearly shown in Figure 4.25. The FERA sum with level 1, level 2 and level 3 triggers are displayed in dashed, solid and dotted curves respectively. Here the FERA sum distributions are not corrected for the downscaling factor, however, the three threshold cuts for  $E_T$  triggers are distinguished by three sharp leading edges.

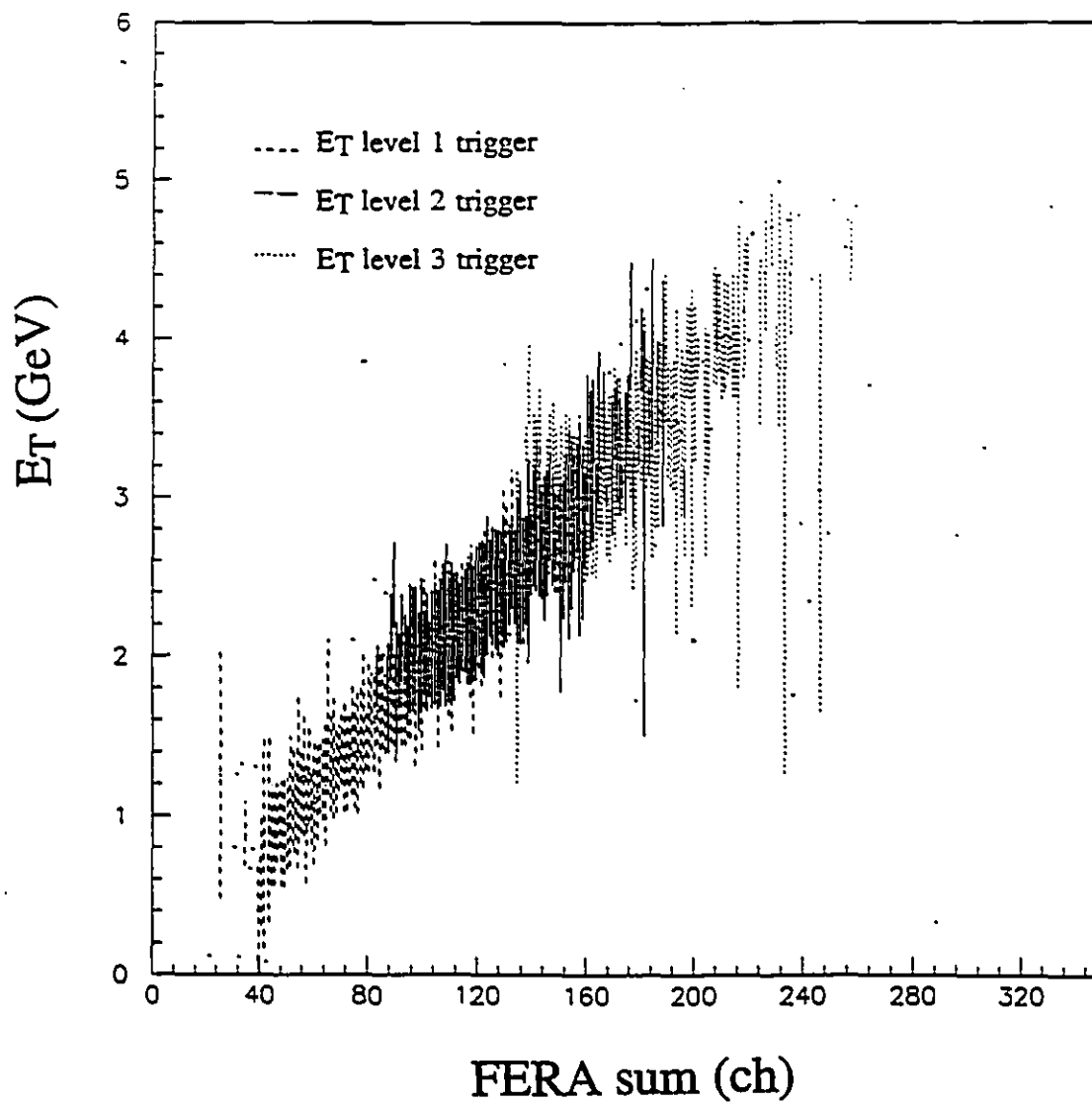


Figure 4.24: Correlation between  $E_T$  and the FERA sum in the participant calorimeter. The dashed lines correspond to  $E_T$  level 1 trigger, solid lines to  $E_T$  level 2 trigger and dotted lines to  $E_T$  level 3 trigger.

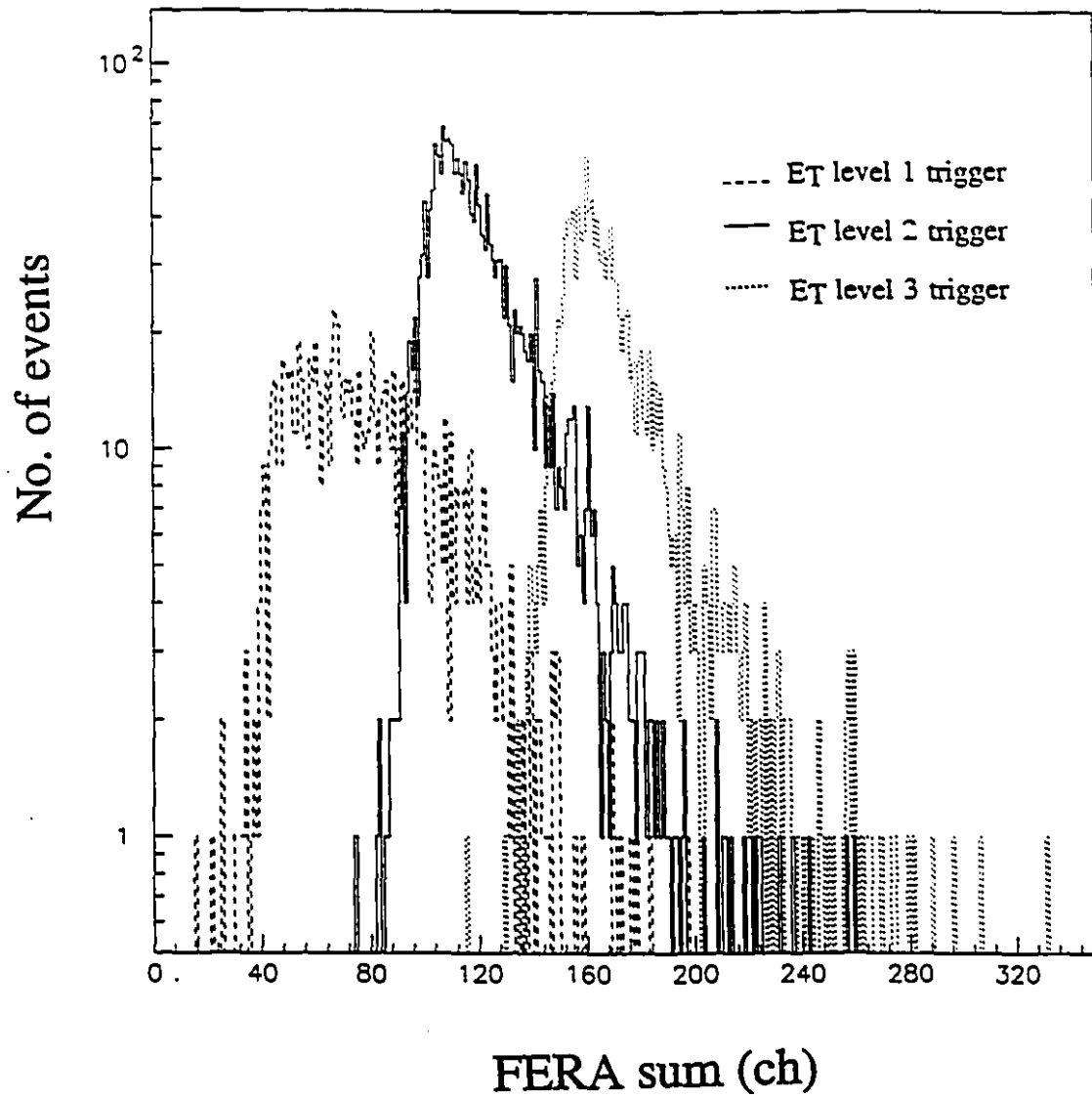


Figure 4.25: FERA sum spectra for three level  $E_T$  triggers in the participant calorimeter. The dashed lines correspond to  $E_T$  level 1 trigger, solid lines to  $E_T$  level 2 trigger and dotted lines to  $E_T$  level 3 trigger.

The transverse energy measured in the participant calorimeter is defined by

$$E_T = \sum_{r=1}^8 \sum_{\phi=1}^{16} \sum_{z=1}^n E(r, \phi, z) \sin\theta(r, \phi, z) \quad (4.18)$$

where  $E_T$  is the transverse energy summed over all the 512 detector cells, the set of variables  $(r, \phi, z)$  refers to the location of a participant calorimeter cell at a certain radial, azimuthal and longitudinal section,  $E(r, \phi, z)$  is the energy deposited in the detector cell  $(r, \phi, z)$ ,  $\theta(r, \phi, z)$  is the polar angle from the beam axis to the center of the face of detector cell  $(r, \phi, z)$ .

Figure 4.26 shows the no-target correction for the transverse energy production with level 1 trigger measured from the participant calorimeter for 14.6 GeV/c protons on the Al and Pb targets. The solid curves refer to measured  $E_T$  production with the target in place. The dashed curves display the empty target contributions, which could be caused by upstream interactions or the interactions of beam on the participant calorimeter. The data with  $E_T$  level 1 trigger are found to contain about 50% empty target events, as shown in Figure 4.26(a) for the Al target and Figure 4.26(b) for the Pb target. In order to clean those unwanted events, we introduce a cut in the offline analysis which removes those events with less than three charged particles detected by the multiplicity detector. This multiplicity cut effectively reduces the empty target contribution to about 15% of the total interactions, as shown in Figure 4.26(c) for the Al target and Figure 4.26(d) for the Pb target. The effect of the new cut on good data is small. The maximum of the  $E_T$  spectra increases by 0.1 GeV after we introduce this multiplicity cut. This cut has been included in our simulation.

Figure 4.27 shows the transverse energy production from 14.6 GeV/c proton on the aluminum target (Figure 4.27(a)) and on the lead target (Figure 4.27(b)). The data have been normalized to differential cross-sections in mb/GeV, and empty target contributions have been subtracted. The solid curves in the figure show the  $E_T$  with the participant calorimeter level 1 trigger, the dotted curves show the  $E_T$  with the participant calorimeter level 2 trigger, and the dashed curves show the  $E_T$  with the participant calorimeter level 3 trigger. Similar shapes of  $E_T$  spectra for both targets

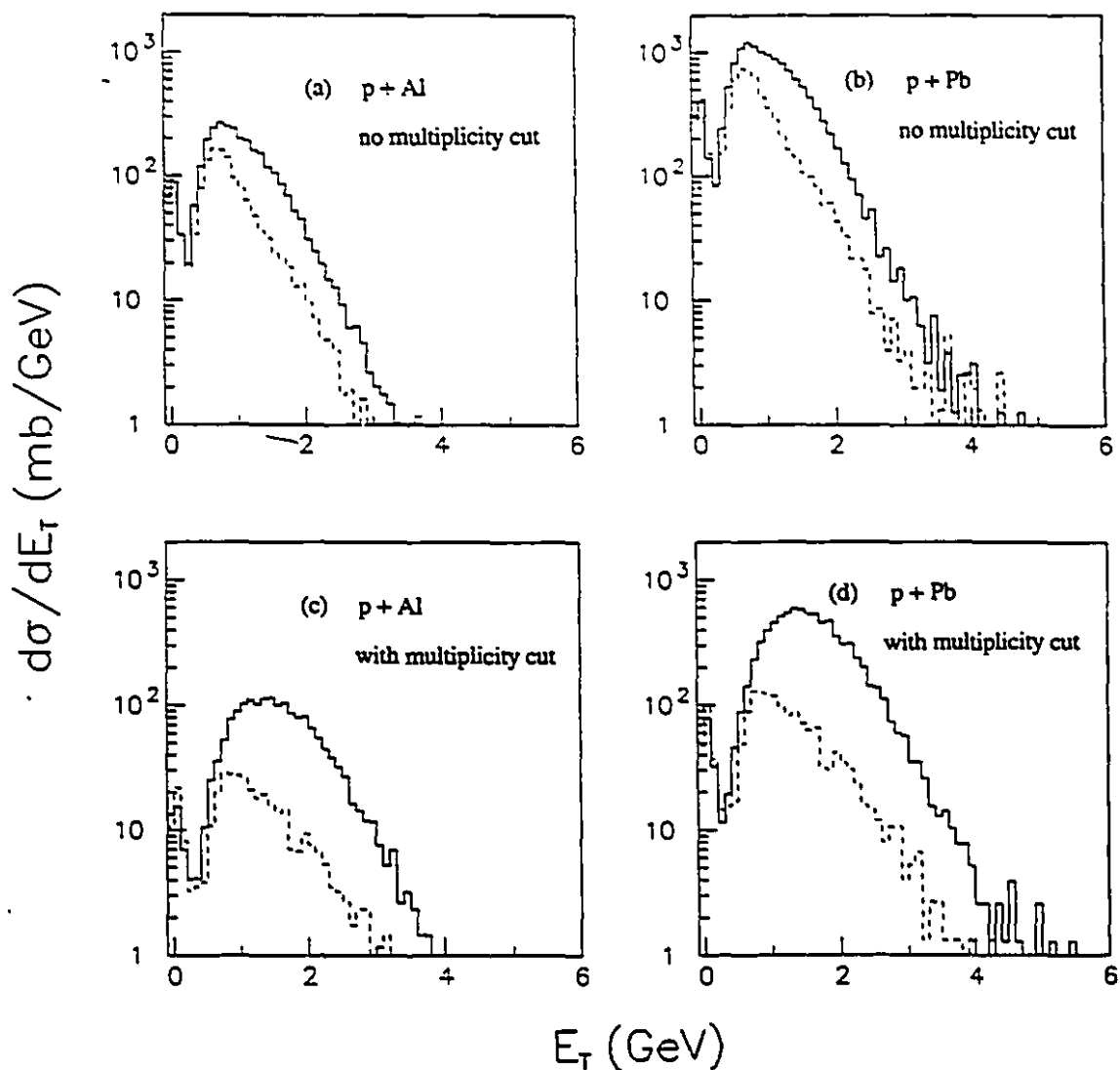


Figure 4.26: Effect of multiplicity cut on the contribution of background interaction to the  $E_T$  spectra measured in the participant calorimeter. The solid histograms are for data with the target in the frame, the dashed histograms are for data with the empty target frame. The spectra shown in (a) for the Al target and (b) for the Pb target are obtained without applying the offline multiplicity cut. The spectra shown in (c) for the Al target and (d) for the Pb target are obtained after applying the offline multiplicity cut. The offline multiplicity cut reduces background contribution significantly.

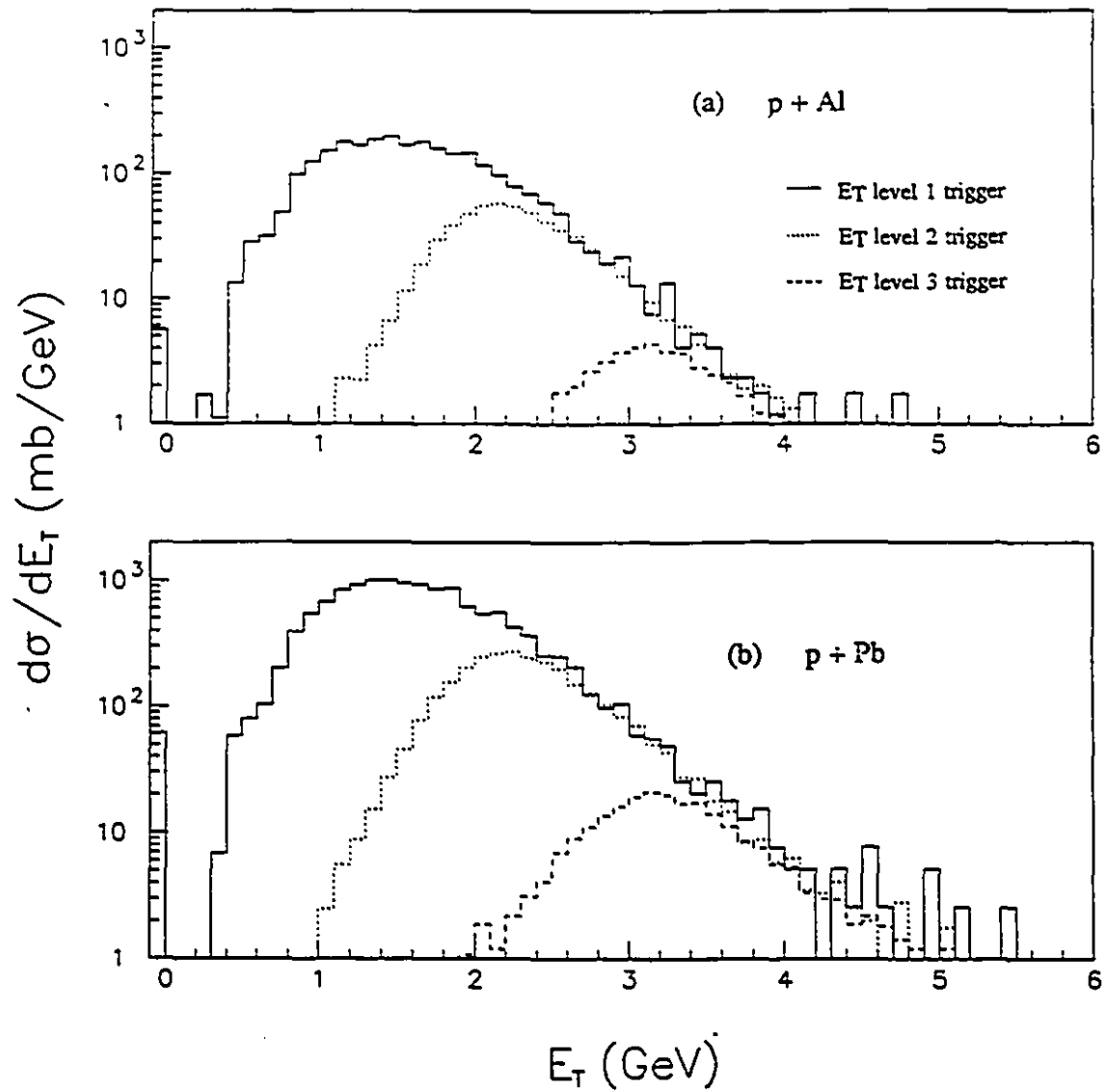


Figure 4.27: Transverse energy spectra for (a) Al target and (b) Pb target as measured by the participant calorimeter. The solid lines correspond to  $E_T$  level 1 trigger, dotted lines to  $E_T$  level 2 trigger and dashed lines to  $E_T$  level 3 trigger.

are observed within the participant calorimeter acceptance. Mainly due to the different offline energy calibration constants for each detector cell, all the three  $E_T$  triggers result in relatively broad leading edges of the transverse energy spectra. This effect will be included in some of our simulations.

The spectra shown in Figure 4.27 have been normalized to the results from the multiplicity trigger. The absolute differential cross-sections (in mb/GeV) are obtained by using equation (4.12) with normalized target thicknesses. The original result of differential cross-sections of transverse energy measured with level 1 trigger for both targets are found to be systematically lower than the corresponding distributions measured with multiplicity trigger by approximately a factor of 2. Reasons for the discrepancy between the two sets of experimental data are not clear. However, the data obtained with the multiplicity trigger are consistent with the theoretical predictions of the total cross-section and the cross-section resulting from beam trigger data. We thus renormalized our  $E_T$  trigger data to the data of multiplicity trigger. Figure 4.28 shows the  $d\sigma/dE_T$  measured in the target calorimeter with the multiplicity pretrigger (dotted curves) and measured with  $E_T$  level 1 trigger after renormalization (solid curves) for the aluminum target (Figure 4.28(a)) and for the lead target (Figure 4.28(b)). The only difference between the data from the  $E_T$  trigger experiment and the data from the multiplicity trigger experiment is the trigger and this should not affect the spectra in the high  $E_T$  region. This is observed in the figure which shows good consistency between the multiplicity pretrigger data and the  $E_T$  trigger data.

In the participant calorimeter there are many dead cells whose  $E_T$  contributions need to be considered. Figure 4.29(a) shows the measured energy deposition in 512 cells of the participant calorimeter for each p+Pb event; Figure 4.29(b) shows the calculated energy deposition per p+Pb collision in 512 detector cells using RQMD events. The detector cells corresponding to channels 1 through 512 in the figure are numbered starting from  $\phi = 1$  to 16 at innermost ring ( $r = 1$ ) of the first section ( $z = 1$ ) and going up to ring 8 ( $r = 8$ ) of the same section, and then going to the next section, and so on. By comparing the two plots we can identify dead detector cells. Channels 161 to 192

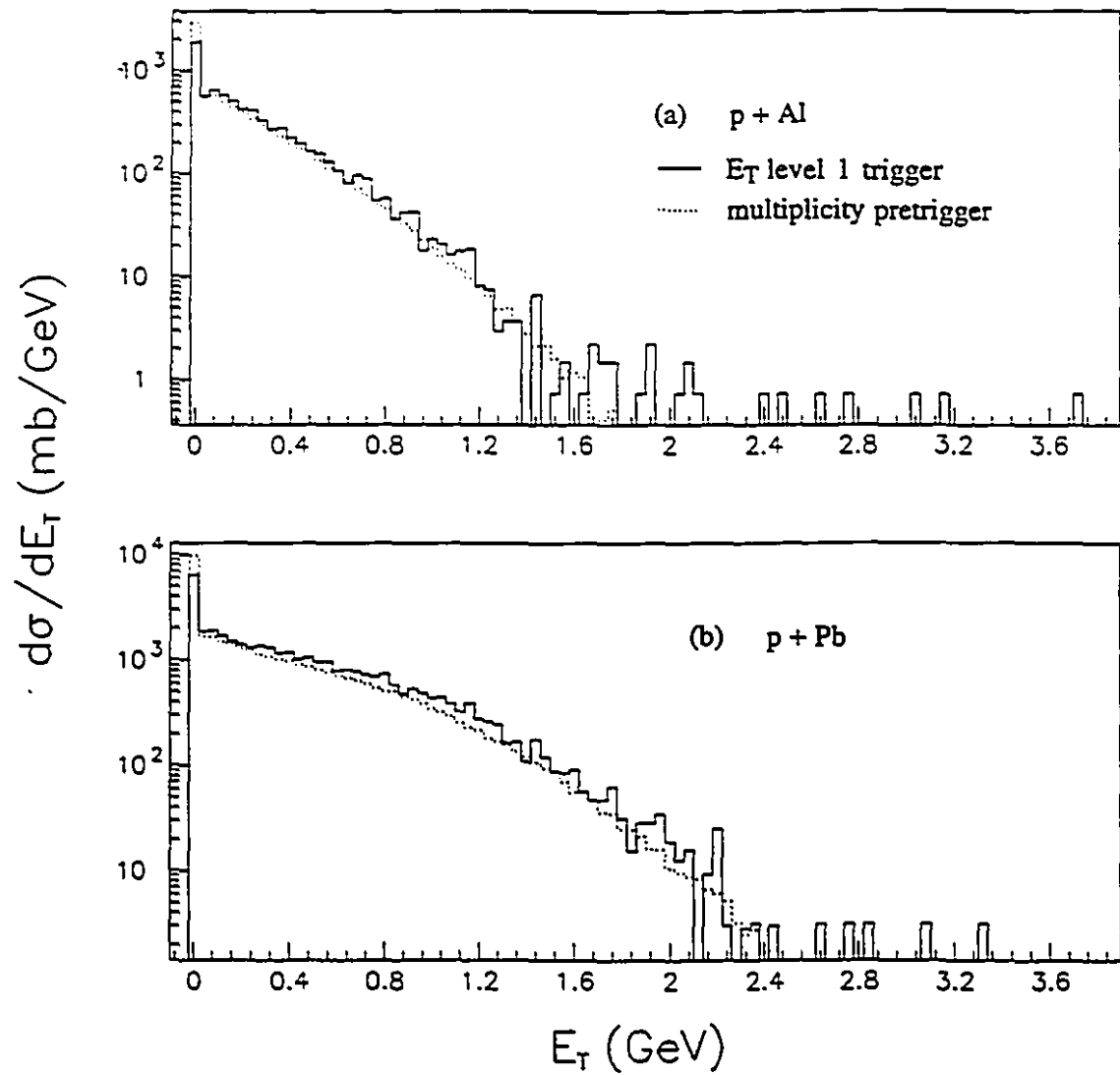
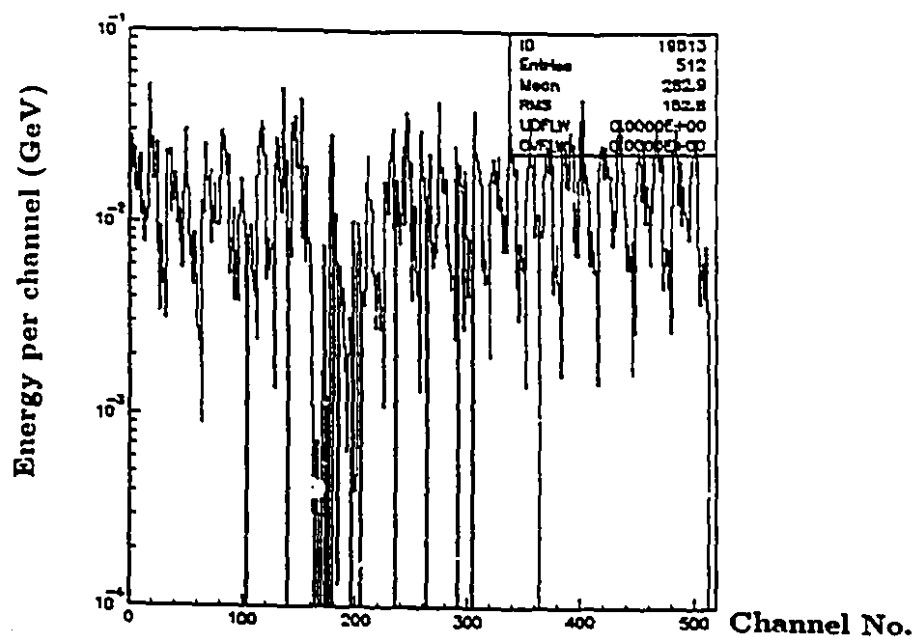
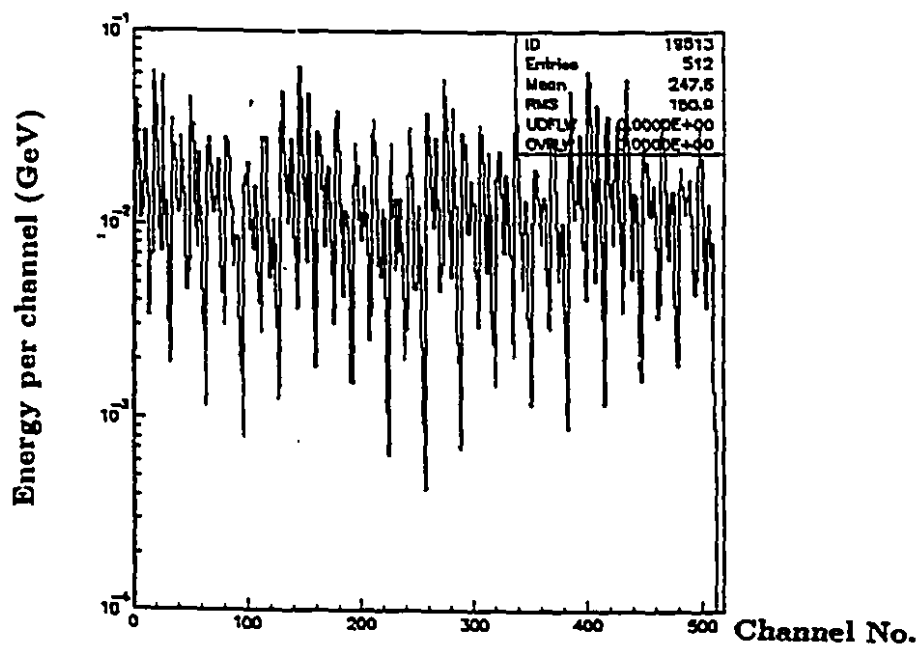


Figure 4.28: Comparison of trigger effect on the  $d\sigma/dE_T$  for p+Al (a) and p+Pb (b) measured in the target calorimeter. The solid lines correspond to  $E_T$  level 1 trigger and the dotted lines correspond to the multiplicity pretrigger.



(a)



(b)

Figure 4.29: Energy deposition in 512 cells of the participant calorimeter for p+Pb from data (a) and simulation (b). The calorimeter cells are numbered by looping on  $\phi = 1$  to 16,  $r = 1$  to 8 and  $z = 1$  to 4 corresponding to channels 1 through 512.

and channels 193 to 224 correspond to two azimuthal slices in a calorimeter quadrant. Most of the dead detector cells are located in those two slices. As  $E_T$  production is on average azimuthally uniform, this feature allows us to correct for the effect due to the two dead slices by forcing azimuthal symmetry. The two slices are treated as totally dead, and the total cross-section of  $E_T$  is thus corrected by a factor of 12.5% (2 slices out of 16 of the calorimeter). The dead cells in other slices of the calorimeter count for about 2% of the total cells. Their effect on the total cross-section of  $E_T$  is small and is therefore neglected. For the  $dE_T/d\eta$  distribution the correction of dead detector cells are included in a response matrix which will be discussed in the next section.

Figure 4.30 shows the uncorrected pseudorapidity distribution of transverse energy for p+Al using  $E_T$  level 1 trigger. The solid curve represents the data measured with the participant calorimeter and the dashed curve represents the data measured with the target calorimeter. There is a small  $\eta$  range from 0.8 to 1.0 in which the two calorimeters' coverage overlaps. Empty target contributions to the pseudorapidity distribution of transverse energy have been subtracted, while energy leakage for both the calorimeters are not corrected for in this figure. The non-projective geometry of the participant calorimeter towers makes part of shower energies leak to the neighboring detector towers which are binned with different  $\eta$ , causing many structures in the  $dE_T/d\eta$  distribution. To avoid these structures in plotting pseudorapidity distribution of  $E_T$ , in the following data analysis, the participant calorimeter is segmented projectively towards the target into eight rings with approximately equal polar angle interval, as shown in Figure 4.31. Each ring is labeled a number from 1 for the inner ring to 8 for the outer ring. The polar angle and pseudorapidity range for each ring is listed in Table 4.3.

A particle incidents on rings 4 or 5 will encounter large calorimetric depth. A particle that enters other rings, especially rings 8 or 1, is likely to leak a substantial fraction of its energy out of the calorimeter due to the small depth of the calorimetric ring. Figure 4.32 shows uncorrected  $dE_T/d\eta$  distribution for p+Al in the acceptance of the target calorimeter (solid curves) and the participant calorimeter with projective binning (dashed curves). The  $dE_T/d\eta$  spectra have not been corrected for energy leakage.

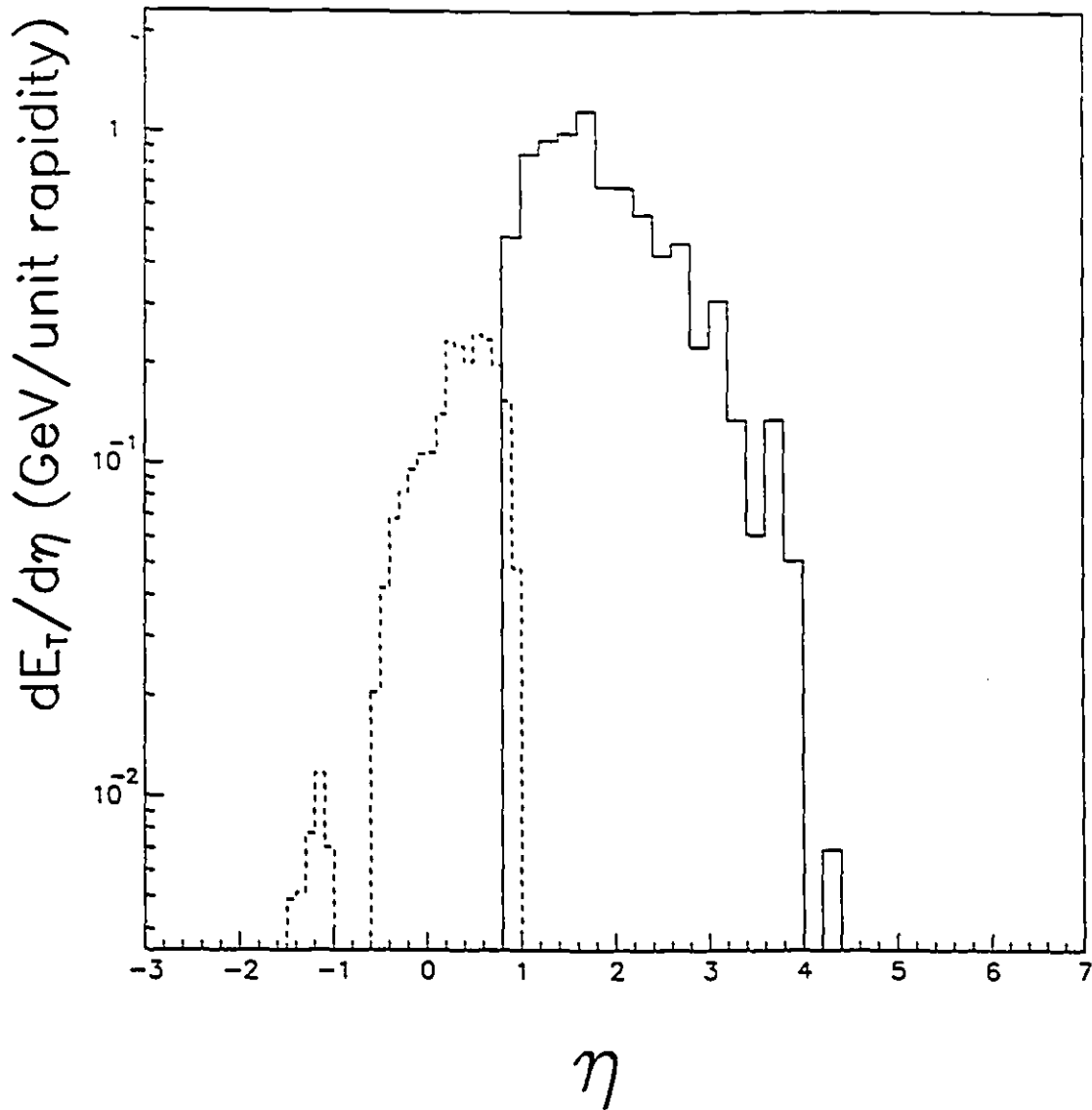


Figure 4.30: The uncorrected pseudorapidity distribution of  $E_T$  for p+Al using  $E_T$  level 1 trigger. The solid curve corresponds to the data measured by the participant calorimeter and the dashed curve corresponds the data measured by the target calorimeter. The distributions measured by the two calorimeters do not match due to different detector response.

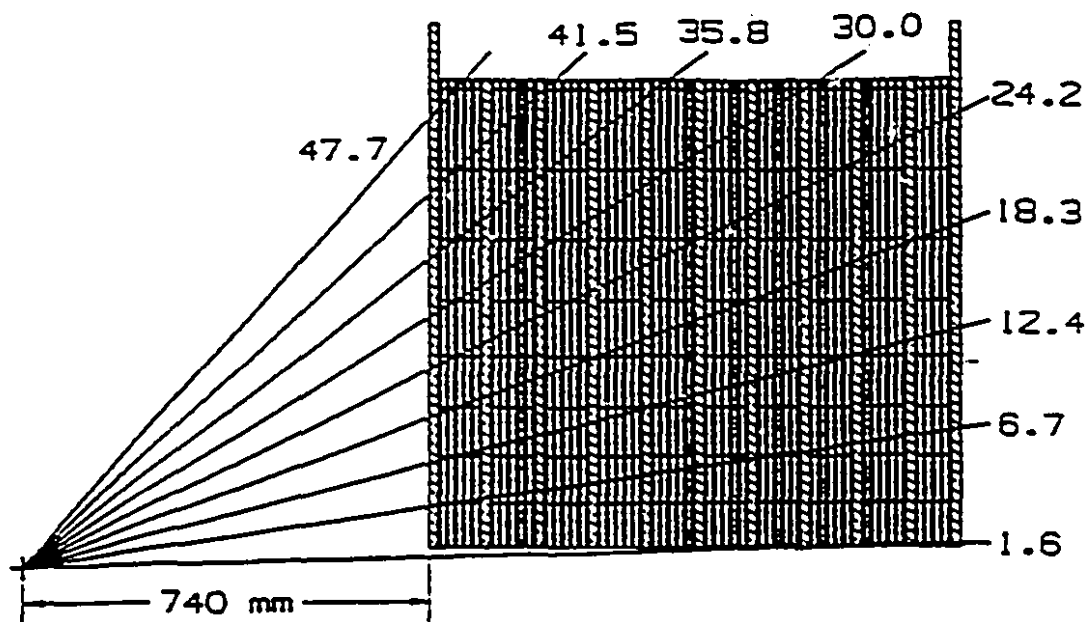


Figure 4.31: Projective segmentation of the participant calorimeter into eight rings used in the leakage correction correction.

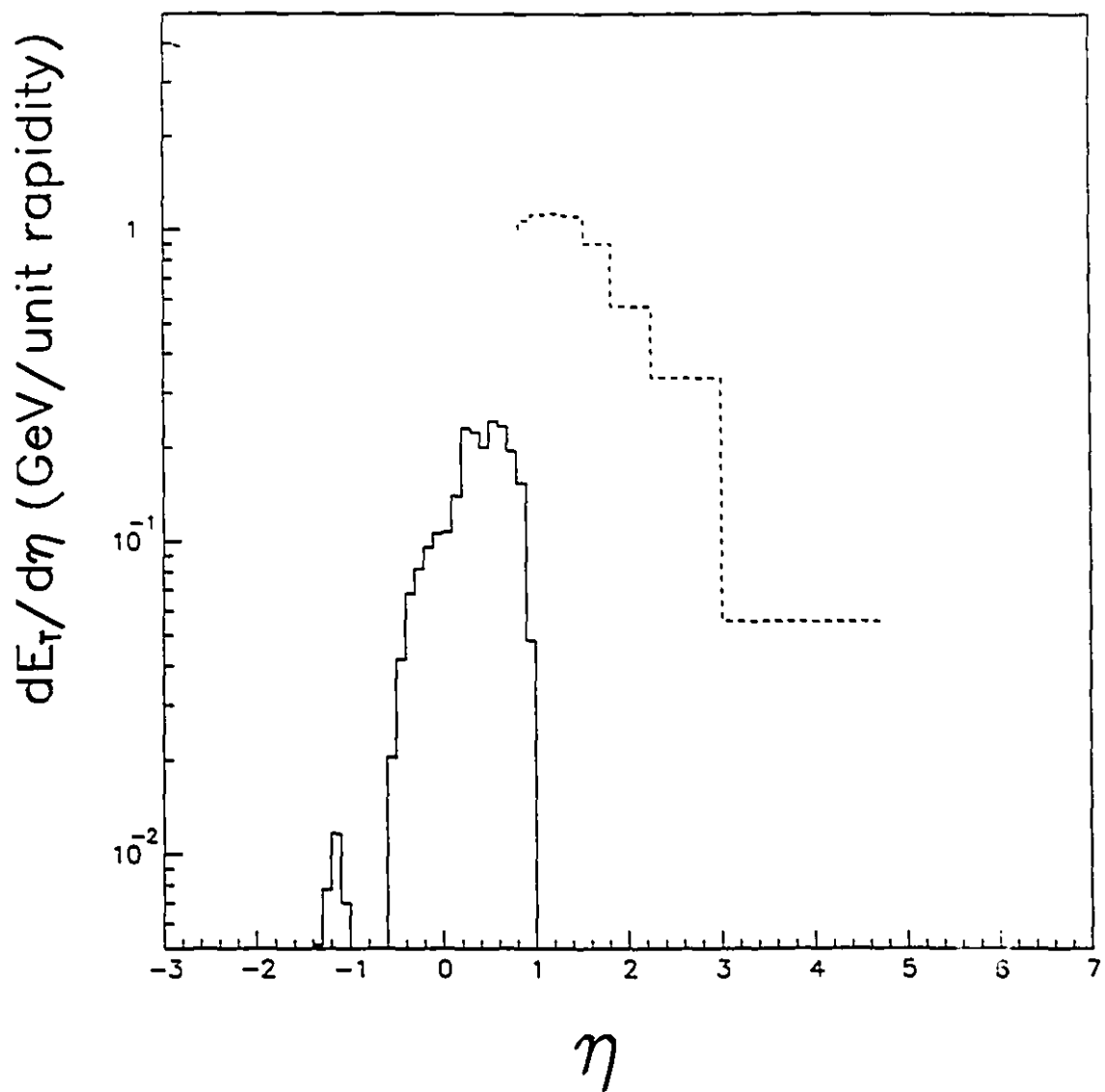


Figure 4.32: Uncorrected  $dE_T/d\eta$  distribution for p+Al in the acceptance of the target calorimeter (solid curves) and the participant calorimeter with projective binning (dashed curves).

Table 4.3: Pseudorapidity binning for the participant calorimeter

Ring #	Polar angle range ( $^{\circ}$ )	Pseudorapidity range
1	1.00 - 5.65	4.74 - 3.01
2	5.65 - 11.95	3.01 - 2.26
3	11.95 - 18.22	2.26 - 1.83
4	18.22 - 24.34	1.83 - 1.53
5	24.34 - 30.29	1.53 - 1.31
6	30.29 - 36.07	1.31 - 1.12
7	36.07 - 41.67	1.12 - 0.97
8	41.67 - 47.13	0.97 - 0.83

As the target calorimeter is much thinner in depth than the participant calorimeter, more leakage correction is expected for the target calorimeter than for the participant calorimeter.

To compensate for energy leakage and shower extensions, simulations have been performed using PROPHET/GEANT package with generated events to determine correction factors for the pseudorapidity dependence of transverse energy. This work will be discussed in the next section.

#### 4.4.2 Monte Carlo Corrections of Participant Calorimeter Response

##### Shower Simulation

In order to correct for detector leakage, a fast energy deposition program, PROPHET, is applied to study the response of the participant calorimeter to incident particles. Instead of tracking every secondary particle as GEANT does, this Monte Carlo simulation program is based on a shower parametrization, which makes it very fast computationally.

High energy particles entering a calorimeter are likely to create electromagnetic showers and hadronic showers. The parameterization of the lateral and longitudinal spread of a shower in a calorimeter have been studied by R. Bock et al. [BOS1].

Fraction of energy deposited at different depth in a calorimeter is characterized by longitudinal development of showers. For an electromagnetic shower, the longitudinal energy deposition is described as

$$\frac{dE}{dx} = kt^a e^{-bt}, \quad (4.19)$$

where  $t$  is the shower depth expressed in radiations length,  $a$  and  $b$  are parameters characterizing the shower profile, and  $k$  is a normalization constant.

The longitudinal energy deposition in a hadronic shower is parameterized by

$$\frac{dE}{dx} = k[wt^a e^{-bt} + (1-w)u^c e^{-du}], \quad (4.20)$$

where  $t$  is the shower depth in radiation lengths measured from shower origin,  $u$  is the same depth characterized in interaction lengths,  $k$  is a normalization constant,  $w$  is the relative fraction of the electromagnetic component in a hadronic shower, and  $a$ ,  $b$ ,  $c$  and  $d$  are shower shape parameters. All parameters used in PROPHET for this work are tuned to best fit the participant calorimeter response to various particles. Detailed discussions can be found in reference [SI91].

The lateral distribution of shower energy is assumed to be gaussian, with a width of one radiation length for a electromagnetic shower or an half absorption length for a hadronic shower.

Since the PROPHET simulation code is based on electron calibration, the energy of a hadronic shower needs to be corrected by the  $e/\pi$  ratio which is the ratio of the responses of a calorimeter to electromagnetic showers and to hadronic showers, and the energy deposited through minimum ionization needs to be corrected by the  $e/mip$  ratio, the ratio of  $dE/dx$  energy of an electron to  $dE/dx$  energy of a minimum ionizing hadron. For the participant calorimeter used for E814, the  $e/\pi$  ratio is 1.06, and the  $e/mip$  ratio is 1/0.79 [ZH93].

Prophet is embedded in the framework of GEANT package which defines detector geometry and performs particle tracking after reactions. Particles produced in an

event are first identified and tracked through GEANT one by one until they stop, decay or interact with the materials of the participant calorimeter. PROPHET starts to process shower development and energy deposition once GEANT finds a hadronic or electromagnetic interaction. Showers are generated within PROPHET. The shower energies are smeared by calorimeter resolutions which are handled using gaussian functions and are preset with appropriate RMS values as stated in Chapter 3. GEANT keeps tracking showers along the particle's incident direction and PROPHET follows and processes showers until all the energy of the particle is exhausted or the particle exits the calorimeter.

### Unfolding Approach

The incident energy distribution and the energy deposited in the participant calorimeter are quite different due to shower spread causing energy leakage either to the neighbor detector cells or through the calorimeter because of its finite thickness.

To correct the measured raw data we employ a response-matrix approach which is described in reference [ZH93]. First we use PROPHET to determine the energy deposition in the calorimeter with simulated events. From the calculated energy distribution the calorimeter response matrix is constructed. This response matrix is then used to unfold the experimental data to obtain the corrected  $dE_T/d\eta$  distributions.

In the present analysis, the incoming energy flow is binned into 8 intervals in pseudorapidity according to the radial granularity of the calorimeter, as shown in Table 4.3. By using RQMD events simulating p+Pb collisions, a matrix  $M$  as a function of pseudorapidity bins and longitudinal sections of the calorimeter is built to represent the response of the detector to multiparticle events.

Events generated by RQMD are filtered in two steps. The first step rejects those nucleons below a kinetic energy threshold, 60 MeV, which is used to cut off those particles of very low kinetic energy originating from the target nuclear Fermi motion.

The second step makes eight pseudorapidity cuts in the participant calorimeter in order to generate the elements of the response matrix. Each pseudorapidity bin is segmented into 4 sections according to the longitudinal granularity of the calorimeter. In this way, the participant calorimeter is grouped into 32 rings.

Mathematically, the detector response to the incoming transverse energy can be expressed in term of a vector equation:

$$\bar{D} = M\bar{\alpha}, \quad (4.21)$$

where  $\bar{\alpha}$  is a vector of eight elements representing the pseudorapidity distribution of incident  $E_T$  to the participant calorimeter,  $\bar{D}$  an array of 32 elements, and each of which is the sum of  $E_T$  in a ring of towers with the same depth,  $M$  a 32 x 8 matrix, each element of which is the fraction of  $E_T$  deposited in a particular ring for incoming transverse energy from a certain polar angle interval.

Once a certain pseudorapidity bin is selected, all the particles not incoming to this bin are filtered out. The surviving particles are tracked through the calorimeter. The transverse energy deposited by these particles in one of the 32 rings of the calorimeter can be expressed as

$$D_i = \sum_{j=1}^{16} E_{ij} \sin\theta_{ij} \quad (i = 1, 2, \dots, 32), \quad (4.22)$$

in which  $j$  is an azimuthal index and  $i$  is an index identifying the radial and longitudinal position of the tower,  $E_{ij}$  the measured transverse energy in the calorimeter cell, and  $\theta_{ij}$  the polar angle of its geometrical center. Each element of  $M$  is obtained from the following relation:

$$M_{ij} = \frac{\sum_{k=1}^N D_{i,k}}{\sum_{k=1}^N E_{j,k}} \quad (i = 1, 2, \dots, 32; j = 1, 2, \dots, 8), \quad (4.23)$$

where  $M_{ij}$  is a matrix element corresponding to the response in the  $i$ th ring of the calorimeter to the incoming transverse energy from the  $j$ th  $\eta$  interval,  $N$  the number of events applied,  $D_{i,k}$  the transverse energy of the event number  $k$  detected in the  $i$ th ring of the calorimeter, and  $E_{j,k}$  the incoming transverse energy of the event number  $k$  in the  $j$ th  $\eta$  interval.

To obtain the corrected  $dE_T/d\eta$  distribution from the experimental data the vector  $\vec{\alpha}$  is treated as a set of 8 parameters that are determined by unfolding the response matrix  $\mathbf{M}$  with the measured transverse energy array  $\vec{D}$ . Since  $\mathbf{M}$  is not a square matrix, inversion of the matrix can not be achieved directly. Instead, we determine the true  $dE_T/d\eta$  array  $\vec{\alpha}$  in the following way:

Equation (4.21) can be rewritten in the form of

$$D_i = \sum_{k=1}^8 M_{ik} \alpha_k \quad (i = 1, 2, \dots, 32). \quad (4.24)$$

Multiplying both sides of the equation by the inverse of response matrix, we have

$$\sum_{i=1}^{32} M_{ji} D_i = \sum_{i=1}^{32} M_{ji} \sum_{k=1}^8 (M_{ik} \alpha_k) \quad (j = 1, 2, \dots, 8), \quad (4.25)$$

$$\sum_{i=1}^{32} M_{ji} D_i = \sum_{k=1}^8 \left( \sum_{i=1}^{32} M_{ji} M_{ik} \right) \alpha_k \quad (j = 1, 2, \dots, 8), \quad (4.26)$$

where  $\sum_{i=1}^{32} M_{ji} M_{ik}$  is a square matrix. By inverting this square matrix, we obtain the corrected  $E_T$  for the  $k$ th  $\eta$  bin.

$$\alpha_k = \sum_{j=1}^8 \left( \sum_{i=1}^{32} M_{ji} M_{ik} \right)^{-1} \sum_{i=1}^{32} M_{ji} D_i \quad (k = 1, 2, \dots, 8). \quad (4.27)$$

The effect of this unfolding procedure will be shown in Figure 4.34 and Figure 4.35.

### Simulations on Trigger Bias

As stated in Chapter 3, the  $E_T$  triggers used in the experiment are obtained by summing signals from the summing box (FERA) of the participant calorimeter. To simulate  $E_T$  triggers we need to determine mean and *RMS* of the  $E_T$  distributions of the trigger thresholds which are set by FERA sums. Figure 4.25 shows FERA sum with level 1, level 2 and level 3 triggers in dashed, solid and dotted curves respectively. Here the FERA sum distributions are not corrected for downscaling factor to better show the FERA sum cuts on a linear scale. The three threshold cuts for  $E_T$  triggers

can be determined by looking into the three leading edges of the distributions. The FERA sum threshold is 45 for level 1 trigger, 95 for level 2 trigger and 145 for level 3 trigger. The three thresholds in FERA sum lead to three thresholds in transverse energy, which are better shown in the correlation between measured  $E_T$  and the total sum of FERA, as seen in Figure 4.24. The width of the line, which is between 0.3 - 0.4 GeV, represents the *RMS* of the correlation. The dashed lines corresponds to level 1 trigger, solid lines to level 2 trigger and dotted lines to level 3 trigger. A good linear relationship is observed between  $E_T$  and FERA sum, though the correlation is not perfectly narrow. To take into account the trigger bias in the simulation, these  $E_T$  and *RMS* values are used for trigger simulations.

Figure 4.33 shows a test of trigger simulations with three generated events. Each model produces four curves, representing minimum biased  $d\sigma/dE_T$ ,  $d\sigma/dE_T$  with level 1 trigger,  $d\sigma/dE_T$  with level 2 trigger and  $d\sigma/dE_T$  with level 3 trigger, respectively. The shapes of  $d\sigma/dE_T$  at three level triggers are well reproduced by RQMD, indicating that the triggers are well simulated. Other two models, HIJET and FRITIOF, yield similar results.

Tests with different thresholds in the  $E_T$  of the events used to calculate the response matrix, 0.8 GeV, 1.0 GeV and 1.2 GeV, show that the calorimeter response matrix is not sensitive to this threshold. Values of the matrix elements do not always increase or decrease with higher  $E_T$  threshold setting. Most of the matrix elements show variation of at most a few percent, while those matrix elements with small values have more variation. These are mainly associated with statistical fluctuation. Since the shift of the  $E_T$  threshold has very little affect on the calorimeter response, we simply employ a sharp  $E_T$  threshold representing the level 1 trigger when generating the response matrix. This matrix unfolding method requires a large number of particles to populate the detector cells, while the multiplicity production in proton-nucleus collisions is very small compared to nucleus-nucleus collisions at the same energy per nucleon. Therefore, we apply this unfolding approach to correct  $dE_T/d\eta$  distributions with  $E_T$  level 1 trigger only.

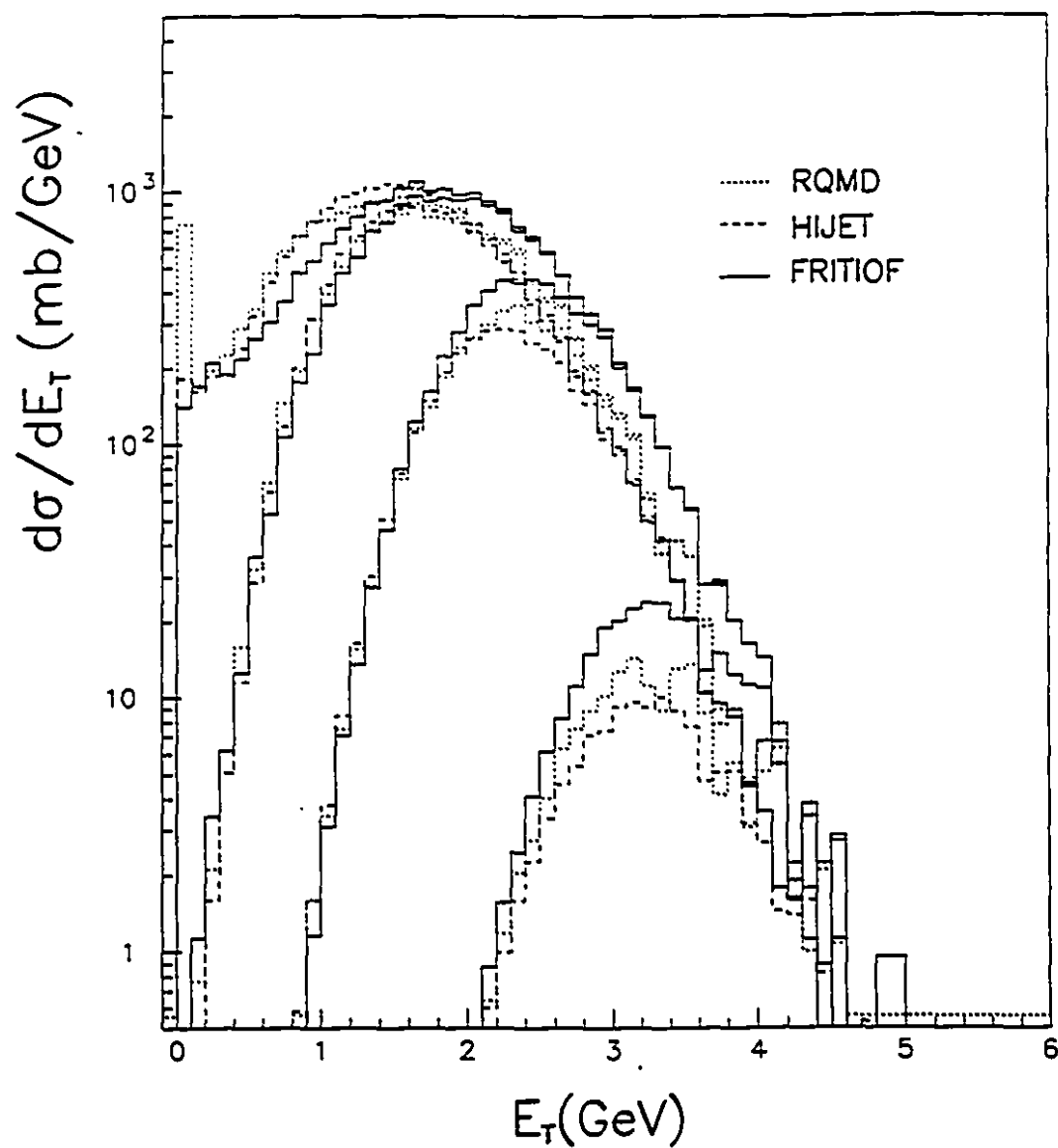


Figure 4.33: Trigger simulations with three generated events: the dotted lines are for RQMD; dashed lines are for HIJET; solid lines are for FRITIOF. Each model produces four curves corresponding to minimum bias,  $E_T$  level 1 trigger,  $E_T$  level 2 trigger and  $E_T$  level 3 trigger respectively.

### Correction on $dE_T/d\eta$ Distributions

To test this unfolding method, we pass the simulated events through GEANT/PROPHET tracking code to obtain the equivalent of experimental data. These calculated data are then unfolded using the matrix method and compared to the original  $E_T$  distribution.

Figure 4.34 shows the correlation between unfolded transverse energy and the incoming transverse energy in the acceptance of the participant calorimeter. The relation is quite linear and in good agreement with the line of slope 1 (shown in the figure) in the range of incoming  $E_T$  less than 3 GeV, which corresponds to 97% of the events. This result indicates a very small systematic error in this unfolding process. The spread of the correlation is mainly caused by shower fluctuations.

The performance of the unfolding method on correcting  $dE_T/d\eta$  distributions with generated RQMD, HIJET and FRITIOF events is shown in Figure 4.35. The x-axes represent the eight  $\eta$  intervals from smaller polar angles to larger polar angles; the y-axes represent  $E_T$  in arbitrary unit. Incoming  $E_T$  before tracking are shown by solid lines,  $E_T$  seen by the calorimeter with GEANT/PROPHET tracking are shown as dashed lines, and  $E_T$  after unfolding with the response matrix are shown as dotted lines. When energetic particles enter a thinner calorimeter section, more energy leakage occurs. As seen in the figure, the participant calorimeter measures about 70% of incoming particle energy on average, while it measures less than 40% of incoming particle energy in the acceptance of inner detector bins (bin 1 and bin 2) and measures approximately 90% of incoming particle energy in the acceptance of detector bin 5 and bin 6. Unfolded  $E_T$  (dotted lines) are consistent with the original incoming  $E_T$  (solid lines) within 10% error range except for section eight which corresponds to the low  $\eta$  corner of the participant calorimeter where the errors reach 20%. The figure shows that the precision of the unfolding is not sensitive to a particular model, indicating that unfolding results are mainly determined by particle kinematics.

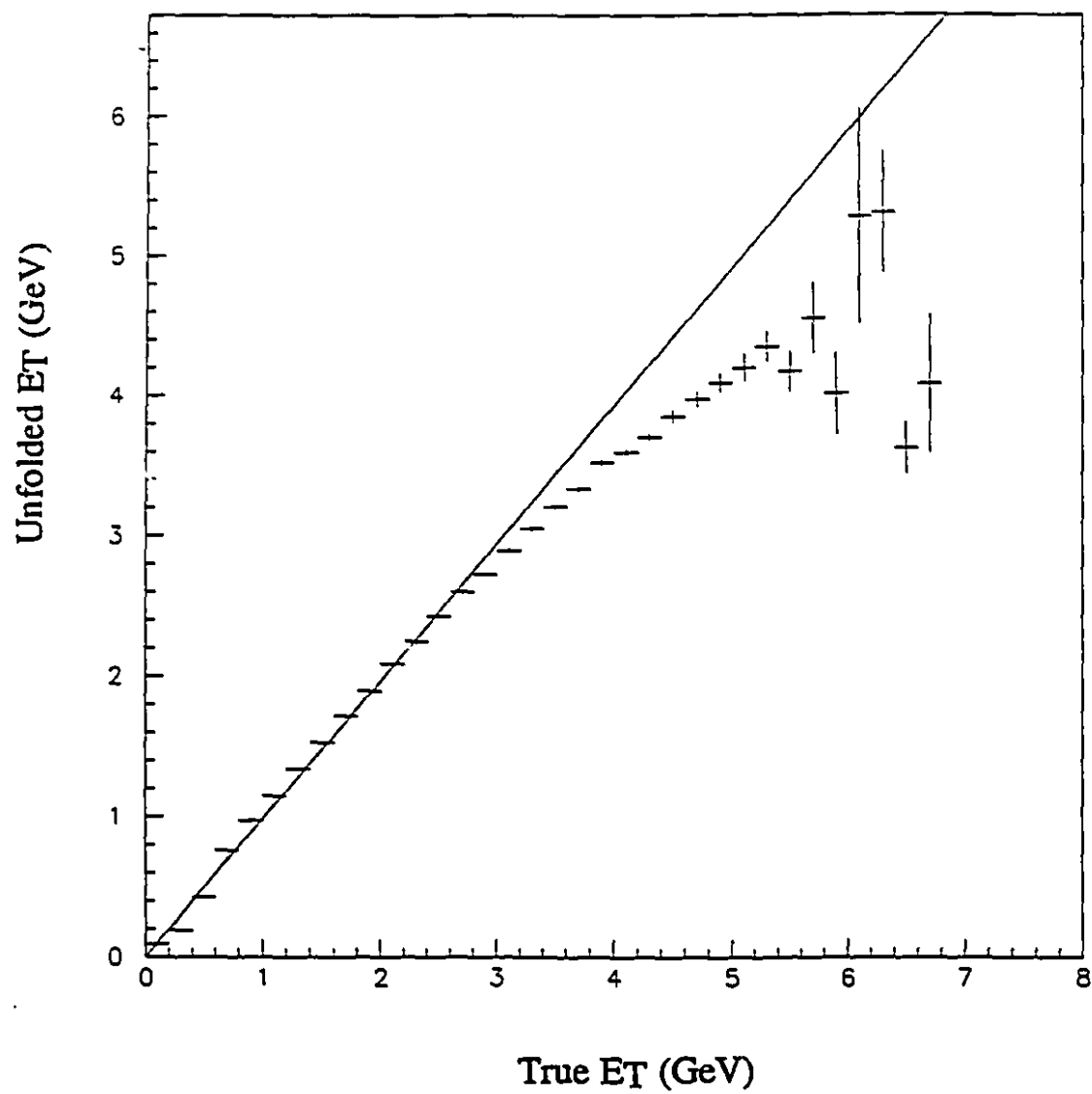


Figure 4.34: Correlation between unfolded transverse energy and the original incident transverse energy in the acceptance of the participant calorimeter.

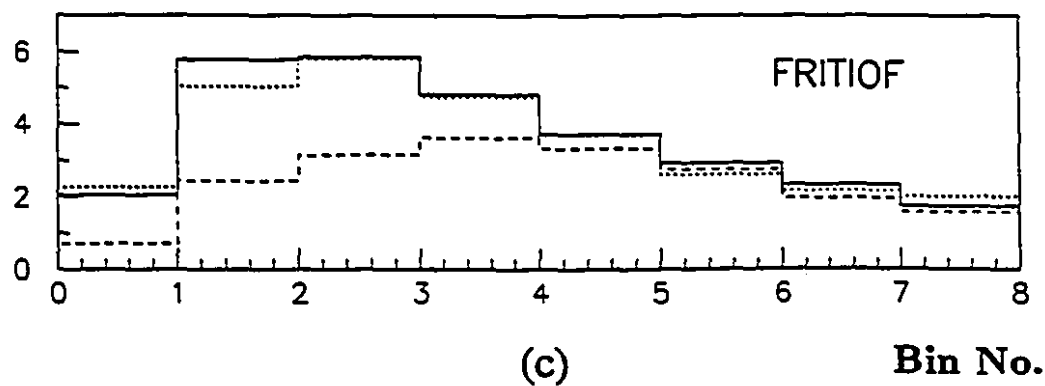
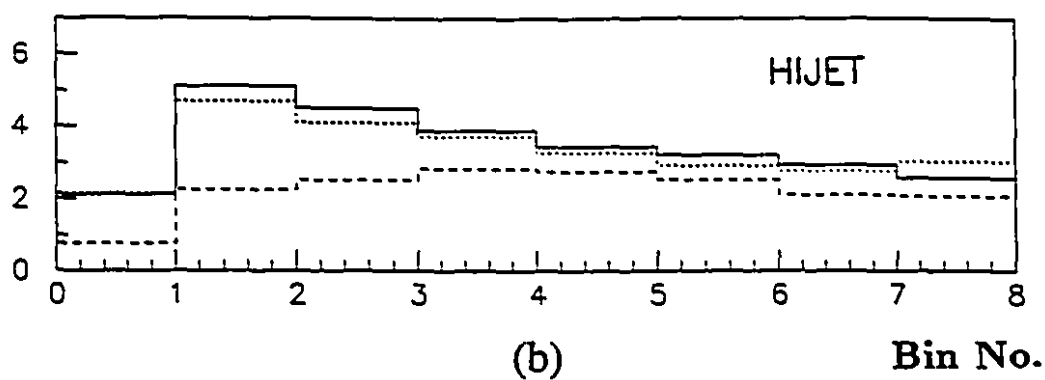
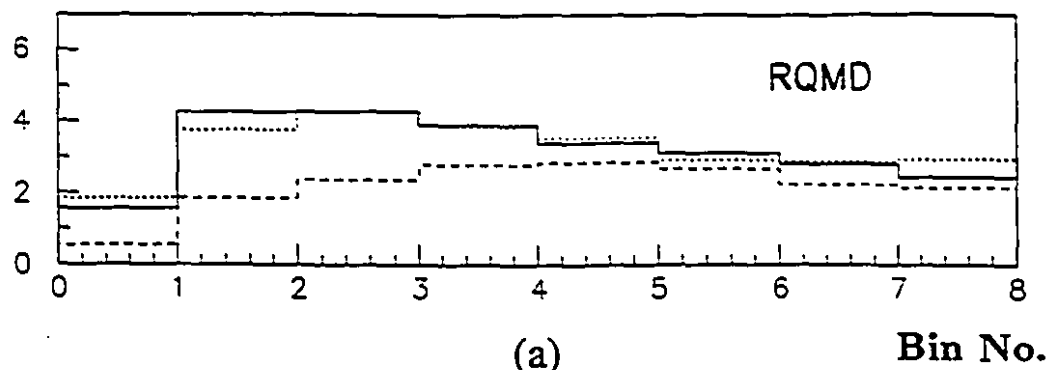


Figure 4.35:  $\eta$  bin distribution of  $E_T$  (in arbitrary unit) calculated using generated events:(a) RQMD; (b) HIJET; (c) FRITIOF. The solid lines are for distributions before tracking, dashed lines for distributions after tracking and dotted lines for unfolded distributions.

Corrected  $dE_T/d\eta$  distributions in the acceptance of the participant calorimeter are thus obtained by employing the response matrix approach. For convenience the empty target contributions are subtracted after unfolding the data with target-in and the data without target respectively. The resulting corrected pseudorapidity distributions of  $dE_T/d\eta$  in the forward acceptance are shown in Figure 4.36 for the p+Pb and p+Al reactions (solid lines). The data before corrections for detector efficiency are shown as dotted lines.

To obtain the complete picture of  $dE_T/d\eta$  distributions over the acceptance of both the target calorimeter and the participant calorimeter, we combine pseudorapidity distributions of transverse energy from multiplicity trigger data, which covers the acceptance of target calorimeter, and from  $E_T$  trigger data in the acceptance of participant calorimeter. Two more corrections on the data are needed to assure a proper comparison. One is a correction to take into account difference in the trigger. The  $E_T$  level 1 trigger on the participant calorimeter is more biased than the multiplicity pretrigger which requires more than two charged particles in the forward acceptance. This correction due to different triggers is determined by applying the two types of cuts to the simulated events. Table 4.4 shows the mean  $E_T$  for three theoretical models with the two different triggers. The trigger correction factor is then calculated by averaging the mean  $E_T$  shift due to trigger type from three models. It is determined that to normalize the trigger bias,  $dE_T/d\eta$  measured in the participant calorimeter acceptance needs to be reduced by 0.9% for Pb target data and by 1.5% for Al target data.

The data measured in the target calorimeter acceptance include many events with zero  $E_T$ , as is shown in Figure 4.20. These events satisfy the pretrigger condition which requires more than two particles registered in the charged multiplicity detector, while they are not detected by the target calorimeter which covers a lower pseudorapidity region than does the multiplicity detector. They include both real events whose products go beyond the acceptance of the target calorimeter, and fake events which should be removed. The correction on zero  $E_T$  events is performed in two steps. First we remove all the zero  $E_T$  events from the data, which will increase the values of mean  $E_T$

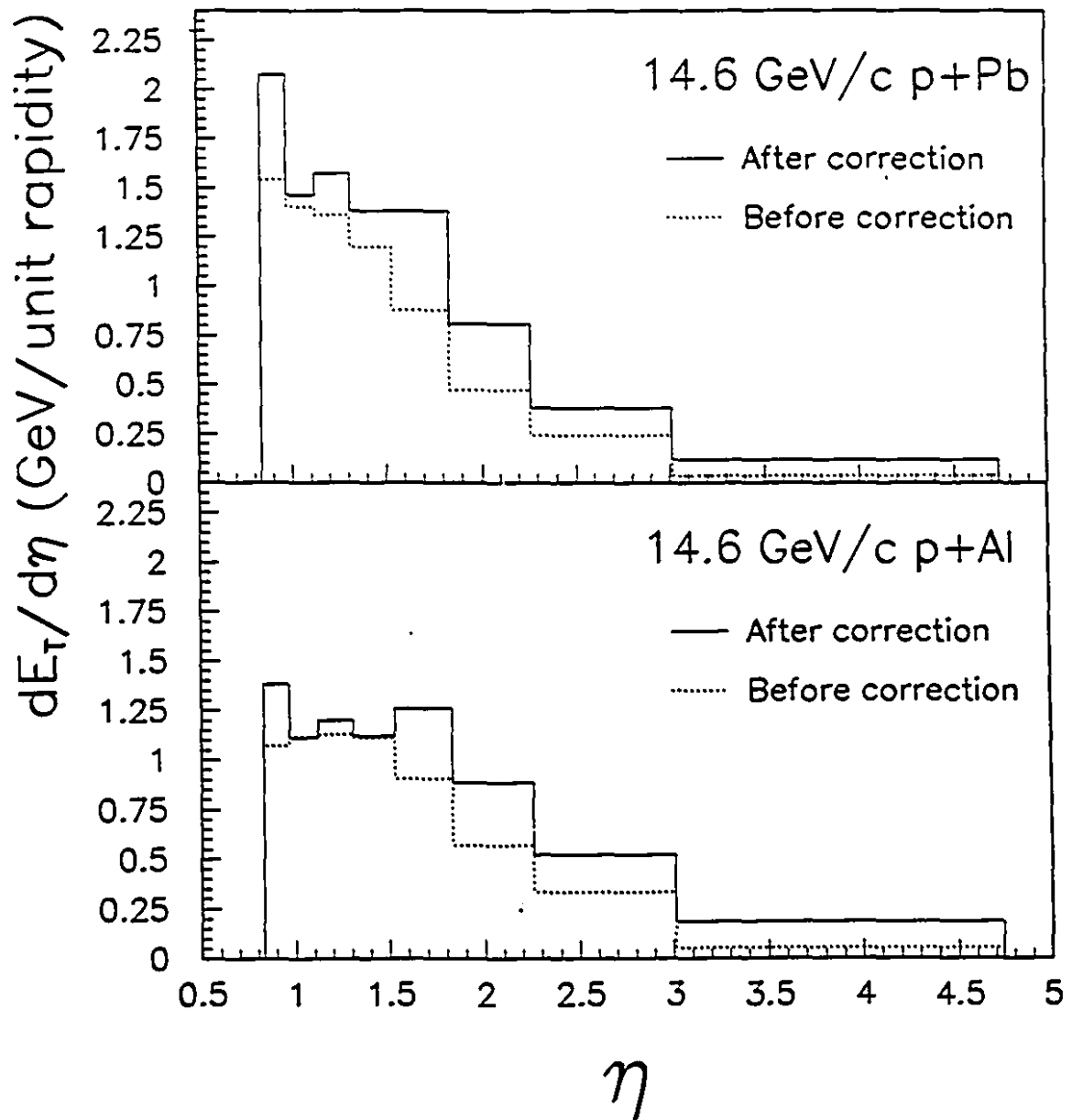


Figure 4.36: Experimental  $dE_T/d\eta$  distributions as measured by the participant calorimeter for the p+Pb (upper part) and p+Al (lower part) reactions. The dotted histograms correspond to distributions before corrections for leakage and the solid histograms correspond to distributions after corrections.

Table 4.4: Model comparison for mean  $E_T$  measured in the participant calorimeter

Target	Model	Pretrigger	$E_T$ Level 1	Mean $E_T$ relative shift
Pb	RQMD	1.829 GeV	1.848 GeV	1.04%
	HIJET	1.777 GeV	1.793 GeV	0.90%
	FRITIOF	1.955 GeV	1.972 GeV	0.87%
	(Average)			0.94%
Al	RQMD	1.694 GeV	1.724 GeV	1.77%
	HIJET	1.679 GeV	1.699 GeV	1.19%
	FRITIOF	1.738 GeV	1.767 GeV	1.66%
	(Average)			1.54%

per event. Then from theoretical models we estimate the decrease fraction in mean  $E_T$  per event due to including those real events with zero  $E_T$ . By combining the increase factor obtained in the first step and the decrease factor obtained in the second step, we can find the over-all correction of the experimental  $dE_T/d\eta$  measured with the target calorimeter. The mean  $E_T$  per event for the data with Pb target measured in the target calorimeter is 0.374 GeV when including zero  $E_T$  events, and it increases by 38.5% to 0.518 GeV when excluding zero  $E_T$  events. Similarly, the mean  $E_T$  per event for Al target measured in the target calorimeter is 0.206 GeV when including zero  $E_T$  events, and it increases by 52.9% to 0.315 GeV when excluding zero  $E_T$  events. The change in mean  $E_T$  per event due to including zero  $E_T$  events is obtained via looking into three theoretical models. Table 4.5 lists mean  $E_T$  and relative shift of mean  $E_T$  due to including zero  $E_T$  events in the acceptance of the target calorimeter from three models. This correction is calculated by averaging the three simulated  $E_T$  shifts, which is 8.8% decrease in the mean  $E_T$  for Pb target or 17.3% decrease for Al target.

Figure 4.37 shows pseudorapidity distributions of  $dE_T/d\eta$  for Pb target (top) and for Al target (bottom) over the acceptance of both the target calorimeter and the participant calorimeter, with detector efficiency, trigger difference and zero  $E_T$  events fully corrected. There is good agreement between the two data sets in the acceptance of two different calorimeters. The  $E_T$  data points at  $\eta = 0.9$  and 1.0, which are geometric

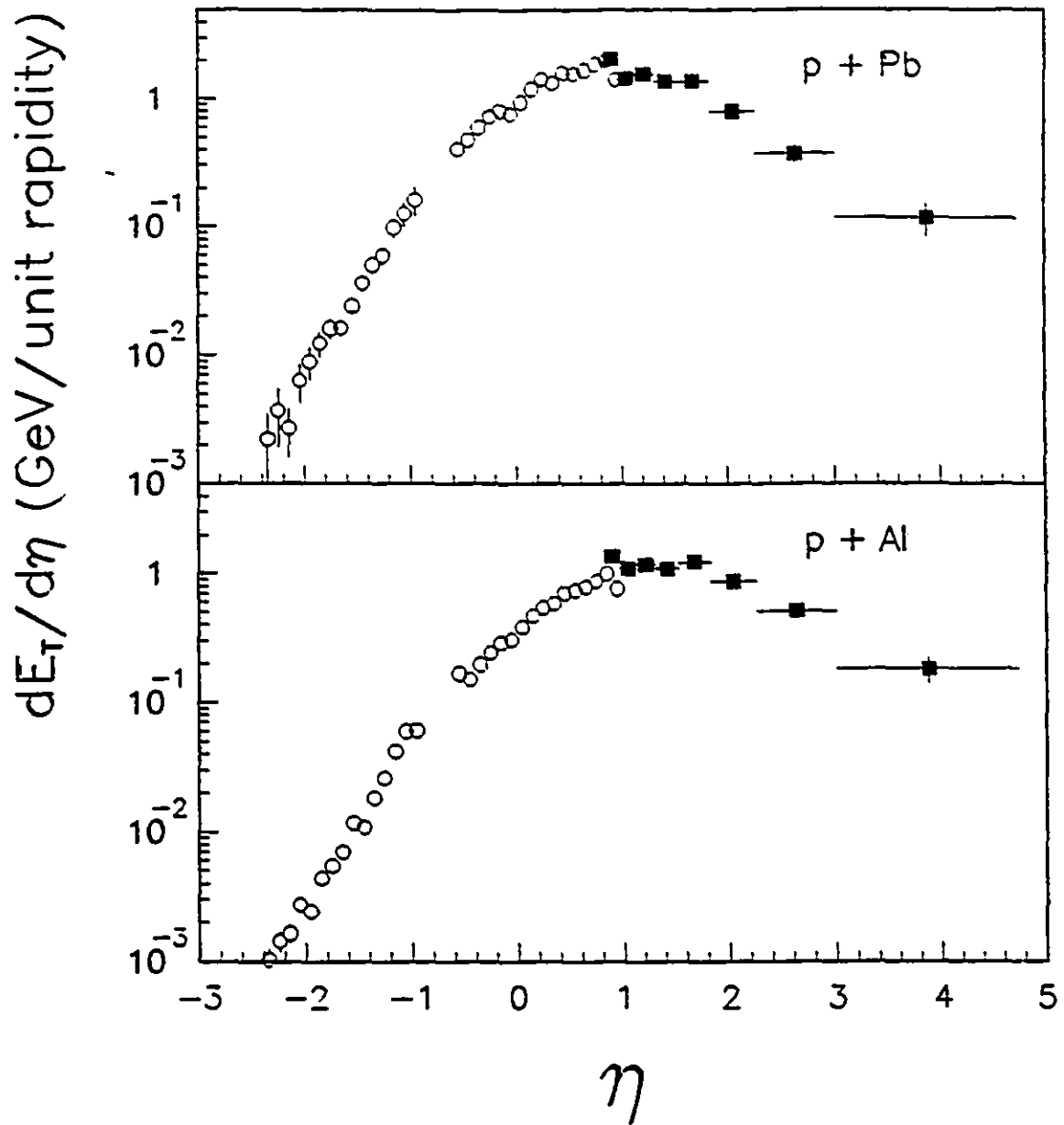


Figure 4.37: Corrected  $dE_t/d\eta$  distribution for p+Pb (upper part) and p+Al reaction (lower part). The open dots are obtained with the target calorimeter while the close dots are obtained with the participant calorimeter.

Table 4.5: Model comparison for mean  $E_T$  measured in the target calorimeter

Target	Model	Incl. 0 $E_T$ events	Excl. 0 $E_T$ events	relative shift of $\langle E_T \rangle$
Pb	RQMD	0.458 GeV	0.499 GeV	8.9%
	HIJET	0.477 GeV	0.510 GeV	6.9%
	FRITIOF	0.276 GeV	0.306 GeV	10.8%
	(Average)			8.8%
Al	RQMD	0.268 GeV	0.315 GeV	17.5%
	HIJET	0.276 GeV	0.316 GeV	14.5%
	FRITIOF	0.207 GeV	0.249 GeV	20.2%
	(Average)			17.3%

edges, carry relatively more uncertainty. The  $dE_T/d\eta$  distributions after leakage and geometrical corrections display Gaussian-like shapes. This will be discussed further in the next chapter.

## 4.5 Data Analysis of Charged Particle Multiplicity

### 4.5.1 Raw Data

The multiplicity data were collected in two separated runs using the participant calorimeter triggers and the multiplicity triggers respectively. The data from the first run are mainly used for the study of correlation between transverse energy and charged particle multiplicity. The data from the second run are used for studying multiplicity distributions. The selection and reduction procedures for the two sets of charged multiplicity data taken with the different types of trigger are very similar.

The beam position and incidence angle at the target are determined by the two beam vertex detectors. As the spatial distribution of charged multiplicity is sensitive to the vertex position of the beam, the offset of the beam from the target center due to geometric misalignment of detectors needs to be corrected. The projection of all beam tracks at the target is shown in Figure 4.38. Figure 4.39 shows the horizontal beam

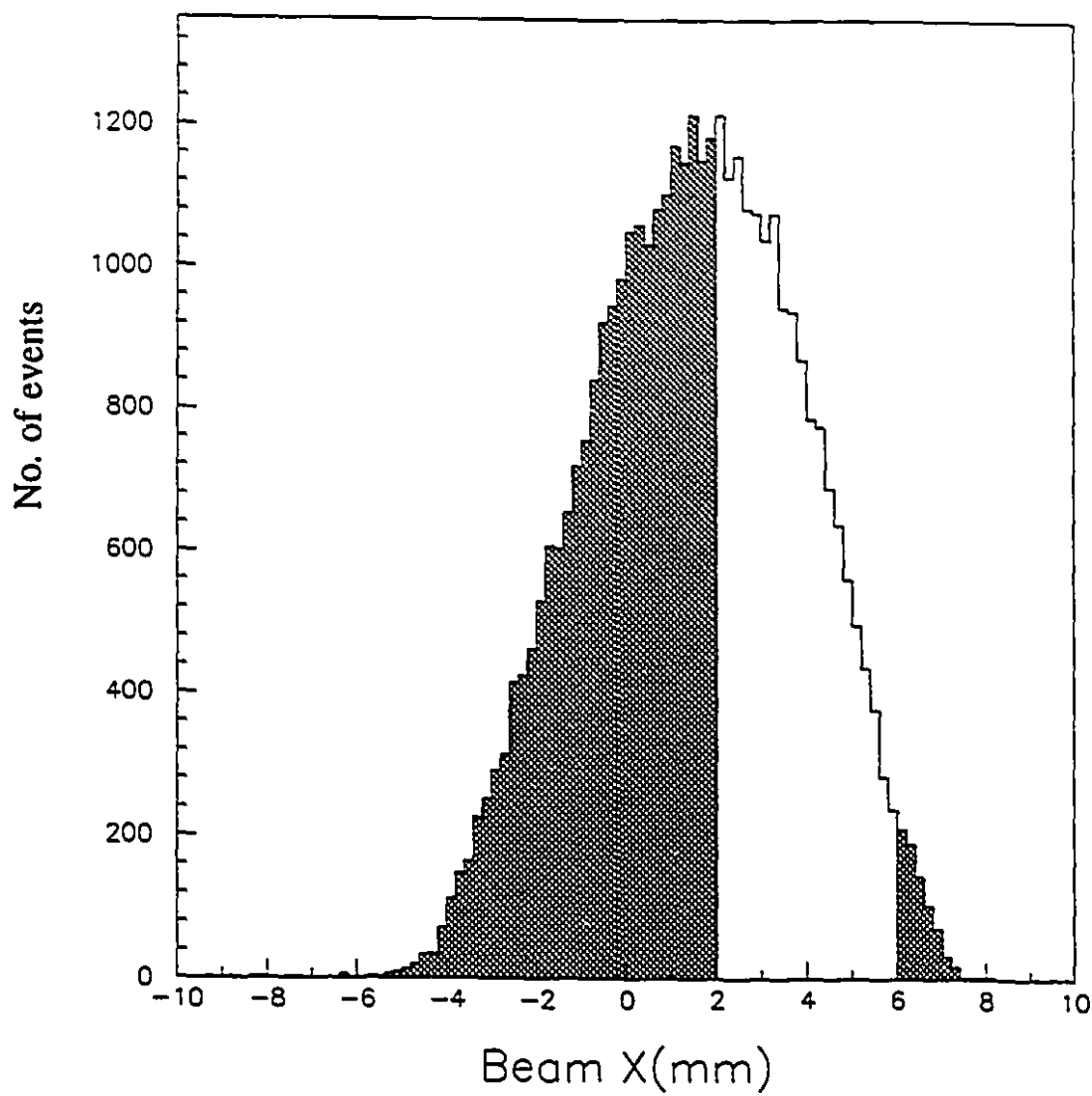


Figure 4.38: Beam track x projection in the target plane for all events. The shaded areas correspond to the events rejected using beam position cut.

position at the first multiplicity detector disk estimated from the average position of the charged multiplicity hits in the multiplicity detector for events with at least four hits registered by the detector,  $X_{MULT}$ , versus the same position measured by the beam vertex detector,  $X_{BVER}$ . The data have been fitted with a straight line which represents the average x position in the multiplicity detector over all events corresponding to each x position at target measured with beam vertex detectors. It appears that there is an offset of 4 mm between the beam position as determined with the beam detector and the multiplicity detector. Therefore in the analysis of the multiplicity distribution, a cut is introduced to accept only those beam particles that pass with  $\pm 2$  mm of the center of the multiplicity detector. The white area in figure 4.38 corresponds to the selected events. About 40% of the events are accepted by this beam vertex cut.

The multiplicity detection inefficiency from various origins need to be corrected before obtaining the true charged multiplicity distributions. Working as a hit detector, the multiplicity detector registers occurrence of a charged particle in a given pad if a signal is present above the threshold which corresponds to approximately one half of the energy loss of a minimum ionizing particle. Therefore, the response of the multiplicity detector is sensitive to the number of noisy and dead pads, the possible charge sharing between neighbouring pads, multiple hits in a same pad, production of  $\delta$  rays, detector noise, etc.

The bad pads are easily identified by plotting hits versus the pad number. Figure 4.40 shows the hit frequency for 512 channels corresponding to the 512 pads in each of the multiplicity detector disk. The channel number starts from  $\phi$  pad of inner rings to outer rings. The first disk of the detector has 8 rings and 64 pads on each ring. The second disk has 12 rings: the two inner rings of the disk have 16 pads each, the next three rings have 32 pads each, then four rings have 48 pads each, and the outer three rings have 64 pads each. The hit distribution for each disk is quite smooth in general. The gross structures represent change in  $dN_c/d\eta$  while the more pronounced substructure with a frequency of 16 to 64 channels corresponding to ring in the counters are due to the beam misalignment discussed above. Dead channels and noisy channels can be

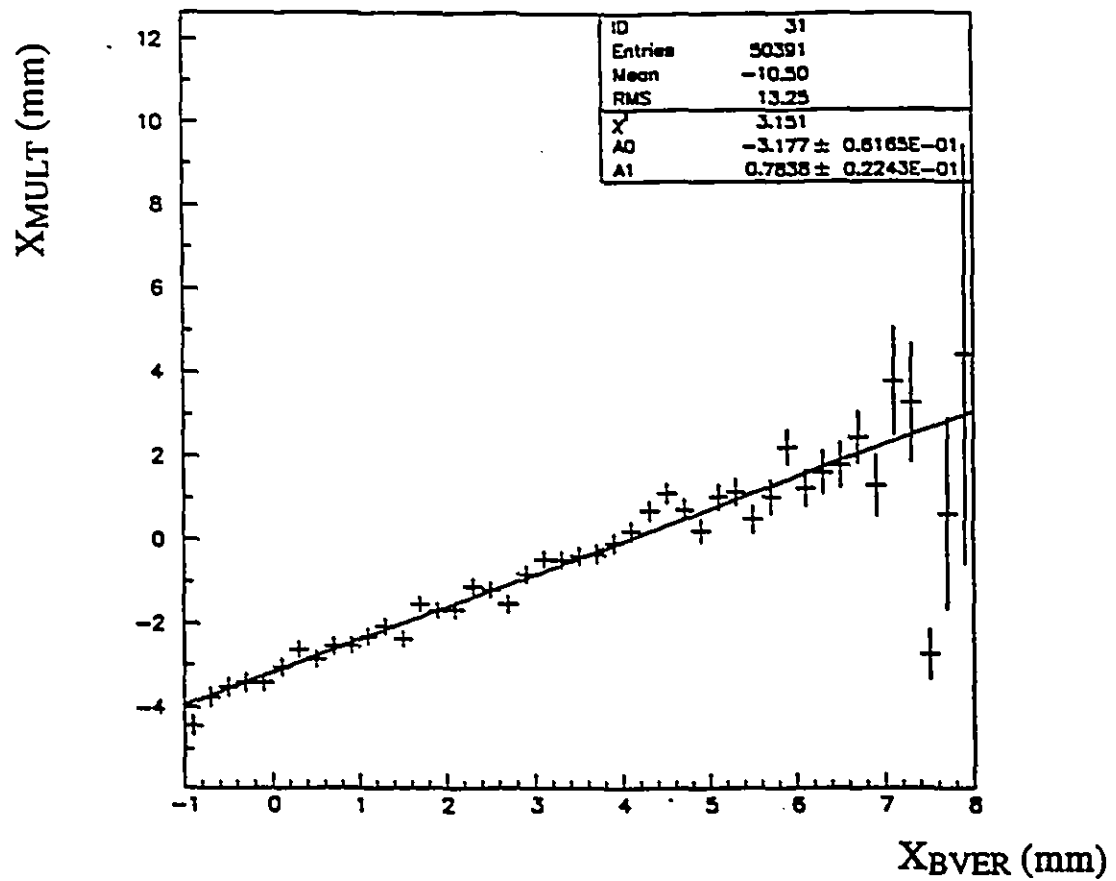
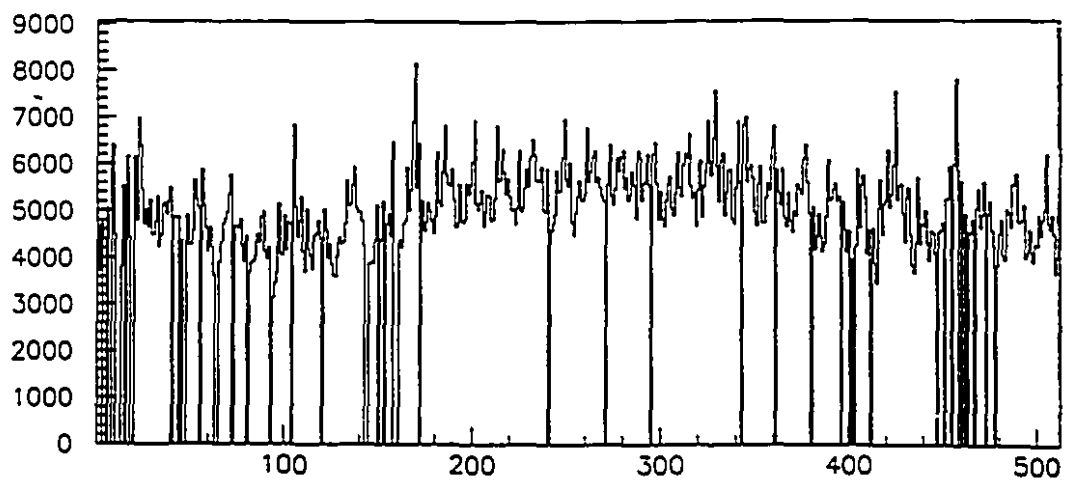
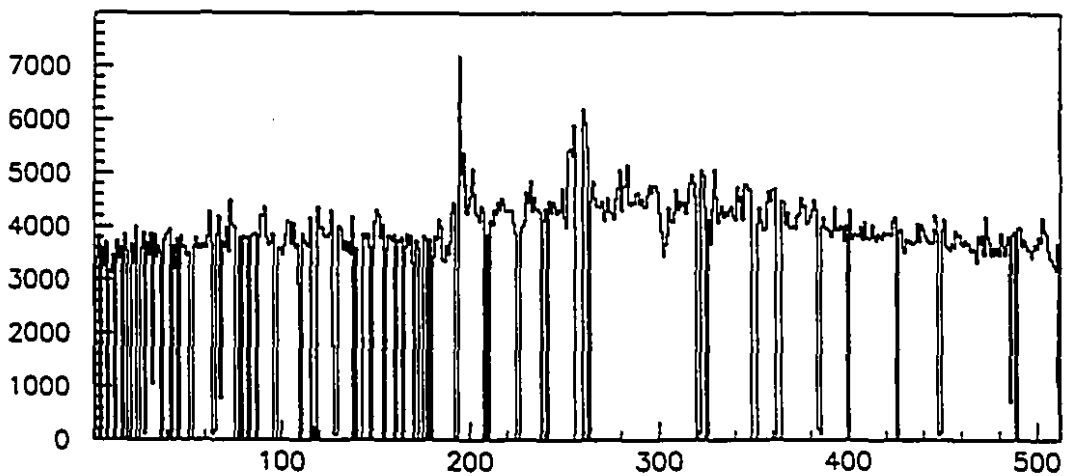


Figure 4.39: Beam track x projection versus the average x position of the multiplicity detector hits. The data are fitted with a line.



(a) Disk 1



(b) Disk 2

Figure 4.40: Hit distribution in 512 channels for each of the multiplicity detector disk: (a) Disk 1 and (b) Disk 2.

easily recognized from this figure. These channels are ignored. Some detector pads with very low gains or high gains are also ignored if their average occupancy deviates by more than two standard deviations from the average occupancy of the other pads in the same ring. Approximately 5% the pads are treated as bad pads. Because of the nonuniform  $dN_c/d\eta$  distribution, the corrections for these pads are made ring by ring. For each ring of the detector, the number of hits is plotted as a function of the pad number. Assuming an azimuthal symmetry, the average hits per channel is estimated over all good pads in the given detector ring. For example, Figure 4.41 shows the number of hits in each pad (solid line) for ring 15 of the multiplicity detector and the calculated average hits per pad (dashed line) for this ring. The corrected number of hits for each ring is thus calculated by multiplying the average hit value by the total number of pads in each ring.

Charge sharing between adjacent pads for a particle going through the detector close to pad boundaries may cause the detector to register double hits. On the other hand, more than one particles from the same event striking a given pad will register as a single hit. The two processes have opposite effects on the number of hits registered in the charged multiplicity detector. The effects of charge sharing on the measured total charged multiplicity has been estimated to be less than 1% for the data obtained with  $^{28}\text{Si}$  projectiles in reference [BA93]. Considering the fact that the mean multiplicity per event for collisions with proton projectiles on Pb is approximately seven particles, we can estimate that multiple hits will reduce the average multiplicity by  $\approx 0.05$  particles. For an event with multiplicity of 20 the multiple hits are estimated to be about 0.4 particles. The effect is even less for an aluminum target.

The effect of charge collection fluctuations on the charged multiplicity detection are estimated using random triggers, and also found to be negligible. Figure 4.42 shows the measured multiplicity hits for events obtained with random triggers. The multiplicity distribution has a mean value of roughly 0.04, which represents the average number of random hits due to charge collection fluctuations during each event.

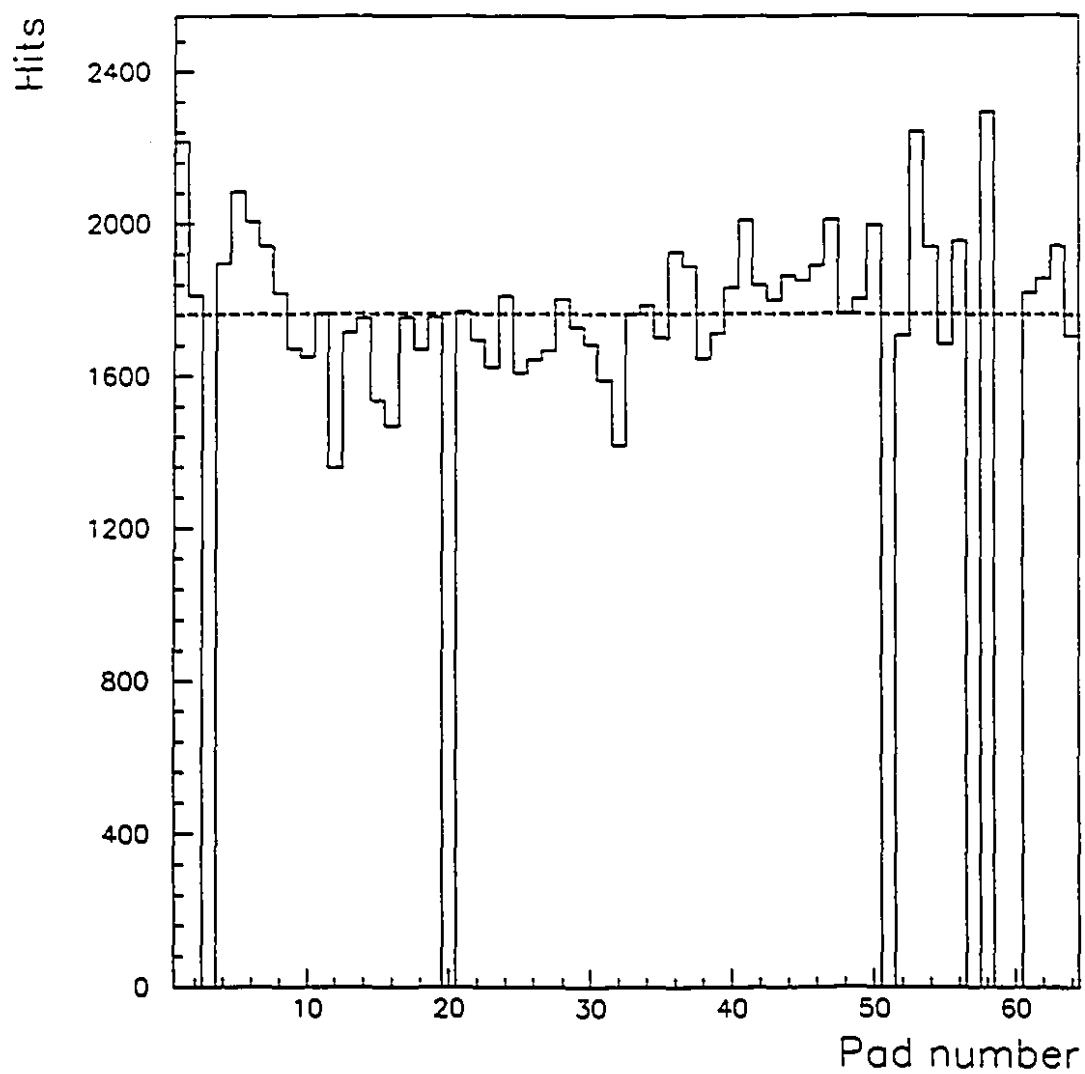


Figure 4.41: Hit distribution in each pad for ring 15 of the multiplicity detector. The dashed line represents the calculated value for the average number of hits.

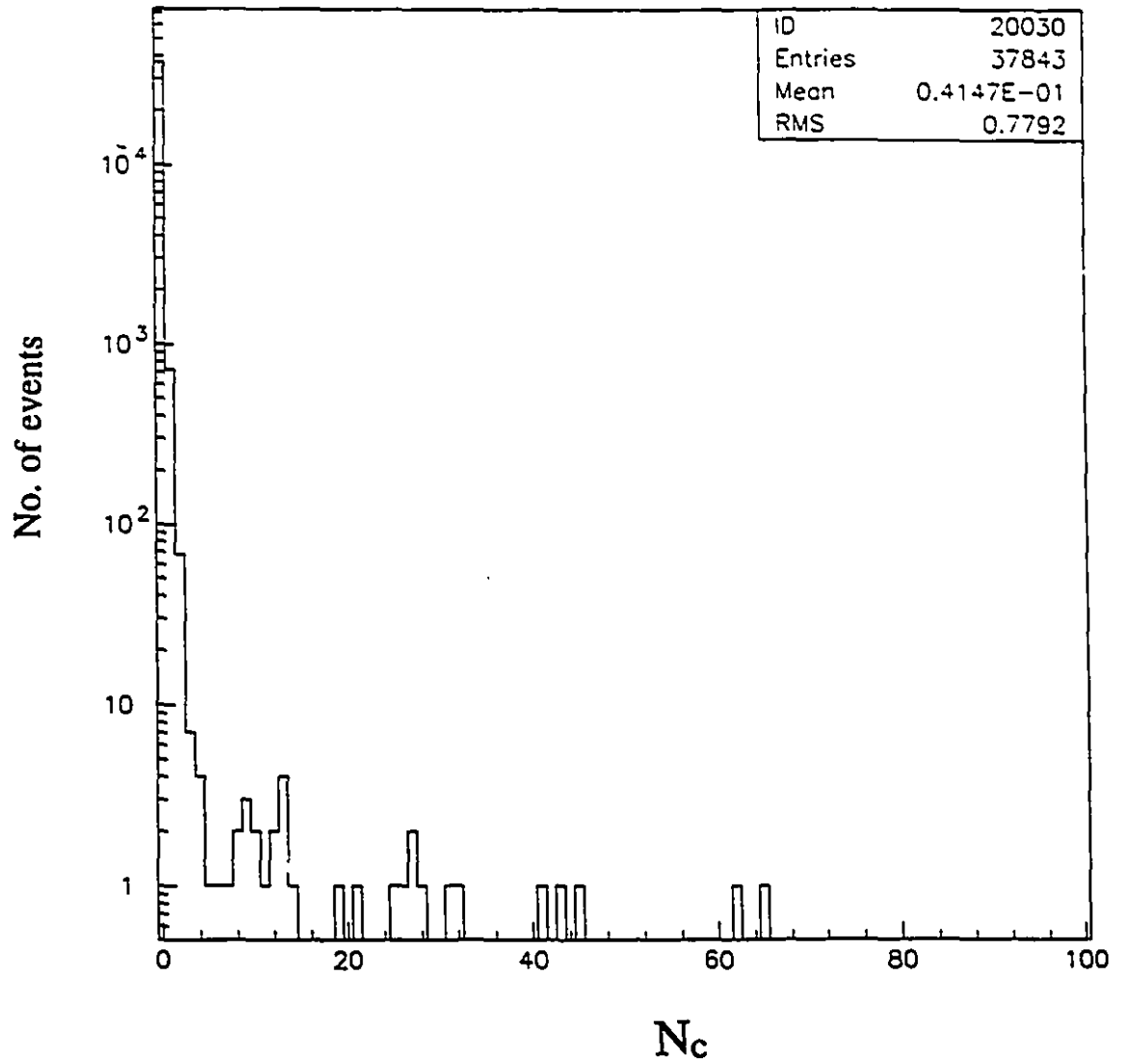


Figure 4.42: Multiplicity hit spectrum for random triggers.

$\delta$  rays produced in the target by a noninteracting charged projectile will also contribute to multiplicity hits in the detector. Since the number of  $\delta$  rays increases with  $Z^2$  of the projectile, we can estimate the mean  $\delta$  production in the proton-nucleus reactions by scaling the results from the Si-nucleus reactions reported in [BA92B]. We estimate the  $\delta$  ray multiplicity to contribute on average 0.1 particle in the proton-lead reaction. All these small effects are insignificant and no corrections for them have been made.

In Figure 4.42 one observes a few events with very high multiplicity. It was determined that most of them are fake events caused by random electronic cross talk in the detector. To eliminate these fake events a cut has been set to reject those events where more than four contiguous electronic channels have fired. This cut does not modify the shape of the  $d\sigma/dN_c$  distribution but removes the events with unreasonably large multiplicity. The cut rejects about 5% of the recorded events.

#### 4.5.2 Charged Particle $dN_c/d\eta$ Distributions

The  $dN_c/d\eta$  distributions are obtained by plotting corrected multiplicity as a function of pseudorapidity bin of the detector. The pseudorapidity granularity of charged multiplicity is determined by the number of detector rings. For each ring of the detector, the removal of bad detector pads from data analysis causes detection inefficiency. Table 4.6 shows the pseudorapidity granularity of the multiplicity detector and the detection efficiency for each detector ring. The first ring of the detector contains many bad pads and is ignored in the analysis. The efficiencies of the other rings are estimated by comparing the actual number of hits with the fitted average hits times the number of pads in the ring.

The multiplicity in each ring from the raw data is divided by the corresponding efficiency listed in the table. Figure 4.43 shows the pseudorapidity distributions of charged particle multiplicity per event before empty target correction and after empty

Table 4.6: Multiplicity detector ring-by-ring detection efficiency

Ring	Pseudorapidity range	Efficiency
1	3.86 - 3.38	small
2	3.38 - 3.18	0.97
3	3.18 - 2.88	0.95
4	2.88 - 2.67	0.94
5	2.67 - 2.52	0.89
6	2.52 - 2.34	0.94
7	2.34 - 2.20	0.88
8	2.20 - 2.07	0.90
9	2.07 - 1.96	0.93
10	1.96 - 1.83	0.68
11	1.83 - 1.72	0.93
12	1.72 - 1.61	0.90
13	1.61 - 1.51	0.87
14	1.51 - 1.41	0.92
15	1.41 - 1.32	0.92
16	1.32 - 1.23	0.92
17	1.23 - 1.14	0.92
18	1.14 - 1.05	0.96
19	1.05 - 0.96	0.95
20	0.96 - 0.88	0.89

target correction for pretrigger. The empty target contribution comes from unwanted interactions which satisfy the trigger conditions. For pretrigger data, the empty target contribution is about 10% for Pb target reactions or 20% for Al target reactions.

### 4.5.3 Charged Particle $d\sigma/dN_c$ Distributions

The raw charged particle multiplicity distribution  $(d\sigma/dN_c)_{raw}$  is shown in Figure 4.44. The pretrigger  $(d\sigma/dN_c)_{raw}$  for the reaction of p+Pb before empty target correction is shown in Figure 4.44(a) while Figure 4.44(b) shows the same distribution after empty target correction. For the Al target the raw charged particle multiplicity

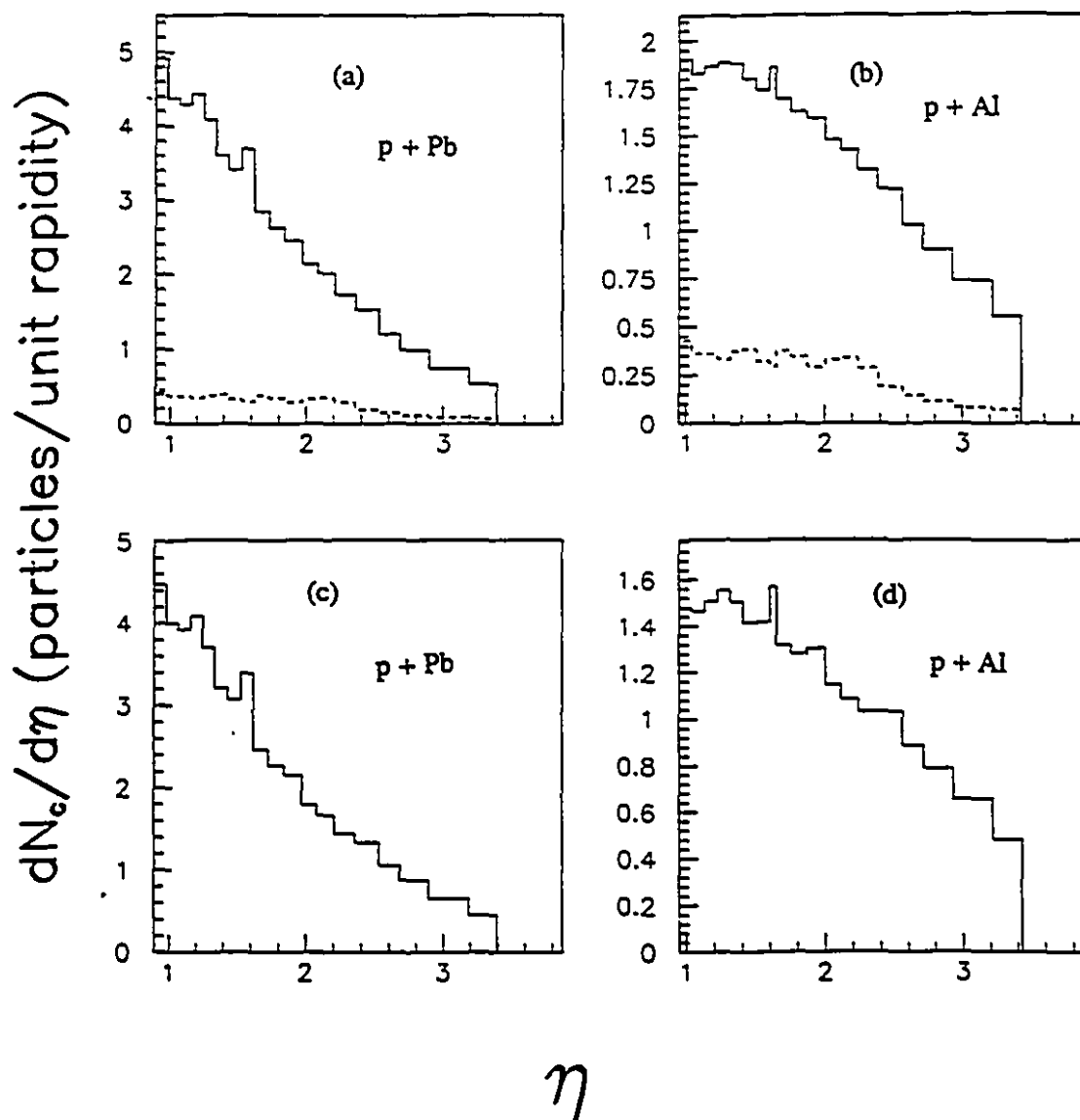


Figure 4.43: Contribution of background interactions to  $dN_c/d\eta$ . (a)  $dN_c/d\eta$  for p+Pb before empty target frame correction, (b)  $dN_c/d\eta$  for p+Al before empty target frame correction, (c)  $dN_c/d\eta$  for p+Pb after empty target frame correction, (d)  $dN_c/d\eta$  for p+Al after empty target frame correction. The dashed histograms are for distributions as measured using empty target frame.

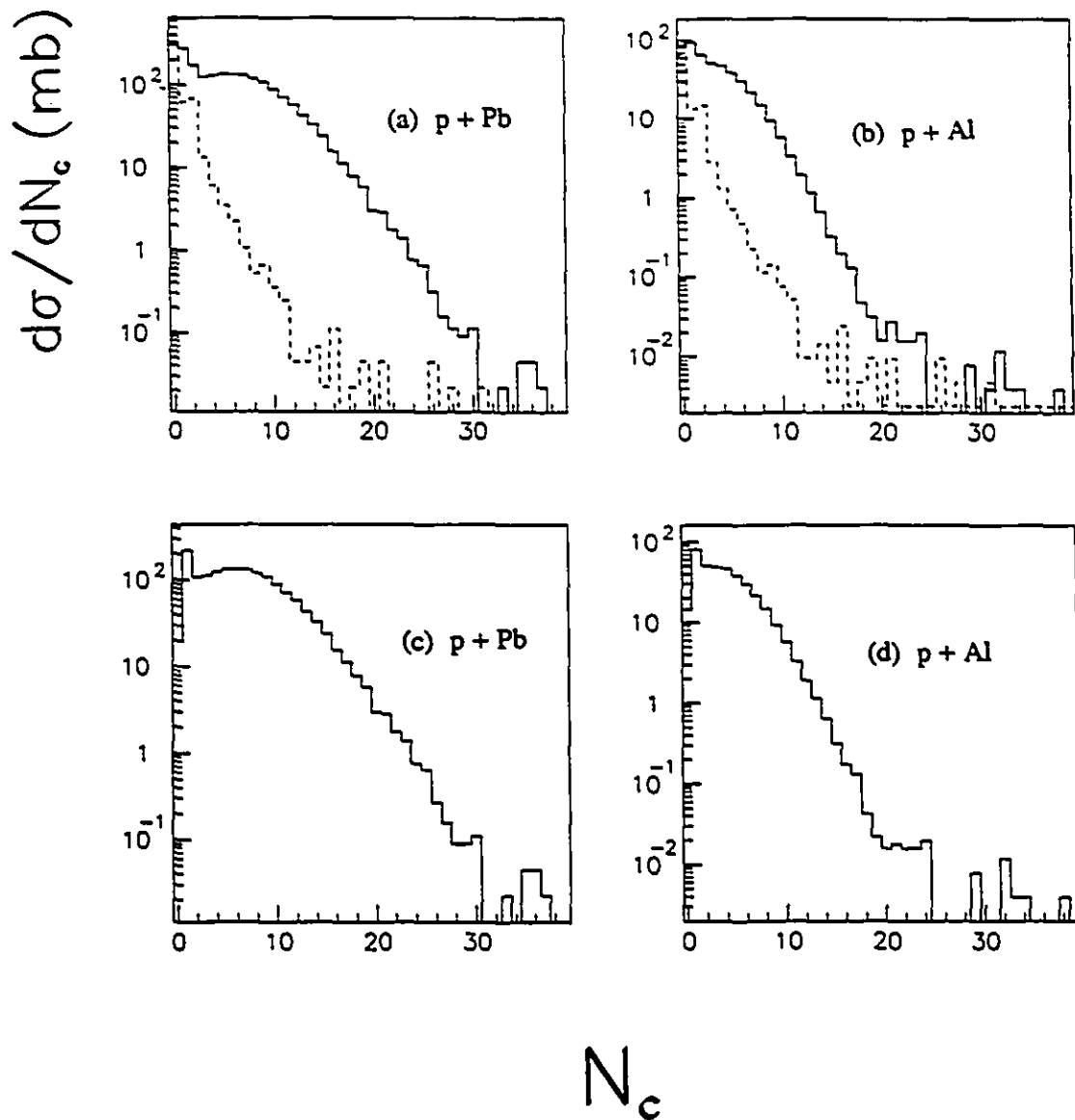


Figure 4.44: Contribution of background interactions to  $d\sigma/dN_c$ . (a)  $d\sigma/dN_c$  for p+Pb before empty target frame correction; (b)  $d\sigma/dN_c$  for p+Al before empty target frame correction; (c)  $d\sigma/dN_c$  for p+Pb after empty target frame correction; (d)  $d\sigma/dN_c$  for p+Al after empty target frame correction. The dashed histograms are for distributions as measured using empty target frame.

distributions before and after empty target correction are shown in Figure 4.44(c) and Figure 4.44(d) respectively. The background reactions associated with the empty target events are observed to produce basically less than 2 charged particles. For events with more than two charged particles in the multiplicity detector acceptance the empty target contribution is negligible.

To take into account the detector efficiency and to find out the true spectra of charged particle multiplicity,  $d\sigma/dN_c$ , a Monte Carlo simulation has been performed. One million Monte Carlo events were generated according to the measured multiplicity distribution for each target. For example, for the Pb target, the distribution shown in Figure 4.44(a) was used as input to the simulation. The average ring efficiency is reported in Table 4.6, and average ring occupancy is listed in Table 4.7 where the occupancy is calculated from the ratio of total number of corrected hits to the total number of events in each ring. A probability table for the true charged multiplicity  $(N_c)_{true}$  associated with a given multiplicity  $(N_c)_{raw}$  uncorrected for the detector efficiency is then constructed.

For example, in a reaction for the lead target an event with  $(N_c)_{raw} = 10$  has a 41.8% probability of being  $(N_c)_{true} = 10$ , 35.9% probability of being  $(N_c)_{true} = 11$ , 16.0% probability  $(N_c)_{true} = 12$ , 4.9% probability of  $(N_c)_{true} = 13$ , 1.0% probability  $(N_c)_{true} = 14$  and 0.3% probability  $(N_c)_{true} = 15$ . Therefore, to obtain the true spectra of charged particle multiplicity  $d\sigma/dN_c$ , for each value of  $(N_c)_{raw}$ , all the possible values of  $(N_c)_{true}$  are unfolded with weights equal to their probabilities. The same procedure is applied to correct for the Al target data and empty target data. Then the empty target distributions are subtracted from the corrected target-in data.

Figure 4.45 shows the corrected  $d\sigma/dN_c$  distributions for the p+Pb reactions (Figure 4.45(a)) and for the p+Al reactions (Figure 4.45(b)). The detector efficiency correction has not changed the trend of the distributions but extended the tails of  $d\sigma/dN_{craw}$  distributions. The mean multiplicity after correction has increased by about 8%.

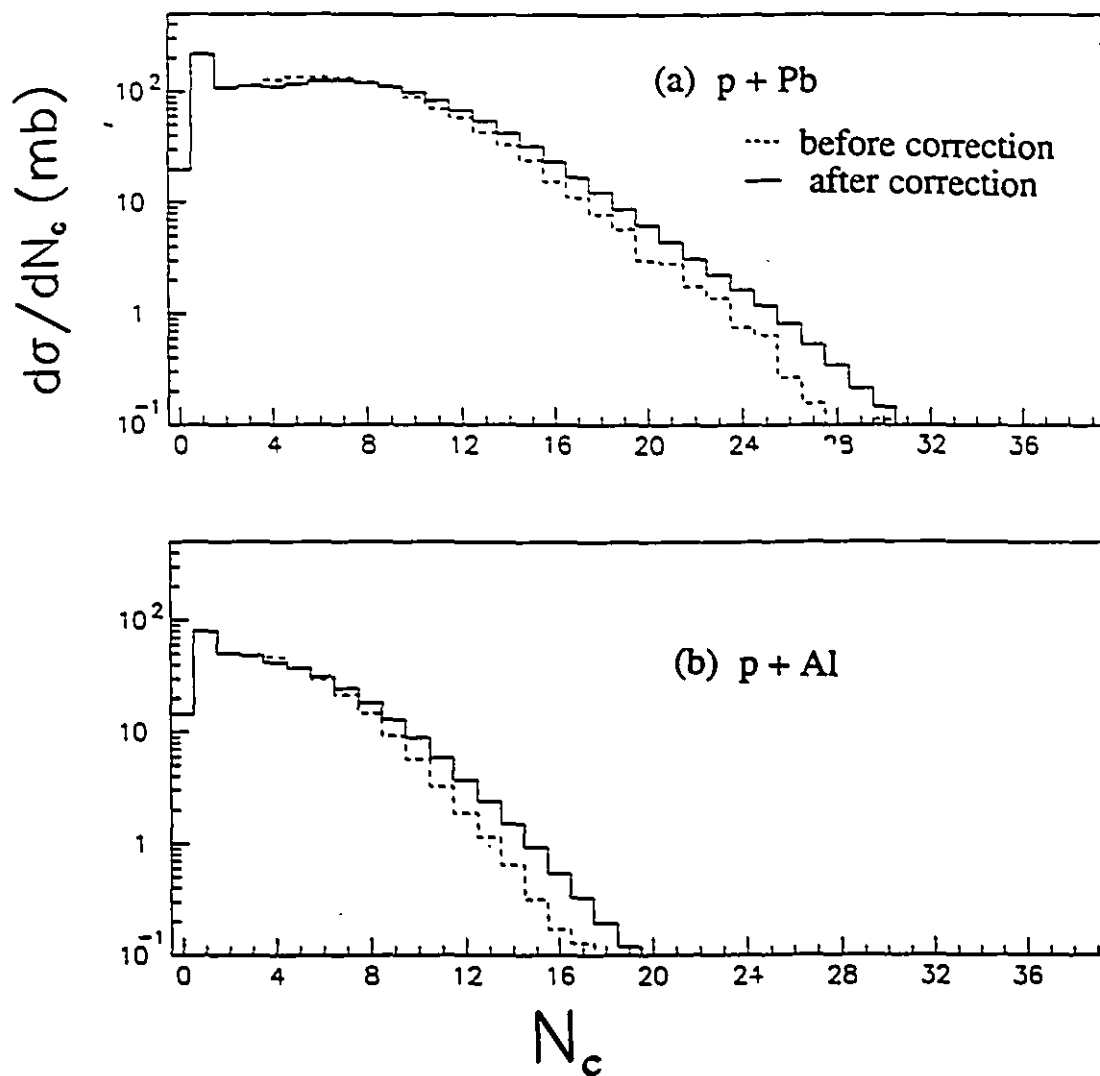


Figure 4.45: Effect of the multiplicity detector efficiency correction on  $d\sigma/dN_c$  distributions for (a) p+Pb and (b) p+Al. The dotted histograms correspond to distributions before corrections for efficiency and the solid histograms correspond to distributions after corrections.

Table 4.7: Multiplicity detector ring-by-ring average occupancy

Ring	Occupancy (Al target)	Occupancy (Pb target)
2	0.034	0.019
3	0.064	0.038
4	0.056	0.037
5	0.046	0.032
6	0.063	0.047
7	0.056	0.044
8	0.052	0.044
9	0.048	0.042
10	0.061	0.056
11	0.056	0.054
12	0.054	0.054
13	0.056	0.066
14	0.050	0.058
15	0.050	0.059
16	0.052	0.066
17	0.051	0.070
18	0.050	0.067
19	0.049	0.069
20	0.052	0.078

## Chapter 5

# DISCUSSIONS

In this chapter a more detailed account of the results is given with a particular emphasis on comparison of the experimental results with the predictions of three event generators: RQMD, HIJET and FRITIOF. The correlation between the transverse energy and multiplicity, the transverse energy per particle, and the scaling properties of the multiplicity distribution will also be discussed.

### 5.1 Transverse Energy Distributions

Figure 5.1 shows the transverse energy spectra for 14.6 GeV/c proton-nucleus reactions with lead and aluminum targets in the pseudorapidity range  $-2.3 < \eta < 1.0$  (the target calorimeter acceptance) for minimum bias multiplicity trigger (pretrigger). The common feature of the  $d\sigma/dE_T$  distributions in this backward acceptance is their monotonic decrease with  $E_T$ . Unlike what is observed in Si+Pb collisions at the same energy [BA90A], there are no flat plateau regions and steep fall-off regions in the transverse energy spectra. This may be an indication that there is more significant fluctuations in transverse energy production in proton-nucleus collisions than in heavy-ion collisions.

As seen in the figure, the transverse energy spectra at large angles show strong target mass dependence. At 1 mb/GeV the measured transverse energy goes up to 2.4 GeV for a lead target, compared to 1.6 GeV for an aluminum target. This effect may originate from the fact that the heavier Pb nuclei will lead to more collisions and rescattering,

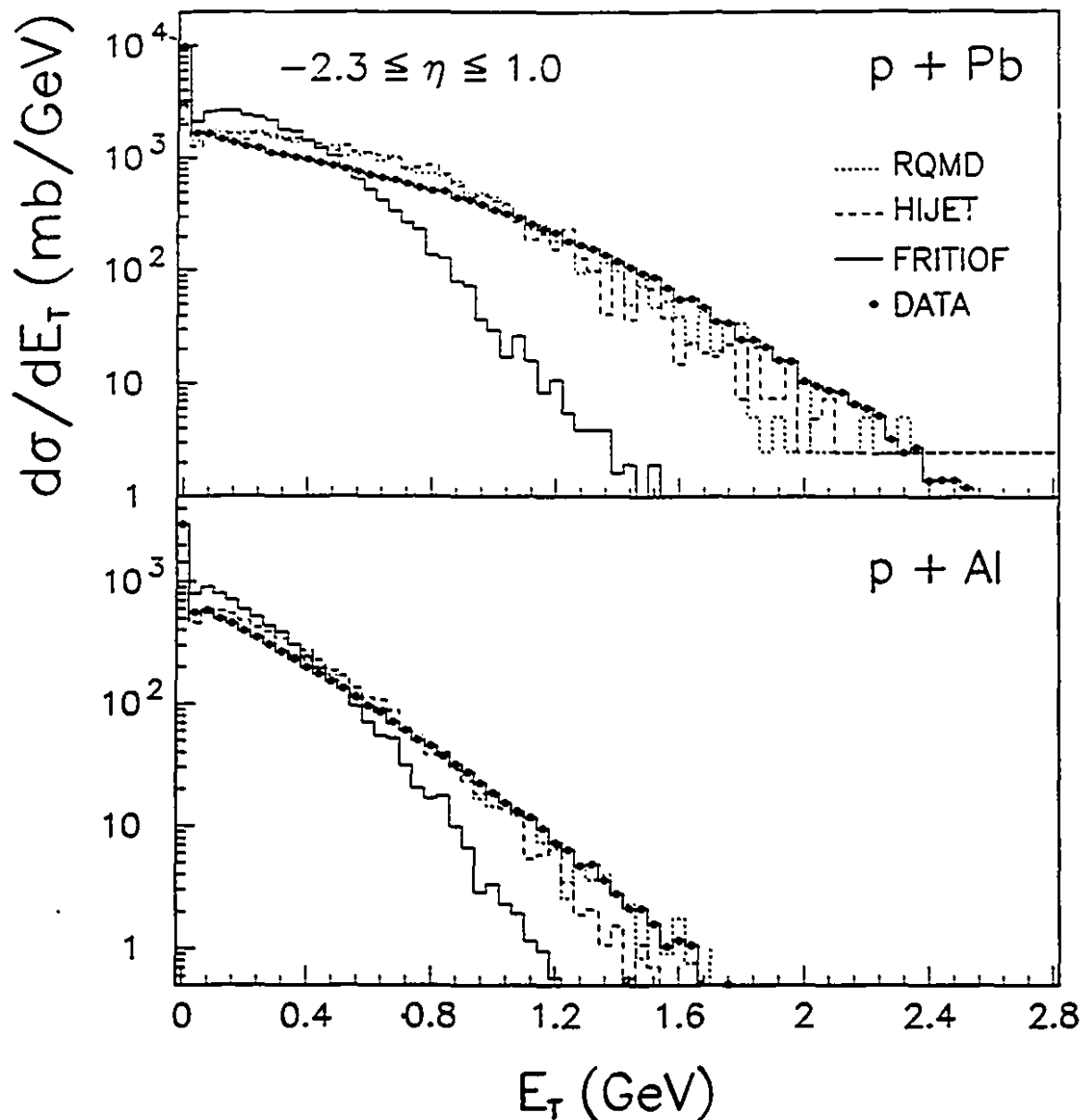


Figure 5.1: Comparison between measured and calculated transverse energy spectra for 14.6 GeV/c proton induced collisions in the target calorimeter acceptance: (top) for Pb target and (bottom) for Al target. Dots denote experimental data, and the histograms denote model predictions.

and thereby produce higher mean transverse energy at backward angles.

In Figure 5.1 the data are compared to the prediction of the various models. The observed target mass dependence is well predicted by all three theoretical models. The results from RQMD and HIJET are in good agreement with the experimental data although RQMD and HIJET have rather different pictures of underlying nucleon-nucleon collision process, while FRITIOF considerably underestimates the production of transverse energy for both lead and aluminum targets. On the other hand, FRITIOF and RQMD predict quite different distributions although they both are based on the string picture of nucleon interactions. The main difference in the models that could explain this result is the lack of rescattering in FRITIOF. Better evidence of this will be shown in the discussion of the  $dE_T/d\eta$  distribution.

Figure 5.2 shows transverse energy differential cross-section  $d\sigma/dE_T$  measured in the pseudo-rapidity range  $0.8 < \eta < 4.7$  (the participant calorimeter acceptance) for the level 1  $E_T$  trigger. The shapes of the distributions below the peak is mainly determined by the threshold on the  $E_T$  trigger. The distributions for both targets peak at the same  $E_T$  mainly due to the effect of the trigger threshold. Contrary to what was observed in the target calorimeter acceptance the distributions for both targets have very similar shapes. The E802 collaboration has reported results on the  $E_T$  distributions for p+Au and p+Al in the pseudo-rapidity range  $1.25 < \eta < 2.50$  [AB92]. They show that the  $d\sigma/dE_T$  ratio for p+Au and p+Al is approximately constant in their calorimeter acceptance. This is consistent with the results of Figure 5.2. However, this approximately constant ratio of differential cross-sections of  $E_T$  for different targets does not extend to the target calorimeter acceptance, as indicated in Figure 5.1. Such a result suggests different spatial distributions of transverse energy for the two targets.

The  $d\sigma/dE_T$  distributions from theoretical calculations are shown in dotted curves for RQMD, dashed curves for HIJET and solid curves for FRITIOF. The shapes of the  $d\sigma/dE_T$  predicted by the three models are very similar. However, while the results from RQMD and HIJET agrees well with data, FRITIOF somewhat overestimates the

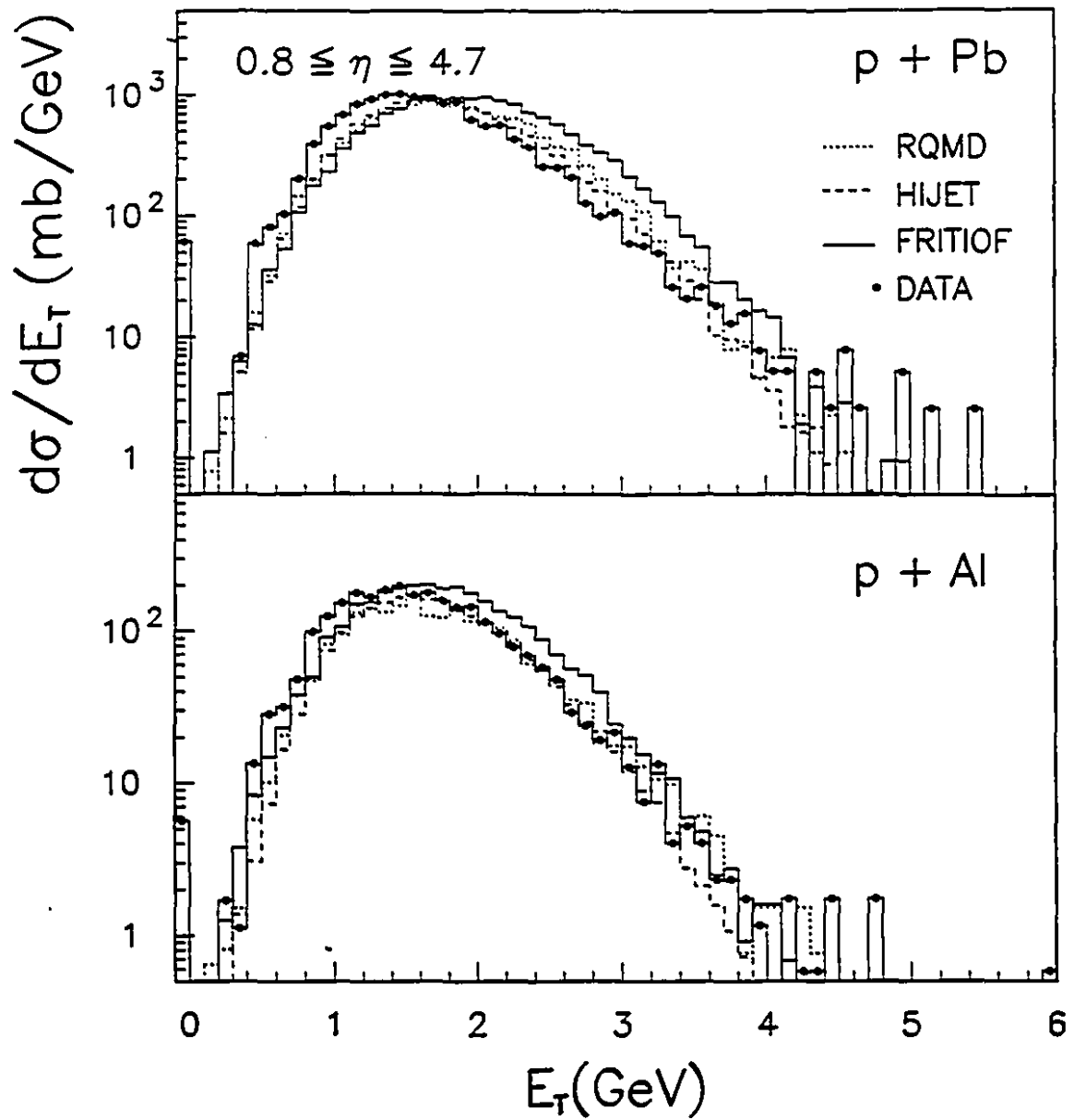


Figure 5.2: Comparison between measured and calculated transverse energy spectra for 14.6 GeV/c proton induced collisions in the participant calorimeter acceptance: (top) for Pb target and (bottom) for Al target.

produced transverse energy.

A better insight into the understanding of the transverse energy production is obtained from the  $dE_T/d\eta$  distribution. Figure 5.3 shows the quantity  $dE_T/d\eta$  per event as a function of the pseudorapidity  $\eta$  for proton-nucleus reactions with lead target (top figure) and aluminum target (bottom figure) at 14.6 GeV/c. The data have been fully corrected for detector efficiency as discussed in Chapter 4. They are shown as open circles for the target calorimeter acceptance and as closed circles for the participant calorimeter acceptance. The data points in the region  $0.8 < \eta < 1.0$  where the two calorimeters are overlapping have relatively larger errors since they are at the edge of the acceptance of each detector.

The measured  $dE_T/d\eta$  distributions for both lead and aluminum targets have roughly a gaussian shape with a width  $\sigma \approx 0.9$  unit of pseudorapidity. Both distributions peak backward of the nucleon-nucleon center-of-mass rapidity ( $\eta = 1.7$ ). The lead target data shows a further shift backward by about one half unit of pseudorapidity relative to the aluminum data, confirming the importance of secondary interactions in heavy target. This target mass dependence of the pseudorapidity distribution is consistent with results of the E802 collaboration [AB92]. A similar shift is observed in the  $dE_T/d\eta$  distributions for events with high  $E_T$ . The lead-glass calorimeter acceptance ( $1.25 < \eta < 2.50$ ) of the E802 set-up does not cover the peak of the  $dE_T/d\eta$  distribution for low  $E_T$  events. These events correspond to a large fraction of the reaction cross-section and thus a more quantitative comparison on the evolution of  $dE_T/d\eta$  with target is not possible.

The pseudorapidity distributions of transverse energy predicted by RQMD, HIJET and FRITIOF are also plotted in Figure 5.3. The calculations from RQMD and HIJET describe very well the experimental data, while FRITIOF predicted distributions are peaked too far forward. In fact, FRITIOF produces distributions for both targets peaked close to the nucleon-nucleon center-of-mass rapidity due to the lack of rescattering in this model. The overly forward peaked distributions obtained with FRITIOF

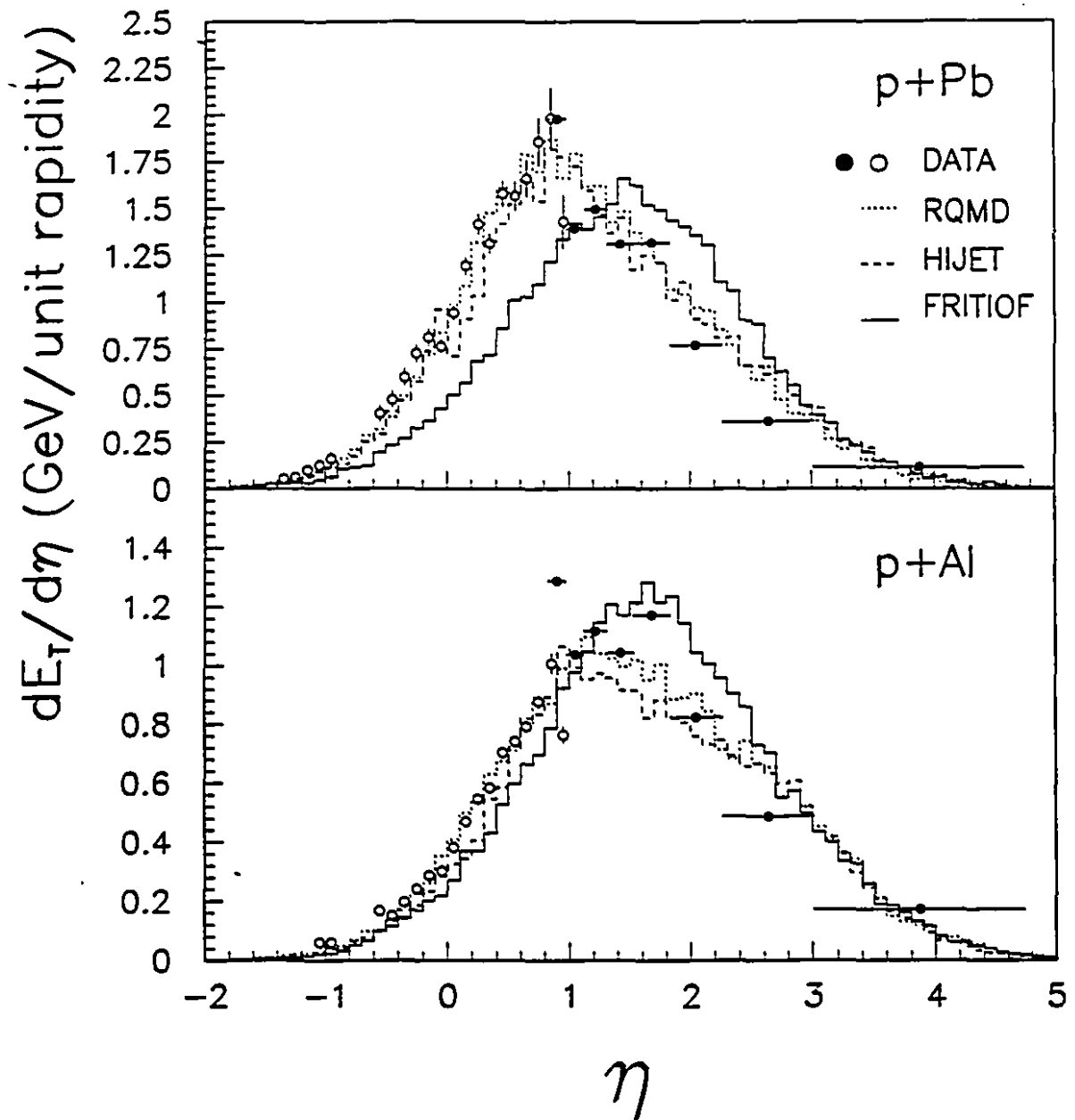


Figure 5.3: Comparison between measured and calculated pseudorapidity distributions of transverse energy for 14.6 GeV/c proton induced collisions: (top) for Pb target and (bottom) for Al target.

explains the observed underestimate of the transverse energy production in the backward region (figure 5.1), and its related overestimate in the forward region (figure 5.2). Our data demonstrate clearly that the target mass dependence of  $d\sigma/dE_T$  depends strongly on the pseudorapidity range over which it is measured, and thus the fact that models describe  $d\sigma/dE_T$  in one region may not be a good test of the model. Our present result shows the importance of obtaining the full  $E_T$  distribution  $dE_T/d\eta$ .

## 5.2 Charged Particle Multiplicity Distributions

Figure 5.4 shows the charged particle multiplicity distributions  $d\sigma/dN_c$  for lead and aluminum targets for the lowest threshold multiplicity pretrigger. The data shows strong target dependence. For the lead target, the charged particle multiplicity spectrum extends up to 35 at differential cross-section of 0.03 mb per charged particle, compared to a maximum multiplicity of about 22 for the aluminum target. As expected, more particles are observed for the lead target, since on average, the incoming protons will have more collisions in a heavier target, and the collision products will also have a larger probability to reinteract.

Predictions by the three models are also shown in Figure 5.4. The calculated multiplicity distribution shown in the figure are obtained by tracking the generated events using GEANT. It includes the detector geometry and, in particular, electrons and positrons originating from  $\gamma$  conversion in the target and the effect of multiple hits on the detector. Figure 5.5 shows the effect of  $\gamma$  conversion from  $\pi^0$  decay in the target on the charged particle multiplicity distribution. The dotted line is the calculated multiplicity of charged particles in the detector acceptance, while the solid line is the distribution obtained after tracking. Because of the large target thickness it is observed that  $\gamma$  ray conversion to electron-positron pairs increases the mean charged multiplicity by one unit for proton on Pb target reactions, while it has negligible effects on the data obtained with the Al target.

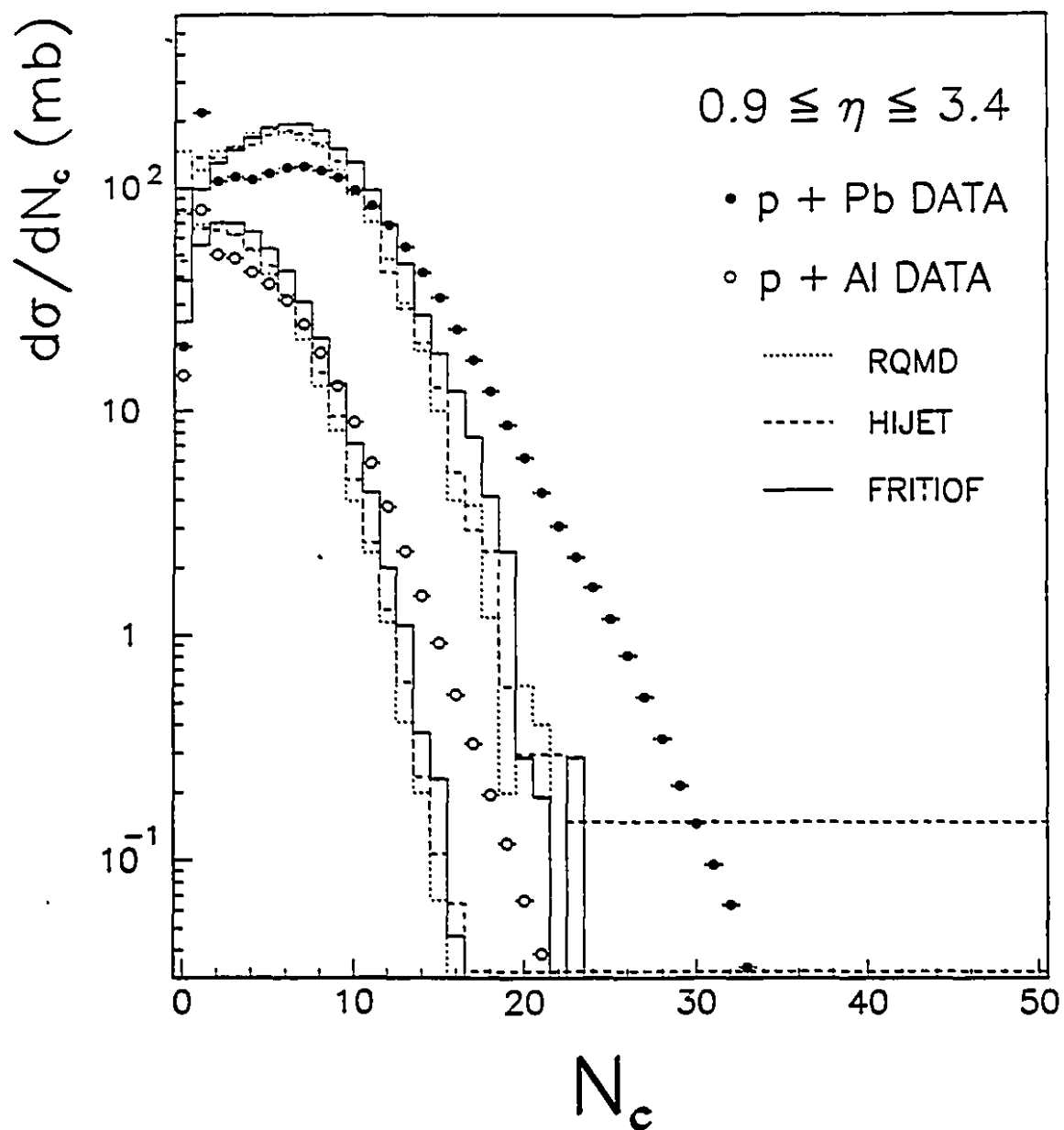


Figure 5.4: Comparison between measured and calculated charged particle multiplicity spectra for 14.6 GeV/c proton induced collisions for Pb target (closed dots) and for Al target (open dots) with models: RQMD (dotted lines), HIJET (dashed lines) and FRITIOF (solid lines)

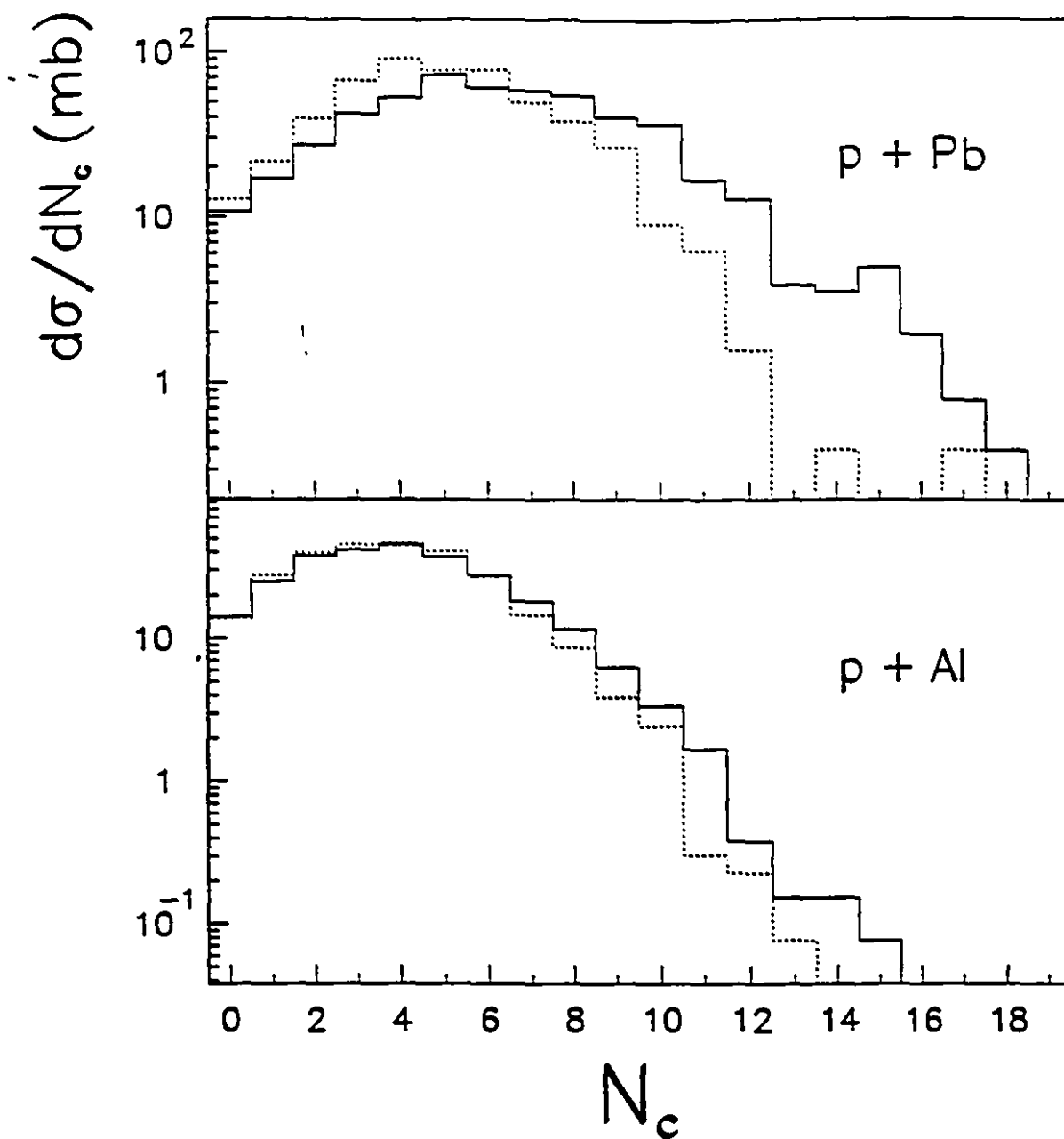


Figure 5.5: Effect of  $\pi^0$  conversion on the charged particle multiplicity distribution. The dotted line shows the distribution before  $\pi^0$  conversion and the solid line shows the distribution after  $\pi^0$  conversion.

All three models, RQMD (dotted curves), HIJET (dashed curves) and FRITIOF (solid curves), give very similar descriptions of the  $d\sigma/dN_c$  distribution. They predict the target dependence of the charged multiplicity very well. But the models underestimate systematically the production of charged particle multiplicity in the high multiplicity region for both targets. It should be noted here that the multiplicity detector has a very low threshold and is sensitive to charged particle of all energy including low energy target fragments and evaporated particles. This could be one of the source of the observed discrepancy at high multiplicity. More detailed information on the difference between the models can be obtained from the spatial distributions of charged particle multiplicity .

Figure 5.6 shows the pseudorapidity distributions of charged particle multiplicity  $dN_c/d\eta$  for lead and aluminum targets. A very important increase in  $dN_c/d\eta$  is observed for the Pb target at low pseudorapidity near the target region. Note that the acceptance of the multiplicity detector does not cover the maximum of the distribution. In the very forward region, near beam rapidity region ( $\eta = 3.4$ ), charged particle multiplicity distributions for both targets converge, showing independence of target mass. These experimental data are well reproduced by RQMD and HIJET, while FRITIOF completely fails. FRITIOF again predicts too forward peaked distributions for both targets.

Figure 5.7 shows the pseudorapidity distributions of charged particle multiplicity for various charged multiplicity windows for proton on the Pb target (top) and for proton on the Al target (bottom). All the distributions for different multiplicity intervals converges near the beam rapidity. The changes of charged multiplicity mainly happens at low rapidity, indicating that high multiplicity is mainly caused by rescattering in the target.

To better illustrate the target effect on the pseudorapidity distributions of charged particle multiplicity, the pseudorapidity distributions of charged particle multiplicity for the same multiplicity window (5 - 7) for the lead and aluminum targets are compared

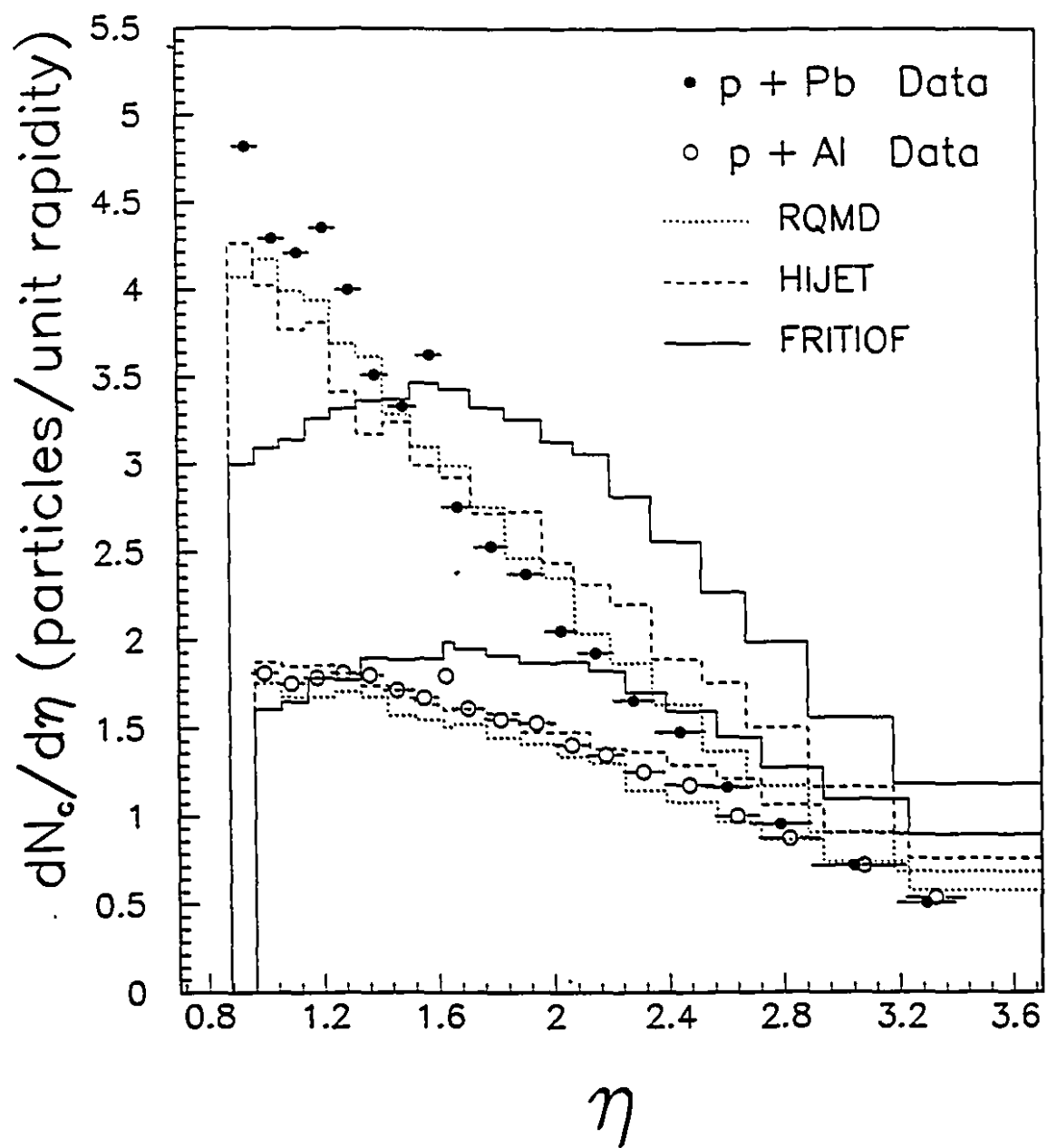


Figure 5.6: Comparison between measured and calculated pseudorapidity distributions of charged particle multiplicity for 14.6 GeV/c p+Pb (solid dots) and p+Al (open dots) reactions.

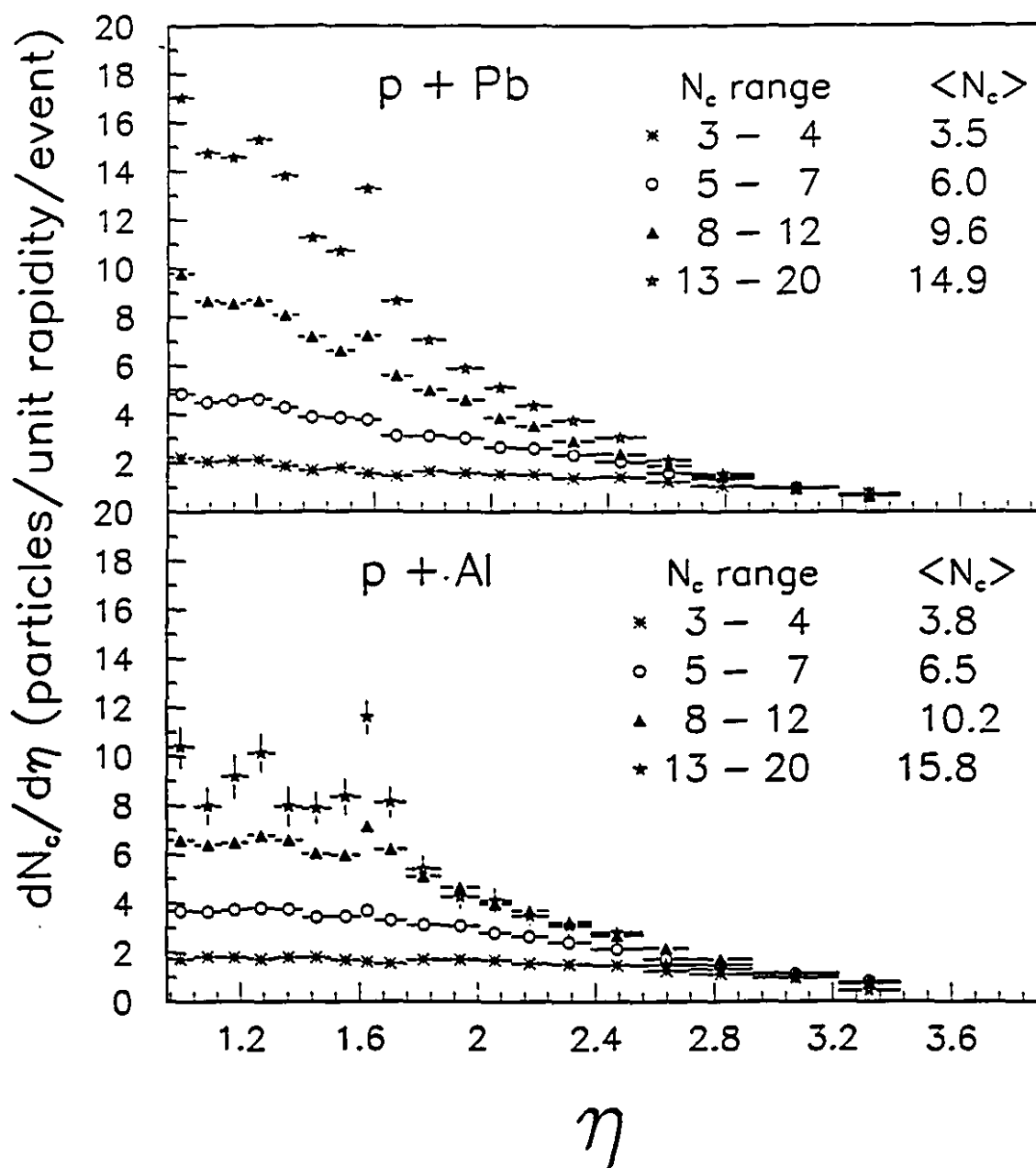


Figure 5.7: Upper part: pseudorapidity distributions of charged particle multiplicity  $dN_c/d\eta$  for p+Pb reaction for various cuts in the total multiplicity. Lower part: same distributions for p+Al reaction.

in Figure 5.8. For the same number of charged particles, the pseudorapidity distributions for the two target are very similar in shape. The main difference appears at low pseudorapidity. A similar behavior is observed for other slices in total multiplicity.

### 5.3 Correlation Between $E_T$ and $N_c$

As the participant calorimeter and the charged particle multiplicity detector cover approximately the same pseudorapidity acceptance, the data measured with these two detectors can be used to study correlation between these two global variables.

It has been observed that in heavy-ion reactions charged multiplicity distributions are strongly correlated to the transverse energy [SI91]. Figure 5.9(a) shows correlations between transverse energy and charged particle multiplicity for Si+Pb at 14.6 GeV/c per nucleon. The heavy-ion data shows a linear relation between these two observables. Although these data have not been corrected for the detector efficiency and the background interactions which contribute less than 10% of the events, the general trend of the correlation is clear. Figure 5.9(b) shows the same correlation between the transverse energy and the charged particle multiplicity for proton on lead at 14.6 GeV/c. Although multiplicity shows somewhat an increase with  $E_T$ , the relationship between these two observables is not evident.

Since three different  $E_T$  triggers from the participant calorimeter have been applied to the charged multiplicity measurement, we can plot multiplicity for different  $E_T$  triggers. However, the online  $E_T$  triggers are not perfect cuts in the transverse energy measured in the participant calorimeter (see Chapter 4). Therefore, we have applied offline sharp  $E_T$  cuts to examine the charged multiplicity spectra for various  $E_T$  windows.

To increase the number of data points without introducing big uncertainties in the  $E_T$  cut, the  $E_T$  window width is selected to be comparable to the calorimeter energy resolution. Figure 5.10 shows the correlation between  $E_T$  of generated events before and after tracking in the acceptance of the participant calorimeter. The energy spread

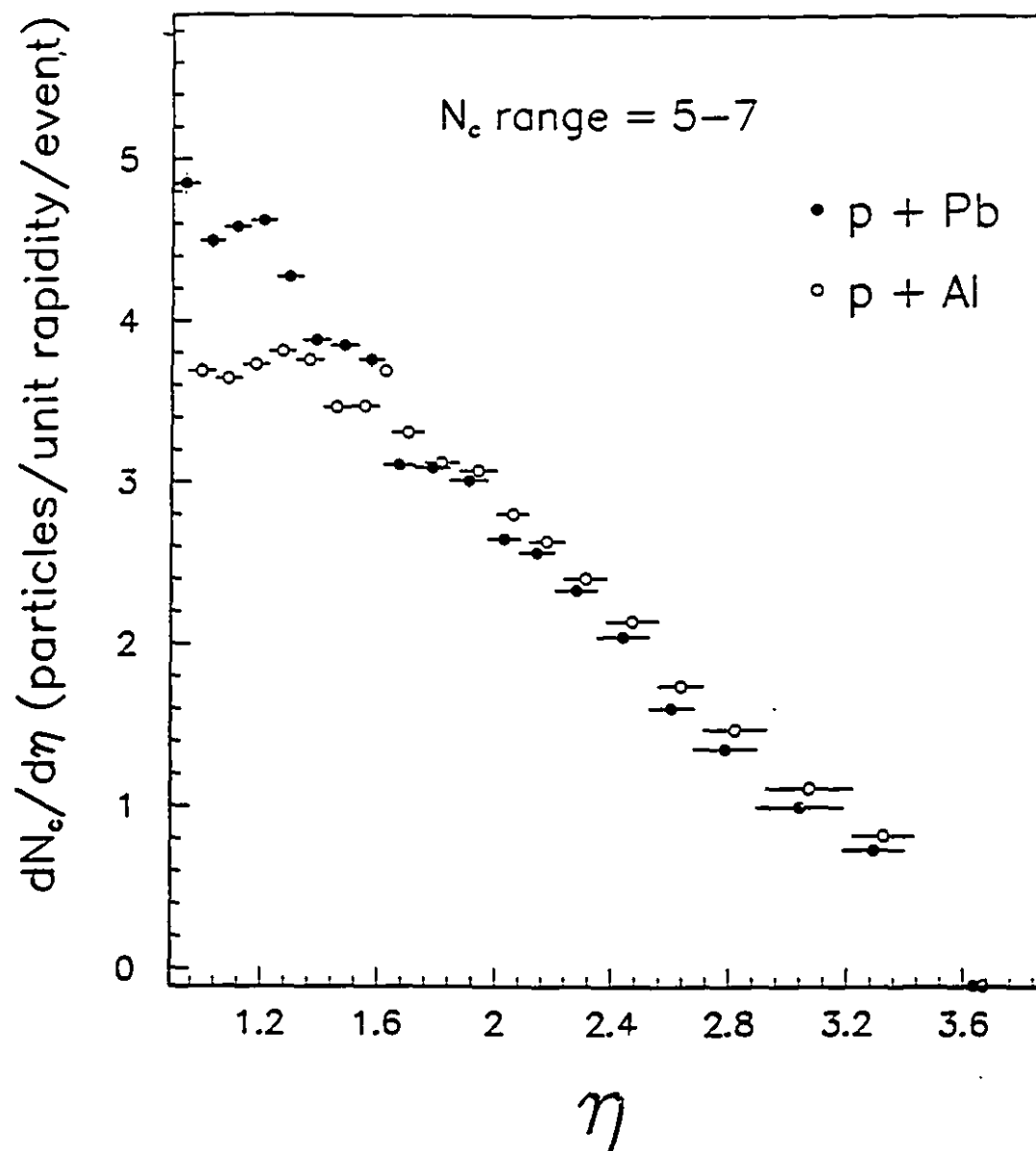


Figure 5.8: Comparison of pseudorapidity distributions of charged particle multiplicity  $dN_c/d\eta$  for p+Pb reaction (solid dots) and for p+Al reaction (open dots) for the same multiplicity window ( $N_c = 5 - 7$ ).

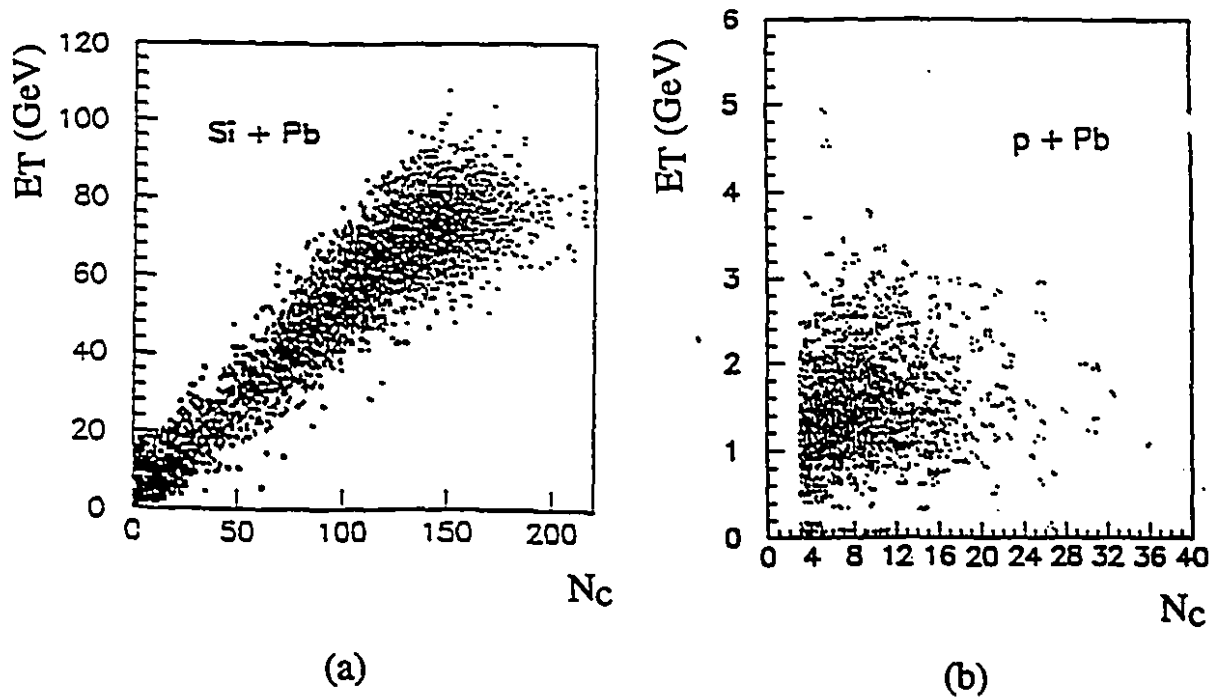


Figure 5.9: Correlations between transverse energy measured in the participant calorimeter and charged particle multiplicity measured in the multiplicity detector for (a) Si+Pb reactions 14.6 GeV/c per nucleon [SI91] and (b) p+Pb reactions at 14.6 GeV/c.

due to calorimeter resolution is about 40% of the incident energy.

Figure 5.11 shows charged particle multiplicity distributions  $d\sigma/dN_c$  for various transverse energy windows. All distributions are similar in shape, except for the distribution corresponding to the lowest  $E_T$  cut where the multiplicity peaks at the trigger threshold of the multiplicity detector. The mean multiplicity of distributions are observed to increase very slowly with the transverse energy. A more quantitative description of this feature is shown in Figure 5.12. The upper part of the figure shows the mean charged particle multiplicity versus the average measured  $E_T$ . In contrast with what is observed in Si+Pb data, the present result shows that the mean charged multiplicity increase only slightly with the transverse energy and this increase tends to saturate at high  $E_T$ . The lower part of Figure 5.12 shows the width (*RMS*) of the multiplicity distribution for the various transverse energy windows. The increase of multiplicity with  $E_T$  is much smaller than the width of the multiplicity distribution, which confirms the very weak correlation between the transverse energy and the charged particle multiplicity in the data. As a comparison, the predictions from RQMD are also shown. RQMD reproduces quite well the trend observed in the data. However, it predicts a somewhat slower rise in mean multiplicity, and a narrower width of multiplicity distributions.

#### 5.4 Transverse Energy per Particle

The transverse energy per particle can be obtained by comparison of the pseudorapidity distribution of transverse energy with the pseudorapidity distribution of particle multiplicity. Figure 5.13 shows the pseudorapidity distributions of  $E_t$  per charged particle in the forward acceptance of the participant calorimeter and the multiplicity detector. The distributions are obtained from the ratio of  $dE_T/d\eta$  (Figure 5.3) to  $dN_c/d\eta$  (Figure 5.6). For this figure the  $dN_c/d\eta$  data have been rebinned according to the  $\eta$  binning of the participant calorimeter. The  $E_t$  per charged particle is observed to be relatively constant over this pseudorapidity region. An average of 0.4 GeV of

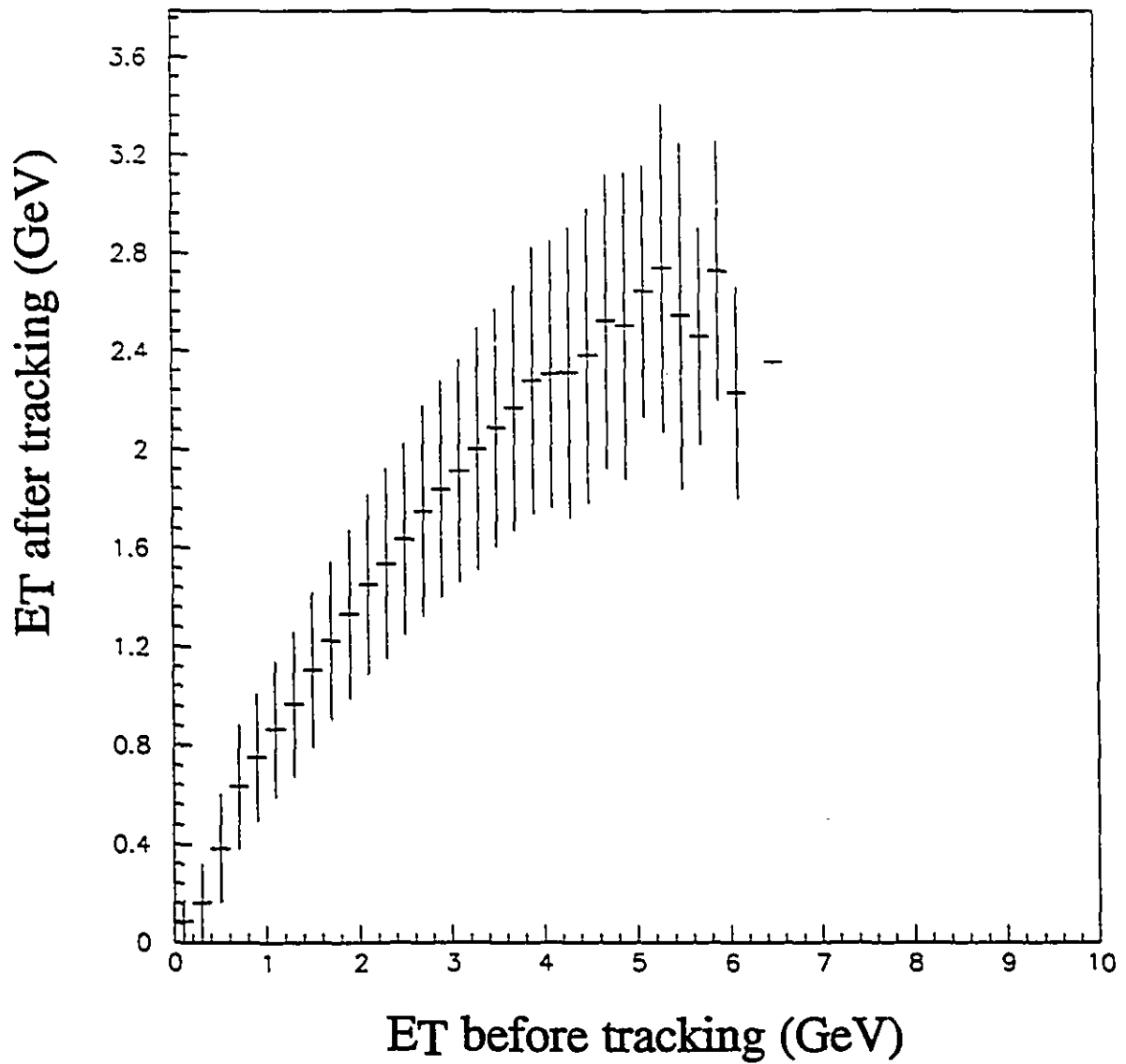


Figure 5.10: Correlation between  $E_T$  before tracking and the  $E_T$  after tracking in the participant calorimeter. The error bars indicate the  $E_T$  magnitude of the event-to-event fluctuations.

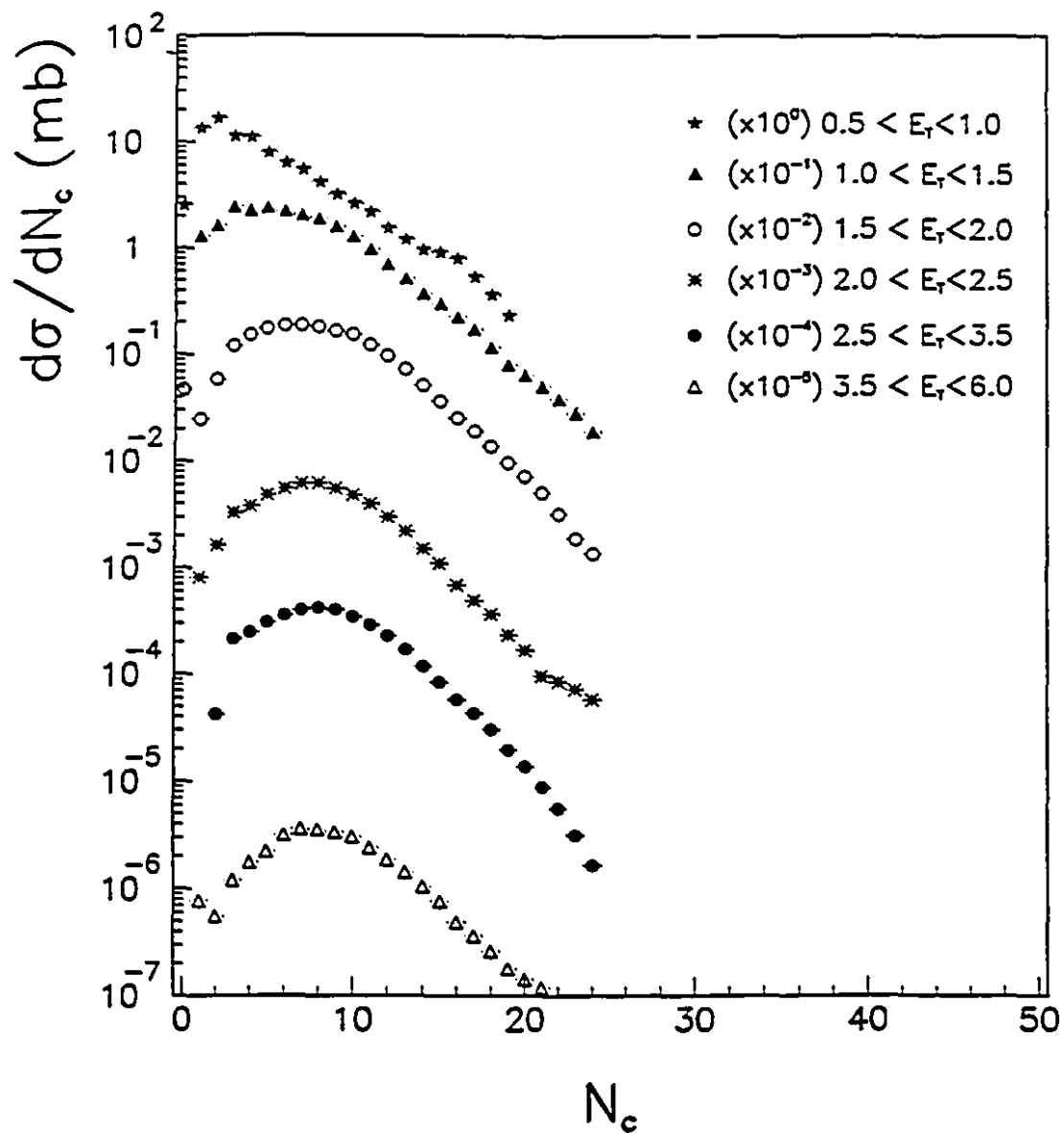


Figure 5.11: Charged particle multiplicity production for various cuts in the transverse energy measured in the participant calorimeter for 14.6 GeV/c p+Pb reactions.

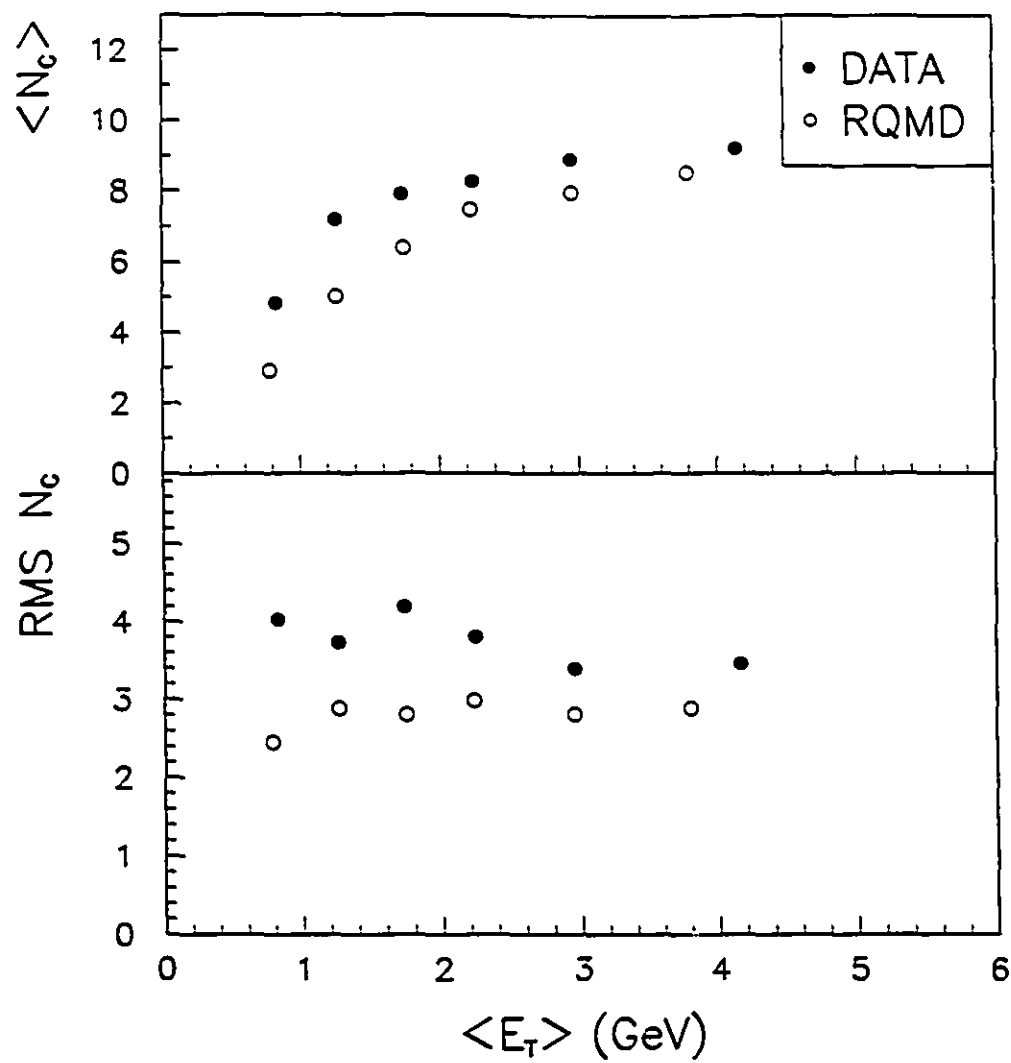


Figure 5.12: Comparison of the mean value and variance of the charged particle multiplicity distributions as a function of the transverse energy in the participant calorimeter for the Pb target (solid dots) with the results from RQMD (open dots).

transverse energy per charged particle is produced for proton on lead, compared to 0.6 GeV for Al, indicating that the available energy is distributed over more nucleons in the heavier target nuclei.

The three model calculations shown in the figure reproduce very well the near flat distributions and the target dependence. For the Al data, HIJET and FRITIOF slightly underestimate the produced energy. Even though FRITIOF predicts too much forward peaked distributions of both  $E_T$  and particle multiplicity, the ratio of the two observables describe the the data quite well. This shows that  $E_T$  per particle is not a very stringent test for models.

In the backward region, the particle distribution is determined by the energy cluster distribution measured in the target calorimeter. The detector response to clusters in the target calorimeter acceptance is corrected by comparison of the distributions of (before and after tracking) generated events using GEANT. Our simulation shows that the efficiency of the target calorimeter varies considerably with the type of particles. Figure 5.14 presents detection efficiency for (a) protons, (b) neutrons, (c)  $\pi^+$  and  $\pi^-$ , (d)  $\pi^0$  and  $\gamma$  in the acceptance of the side wall of the target calorimeter. There is about 70% probability that a charged hadron emitted in the  $\eta$  acceptance of the target calorimeter produces a cluster, while there is only about 10% probability for a neutron to produce a cluster. Because of the sensitivity of this calorimeter to photons, on average more than one cluster is observed by emitted  $\pi^0$ .

The ratio of  $E_T$  to the number of clusters as a function of pseudorapidity is shown in Figure 5.15. The  $E_T$  per cluster in the plateau region is about 200 MeV for the Pb target and 250 MeV for the Al target. Predictions from the three models are shown by different histograms in the figure. All models describe very well the trend of the distributions, but FRITIOF slightly underestimate the  $E_T$  per cluster.

Since the clusters measured in the target calorimeter include the contribution from both charged and uncharged particles, one cannot compare the value of this  $E_T$  per cluster with that of  $E_T$  per charged particle in the forward acceptance. However, for

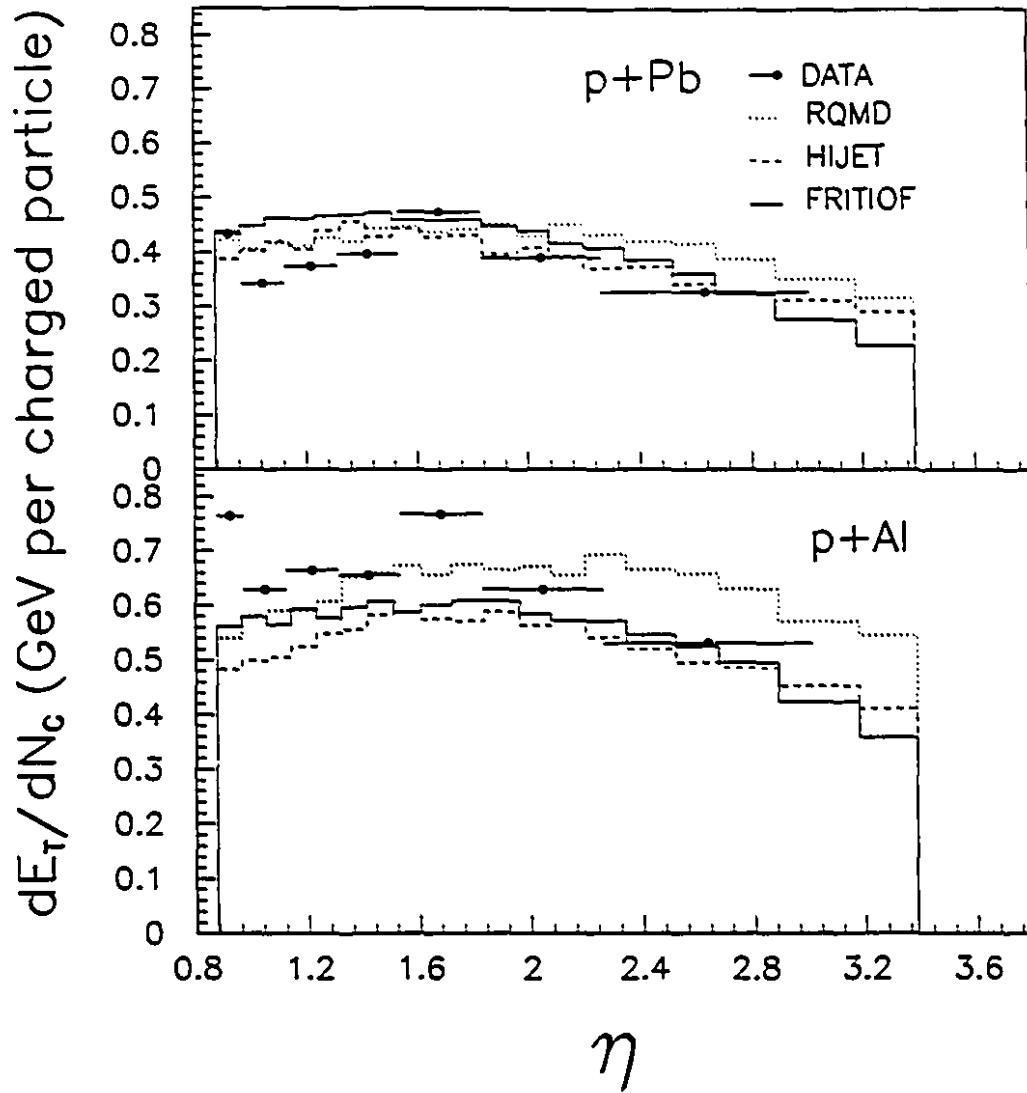


Figure 5.13: Transverse energy per charged particle for the p+Pb (upper part) and p+Al (lower part) reactions.

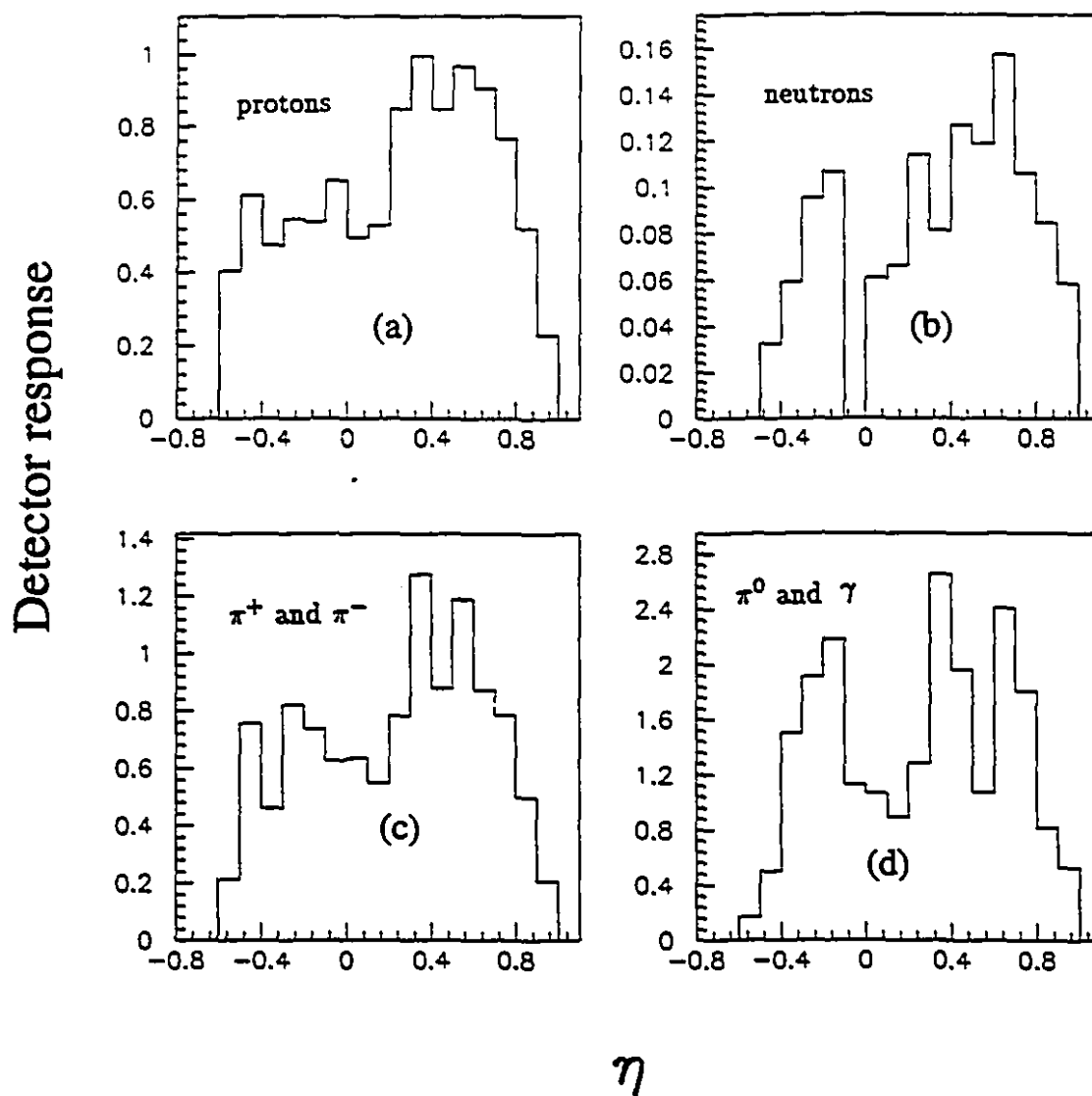


Figure 5.14: Detection efficiency for (a) protons, (b) neutrons, (c)  $\pi^+$  and  $\pi^-$ , (d)  $\pi^0$  and  $\gamma$  in the acceptance of the side wall of the target calorimeter.

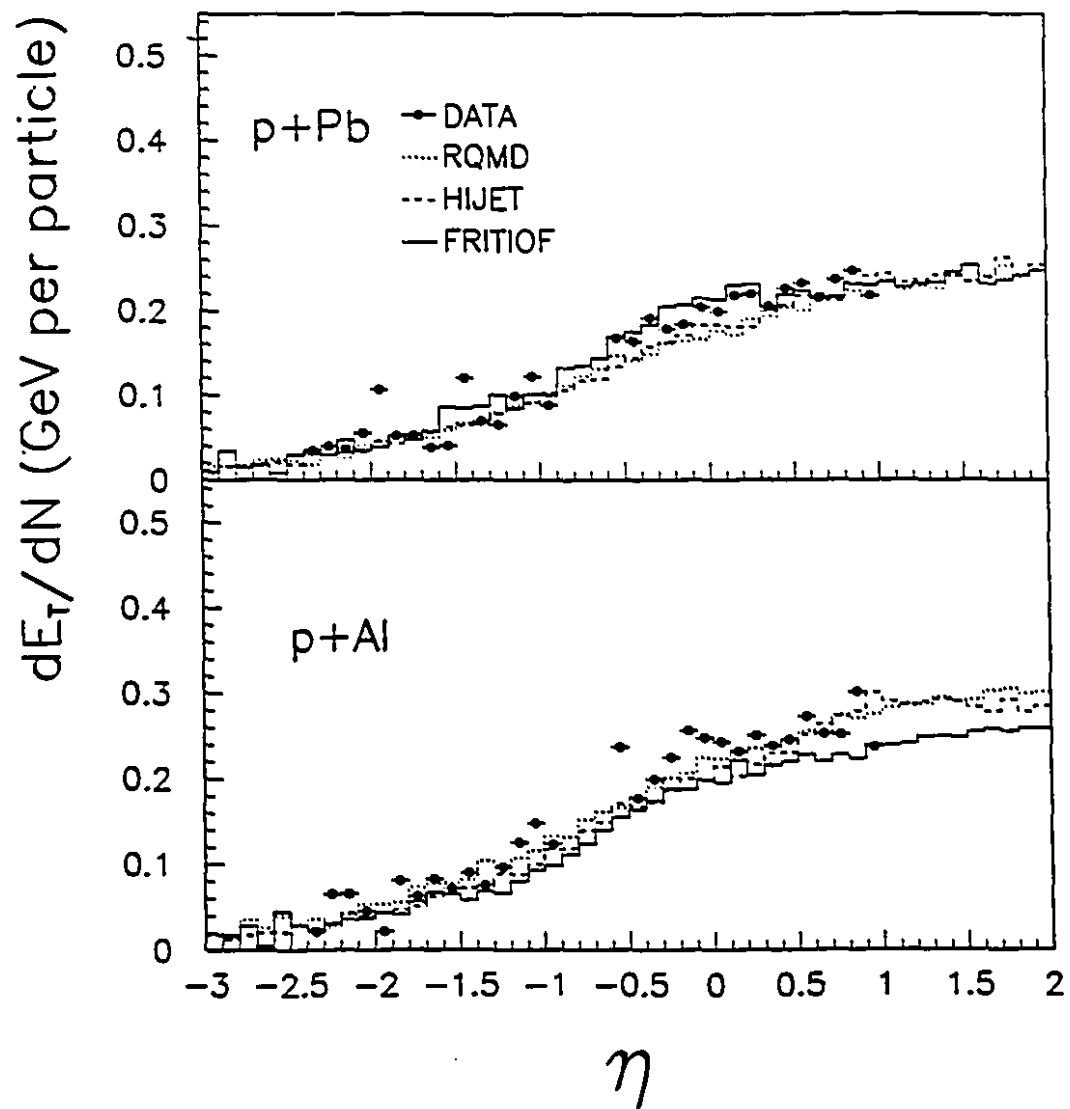


Figure 5.15: Transverse energy per cluster for p+Pb (upper part) and p+Al (lower part) over the pseudorapidity acceptance of the target calorimeter. The histograms are predictions of various event generators.

each target the shape of the two distributions (Figure 5.13 and Figure 5.15) match smoothly in the overlapping pseudorapidity. The near flat distribution over the participant calorimeter acceptance extends down to near  $\eta = 0$  in the target calorimeter acceptance, and then the energy per cluster becomes much smaller as we move to backward angle, reflecting the quick decrease of the available energy. This trend of the distribution is well reproduced by all three calculations.

Figure 5.16 shows comparison of  $E_T$  per charged particle for p+Pb and Si+Pb reactions at the same beam energy per nucleon. The data for Si+Pb are taken from refs. [BA92B] and [ZH93] and correspond to the most central 7% of the events. The two distributions are relatively constant against pseudorapidity and are similar in shape. The average transverse energy per charged particle for Si+Pb is about 0.45 GeV, 10 to 20% higher than what is observed for p+Pb data.

This projectile dependence is also seen in the  $P_T$  data obtained by the E802 Collaboration [CH93, AB91, ZA92]. The particle invariant cross-section plotted as a function of the transverse mass ( $m_T$ ) at fixed rapidity are well described by an exponential. Over the pseudorapidity range  $\eta = 1.2$  to 1.4, the value of the inverse slope parameter (Boltzmann temperature) for charged pions increases from 154 MeV for p+Au collisions to 163 MeV for Si+Au central collisions. For protons the observed increase is from 150 MeV to 220 MeV. The overall trend of the change in the inverse slope parameter for charged pions and protons is consistent with the present result.

## 5.5 Scaling of Charged Particle Multiplicity

It was predicted by Koba, Nielsen and Olesen [KO72] that in high energy hadron-hadron collisions multiplicity distributions  $P(N_c)$  obey the scaling law

$$\langle N_c \rangle P(N_c) = f(N_c / \langle N_c \rangle), \quad (5.1)$$

where  $\langle N_c \rangle$  is mean multiplicity of charged particles and  $f$  is an energy independent function. This scaling law is often referred to as KNO scaling.

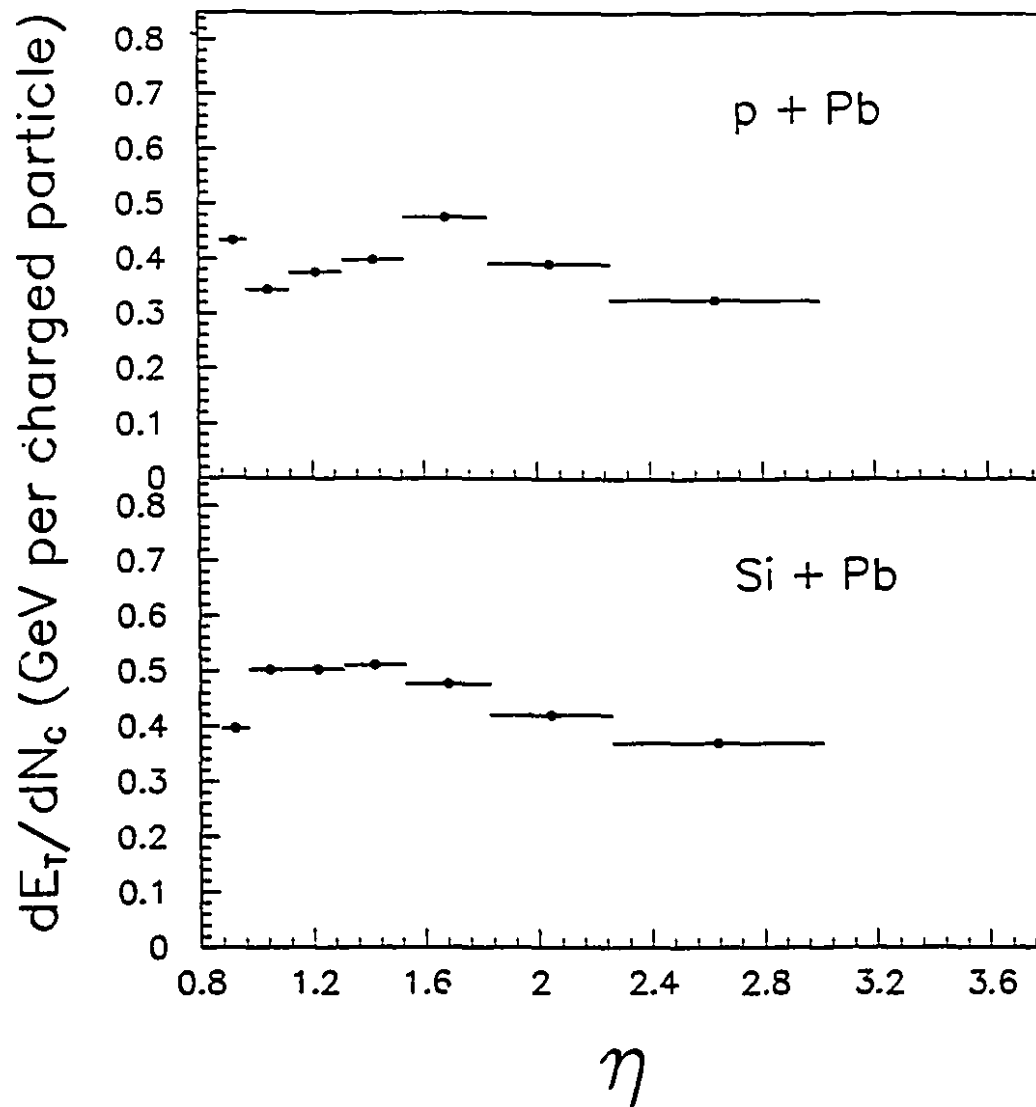


Figure 5.16: Transverse energy per particle for the p+Pb (upper part) and Si+Pb (lower part) reactions. The data for Si+Pb are obtained from refs. [BA92B] and [ZH93].

It has been reported in ref. [BA92B] that the multiplicity distributions of charged particles for central Si induced collisions show scaling properties similar to KNO scaling. Figure 5.17 shows charged particle multiplicity data from several pseudorapidity intervals for three targets as a function of KNO variable  $N_c / \langle N_c \rangle$ . It was observed that multiplicity distributions at various pseudorapidity intervals are very similar in shape, approximately Gaussian with a slight tail, and have similar fractional width (i.e.  $\sigma / \langle N_c \rangle$ ) except near beam rapidity where the distributions are much broader for all three targets.

In Figure 5.18 the relative distributions for the same pseudorapidity interval are shown for the three targets. The Cu data and Al data are scaled up to the Pb data for comparison. It is observed that the scaled multiplicity distributions are very similar for the different targets and the widths of the distributions are comparable.

To try to better understand the origin of this scaling in the Si-nucleus data, we have performed a similar analysis for the p+Pb reaction. As shown in Figure 5.19 the charged multiplicity distributions produced in the p+Pb collisions also seem to have this scaling property. However, in contrast to what is observed in heavy-ion induced reactions, the distributions for the p+Pb are not Gaussian but peak at  $N_c=0$  and are closer to binomial or Poisson distributions, indicating the characteristic of low multiplicity behaviour.

Table 5.1: Relative width  $\sigma / \langle N_c \rangle$  of the multiplicity distribution for p+Pb. The third column gives average number of particles in the  $\eta$  range considered. The last column gives the expected statistical variance for  $N_c$ .

$\eta$ Range	$\sigma / \langle N_c \rangle$	$N_c$	$1/\sqrt{N_c}$
0.88-1.23	1.05	1.57	0.80
1.23-1.61	1.04	1.38	0.85
1.61-2.08	1.02	1.13	0.94
2.08-2.67	1.00	0.92	1.04
2.67-3.39	1.17	0.52	1.39
Average	1.05	1.10	1.00

In order to better quantify the shape of the measured distributions, Table 5.1 presents

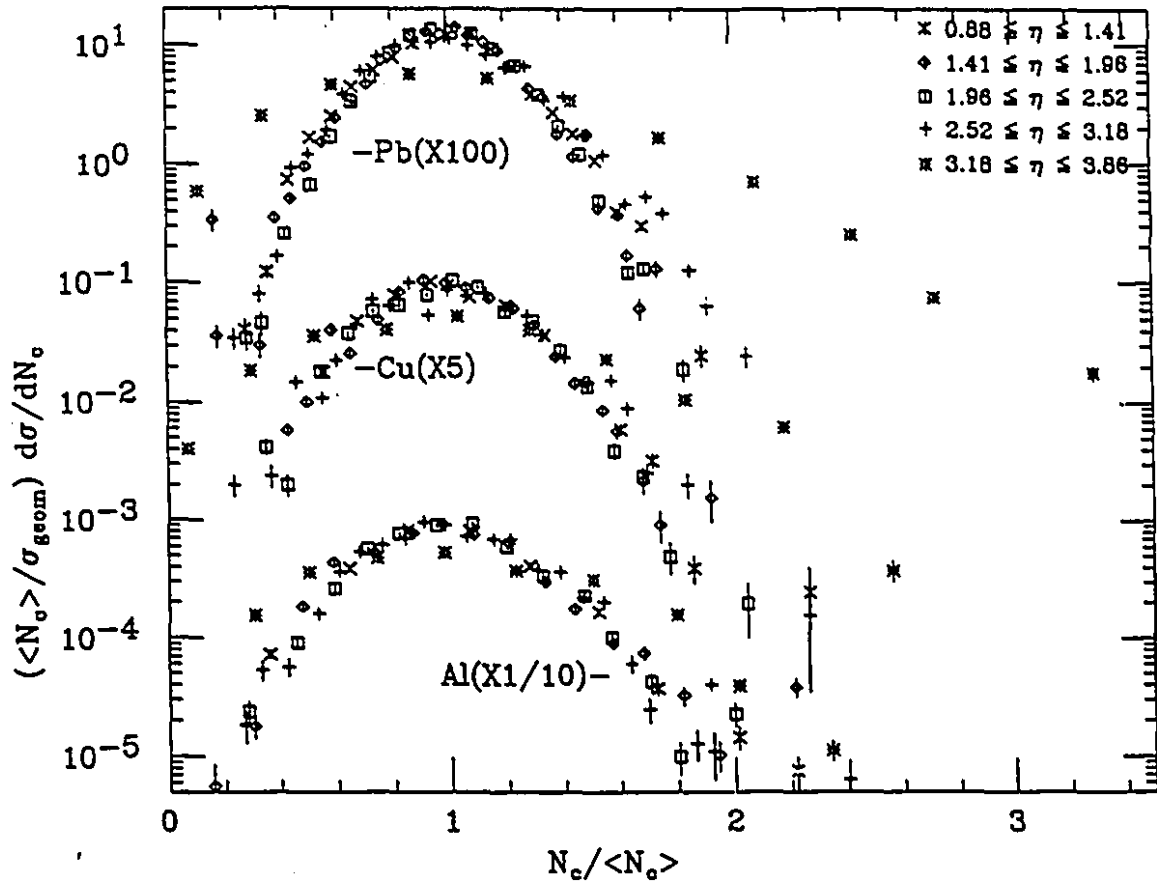


Figure 5.17: Observed multiplicity distributions, plotted in KNO variables for Si induced reactions at various pseudorapidity intervals[BA92B].

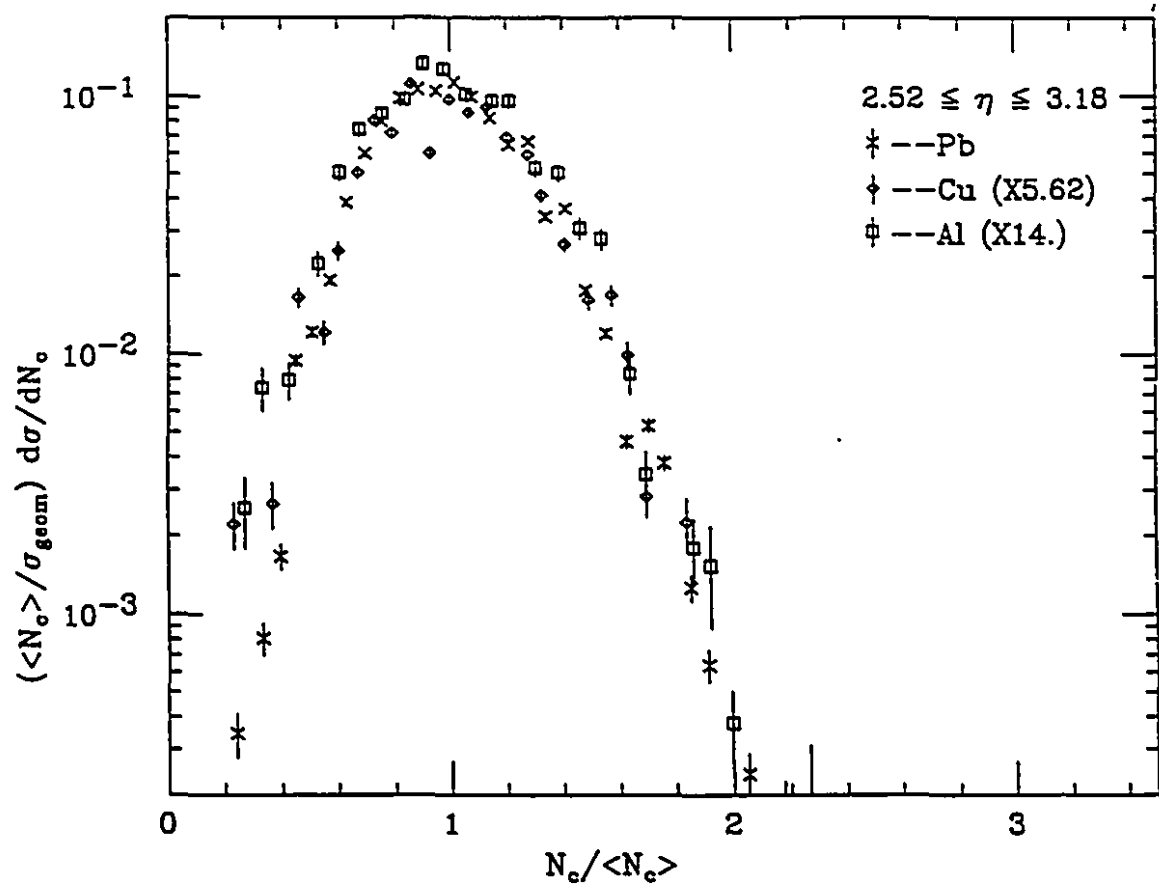


Figure 5.18: Relative multiplicity distributions, plotted in KNO variable for reactions from Si on the three targets at the same pseudorapidity interval [BA92B].

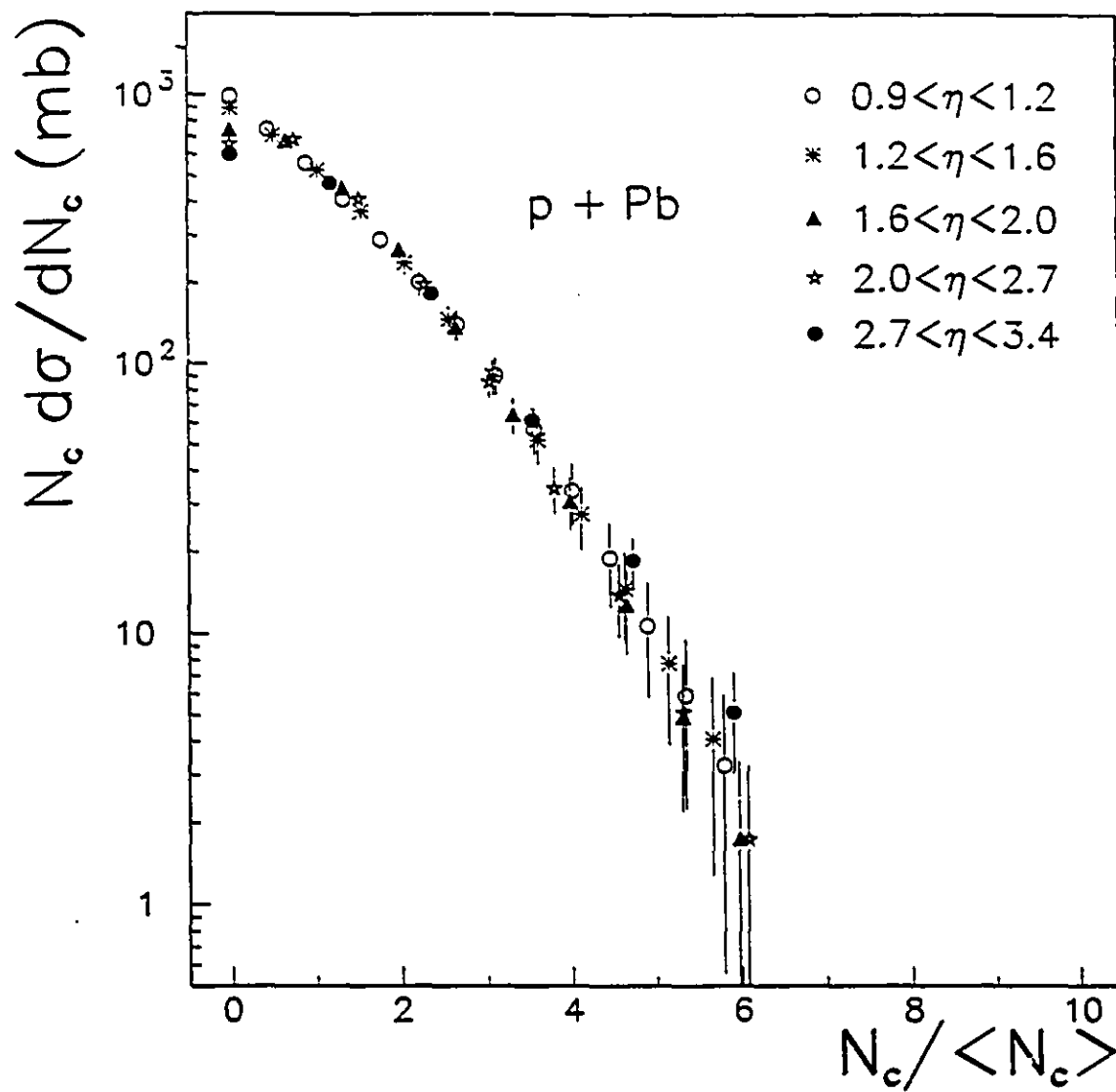


Figure 5.19: Experimental multiplicity distribution plotted in KNO variable for the p+Pb reaction at various pseudorapidity intervals.

the ratio of the variance of the multiplicity distributions to the average multiplicity (i.e. the variance of the distributions  $\sigma / \langle N_c \rangle$  plotted in KNO variables) for p+Pb. The values are obtained directly from the data and are listed in the second column of the table. The third column lists the average number of particles in the  $\eta$  range considered. The last column gives the expected statistical variance for  $N_c$ . It is observed that on average the relative width  $\sigma / \langle N_c \rangle$  of the multiplicity distribution is consistent as being mainly determined by statistical fluctuations in the number of detected particles.

This unexpected observation prompted us to perform a similar analysis for the Si induced reactions. For this purpose the Si data of Figure 5.17 was fitted to a Gaussian. As in Table 5.1, results for Si+Pb, Si+Cu and Si+Al are listed in Tables 5.2, 5.3 and 5.4 respectively. One observes that except for the highest rapidity bin where the data are not Gaussian, the width of the distributions are almost constant for a given target. However, contrary to what is indicated in ref. [BA92B] and what is suggested by Figure 5.18, the Si data present a weak but significant dependence of the average fractional width  $\sigma / \langle N_c \rangle$  on the mass of the target nucleus. Furthermore, the width of the distributions are in general consistent, within error, with that expected from statistical fluctuations in the number of particle in the  $\eta$  range considered. The only exception is for the Pb target at small pseudorapidity where the measured width is significantly larger than that expected from statistical fluctuations. Thus one can conclude from the present analysis that contrary to what had been suggested, the multiplicity distributions do not really follow KNO scaling.

Table 5.2: Same as Table 5.1 for Si+Pb

$\eta$ Range	$\sigma / \langle N_c \rangle$	$N_c$	$1/\sqrt{N_c}$
0.88-1.41	0.225	47.6	0.145
1.41-1.96	0.209	43.9	0.151
1.96-2.56	0.203	31.4	0.177
2.52-3.18	0.202	19.2	0.228
3.18-3.86*	0.467	7.3	0.370
Average	0.210	35.5	0.175

\*  $\eta$  range not used in calculating the average.

Table 5.3: Same as Table 5.1 for Si+Cu

$\eta$ Range	$\sigma / \langle N_c \rangle$	$N_c$	$1/\sqrt{N_c}$
0.88-1.41	0.256	20.4	0.221
1.41-1.96	0.243	23.8	0.205
1.96-2.56	0.239	21.5	0.216
2.52-3.18	0.264	15.7	0.252
3.18-3.86*	0.467	7.9	0.356
Average	0.250	20.4	0.224

\*  $\eta$  range not used in calculating the average.

Table 5.4: Same as Table 5.1 for Si+Al

$\eta$ Range	$\sigma / \langle N_c \rangle$	$N_c$	$1/\sqrt{N_c}$
0.88-1.41	0.288	11.7	0.292
1.41-1.96	0.275	15.8	0.252
1.96-2.56	0.266	16.1	0.249
2.52-3.18	0.275	14.5	0.263
3.18-3.86*	0.481	8.3	0.347
Average	0.276	14.5	0.264

\*  $\eta$  range not used in calculating the average.

## Chapter 6

### SUMMARY AND CONCLUSIONS

Transverse energy and charged particle multiplicity in 14.6 GeV/c p+Al and p+Pb collisions have been studied using ES14 setup at BNL-AGS. The distribution of transverse energy was measured in the pseudorapidity range  $-2.3 < \eta < 4.7$  and charged particle multiplicity was measured in the pseudorapidity range  $0.9 < \eta < 3.4$ .

As the target nuclear mass increases, the pseudorapidity spectrum of transverse energy and charged particle multiplicity show an increase in the central and target fragmentation regions, and the peak of the distributions exhibit a backward shift to lower rapidities. While only a small shift relative to the nucleon-nucleon center-of-mass rapidity ( $\eta = 1.7$ ) is observed for the lighter aluminum target, the peak of  $dE_T/d\eta$  shifts towards lower pseudorapidities by 0.9 units for the lead target. This result indicates the importance of secondary interactions in the dissipation of energy in reactions at AGS energy.

The correlation between the transverse energy and the charged particle multiplicity was also investigated in this experiment. The proton-nucleus data are dominated by fluctuations and display a very weak correlation between transverse energy and charged particle multiplicity, in contrast to what has been observed in nucleus-nucleus collisions.

From our data one has extracted the mean transverse energy per charged particle, which is observed to be relatively independent of pseudorapidity rapidity in the forward acceptance of the participant calorimeter. From the data measured with the target calorimeter, the transverse energy per particle has also been determined in the target fragmentation region using the detected energy cluster in the target calorimeter

acceptance as a measure of the particle multiplicity. The  $E_T$  per particle is observed to decrease significantly in that part of the pseudorapidity space. The mean energy per particle for the proton-nucleus reaction is found to be slightly lower than that observed with Si beam at the same energy per nucleon. Such a result is in agreement with the spectrometer data on the transverse momentum of the identified particles, confirming that a higher Boltzmann temperature is achieved in heavy-ion induced reactions.

The scaling property of the charged particle multiplicity has also been studied. This work was motivated by the observation that multiplicity distributions measured in Si-nucleus reactions at the ACS follow KNO scaling. Although the pseudorapidity dependence of the number of charged particles for the proton-nucleus data seems to be consistent with the KNO scaling, a more detailed study of both proton-nucleus and Si-nucleus data shows that the width of the multiplicity distribution is mainly determined by statistical fluctuations in the number of detected particles. Contrary to what had been suggested, the present study concludes that the pseudorapidity dependence of charged particle multiplicity distributions do not have scaling properties.

The experimental results have been compared with three theoretical models used to describe nucleus-nucleus collisions. RQMD and HIJET reproduce well the pseudorapidity distributions of transverse energy and charged particle multiplicity, while FRITIOF predicts too forward peaked pseudorapidity distributions for both observables. These models describe very well the observed trend of the correlation between transverse energy and charged particle multiplicity for the proton-nucleus collisions, but underestimate fluctuations. The models also reproduce well the measured average transverse energy per particle over the full pseudorapidity range of the present data. Although models like FRITIOF do not include rescattering, they can reproduce well the  $d\sigma/dE_T$  distributions in certain pseudorapidity range as well as the observed  $E_T$  per particle distributions.

In conclusion, the evolution of the measured global observables with the mass of the target in the proton-nucleus reactions reinforces the conclusion reached with heavier

beams that significant rescattering or multiple scattering is present and contributes to the evolution of the energy deposition in the colliding system. This must be taken into account in the models used to describe heavy-ion collisions since rescattering of the secondaries should strongly influence the space-time evolution of the energy density distribution in heavy-ion reactions and thus is relevant to the maximum energy density reached in such collisions.

The RQMD event generator reproduces very well all the features of the data. This adds confidence that this model provides a good representation of heavy-ion collisions at AGS energy as long as the system stays in the hadronic sector.

On the other hand, our simulations shows that models like FRITIOF that do not include rescattering fail to reproduce the pseudorapidity distribution of the transverse energy and particle multiplicity. However the total transverse energy produced by FRITIOF is close to that observed. This explains that this model has some success in reproducing experimental  $d\sigma/dE_T$  distributions and also the  $dE_T/d\eta$  distribution for symmetric or nearly symmetric systems like Si+Al or Au+Au.

## Appendix A

### Members of the E814 Collaboration

J. Barrette<sup>3</sup>, R. Bellwied<sup>6</sup>, P. Braun-Munzinger<sup>6</sup>, W.E. Cleland<sup>5</sup>, T. Cormier<sup>8</sup>, G. David<sup>6</sup>, J. Dee<sup>6</sup>, G.E. Diebold<sup>9</sup>, O. Dietzsch<sup>7</sup>, E. Duck<sup>1</sup>, M. Fatyga<sup>1</sup>, D. Fox<sup>2</sup>, S. Gilbert<sup>3</sup>, S.V. Greene<sup>9</sup>, J.V. Germani<sup>9</sup>, J.R. Hall<sup>4</sup>, T.K. Hemmick<sup>9</sup>, N. Herrmann<sup>6</sup>, R.W. Hogue<sup>1</sup>, B. Hong<sup>6</sup>, K. Jayananda<sup>5</sup>, D. Kraus<sup>5</sup>, B. Shiva Kumar<sup>9</sup>, R. Lacasse<sup>3</sup>, D. Lissauer<sup>1</sup>, W.J. Llope<sup>6</sup>, T. Ludlam<sup>1</sup>, R. Majka<sup>9</sup>, D. Makowiecki<sup>1</sup>, S.K. Mark<sup>3</sup>, J.T. Mitchell<sup>9</sup>, M. Muthuswamy<sup>6</sup>, E. O'Brien<sup>1</sup>, V. Polychronakos<sup>1</sup>, C. PrunEAU<sup>3</sup>, M. Rosati<sup>3</sup>, F.S. Rotondo<sup>9</sup>, J. Sandweiss<sup>9</sup>, N.C. da Silva<sup>7</sup>, J. Simon-Gillo<sup>8</sup>, U. Sonnadara<sup>5</sup>, J. Stachel<sup>6</sup>, H. Takai<sup>1</sup>, E.M. Takagui<sup>5</sup>, T.G. Throwe<sup>1</sup>, G. Wang<sup>3</sup>, L. Waters<sup>6</sup>, C. Winter<sup>9</sup>, K. Wolf<sup>8</sup>, D. Wolfe<sup>4</sup>, C.L. Woody<sup>1</sup>, N. Xu<sup>6</sup>, Y. Zhang<sup>6</sup>, C. Zhang<sup>5</sup>, Z. Zou<sup>6</sup>

1. Brookhaven National Lab, Upton, NY 11973
2. Los Alamos National Laboratory, Los Alamos, NM 87545
3. McGill University, Montreal, Canada H3A 2B2
4. University of New Mexico, Albuquerque, NM 87131
5. University of Pittsburgh, Pittsburgh, PA, 15260
6. State University of New York, Stony Brook, NY 11794
7. Universidade de São Paulo, São Paulo, Brazil
8. Texas A&M University, College Station, TX 77843
9. Yale University, New Haven, CT 06511

## References

1. [AB92] T. Abbott *et al.*, the E802 collaboration, Phys. Rev. **C45**, 2933(1992).
2. [AB91] T. Abbott *et al.*, the E802 collaboration, Phys. Rev. Lett. **66**, 1567(1991).
3. [AB89] T. Abbott *et al.*, the E802 collaboration, Nucl. Phys. **A498**, 67c(1989).
4. [AD92] D.L. Adams *et al.*, the E810 collaboration, Nucl. Phys. **A544**, 335c(1992).
5. [AH94] L. Ahle *et al.*, the E802 collaboration, Nucl. Phys. **A566**, 443c(1994).
6. [AK94] Y. Akiba *et al.*, the E802 collaboration, Nucl. Phys. **A566**, 269c(1994).
7. [AK92] Y. Akiba *et al.*, the E802 collaboration, Nucl. Phys. **A544**, 445c(1992).
8. [ANS7] B. Andersson, G. Gustafson, and B. Nilsson-Almqvist, Nucl. Phys. **B281**, 289(1987).
9. [BA94] J. Barrette *et al.*, the E814 collaboration, Nucl. Phys. **A566**, 183c(1994).
10. [BA93A] J. Barrette *et al.*, the E814 collaboration, Z. Phys. **C59**, 211(1993).
11. [BA93B] J. Barrette *et al.*, the E814 collaboration, Phys. Rev. Lett. **70**, 2996(1993).
12. [BA92A] J. Barrette *et al.*, the E814 collaboration, Nucl. Phys. **A544**, 137c(1992).

13. [BA92B] J. Barrette *et al.*, the ES14 collaboration, Phys. Rev. **C46**, 312(1992).
14. [BA92C] J. Barrette *et al.*, the ES14 collaboration, Phys. Rev. **C45**, S19(1992).
15. [BA90A] J. Barrette *et al.*, the ES14 collaboration, Phys. Rev. **C64**, 1219(1990).
16. [BA90B] J. Barrette *et al.*, the ES14 collaboration, Phys. Rev. **C41**, 1512(1990).
17. [BA90C] J. Barrette *et al.*, the ES14 collaboration, Phys. Lett. **B252**, 550(1990).
18. [BA90D] G. Baym *et al.* in *Proceedings of the Workshop on Heavy Ion Physics at the AGS*, edited by Ole Hansen, BNL-44911, 1990, p.102.
19. [BJS83] J.D. Bjorken, Phys. Rev. **D27**, 140(1983).
20. [BAS9] J. Bartke, Int. J. Mod. Phys. **A4**, No.6 1319(1990).
21. [BOS1] R.K. Bock, T. Hansl-Kozanecka and T.P. Shah, Nucl. Inst. Meth. **186**, 533(1981).
22. [BR87] R. Brun *et al.*, *GEANT 3.15 User's Guide*, CERN Data Handling Division Report Nr. DD/EE/84-1, revised 92-1, 1992 (unpublished)
23. [BU88] W. Busza and R. Ledoux, Annu. Rev. Nucl. Part. Sci., **38**, 119(1988).
24. [CAS9] M. Tincknell in *Hadronic Matter in Collision 1988*, edited by P. Carruthers and J. Rafelski, World Scientific, Singapore, 1989, p.387.
25. [CH93] Z. Chen, Int. J. Mod. Phys. **E2**, No.2 285(1993).
26. [CIS7] N. Cindro, W. Greiner and R. Caplar (Editors), *Frontiers of Heavy-ion Physics*, Dubrovnik, Croatia, 1987.
27. [CO88] J.B. Costales, Internal Report to E802 Collaboration, E-802-MEM-8, 1988.

28. [FR87] S. Fredriksson *et al.*, Physics Reports, 144, Nos. 4 and 5, 187(1992).
29. [FO92] D. Fox *et al.*, Nucl. Inst. Meth. A317, 474(1992).
30. [GI94] S. Gilbert, Ph.D. Thesis, McGill University, Montréal, (1994), in preparation
31. [GO94] Michel Gonin for the E802/E866 collaboration, Nucl. Phys. A566, 601c(1994).
32. [HA94] H. Hamagaki *et al.*, Nucl. Phys. A566, 27c(1994).
33. [HI93] HIPAGS'93, Proc. Workshop on Heavy-Ion Physics at the AGS, Massachusetts Institute of Technology, January 13-15, 1993, Edited by G.S.F. Stephans, S.G. Steadman and W.L. Kehoe, MITLNS-2158.
34. [HI90] HIPAGS'90, Proc. Workshop on Heavy-Ion Physics at the AGS, Brookhaven National Laboratory, January 5-7, 1990, Edited by Ole Hansen, BNL-44911
35. [JA91] M. Jayawanda, Ph.D. Thesis, University of Pittsburg, Pittsburg, (1991)
36. [LA91] R. Lacasse, M.S. Thesis, McGill University, Montréal, (1991)
37. [LO94] R.S. Longacre *et al.*, the ES10 collaboration, Nucl. Phys. A566, 167c(1994).
38. [KO72] Z. Koba, H.B. Nielson and P. Oleson, Nucl. Phys. B40, 317(1972).
39. [LI86] D. Lissauer *et al.*, *Proposal 814 submitted to the AGS Program Committee*, BNL, (1986), unpublished.
40. [LI91] D. Lissauer *et al.*, *Proposal 877 submitted to the AGS Program Committee*, BNL, (1991), unpublished
41. [LUS5] T. Ludlam, A. Pfoh, and A. Shor, Proceedings of RHIC Workshop I, ed. P. Haustein and C. Woody, BNL-51921, 373(1985).
42. [Mi92] J. Mitchell, Ph.D. Thesis, Yale University, (1992)

43. [NA92] S. Nagamiya, Nucl. Phys. **A544**, 5c(1992).
44. [NA88] S. Nagamiya, Nucl. Phys., **A488**, 3c(1988).
45. [NA85] S. Nagamiya, Progress in Part. and Nucl. Phys., **15**, 363(1985).
46. [PA92] Y. Pang, T. J. Schlagel and S. H. Kahana, Phys. Rev. Lett. **68**, 2743(1992).
47. [PA90] F.E. Paige and S.D. Protopopescu, *ISAJET: A Monte Carlo Event Generator for pp and p $\bar{p}$  Interactions*, Brookhaven National Laboratory, 1990
48. [QM93] Quark Matter '93, Proc. Tenth Int. Conf. on Ultra-Relativistic Nucleus-Nucleus Collisions, Borlange, Sweden, June 20-24, 1993. Edited by E. Stenlund, H.A. Gustafsson, A. Oskarsson and I. Otterlund, Nucl. Phys., **A566**, (1994).
49. [QM91] Quark Matter '91, Proc. ninth Int. Conf. on Ultra-Relativistic Nucleus-Nucleus Collisions, Gatlinburg, Tennessee, November 11-15, 1991, Edited by T.C. Awes, F.E. Obenshain, F. Plasil, M.R. Strayer and C.Y. Wong, Nucl. Phys., **A544**, Nos. 1,2, (1992).
50. [SC93] H. Schmidt and J. Schukraft J. Phys. G **19**, 1705(1993).
51. [SH90] B. Shiva Kumar *et al.*, *the E814 Colloboration*, Proc. Workshop on Heavy Ion Physics at the AGS (HIPAGS), March 1990, O. Hansen, editor, BNL-44911.
52. [SH89] A. Shor and R. Longacre, Phys. Lett. **B218**, 100(1989).
53. [SI91] J. Simon-Gillo, Ph.D. Thesis, Texas A and M University, College Station, Texas, (1991)
54. [SO90] H. Sorge, A. von Keitz, R. Mattiello, H. Stöcker and W. Greiner, Phys. Lett **B243**, 7(1990).
55. [SO89] H. Sorge, H. Stöcker, and W. Greiner, Ann. Phys. **192**, 266(1989).
56. [ST92] J. Stachel and G.R. Young, Annu. Rev. Nucl. Part. Sci., **42**, 537(1992).

57. [ST91] J. Stachel, Quark Matter '90, Nucl. Phys., **A525**, 23c(1991).
58. [TI88] M. Tincknell, Hadronic Matter in Collision 1988, Ed. P. Carruthers and J. Rafelski, World Scientific, Singapore, 378(1989).
59. [WA90] L. Waters, Ph.D. Thesis, State University of New York at Stony Brook, (1990)
60. [WE93] K. WERNER, Phys. Reports **A232**, Nos. 2-5, 87(1993).
61. [WE90] K. WERNER, Proc. Workshop on Heavy Ion Physics at the AGS (HIPAGS), March 1990, O. Hansen, editor, BNL-44911.
62. [ZA92] W.A. Zajc for the E802 collaboration, Nucl. Phys. **A544**, 237c(1992).
63. [Zh93] Z. Zhang, Ph.D. Thesis, University of Pittsburg, Pittsburg, (1993)